



Theses and Dissertations

---

2024-11-11

## Advancements of a Vibration-Based Sound Power Method for Direct and Indirect Applications

Ian Charles Bacon  
*Brigham Young University*

Follow this and additional works at: <https://scholarsarchive.byu.edu/etd>



Part of the [Physical Sciences and Mathematics Commons](#)

---

### BYU ScholarsArchive Citation

Bacon, Ian Charles, "Advancements of a Vibration-Based Sound Power Method for Direct and Indirect Applications" (2024). *Theses and Dissertations*. 10585.

<https://scholarsarchive.byu.edu/etd/10585>

This Dissertation is brought to you for free and open access by BYU ScholarsArchive. It has been accepted for inclusion in Theses and Dissertations by an authorized administrator of BYU ScholarsArchive. For more information, please contact [ellen\\_amatangelo@byu.edu](mailto:ellen_amatangelo@byu.edu).

Advancements of a Vibration-Based Sound Power Method for Direct and Indirect Applications

Ian Charles Bacon

A dissertation submitted to the faculty of  
Brigham Young University  
in partial fulfillment of the requirements for the degree of

Doctor of Philosophy

Micah R. Shepherd, Chair  
Scott D. Sommerfeldt  
Tracianne B. Neilsen  
Brian E. Anderson  
Jonathan D. Blotter

Department of Physics and Astronomy

Brigham Young University

Copyright © 2024 Ian Charles Bacon

All Rights Reserved



## ABSTRACT

### Advancements of a Vibration-Based Sound Power Method for Direct and Indirect Applications

Ian Charles Bacon  
Department of Physics and Astronomy, BYU  
Doctor of Philosophy

This dissertation advances the Vibration-Based Sound Power (VBSP) method for measuring the sound power of vibrating structures, expanding its applicability to a wider range of geometries and acoustic environments. The research addresses limitations of traditional sound power measurement techniques by developing an alternative method that achieves near Precision (Grade 1) accuracy while maintaining feasibility for *in situ* testing under uncontrolled acoustic conditions.

After reviewing the current VBSP method in Unit 1, Unit 2 introduces stitching techniques for Scanning Laser Doppler Vibrometer (SLDV) measurements, enabling accurate 3D scans and extending the method to complex geometries. Experimental validation is provided for baffled simply curved plates and arbitrarily curved plates. The method also estimates sound power in uncontrolled acoustic environments, where traditional approaches are less effective. Initial work on thin unbaffled flat plates is presented, with a practical demonstration using pickleball paddles as a representative unbaffled configuration.

Unit 3 addresses the computational demand of constructing radiation resistance ( $\mathbf{R}$ ) matrices, a key limitation of the VBSP method. Symmetry-based techniques leveraging acoustic reciprocity and geometric symmetries are applied to reduce computational demands by up to 75% for unbaffled structures. For baffled configurations, translational symmetry of acoustic reciprocity between elements results in the  $\mathbf{R}$  matrix having Toeplitz symmetry, reducing the computational complexity from  $n^2$  to  $n$ , where  $n$  is the number of mesh elements.

Unit 4 introduces an indirect VBSP (I-VBSP) method to estimate sound power from encased sources, achieving near Precision (Grade 1) accuracy relative to the ISO 3741 standard using only a single surface scan. Validated on a Bluetooth speaker, this approach provides a simplified alternative to conventional methods, offering a practical solution for sound power measurement in structures with encased noise sources.

Overall, this dissertation demonstrates that the VBSP method serves as a viable alternative to conventional sound power techniques, effectively applied across various geometries and scenarios. While the current VBSP method does not accommodate structures with multiple vibrating surfaces in contact, the I-VBSP method can theoretically achieve this by enclosing a structure and scanning one vibrating side. This research lays the foundation for future studies through the development of a generalized  $\mathbf{R}$  matrix and application of foundational symmetries, enhancing the understanding of acoustic radiation from vibrating structures. Ultimately, this work aims to reduce noise pollution in consumer products through improved acoustic design and measurement strategies.

Keywords: acoustic radiation modes, acoustic radiation resistance matrix, baffled arbitrarily curved plates, baffled simply curved plates, bisymmetry, centrosymmetry, indirect vibration-based sound power method, I-VBSP method, mylar, pickleball paddle dynamics, scanning laser Doppler vibrometer, SLDV, thin unbaffled flat plates, Toeplitz symmetry

## ACKNOWLEDGMENTS

I thank my Heavenly Father for this opportunity to further my education at BYU and for my advisors, Dr. Scott Sommerfeldt and Dr. Micah Shepherd. Dr. Sommerfeldt's unwavering patience and belief in my potential gave me the confidence to continue this journey after starting with no acoustics background. I appreciate his genuine support for my academic and personal growth. He showed me that simpler solutions often exist for complex problems and the need for meaningful comparisons in research. His encouragement to maintain balance in my life has had a lasting impact that I strive for. I also thank Dr. Micah Shepherd for his support as my follow-up advisor, which helped me uncover skills I never knew I had and fostered my independence as a researcher.

I thank Dr. Brian Anderson for challenging my ideas, which clarified my thinking, and Dr. Jon Blotter for his vibration expertise, passion for research, and facility use. Special thanks to Dr. Traci Neilsen for her mentorship and inclusion at BYU; her guidance greatly improved my communication. I also thank Beky Quintero and Jesse Crisler for their invaluable writing feedback.

To my friends and colleagues Cameron Vongsawad, Trent Bates, Adam Kingsley, Brian Patchett, Jeremy Peterson, Tysum Ruchti, and John Ebeling—thank you. Your encouragement helped me persevere through challenges, and collaborating with you made this journey enjoyable. I appreciate Daniel Hodge, Raju Baral, Dr. Leishman, Dr. Colton, and Dr. Peatross for their help in preparing for the qualifying exam and enhancing my understanding of physics. Thanks to Jay Clift, Andrew Basham, Rylee Russell, Josh Mills, and Jacob Sampson for your support.

Finally, I express my deepest appreciation to my wife, Emily. Your belief in me, love, and cheerfulness have anchored me during long days and late nights. Your presence has been a source of strength. I sincerely thank everyone else who supported me. Funding was provided by the National Science Foundation and BYU's College of Physical and Mathematical Sciences.

## TABLE OF CONTENTS

<b>LIST OF TABLES .....</b>	<b>vii</b>
<b>LIST OF FIGURES .....</b>	<b>viii</b>
<b>Dissertation Outline .....</b>	<b>xix</b>
<b>Unit 1 Introduction .....</b>	<b>1</b>
<b>Chapter 1 Research Context and Objectives .....</b>	<b>2</b>
1.1 Background and Motivation .....	2
1.2 Overview of Models Used for Sound Power Estimation .....	5
1.3 The Vibration-Based Sound Power Method .....	7
1.4 My Contribution .....	9
1.5 References .....	11
<b>Unit 2 Advancing the Vibration-Based Sound Power Method .....</b>	<b>16</b>
<b>Chapter 2 Transition from 2D to 3D Measurements .....</b>	<b>17</b>
2.1 Previous Methodology .....	17
2.2 Stitching .....	18
2.3 References .....	27
<b>Chapter 3 Extension to Baffled Simply Curved Plates .....</b>	<b>28</b>
3.1 Introduction .....	28
3.2 Required Copyright Notice .....	30
3.3 Title .....	31
3.4 Authors and Affiliations .....	31
3.5 Abstract .....	32
3.6 Introduction .....	33
3.7 Curved Plate Radiation Resistance Matrix Theory .....	36
3.7.1 Simply Curved Plate Radiation Resistance Matrix .....	36
3.7.2 Uniform Theory of Diffraction .....	40
3.8 Experimental Setups for Sound Power Measurement .....	44
3.8.1 Design and Setup of the Three Curved Plates .....	44
3.8.2 The VBSP Method for 3D Structures .....	46
3.8.3 Reverberation Chamber and the ISO 3741 Standard .....	47
3.8.4 Anechoic Chamber and the ISO 3745 Standard .....	48
3.8.5 The VBSP Method in Uncontrolled Acoustic Environments .....	49
3.9 Experimental Results of Sound Power Measurements .....	51
3.9.1 Reverberant (Diffuse) Environment .....	51
3.9.2 Anechoic and Uncontrolled Acoustic Environments .....	54
3.10 Conclusions .....	56
3.11 Acknowledgments .....	58
3.12 Appendix 3A .....	59
3.12.1 Introduction .....	59

3.12.2	Bessel and Hankel Functions .....	59
3.12.3	Fock-type Airy Function .....	60
3.12.4	The Fock V Coupling Function.....	61
3.13	References .....	62
<b>Chapter 4</b>	<b>Application to Baffled Arbitrarily Curved Plates.....</b>	<b>67</b>
4.1	Introduction .....	67
4.2	Required Copyright Notice .....	68
<b>Chapter 5</b>	<b>Expansion for Thin Unbaffled Flat Plates .....</b>	<b>79</b>
5.1	Introduction .....	80
5.2	The Unbaffled Distance Matrix.....	83
5.3	Unbaffled Flat Plate <b>R</b> Matrix.....	86
5.4	Experimental Setup .....	90
5.5	VBSP Results .....	94
5.6	Computational Model.....	97
5.7	Conclusions .....	100
5.8	References .....	101
<b>Chapter 6</b>	<b>Vibroacoustic Response of Pickleball Paddles .....</b>	<b>103</b>
6.1	Title .....	104
6.2	Authors and Affiliations.....	104
6.3	Abstract .....	105
6.4	Introduction .....	106
6.5	Hammer Testing.....	109
6.5.1	Pickleball Paddles .....	109
6.5.2	Experimental Setup.....	109
6.5.3	Hammer Test Data .....	112
6.5.4	Pickleballs .....	114
6.6	Vibrometer Testing.....	115
6.7	Acoustic Testing.....	117
6.8	Sound Power Prediction .....	119
6.9	Results .....	127
6.10	Conclusions .....	129
6.11	Acknowledgments .....	130
6.12	References .....	131
<b>Chapter 7</b>	<b>A Generalized Radiation Resistance Matrix .....</b>	<b>132</b>
7.1	Introduction .....	133
7.2	Numerical Model Process .....	133
7.3	Acoustic Radiation Modes .....	134
7.4	Radiation Resistance Approximation.....	135
7.5	Conclusions .....	139
7.6	References .....	140
<b>Unit 3</b>	<b>Symmetry Enhancements for Sound Power Computation.....</b>	<b>141</b>
<b>Chapter 8</b>	<b>Symmetry in Baffled R Matrices .....</b>	<b>142</b>

8.1	Introduction .....	142
8.2	Required Copyright Notice .....	143
<b>Chapter 9 Symmetry in Unbaffled R Matrices and KHIT.....</b>		<b>151</b>
9.1	Introduction .....	152
9.2	Review of <b>R</b> Matrices and the Role of Symmetry .....	154
9.3	Reflection Symmetry and Bisymmetric Matrices .....	158
9.4	Rotational Symmetry and Centrosymmetric Matrices .....	160
9.5	Translational Symmetry and Toeplitz Matrices .....	164
9.6	Unbaffled Flat Plate Radiation Resistance Matrix .....	166
9.7	Impact of Element Selection and Arrangement .....	169
9.8	Conclusions .....	173
9.9	Acknowledgments .....	175
9.10	References .....	176
<b>Unit 4 Development of the Indirect Vibration-Based Sound Power (I-VBSP) Method.....</b>		<b>182</b>
<b>Chapter 10 Method Development for Cube Enclosures .....</b>		<b>183</b>
10.1	Introduction .....	183
10.2	Required Copyright Notice .....	184
<b>Chapter 11 Source Placement and VA One Validation.....</b>		<b>195</b>
11.1	Introduction .....	195
11.2	Required Copyright Notice .....	196
<b>Chapter 12 Development for Rectangular Enclosures .....</b>		<b>211</b>
12.1	Introduction .....	212
12.2	VA One Model .....	215
12.3	Experimental Work .....	217
12.4	Results .....	219
12.5	Conclusions .....	222
12.6	References .....	224
<b>Chapter 13 Rectangular Enclosure Calibration.....</b>		<b>225</b>
13.1	Introduction .....	225
13.2	Required Copyright Notice .....	226
<b>Unit 5 Conclusions and Future Work.....</b>		<b>237</b>
<b>Chapter 14 Summary of Findings and Contributions .....</b>		<b>238</b>
<b>Chapter 15 Recommendations for Future Research.....</b>		<b>241</b>
15.1	VBSP Method.....	241
15.2	Symmetry .....	241
15.3	I-VBSP Method.....	242
15.4	References .....	244

## LIST OF TABLES

3.1	Summary of the curved plate dimensions used for experimental testing. ....	49
3.2	The absolute difference in sound power measurements for the MR, TR, and WR curved plates using the VBSP method and ISO 3741. Similarly, for the WR curved plate in two uncontrolled acoustic environments.....	59
3A.1	The first ten zeros of $W_2(\tau)$ : $W_2(\tau'_n) = 0$ and $W'_2(\tau_n) = 0$ , where $\tau_n =  \tau_n e^{-\frac{j\pi}{3}}$ and $\tau'_n =  \tau'_n e^{-\frac{j\pi}{3}}$ .....	63
6.1	<i>(color online)</i> The names of the 13 paddles with their corresponding fundamental frequencies and damping ratios. ....	116
6.2	The peak acoustic frequency compared to the frequency of the first membrane mode for ten paddles shows that the first membrane mode is responsible for the primary noise signature produced by each paddle. The table also illustrates the damping ratios of the first membrane mode and the percent difference between vibration and acoustic frequencies. ....	122
12.1	OTO band sound power levels from ISO 3741 and I-VBSP method. The difference in the overall sound power level is 0.8 dB, and the difference in OTO band sound power levels is within 1 to 2 dB from 315 Hz to 8 kHz. ....	225

## LIST OF FIGURES

1.1	Illustration of different approaches used to model the radiation from vibrating structures similar to Fig. 4 in Hill <i>et al.</i> [18]. .....	5
2.1	A 2D scan of a cylinder conducted by Cameron Jones [2] in BYU's reverberation chamber, demonstrating the scanning and rotation process at the time. (Used with permission.).....	18
2.2	A Polytec PSV-A-450 Reference Object was used to perform the 3D calibration of the three SLDV scan heads for a flat plate. The coordinates are in millimeters.....	19
2.3	a) The stitched 3D response of a flat plate. b) The 3D response of a flat plate without stitching.....	19
2.4	Part of the 3D global coordinate report from Dr. Eric McKell (BYU Department of Manufacturing Engineering) on the cylinder. Along the axis of the cylinder are three rings of register points. The coordinates are in mm to match the unit option on the SLDV easily when performing 3D calibration. A minimum of five register points is required for the calibration.....	21
2.5	The cylinder setup for a 3D vibration measurement in BYU's large reverberation chamber.....	22
2.6	An example of one section of the cylinder scanned using the 3D SLDV.....	22
2.7	On the left is a 3D measurement of one section of the cylinder with stitched response of the six sections of the cylinder shown on the right.....	23

2.8	The vibrational motion at resonance illustrates the stitched response of the cylinder. This figure also shows a rigid body mode and three modes of the cylinder in (a)-(d) respectively. ....	23
2.9	A stitched 3D response of a simply curved plate. The stitch is not as clean as previous figures due to the alignment of the scan grids and the overlap.....	24
2.10	A stitched 3D response of an arbitrarily curved plate with two different radii of curvature. ....	25
2.11	A stitched 3D response in five sections of an arbitrarily curved plate with three different radii of curvature, hereafter referred to as the “M-curved plate.” This stitching was more seamless for the five sections. ....	25
3.1	Schematic of the infinitely baffled cylinder geometry. The non-rigid portion of the cylinder is discretized, and the radiator described in Eqn. 3.3 is highlighted in blue (left). An end view of the cylinder of radius $a$ shows the dimensions of an arbitrary element, represented by the length $z_2 - z_1$ and width $a(\theta_2 - \theta_1)$ (right). ....	37
3.2	The geometric values and the area of an element in the baffled curved plate are shown. These elements represent the radiators that produce the pressure at the $p$ th location in response to vibration at the $q$ th location. ....	39
3.3	This plot shows the real part, imaginary part, and magnitude of the hard Fock $V$ coupling function. As $\xi$ approaches zero, $V(\xi)$ behaves similarly to a $\text{sinc}(kd_{pq})$ function and showcases the asymptotic behavior near zero for small curvature or large frequency.....	43



3.4	Annotated image of the TR curved plate, with the outer surface on the left and the inner surface on the right. The width corresponds to the clamped edges. Plate excitation was achieved through a piezoelectric transducer (PZT). .....	45
3.5	Images of (a) the MR curved plate and (b) the WR curved plate. ....	45
3.6	An example scan section taken over the surface of the TR curved plate to measure complex surface velocities. After each section is scanned and then stitched together to provide a complete response of the plate. During post-processing, the stitching is smoothed in case of any imperfect overlap of the sections. ....	47
3.7	Experimental setup of the DMS (arc array) and wall inside an anechoic chamber. ....	49
3.8	Experimental setup of the WR curved plate in a hallway inside BYU's engineering building. ....	50
3.9	Experimental setup of the WR curved plate outside of BYU's engineering building. ....	51
3.10	Results of the sound power measurements using the VBSP method compared to the ISO 3741 standard for (a) the TR curved plate and (b) the WR curved plate. ....	53
3.11	Results of the sound power measurements using the VBSP method compared to the ISO 3741 standard for the MR curved plate. Background noise results from the reverberation chamber are also included (ISO 3741, Plate off). ....	54
3.12	The VBSP results of the WR curved plate in two uncontrolled acoustic environments compared to the ISO 3741 and ISO 3745 standards. ....	55
3A.1	Contours in the complex $\tau$ -plane for Fock V integration. ....	60

5.1	The front of the unbaffled flat plate (dark gray) and the back (light gray) are shown in an “unfolded” view. Elements “1” on the front and “4” on the back are used for illustration. The shaded element “4” represents the element is now on the same side of the plate as element “1.” .....	84
5.2	The distances between the front element “1” and the back element “4” are indicated by blue arrows connecting the element centers. The shortest path is selected for the corresponding $d_{ij}$ entry. ....	85
5.3	An example distance matrix, $\mathbf{d}$ , for a thin unbaffled flat plate with a 9 x 9 element grid on the front and back of a thin unbaffled flat plate. This includes all combinations of elements on the front with itself, front and back, back and front, and back with itself.....	86
5.4	A 242 x 242 $\mathbf{R}_{\text{unbaffled}}$ matrix displaying the four 121 x 121 $\mathbf{R}$ matrices from Eqn. 5.1 for an 11 x 11 scan grid of an unbaffled flat plate. The submatrices are normalized to illustrate the double-layered Toeplitz and centrosymmetric symmetries better. The computation of sound power using Eqn. 5.1 employs this form of the $\mathbf{R}$ matrix. ....	87
5.5	Flat plate setup for an SLDV scan in a reverberation chamber. ....	91
5.6	SLDV scan of the thin flat plate illustrating a 63x63 grid (~6.6 mm spacing).....	92
5.7	Fundamental mode of the thin flat plate with free boundary conditions from the SLDV.....	92
5.8	Nine of the structural modes of the unbaffled flat plate with free boundary conditions obtained from the SLDV scan.....	93

5.9	Sound power levels ( $L_w$ ) of the thin unbaffled aluminum plate, showing the ISO 3741 standard results (red) and the VBSP results using $\mathbf{R}_{\text{unbaffled}}$ (black). An additional ISO 3741 measurement with the SLDV active (blue) indicates that the extra noise did not bias the VBSP results.....	95
5.10	Sound power levels ( $L_w$ ) of the thin unbaffled aluminum plate, comparing results from the ISO 3741 standard (red), the VBSP method using the $\mathbf{R}_{\text{unbaffled}}$ matrix (Eqn. 5.7) (blue), and the VBSP method using the $\hat{\mathbf{R}}_{\text{unbaffled}}$ matrix (Eqn. 5.10) (black). The $\hat{\mathbf{R}}_{\text{unbaffled}}$ matrix was derived using the dipole relationship $1 - \text{sinc}(kd_{\text{unbaffled}})$ for two out-of-phase sources. The overall sound power level differences between the ISO 3741 and the VBSP methods are 0 dB and 2.8 dB, respectively.....	96
5.11	Sound power levels ( $L_w$ ) of the thin unbaffled steel plate, comparing results from the ISO 3741 standard (red), the VBSP method using the $\mathbf{R}_{\text{unbaffled}}$ matrix (Eqn. 5.7) (blue), and the VBSP method using the $\hat{\mathbf{R}}_{\text{unbaffled}}$ matrix (Eqn. 5.10) (black). The $\hat{\mathbf{R}}_{\text{unbaffled}}$ matrix was derived using the dipole relationship $1 - \text{sinc}(kd_{\text{unbaffled}})$ for two out-of-phase sources. The overall sound power level differences between the ISO 3741 and both VBSP methods is 0.2 dB.....	97
5.12	The thin unbaffled steel flat plate used in this work, created in COMSOL®. The 41x41 element grid shown matches the grid used for the VBSP method. The complex acoustic pressure produced by a single element excited at 2,475 Hz is shown across the front of the plate. 2,475 Hz is about three times the acoustic wavelength of the plate's characteristic dimension.....	98

5.13	a) Sound pressure level (SPL) distribution on the front side of a thin unbaffled flat plate in COMSOL® when a corner element is excited, with the remaining elements acting as receivers. b) SPL distribution on the back side of the same plate, where a significant drop in pressure compared to the front is expected. ....	99
6.1	<i>(color online)</i> The relative size and shapes of different paddles and rackets used in sports with average dimensions and individual graphics obtained from dimensions.com. ....	107
6.2	<i>(color online)</i> a) Twelve pickleball paddles used for testing, identified by brand name and color/pattern (left to right): Lifetime, Gonex, Panel Sound, Monarch, checkered Ghost, Triangle, red Ghost, Niupipo, green Stryker, Bykuta, purple Stryker, and blue Stryker. b) The 13th paddle, labeled YDXIZCQ, resting on bungee cords in preparation for impact testing, showing the coarse grid. c) The red Ghost paddle is set up for impact testing with the fine grid, indicating the impact locations at the grid intersections. ....	110
6.3	The average FRF for the purple Stryker paddle using the coarse configuration measured through impact testing showing the natural frequencies of the paddle, as recorded by accelerometers in the coarse configuration.....	112
6.4	<i>(color online)</i> An example of six of the vibrational modes common to the paddles. These images came from the red Ghost model, but other paddles showed similar shapes, though at different frequencies. (a) lengthwise bending, (b) first torsion, (c) torsion about diagonal, (d) first membrane, (e) second bending, (f) second torsion about axis. ....	113

6.5	( <i>color online</i> ) a) The average FRF for the pickleball using 30 measured FRFs (obtained from ten input locations and the three accelerometer locations as outputs). b) A Niupipo brand pickleball set up for impact testing.....	115
6.6	( <i>color online</i> ) The SLDV experimental set up for the pickleball paddles.....	116
6.7	( <i>color online</i> ) Eight operational deflection shapes of the Triangle pickleball paddle obtained from the SLDV.....	117
6.8	( <i>color online</i> ) The acoustic response (blue) overlaying the vibrational response of the purple Stryker paddle (black) highlighting this vibrational mode as the primary contributor to the sound the paddle produces. ....	118
6.9	SLDV scan locations on the Red Ghost paddle used to measure vibration response, with horizontal and vertical spacings of 8.6 mm and 10.1 mm, respectively. (a) Front side scan locations. (b) Backside scan locations aligned identically in the xy-plane but offset in the z-direction by the paddle thickness, as used in sound power calculations. .....	120
6.10	Distance matrix produced from the Red Ghost paddle scan data. ....	121
6.11	Comparison of sound power predictions for the Bykuta paddle using the VBSP method, calculated with three <b>R</b> matrix models: the monopole-based model (Eqn. 1.1, black), the dipole-based model (Eqn. 5.10, blue), and the combination model (Eqn. 5.7, burnt orange).....	122
6.12	Comparison of sound power predictions for the Red Ghost paddle using the VBSP method, following the same approach as in Fig. 6.11. ....	124

6.13	Comparison of sound power predictions for the Triangle paddle using the VBSP method, following the same approach as in Fig. 6.11. ....	125
6.14	Sound power comparison of the Red Ghost and Triangle pickleball paddles using the combined <b>R</b> matrix (Eqn. 5.7) to assess relative loudness across OTO bands. Both paddles were excited at the upper corner. ....	126
7.1	Two generated simply curved plate ARMs illustrated in 3D. ....	136
7.2	ARMs for a 0.5 m square plate at 480 Hz. a) Flat plate ARMs. b) Simply curved plate ARMs with a 1 cm radius of curvature, both mapped to the same square plate dimensions. ....	136
9.1	An illustration depicting the unique portion of a rectangle, square, and circle. ....	159
9.2	An illustration depicting the centrosymmetry or inversion symmetry about the central element. (Author generated; image inspired by Quartl, CC BY-SA 3.0 < <a href="https://creativecommons.org/licenses/by-sa/3.0/">https://creativecommons.org/licenses/by-sa/3.0/</a> >, via Wikimedia Commons) ....	161
9.3	A double-layered centrosymmetric pattern is observed in the 25 x 25 <b>d<sub>FB</sub></b> and <b>d<sub>BF</sub></b> matrices for a square flat plate, assuming constant grid spacing. The first layer of symmetry within the blocks indicates symmetry about the vertical centerline of the flat plate. The second layer of symmetry within the entire matrix shows inversion symmetry around the central element of the plate. The symmetries are evident when any element or block in the matrix is visually rotated by 180° around the central element or block, resulting in identical configurations. ....	162

9.4	<p>A double-layered Toeplitz pattern is found within the 25 x 25 <math>\mathbf{d}_{FF}</math> and <math>\mathbf{d}_{BB}</math> matrices for a square flat plate, assuming constant grid spacing. The x-coordinate distances between any two element radiators exhibit Toeplitz symmetry within each block (constant values along each diagonal), while the y-coordinate distances reveal Toeplitz symmetry between blocks in the entire matrix (constant values along each block diagonal).....</p>	166
9.5	<p>A 162 x 162 <math>\mathbf{d}_{unbaffled}</math> matrix displaying the four 81 x 81 <math>\mathbf{d}</math> matrices from Eqn. 9.12 for a 9 x 9 grid of elements used for an unbaffled flat plate. This form of the <math>\mathbf{d}</math> matrix was used to compute sound power using Eqn. 9.13. ....</p>	168
9.6	<p>(a) A circular plate discretized into 126 voussoir elements. The numbers are used to identify the number of elements within each ring. (b) The 126 x 126 <math>\mathbf{d}</math> matrix for this circular plate. The diagonal blocks are Toeplitz due to the symmetry within each ring. The off-diagonal blocks have centrosymmetry, bisymmetry, and block-circulant symmetry within them. ....</p>	170
9.7	<p>(a) A circular plate discretized into 210 rectangular elements. The dots represent the element centers. (b) The 210 x 210 <math>\mathbf{d}</math> matrix for this circular plate using the rectangular discretization. The diagonal blocks are Toeplitz due to the symmetry within each row or column. This <math>\mathbf{d}</math> matrix now has double-layered centrosymmetry. This symmetry comes from the centerline and central point of the plate. ....</p>	171

12.1	a) A model of the rectangular enclosure used for the I-VBSP method. The steel frame (black) clamps down the thin flexible aluminum panel (light gray). The ports in the bottom are necessary for cabling and are sealed off, using weather stripping during measurements. The hinge on the left tilts the enclosure back so the source can easily be moved internally for testing. b) A blender inside the enclosure. This view shows treated foam with constrained layer damping between the boxes. ....	213
12.2	Illustration of an acoustic source radiating within the enclosure and the acoustically induced vibration of the aluminum panel which radiates the transmitted sound power. ....	214
12.3	a) The VA One model showing the blue BEM measurement surfaces, and the purple hemisphere represents the fluid. b) The BEM model of the enclosure shows the flexible panel (green), location of the internal noise source (purple), and air cavity (gray).....	216
12.4	a) The vibroacoustic response of the enclosure showing the first mode of the enclosure and mode of the clamped plate. b) A higher order mode of the enclosure. ....	217
12.5	The microphones set up to take the ISO 3741 measurement and the absorption measurements with the experimental set up in the reverberation chamber. ....	218
12.6	a) The SLDV set up to scan the aluminum plate while using a point-and-shoot laser as a reference for the source. b) Illustration of the Polytec SLDV scanning the vibrating surface of the flat plate to obtain sound power using the VBSP method. The pale laser color shows where the laser had been during the scanning process. ....	219



12.7	The sound power levels for a Bluetooth speaker in the rectangular enclosure obtained via the VBSP method and ISO 3741 are compared.....	220
12.8	Comparison of I-VBSP and free-field ISO 3741 for sound power levels of the Bluetooth speaker outside of the enclosure. ....	221
15.1	An example of the discretized circular plate using the methods described in [9]. ....	243

# Dissertation Outline

This dissertation attempts to bring together all advances that have been made toward the development of the vibration-based sound power (VBSP) method. Since many of the chapters have been previously published as papers, references appear at the end of each chapter.

Each of the five primary units of the dissertation focuses on a different aspect of sound power measurement with a particular emphasis on the development and application of the VBSP method, as outlined below in the content and objectives of each chapter.

## **Unit 1: Introduction**

Provides an overview of the research background and introduces the VBSP method.

- **Chapter 1: Research Context and Objectives**

Discusses the benefits and limitations of traditional sound power measurement techniques, the necessity for an alternative method, introduces the VBSP method, and outlines the research objectives.

## **Unit 2: Advancing the Vibration-Based Sound Power Method**

Explores the advancements in applying the VBSP method to different geometries and conditions.

- **Chapter 2: Transition from 2D to 3D Measurements**

- Discusses the evolution from 2D to 3D measurements, improving accuracy through scanning and stitching techniques.

- **Chapter 3: Extension to Baffled Simply Curved Plates**

- Extends the VBSP method to baffled curved plates, validating theoretical models with experimental data.

- **Chapter 4: Application to Baffled Arbitrarily Curved Plates**

- Applies the VBSP method to arbitrarily curved geometries, focusing on radiation resistance matrices.

- **Chapter 5: Expansion for Thin Unbaffled Flat Plates**

- Adapts the VBSP method for thin unbaffled plates, addressing modifications in the radiation resistance matrix.

- **Chapter 6: Vibroacoustic Response of Pickleball Paddles**
  - Demonstrates the VBSP method's application to pickleball paddles for vibroacoustic analysis.
- **Chapter 7: A Generalized Radiation Resistance Matrix**
  - Introduces a generalized radiation resistance matrix formulation for baffled structures using  $\text{sinc}(kd)$  functions.

### **Unit 3: Symmetry Enhancements for Sound Power Computation**

Focuses on leveraging symmetry in acoustic structures to optimize computational processes.

- **Chapter 8: Symmetry in Baffled R Matrices**
  - Examines how symmetry in baffled structures expedites the computation of radiation resistance matrices.
- **Chapter 9: Symmetry in Unbaffled R Matrices and KHIT**
  - Expands symmetry applications for unbaffled structures and KHIT to enhance computational efficiency.

### **Unit 4: Development of the Indirect Vibration-Based Sound Power (I-VBSP) Method**

Details the formulation, calibration, and validation of the I-VBSP method for sound power estimation from sources where direct vibration measurements are impractical.

- **Chapter 10: Method Development for Cube Enclosures**
  - Introduces the foundational development of the I-VBSP method, using a cube enclosure with a mylar face.
- **Chapter 11: Optimal Source Placement and VA One Model Validation**
  - Focuses on calibration improvements and VA One model validation.

- **Chapter 12: Development for Rectangular Enclosures**
  - Discusses the transition to a rectangular enclosure with a thin aluminum face and experimental testing.
- **Chapter 13: Rectangular Enclosure Calibration**
  - Details a refined calibration for a rectangular enclosure.

## **Unit 5: Conclusions and Future Work**

Restates research findings and proposes future directions for sound power measurement.

- **Chapter 14: Summary of Findings and Contributions**
  - Summarizes key research outcomes and contributions.
- **Chapter 15: Recommendations for Future Research**
  - Proposes future work to refine computational techniques and expand methodological applications.

# Unit 1

## Introduction

This unit provides foundational concepts for understanding the scope of the research, beginning with an overview of traditional sound power measurement techniques, their benefits, their limitations, and the motivation for this study. The need for an accurate, versatile method, such as the Vibration-Based Sound Power (VBSP) method, is described, followed by the research objectives and contributions.

# Chapter 1 Research Context and Objectives

## 1.1 Background and Motivation

Sound power is the rate at which a source emits acoustic energy and is a key metric for assessing the noise produced by that source [1]. According to Sommerfeldt and Blotter [2], it is defined as “the main quantity by which consumer products, such as sound systems and kitchen appliances, are compared since sound power is a constant for a given source and is independent of location relative to the source.”

Despite its importance in product design and comparison, sound power testing can be both technically challenging and expensive, making it inaccessible for many companies. As a result, these factors often lead to a lack of sound power testing, which can result in products with suboptimal acoustic designs. This can negatively impact overall consumer perception and potentially pose risks to hearing [1].

The International Organization for Standardization (ISO) mandates that sound power must be determined through measurement [3], using two traditional methods:

1. **Microphones in a controlled acoustic environment** to sample energy density via pressure measurements,
2. **Acoustic intensity probes** to measure sound intensity around a source.

ISO has established ten standards for these methods, categorized into three accuracy grades based on the standard deviation of results, application requirements, and repeatability of results.

- **Precision (Grade 1)** provides the highest accuracy and requires the use of controlled environments such as anechoic or reverberation chambers. It is used for certification and

in situations where high precision is necessary, maintaining a tolerance of  $\pm 0.5$  dB to  $\pm 1$  dB across most frequency bands.

- **Engineering (Grade 2)** offers good accuracy in environments with some controlled variables, suitable for most industrial needs, typically maintaining a tolerance of  $\pm 1$  dB to  $\pm 2$  dB across most frequency bands.
- **Survey (Grade 3)**, the least accurate grade, is utilized for preliminary *in situ* assessments with minimal control over environmental conditions. It employs basic instruments and straightforward procedures, making it quick and easy to perform. It usually maintains a tolerance of  $\pm 3$  dB or more.

While these methods adhere to established standards and provide significant benefits, they also present limitations that can render them impractical for many applications.

Pressure-based methods, as outlined in ISO 3741-3745 [4]-[8], can deliver Precision (Grade 1) and Engineering (Grade 2) results. However, these methods require controlled environments, such as anechoic or reverberation chambers, which limits their applicability to specific testing scenarios and makes them impractical for *in situ* measurements. The other two standards, ISO 3746 [9] and ISO 3747 [10], are less stringent in terms of acoustic environment, but their lower accuracy limits their reliability.

ISO 3746 requires a reflective acoustic plane near the noise source being measured and can only yield Survey (Grade 3) results. ISO 3747 requires that the noise source occur in a reverberant environment and provides Engineering (Grade 2) results for broadband measurements but only Survey (Grade 3) results for narrowband or tonal noise sources. Furthermore, ISO 3747 stipulates that background noise must be significantly lower than the noise source being measured.



The intensity-based methods outlined in ISO 9614-1 to ISO 9614-3 are highly accurate, yet they come with certain constraints [11]-[13]. These methods require the noise source to be completely or hemispherically enclosed, which can pose difficulties when dealing with sources on large, reflective surfaces. These standards are capable of measuring sound power across various sources but often struggle to isolate contributions from smaller sources or individual components. Furthermore, their effectiveness diminishes according to the limited bandwidth of the acoustic intensity probes used and the influence of absorptive materials in the measurement area.

Both pressure- and intensity-based methods are particularly sensitive to environmental variables such as background noise, fluid flow, and temperature fluctuations. These variables highlight the need for a viable alternative that can overcome such constraints when needed. One such alternative is the Vibration-Based Sound Power (VBSP) method, detailed in Sec 1.3, which offers a more robust approach for achieving accurate sound power measurements even in variable conditions.

A third approach involves vibration measurements. Currently, ISO provides two technical specifications (ISO/TS 7849-1:2009 and ISO/TS 7849-2:2009) for such measurements, though these can only achieve Engineering (Grade 2) accuracy [14], [15]. These methods estimate sound power based on equivalent baffled pistons and are intended for use when intensity standards cannot be applied, particularly when significant radiation is due to structural vibration. To date, no vibration-based standards yield Precision (Grade 1) results.

## 1.2 Overview of Models Used for Sound Power Estimation

Beyond the established ISO standards, researchers have developed several theoretical and computational methods to estimate sound power, each with its unique strengths and weaknesses. As depicted in Fig. 1.1, these approaches tend to be divided by how they model the radiating structure. The **Sum of Modal Contributions** developed by Snyder and Tanaka [16] offers a systematic approach for analyzing structural vibrations by aggregating modal contributions. This method performs well when detailed modal data is accessible, yet it can fall short for structures with complex or poorly understood modal behavior.

The second model presented in Fig. 1.1 is Elliott and Johnson's **Method of Elementary Radiators** [17], a method that offers a strong framework for sound power estimation and is the foundation for the VBSP method. The advantages and disadvantages associated with this approach appear below, beginning in Sec. 1.3. Finally, the **Array of Monopole Sources** method developed by Snyder [19] is an effective way to model sound radiation using multipoles, but it faces difficulties with spatial resolution and accuracy in complex configurations.

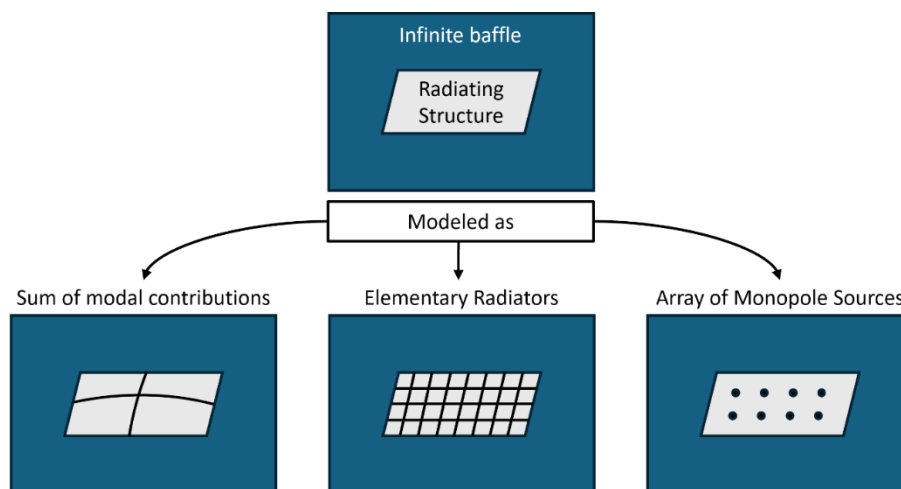


**Figure 1.1:** Illustration of different approaches used to model the radiation from vibrating structures similar to Fig. 4 in Hill *et al.* [18].

Beyond the models illustrated in Fig. 1.1, other models have been developed to assess acoustic radiation from vibrating structures and calculate sound power. One such model is Hashimoto's **Discrete Calculation Method** [20], which is known for its precision in low-frequency and noisy environments. It excels in measuring structure-borne sound, which is crucial for applications like construction sites. However, the method's computational intensity and difficulty with complex geometries limit its broader application.

Fahnline and Koopmann's **Lumped Parameter Model** [21], [22], based on the Kirchoff-Helmholtz integral equation with Neumann boundary conditions, simplifies sound power estimation by dividing the vibrating surface into discrete elements, each acting as an independent source and represented by a multipole. This approach reduces computational demands and is effective for early design stages, allowing for quick acoustic predictions without detailed modal data. However, the model's accuracy decreases as structural complexity increases, and its precision relies heavily on how well the elements represent the actual acoustic behavior. Additionally, solving for source amplitudes can become computationally intensive.

These methods along with computational techniques such as finite element analysis (FEA) and the boundary element method (BEM) contribute to the diverse landscape of sound power estimation. Each method offers valuable insights into the behavior of radiating structures, yet they also have shortcomings in terms of practicality, accuracy, and computational demands.

Another approach for estimating sound power from a vibrating structure focuses on the vibration itself, known as the VBSP method.

### 1.3 The Vibration-Based Sound Power Method

The VBSP method, currently under development at Brigham Young University (BYU), offers a promising alternative that effectively addresses several environmental limitations of existing sound power standards while consistently achieving near Precision (Grade 1) results.

The method uses a 3D scanning laser Doppler vibrometer (SLDV) on the vibrating surface, with elements being created around every measurement location across the surface. These elements are designed to be much smaller than the structural and acoustic wavelength, allowing each element to radiate as an acoustic monopole source [23]. Finally, the method is concluded by measuring the surface velocities from which the complex velocities normal to the surface for each element,  $\mathbf{v}_e$ , can be computed [24], [25].

A key advantage of the VBSP method lies in its reliance on the Kirchhoff-Helmholtz integral theorem (KHIT) for computing the pressure radiated by each of these discrete elements [26]-[28]. This theorem allows the calculation of the sound pressure field of any closed arbitrary body vibrating harmonically at a specific frequency by distributing monopole and dipole sources across the surface and using superposition to add up the field. In cases where baffling is present, the KHIT greatly simplifies to the Rayleigh integral, which is used for computing the monopole pressure radiated by every element of the surface [26]-[28]. Whether obtained through the KHIT or the Rayleigh integral, the pressure produced by the vibration of a single element is referred to as self-impedance.

In addition to self-impedance, the overall pressure radiated by the vibrating structure also depends on mutual impedance. Mutual impedance describes how one element influences the pressure radiated by every other element that is close, relative to a wavelength due to the coupled nature of these elements. The acoustic radiation impedance matrix,  $\mathbf{Z}$ , for this vibrating structure

contains combination of self- and mutual impedances. The real part of  $\mathbf{Z}$ , known as the radiation resistance matrix,  $\mathbf{R}$ , describes the acoustic radiation produced by any arbitrarily vibrating surface.

An example of the radiation resistance matrix for a baffled flat plate is given by [29], [30]:

$$\mathbf{R}(\omega) = \frac{\omega^2 \rho_0 A_e^2}{4\pi c} \begin{bmatrix} 1 & \frac{\sin kd_{12}}{kd_{12}} & \dots & \frac{\sin kd_{1N}}{kd_{1N}} \\ \frac{\sin kd_{21}}{kd_{21}} & 1 & \ddots & \vdots \\ \vdots & \ddots & \ddots & \vdots \\ \frac{\sin kd_{N1}}{kd_{N1}} & \dots & \dots & 1 \end{bmatrix} \quad (1.1)$$

where:

- $A_e$  is the area of a single radiator (assumed constant in this equation),
- $c$  is the speed of sound in the surrounding fluid,
- $d_{ij}$  is the distance between the  $i^{th}$  element and the  $j^{th}$  element,
- $k$  is the acoustic wavenumber, and
- $\rho_0$  is the fluid density surrounding the vibrating surface.

The VBSP method uses  $\mathbf{R}$  and  $\mathbf{v}_e$  to estimate sound power,  $\Pi$ , for a given frequency,  $\omega$ :

$$\Pi(\omega) = \mathbf{v}_e^H(\omega) \mathbf{R}(\omega) \mathbf{v}_e(\omega), \quad (1.2)$$

where  $(\cdot)^H$  denotes a Hermitian transpose. The VBSP estimations of  $\Pi$  were validated by researchers at BYU using the ISO 3741 standard in the university's reverberation chamber, achieving Precision (Grade 1) results. Additionally, two specific standards were employed to encompass the general frequency range pertinent to this research, including one-third octave bands with mid-band frequencies ranging from 100 to 10,000 Hz. Details regarding these standards will be provided in the following section.

ISO 3741 requires a diffuse acoustic field, which can only be achieved above the Schroeder frequency of the reverberation chamber. Below this frequency, the chamber exhibits significant variations in acoustic pressure due to the presence of few resonant modes. The Schroeder

frequency of the reverberation chamber used was about 385 Hz. Sound power estimates obtained via ISO 3741 were compared to the VBSP method estimates for frequencies above 385 Hz, as reported in Chs. 3-5 and 11-12 for different vibrating structures.

Below 385 Hz, the ISO 3745 standard cannot ensure Precision (Grade 1) results. Consequently, for frequencies below the 400 Hz OTO band, the ISO 3745 standard is used. An example of using ISO 3745 is found in Ch. 3. For assessing frequencies above 10,000 Hz, the ISO 9295 standard is recommended [31], though such assessment exceeds the scope of this dissertation.

## 1.4 My Contribution

This dissertation focuses on expanding the capabilities of the VBSP method beyond its prior application to flat plates and cylindrical shells using 2D vibration scans [32]-[34]. The initial phase introduces stitching techniques for SLDV measurements, enabling accurate 3D scans and extending the method's applicability to more geometries. Experimental results confirm the effectiveness of this approach for baffled simply curved plates and arbitrarily curved plates. The VBSP method also demonstrates potential for *in situ* testing under uncontrolled acoustic environments with background noise, providing a viable alternative when traditional methods are impractical. Preliminary work is also presented on adapting the method for thin unbaffled flat plates. Additionally, an initial investigation into estimating the sound power of pickleball paddles is included as a practical demonstration of the VBSP method's utility for unbaffled flat configurations.

Despite these advancements, extending the VBSP method to complex coupled structures is left as future work. To lay the groundwork for such extensions, this dissertation introduces the development of a generalized **R** matrix as a foundation for broader applications.

Another significant focus of this research is addressing the high computational demand associated with constructing  $\mathbf{R}$  matrices, a critical bottleneck for the VBSP method. Symmetry-based computational techniques are implemented to reduce this demand, particularly for baffled and unbaffled configurations. However, the issue of lengthy scan times for large structures or high-frequency analyses is not addressed and remains open for future exploration.

Furthermore, this dissertation introduces an indirect approach for measuring sound power from commercial products with steady acoustic responses, achieving near Precision (Grade 1) accuracy relative to the ISO 3741 standard. This method also shows promise for estimating sound power levels by scanning only a single surface with a simple geometry, such as a rectangle or circle, instead of all radiating surfaces of a structure.

Overall, this research advances the development of an efficient, vibration-based sound power estimation technique that can be applied under diverse conditions. Although it does not yet extend to coupled or complex structures, the groundwork established here paves the way for a more precise alternative standard for sound power measurement. These contributions enhance the understanding of acoustic radiation from vibrating structures and support improved acoustic design, ultimately helping to reduce noise pollution in consumer products.

## 1.5 References

- [1] T. P. Bates, I. C. Bacon, J. D. Blotter, and S. D. Sommerfeldt, “Vibration-based sound power measurements of arbitrarily curved panels,” *J. Acoust. Soc. Am.* **151**(2), 1171-1179 (2022). doi: 10.1121/10.0009581
- [2] S. D. Sommerfeldt, J. D. Blotter, National Science Foundation Project Proposal, BYU.
- [3] ISO 3740:2019, *Acoustics – Determination of sound power levels of noise sources – Guidelines for the use of basic standards*, 3rd ed. (International Organization for Standardization, Geneva, 2019).
- [4] ISO 3741, *Acoustics – Determination of sound power levels and sound energy levels of noise sources using sound pressure – Precision methods for reverberation test rooms*, 4th ed. (International Organization for Standardization, Geneva, 2010).
- [5] ISO 3743-1, *Acoustics – Determination of sound power levels and sound energy levels of noise sources using sound pressure – Engineering methods for small movable sources in reverberant fields – Part 1: Comparison method for a hard-walled test room*, 2nd ed. (International Organization for Standardization, Geneva, 2010).
- [6] ISO 3743-2, *Acoustics – Determination of sound power levels and sound energy levels of noise sources using sound pressure – Engineering methods for small movable sources in reverberant fields – Part 2: Methods for special reverberation test rooms*, 2nd ed. (International Organization for Standardization, Geneva, 2018).
- [7] ISO 3744, *Acoustics – Determination of sound power levels and sound energy levels of noise sources using sound pressure – Engineering methods for an essentially free field over a reflecting plane*, 3rd ed. (International Organization for Standardization, Geneva, 2010).



- [8] ISO 3745, *Acoustics – Determination of sound power levels and sound energy levels of noise sources using sound pressure – Precision methods for anechoic rooms and hemi-anechoic rooms*, 3rd ed. (International Organization for Standardization, Geneva, 2012).
- [9] ISO 3746, *Acoustics – Determination of sound power levels and sound energy levels of noise sources using sound pressure – Survey method using an enveloping measurement surface over a reflecting plane*, 3rd ed. (International Organization for Standardization, Geneva, 2010).
- [10] ISO 3747, *Acoustics – Determination of sound power levels and sound energy levels of noise sources using sound pressure – Engineering/survey methods for use in situ in a reverberant environment*, 3rd ed. (International Organization for Standardization, Geneva, 2010).
- [11] ISO 9614-1:1993, *Acoustics – Determination of sound power levels of noise sources using sound intensity – Part 1: Measurement at discrete points*, 1st ed. (International Organization for Standardization, Geneva, 1993).
- [12] ISO 9614-2:1996, *Acoustics – Determination of sound power levels of noise sources using sound intensity – Part 2: Measurement by scanning*, 1st ed. (International Organization for Standardization, Geneva, 1996).
- [13] ISO 9614-3:2002, *Acoustics – Determination of sound power levels of noise sources using sound intensity – Part 3: Precision method for measurement by scanning*, 1st ed. (International Organization for Standardization, Geneva, 2002).
- [14] ISO/TS 7849-1:2009, *Acoustics – Determination of airborne sound power levels emitted by machinery using vibration measurement – Part 1: Survey method using a fixed radiation factor*, 1st ed. (International Organization for Standardization, Geneva, 2009).

- [15] ISO/TS 7849-2:2009, *Acoustics – Determination of airborne sound power levels emitted by machinery using vibration measurement – Part 2: Engineering method including determination of the adequate radiation factor*, 1st ed. (International Organization for Standardization, Geneva, 2009).
- [16] S. D. Snyder and N. Tanaka, “On feedforward active control of sound and vibration using vibration error signals,” *J. Acoust. Soc. Am.* **94**(4), 2181-2193 (1993). doi: 10.1121/1.407489
- [17] S. J. Elliott and M. E. Johnson, “Radiation modes and the active control of sound power,” *J. Acoust. Soc. Am.* **94**(4), 2194-2204 (1993). doi: 10.1121/1.407490
- [18] S. G. Hill, S. D. Snyder, and N. Tanaka, “Acoustic based sensing of orthogonal radiating functions for three-dimensional noise sources: Background and experiments,” *J. Sound Vib.* **318**(4-5), 1050-1076 (2008). doi: 10.1016/j.jsv.2008.04.044
- [19] S. D. Snyder, N. C. Burgan, and N. Tanaka, “An acoustic-based modal filtering approach to sensing system design for active control of structural acoustic radiation: theoretical development,” *Mech. Syst. Signal Process.* **16**(1), 123-139 (2002). doi: 10.1006/mssp.2001.1436
- [20] N. Hashimoto, “Measurement of sound radiation efficiency by the discrete calculation method,” *Appl. Acoust.* **62**(4), 429-446 (2001). doi: 10.1016/S0003-682X(00)00025-6
- [21] J. B. Fahnlne and G. H. Koopman, “A lumped parameter model for the acoustic power output from a vibrating structure,” *J. Acoust. Soc. Am.* **100**(6), 3539-3547 (1996). doi: 10.1121/1.417330

- [22] J. B. Fahnlne and G. H. Koopman, “Numerical implementation of the lumped parameter model for the acoustic power output of a vibrating structure,” *J. Acoust. Soc. Am.* **102**(1), 179-192 (1997). doi: 10.1121/1.419781
- [23] F. Fahy and P. Gardonio, *Sound radiation by vibrating structures, in Sound and Structural Vibration, in Radiation, Transmission and Response*, 2nd ed. (Academic Press, Oxford, UK, 2007), pp. 165-175.
- [24] I. Bacon, S. D. Sommerfeldt, and J. D. Blotter, “Determination of radiated sound power from acoustic sources using the VBSP method and a mylar boundary,” *Proc. Mtgs. Acoust.* **46**, 065003 (2022). doi: 10.1121/2.0001663
- [25] I. C. Bacon, S. D. Sommerfeldt, and J. D. Blotter, “Developing an indirect vibration-based sound power method to determine the sound power radiated from acoustic sources,” *Proc. Mtgs. Acoust.* **50**, 065003 (2022). doi: 10.1121/2.0001732
- [26] M. Junger and D. Feit, *Sound, Structures, and Their Interaction*, 2nd ed. (The MIT Press, Cambridge, MA, 1986), pp. 75-90, 313-341.
- [27] A. D. Pierce, *Acoustics: An Introduction to Its Physical Principles and Applications*, (Springer, Cham, Switzerland, 2019), pp. 222-229.
- [28] J. W. B. S. Rayleigh, *The Theory of Sound*, 2nd. ed. (Dover Publications, New York, 1896), pp. 143-148.
- [29] J. Milton, J. Cheer, and S. Daley, “Experimental identification of the radiation resistance matrix,” *J. Acoust. Soc. Am.* **145**, 2885-2894 (2019). doi: 10.1121/1.5102167
- [30] M. R. Bai and M. Tsao, “Estimation of sound power of baffled planar sources using radiation matrices,” *J. Acoust. Soc. Am.* **112**, 876-883, (2002). doi: 10.1121/1.1499133

- [31] ISO 9295, “Acoustics - Determination of high-frequency sound power levels emitted by machinery and equipment,” 2nd ed. (International Organization for Standardization, Geneva, 2005).
- [32] C. B. Goates, C. B. Jones, S. D. Sommerfeldt, and J. D. Blotter, “Sound power of vibrating cylinders using the radiation resistance matrix and a laser vibrometer,” *J. Acoust. Soc. Am.* **148**(6), 3553–3561, (2020). doi: 10.1121/10.0002870
- [33] C. B. Jones, C. B. Goates, J. D. Blotter, and S. D. Sommerfeldt, “Experimental validation of determining sound power using acoustic radiation modes and a laser vibrometer,” *Appl. Acoust.* **164**, 107254, (2020). doi: 10.1016/j.apacoust.2020.107254
- [34] P. Aslani, S. D. Sommerfeldt, and J. D. Blotter, “Analysis of external radiation from circular cylindrical shells,” *J. Sound Vib.* **408**, 154-167 (2017). doi: 10.1016/j.jsv.2017.07.021

# Unit 2

## Advancing the Vibration-Based Sound Power Method

This unit focuses on the continued development of the VBSP method, expanding its application from 2D to 3D geometries and enhancing its accuracy across 100 Hz to 10 kHz one-third octave (OTO) bands. The advancements include adjustments to accommodate both baffled and unbaffled structures, ensuring the method's versatility across various acoustic environments. Additionally, this unit introduces preliminary work toward the development of a generalized radiation resistance (**R**) matrix, paving the way for future extensions of the VBSP method to more complex geometries.

## Chapter 2 Transition from 2D to 3D Measurements

This chapter details the transition from 2D to 3D measurements in the VBSP method. It discusses how the VBSP method was originally implemented using 2D scans, the challenges encountered, and the advancements made through 3D scanning and the stitching process. As the sound power results for flat plates and cylinders have already been published using the VBSP method [1]-[3], this chapter focuses on the scanning and stitching techniques, highlighting the images of the stitched responses for various geometries. The sound power results for simply curved plates and arbitrarily curved plates are shown in Chs. 3 and 4.

### 2.1 Previous Methodology

In its initial implementation in BYU's reverberation chamber, the VBSP method used 2D scans to measure sound power, particularly for cylindrical structures. This process involved scanning a single strip of the cylinder and then slightly rotating the cylinder and repeating the scan until the entire surface was covered. While effective, this method was time-consuming and labor-intensive. For instance, as shown in Fig. 2.1, Jones *et al.* [3] performed a 2D scan of a cylinder, demonstrating that scanning at  $5^\circ$  increments required 72 rotations, with each rotation necessitating a separate scan. Although accurate, this approach was particularly slow and cumbersome, especially for larger structures.

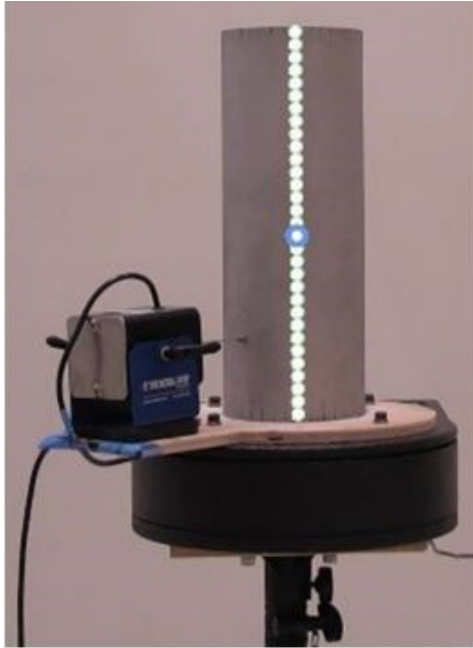


**Figure 2.1:** A 2D scan of a cylinder conducted by Cameron Jones [2] in BYU’s reverberation chamber, demonstrating the scanning and rotation process at the time. (Used with permission.)

## 2.2 Stitching

The introduction of a 3D scanning laser Doppler vibrometer (SLDV) enabled more comprehensive data collection with fewer scans. A stitching technique merged multiple scanned sections from different parts of a structure into a single, cohesive data set, which not only reduced scanning time but also improved accuracy and extended the method’s application to more complex geometries.

Research involved conducting sound power measurements on a known flat plate to become familiar with the equipment and methodology using the Polytec 3D calibration device (see Fig. 2.2). This included calibrating the three scan heads, scanning the flat plate in two halves, combining results to calculate sound power, and comparing a vibration mode from the combined scan (Fig. 2.3a) with that from a single scan (Fig. 2.3b), demonstrating excellent agreement.

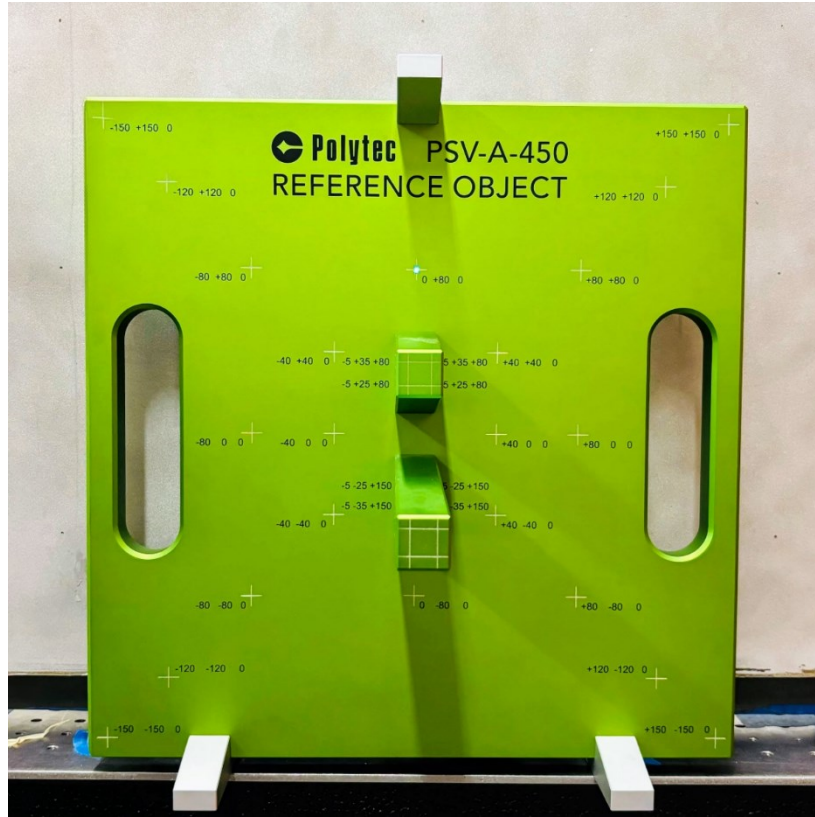


**Figure 2.2:** A Polytec PSV-A-450 Reference Object was used to perform the 3D calibration of the three SLDV scan heads for a flat plate. The coordinates are in millimeters.

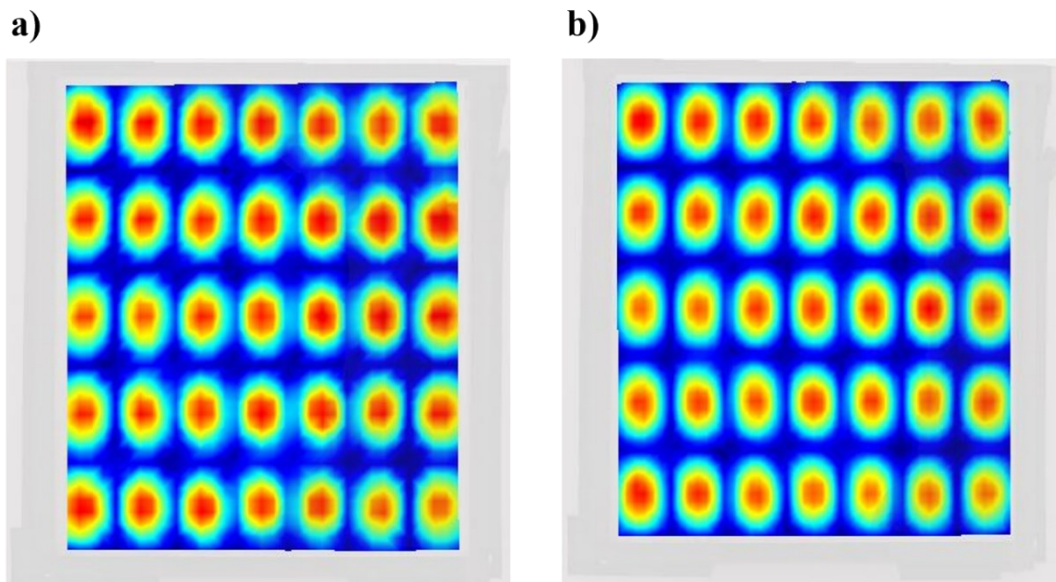


**Figure 2.3:** a) The stitched 3D response of a flat plate. b) The 3D response of a flat plate without stitching.



For cylindrical structures and curved plates, a global coordinate system was established on the surface using a 3D coordinate probe. This system was crucial for maintaining the correct positioning of the scans when they were combined. Figure 2.4 illustrates part of the 3D global coordinate system report for the cylinder, showing the setup used to ensure accurate alignment during the stitching process.

For example, a cylinder that previously required 72 scans can now be effectively captured in just six sections, using Polytec's PSV-500 3D SLDV, significantly reducing scan time while maintaining the accuracy of the sound power measurement. Figure 2.5 illustrates the experimental setup. A scan of one section of the cylinder is shown in Fig. 2.6, with the operational deflection shape of that section displayed in Fig. 2.7, which also presents the final stitched result of all six sections of the cylinder. Figure 2.8 further demonstrates how the stitched response enhances an understanding of the cylinder with additional modes of the cylinder also shown.

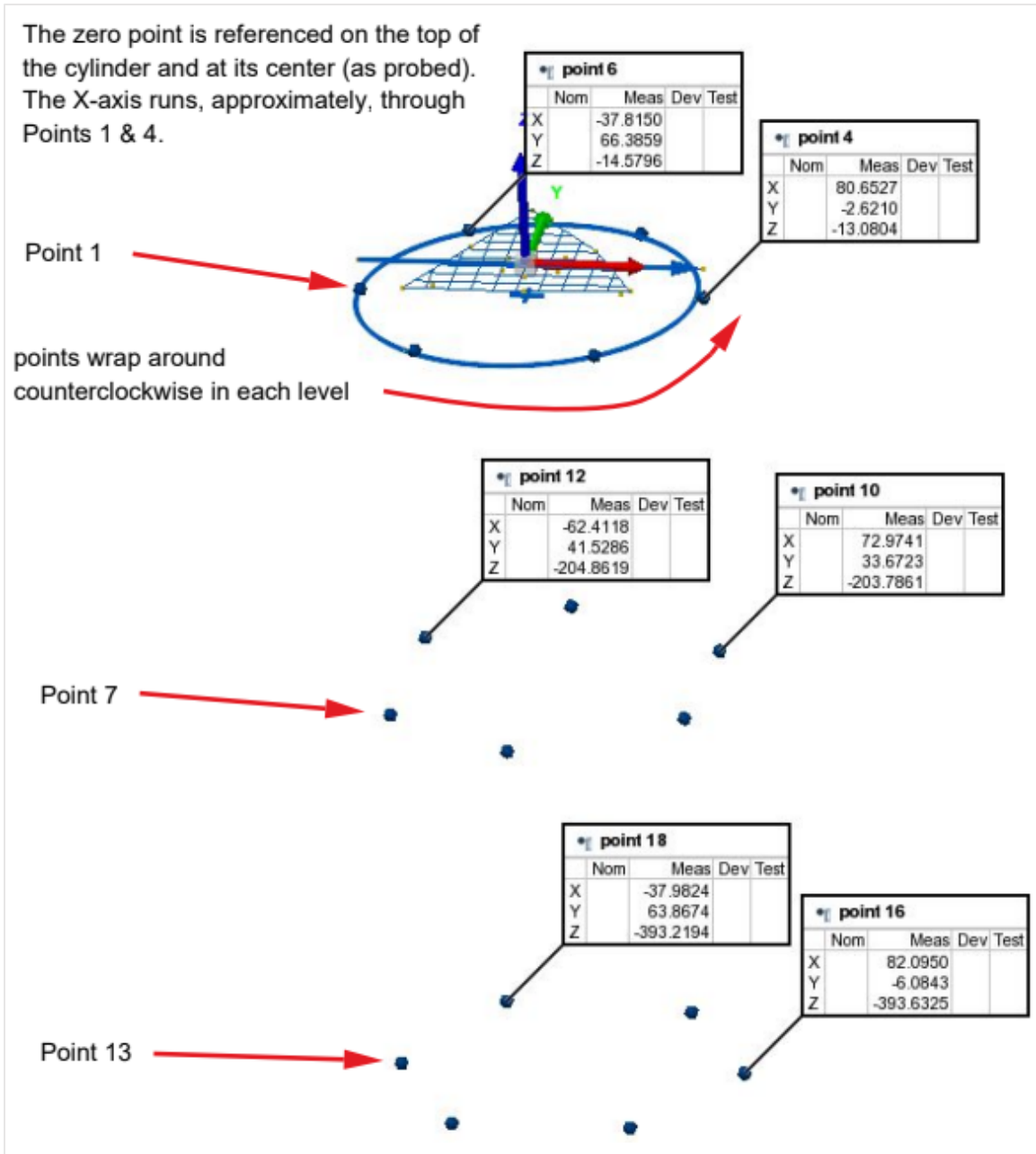


**Figure 2.4:** Part of the 3D global coordinate report from Dr. Eric McKell (BYU Department of Manufacturing Engineering) on the cylinder. Along the axis of the cylinder are three rings of register points. The coordinates are in mm to match the unit option on the SLDV easily when performing 3D calibration. A minimum of five register points is required for the calibration.



**Figure 2.5:** The cylinder setup for a 3D vibration measurement in BYU's large reverberation chamber.

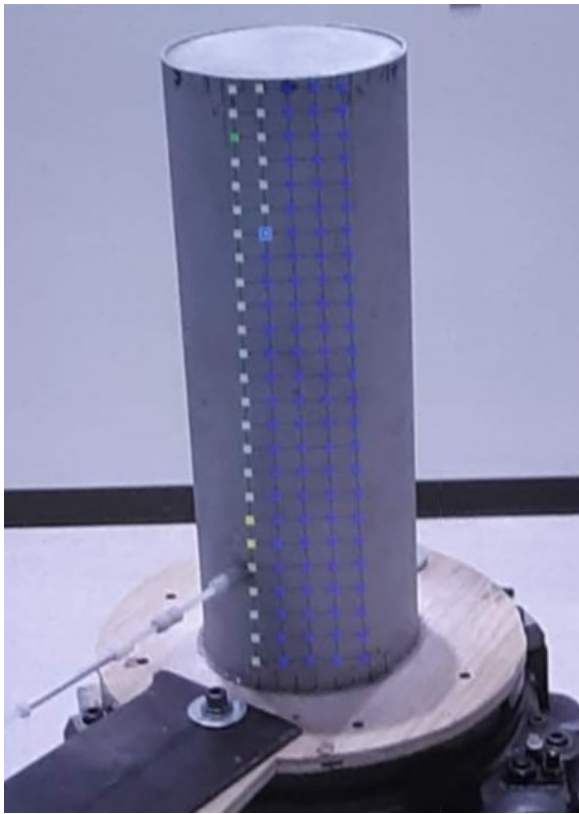


**Figure 2.6:** An example of one section of the cylinder scanned using the 3D SLDV.

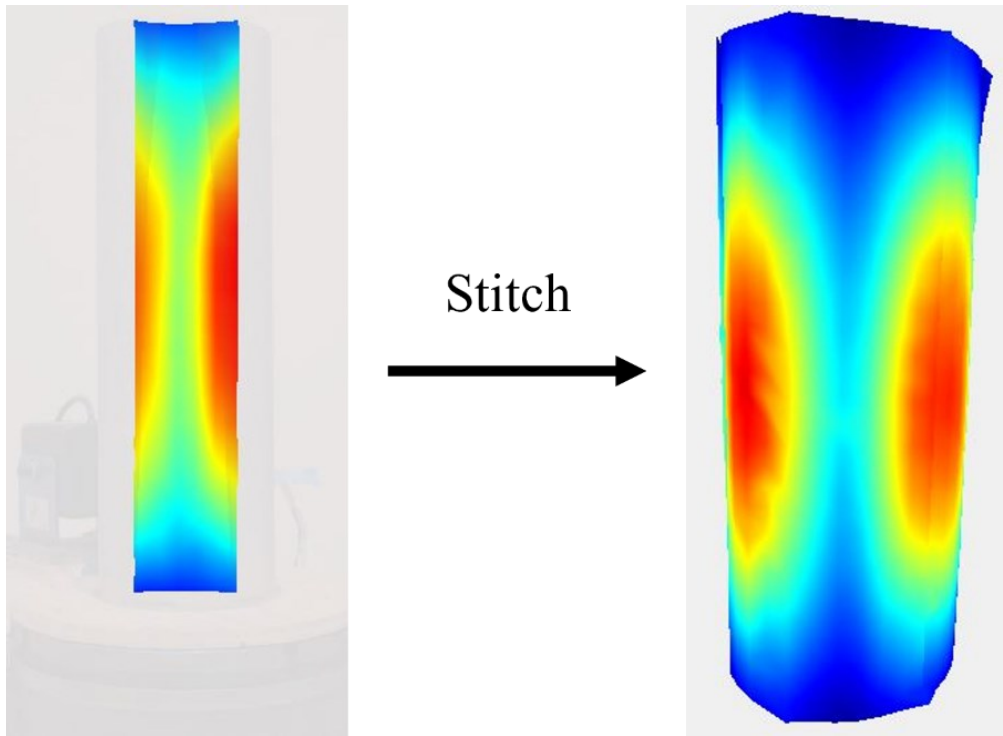


**Figure 2.7:** On the left is a 3D measurement of one section of the cylinder with stitched response of the six sections of the cylinder shown on the right.

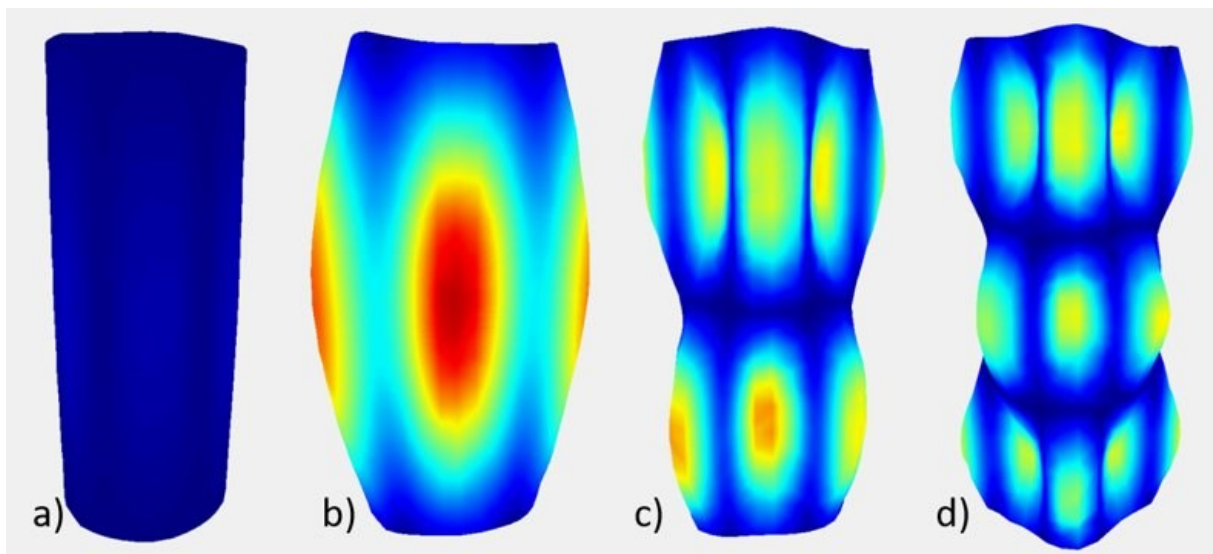


**Figure 2.8:** The vibrational motion at resonance illustrates the stitched response of the cylinder. This figure also shows a rigid body mode and three modes of the cylinder in (a)-(d) respectively.

Figures 2.9-2.11 display successful application of the stitching process to simply curved and arbitrarily curved plates. For these more complex geometries, establishing a global coordinate system was important to ensure that all scanned sections were accurately aligned during the stitching process. Chapters 3 and 4 discuss sound power results for these simply and arbitrarily curved plates in detail.

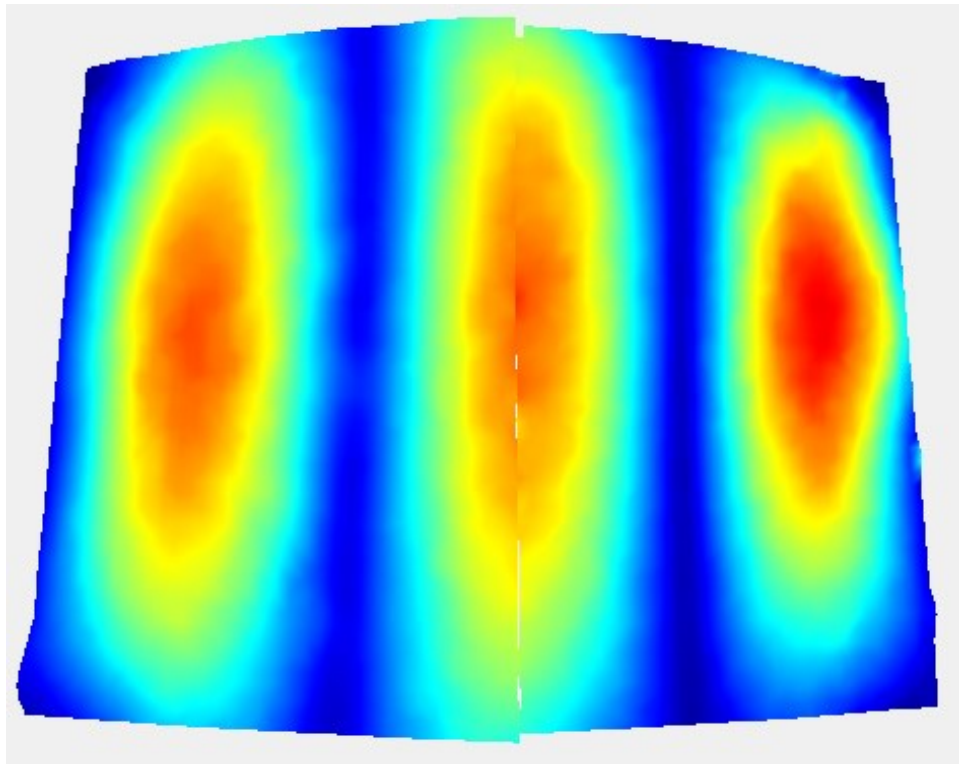


**Figure 2.9:** A stitched 3D response of a simply curved plate. The stitch is not as clean as previous figures due to the alignment of the scan grids and the overlap.

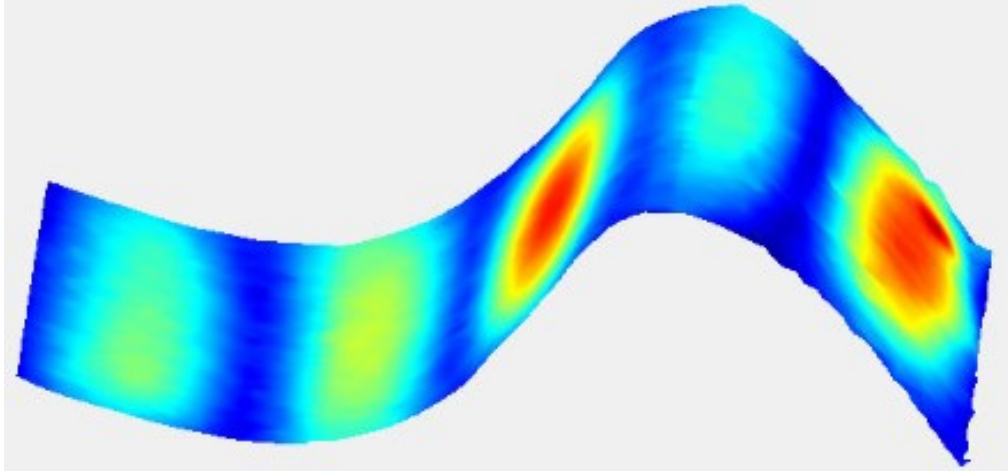


**Figure 2.10:** A stitched 3D response of an arbitrarily curved plate with two different radii of curvature.

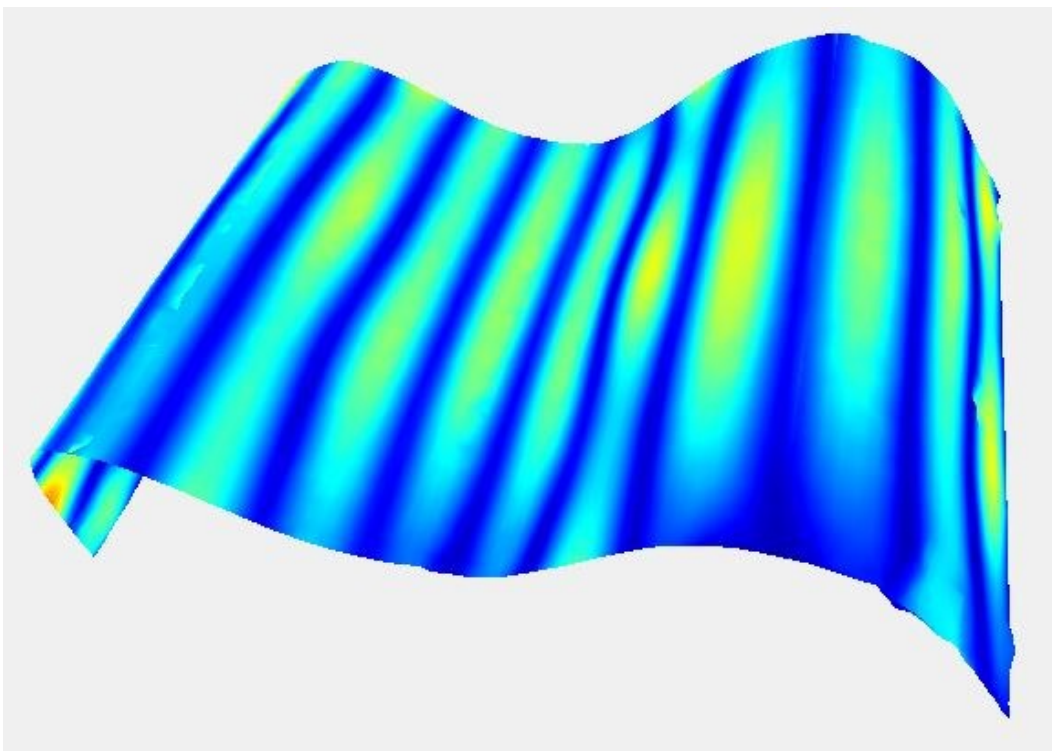


**Figure 2.11:** A stitched 3D response in five sections of an arbitrarily curved plate with three different radii of curvature, hereafter referred to as the “M-curved plate.” This stitching was more seamless for the five sections.

The transition from 2D to 3D measurements and the development of the stitching process represent significant advancements in the VBSP method. These improvements not only enhance the efficiency of the measurement process but also expand its applicability to a broader range of geometrical configurations. Using these advancements, Chs. 3-7 discuss the results of the VBSP method on different vibrating structures, highlighting the significance of the 3D stitching process for the VBSP method.

## 2.3 References

- [1] C. B. Goates, C. B. Jones, S. D. Sommerfeldt, and J. D. Blotter, “Sound power of vibrating cylinders using the radiation resistance matrix and a laser vibrometer,” *J. Acoust. Soc. Am.* **148**(6), 3553–3561 (2020). doi: 10.1121/10.0002870
- [2] C. B. Jones, C. B. Goates, J. D. Blotter, and S. D. Sommerfeldt, “Experimental validation of determining sound power using acoustic radiation modes and a laser vibrometer,” *Appl. Acoust.* **164**, 107254 (2020). doi: 10.1016/j.apacoust.2020.107254
- [3] P. Aslani, S. D. Sommerfeldt, and J. D. Blotter, “Analysis of external radiation from circular cylindrical shells,” *J. Sound Vib.* **408**, 154-167 (2017). doi: 10.1016/j.jsv.2017.07.021



## Chapter 3 Extension to Baffled Simply Curved Plates

### 3.1 Introduction

This chapter features a peer-reviewed article published in the *Noise Control Engineering Journal*, presenting significant advancements in applying the VBSP method to baffled simply curved plates. Trent Bates led the preliminary experiments in the reverberation chamber with my support and drafted an initial manuscript. After Trent graduated, I took over the leadership of the project, substantially reshaping its scope and steering it to publication as the primary author. These efforts have not only validated the VBSP method under a variety of conditions but have also broadened its potential applications across a wider frequency spectrum.

*\*\* My contributions expanded this work significantly to include several critical theoretical and computational enhancements. In refining the manuscript, I conducted a literature review with 22 additional references, deepening and strengthening the context of the research. I clarified the mathematical foundations laid by Caleb Goates, in his master's thesis, concerning the curved plate radiation resistance matrix and supplemented this with comprehensive appendices to aid readers in understanding the advanced mathematical techniques. Additionally, I personally managed advanced experimental setups, ranging from BYU's large anechoic chamber to challenging outdoor settings, and validated the VBSP method's robustness and accuracy against ISO standards, with sound power discrepancies within 2 dB for relevant octave bands.*

*I led the construction of a modular wall in BYU's anechoic chamber — a pioneering effort at the university — designed with Jeremy Peterson and Josh Mills for straightforward assembly and*

*disassembly to support future research and educational initiatives. In collaboration with Sam Bellows and Jacob Sampson, I learned to operate BYU's directivity measurement system (DMS) and further developed MATLAB© scripts to create hemispherical directivity plots of the baffled plates and compute sound power according to the ISO 3745 standard. I demonstrated that the VBSP method accurately estimates sound power below 400 Hz, a range previously untested due to limitations in the reverberation chamber standard, which has a Schroeder frequency of 385 Hz.*

**\*\***

## 3.2 Required Copyright Notice

This chapter is based on an article published in the Noise Control Engineering Journal, which can be found at <https://doi.org/10.3397/1/37728> titled “Radiation resistance matrix for baffled simply curved plates for sound power applications.” The version included here is the original submission by the authors, prior to any journal-specific formatting or editing. It has been modified to meet the formatting requirements of this ETD.

Citation:

I. C. Bacon, T. P. Bates, C. B. Goates, M. R. Shepherd, J. D. Blotter, and S. D. Sommerfeldt, “Radiation resistance matrix for baffled simply curved plates for sound power applications,” *Noise Control Eng. J.* **72**(2), 65-78 (2024).

An INCE-USA re-print permission form was signed by the executive director, Joe Cuschieri on 11 July 2024 to allow the content from this journal article to be included in this dissertation.

I hereby confirm that the use of this article is compliant with all publishing agreements.

### 3.3 Title

Radiation resistance matrix for baffled simply curved plates for sound power applications

### 3.4 Authors and Affiliations

Ian C. Bacon,<sup>a)</sup> Trent P. Bates,<sup>b)</sup> Caleb B. Goates,<sup>a)</sup> Micah R. Shepherd,<sup>a)</sup> Jonathan D. Blotter,<sup>b)</sup> and Scott D. Sommerfeldt<sup>a)</sup>

<sup>a)</sup> *Department of Physics and Astronomy, Brigham Young University, Provo, Utah 84602.*  
[icbacon@byu.edu](mailto:icbacon@byu.edu), [calebgoates@gmail.com](mailto:calebgoates@gmail.com), [scott\\_sommerfeldt@byu.edu](mailto:scott_sommerfeldt@byu.edu).

<sup>b)</sup> *Department of Mechanical Engineering, Brigham Young University, Provo, Utah 84602.*  
[tbateslefty24@gmail.com](mailto:tbateslefty24@gmail.com), [jblotter@byu.edu](mailto:jblotter@byu.edu).

### 3.5 Abstract

Sound power, a standard metric used to quantify product noise, is determined through the vibration-based sound power (VBSP) method. This method involves measuring surface velocities and utilizing an acoustic radiation resistance matrix,  $\mathbf{R}$ , dependent on the structure's geometry. While  $\mathbf{R}$  matrix expressions have been established for baffled flat plates, fully closed cylinders, and fully closed spheres, this work presents the first analytical expression tailored for baffled simply curved plates with uniform curvature. This development, based on eigenfunction expansion and the uniform theory of diffraction, extends the VBSP method's capabilities for accurate sound power assessment from these structures. Experimental validation involved testing three plates of varying curvature in a reverberation chamber, comparing the VBSP method with the ISO 3741 pressure-based standard. One of the curved plates underwent additional testing in an anechoic chamber following the ISO 3745 standard, confirming the VBSP method's accurate sound power measurements down to the 160 Hz one-third octave (OTO) band. The same plate was tested in uncontrolled acoustic environments—a busy hallway and an outdoor location. The VBSP results showed strong agreement with ISO 3741, affirming the method's robustness for measuring sound power from baffled simply curved plates in acoustically challenging real-world conditions. This underscores the practicality of the VBSP method, enabling accurate sound power measurements of baffled curved plates in the presence of substantial background noise and environmental variability.

Primary subject classification: 72.4 Sound power; Secondary subject classification: 21.2.1 Vibrating bodies

### 3.6 Introduction

Sound power is a widely used metric for comparing radiated noise levels across various products, from home appliances to construction vehicles. Many existing standards for sound power measurement require specific acoustic environments, such as anechoic and reverberation chambers, that are cost prohibitive. Consequently, designers often do not have sound power data to effectively prioritize noise reduction in product development. Vibration-based sound power (VBSP) measurement methods offer a potential solution by reducing the constraints of acoustic environments and the associated costs, making sound power measurements more feasible for designers to utilize sound power data to develop quieter products.

The foundational theory for computing sound power using vibration-based methods is often referred to as the method of elementary radiators, which originated in the early 1990s [1]-[4]. In this method, the structure is discretized into an array of small individual radiators, and the velocity of each radiator is measured. Using a radiation resistance matrix,  $\mathbf{R}$ , the sound power is computed as

$$\Pi(\omega) = \mathbf{v}_e^H(\omega)\mathbf{R}(\omega)\mathbf{v}_e(\omega), \quad (3.1)$$

where  $\mathbf{v}_e$  is a vector of the velocity of each individual radiator,  $(\cdot)^H$  is the Hermitian transpose, and  $\omega$  is the frequency [2]-[5].

Arenas described the  $\mathbf{R}$  matrix as a transfer function linking the surface normal velocities of a structure to the acoustic pressures on the surface of each radiator [6]. The individual terms in the  $\mathbf{R}$  matrix,  $R_{pq}$ , represent the radiation resistance on radiator  $p$  due to radiator  $q$ . Thus, the  $\mathbf{R}$  matrix is a square symmetric matrix where both the rows and columns equal the number of radiators, and the number of elements is equal to the total number of radiators squared. The  $\mathbf{R}$  matrix is primarily

a function of the acoustic pressure propagation distances between the individual radiators, leading to different expressions for these distances between flat and curved geometries.

Historically, acoustic radiation modes were derived from the  $\mathbf{R}$  matrix corresponding to a specific geometry, and then utilized to compute sound power [1]-[4] or as a tool to improve structural design and active noise control techniques [7]. Radiation modes explain how the vibrational energy of a structure transforms into acoustic energy by analyzing the distribution of velocity across its surface [2], [8], [9]. Goates *et al.* previously referred to this method as the vibration-based radiation mode (VBRM) method [10], [11]. Cunefare *et al.* showed the convergence of a sufficient number of these modes to obtain good resolution for the sound power within a given range [4].

It was found within this work that when higher frequencies are of interest, using radiation modes to compute sound power does not yield significant computational savings compared to simply using the entire  $\mathbf{R}$  matrix and computing the matrix multiplication in Eqn. 3.1. This is primarily due to the extensive computations required to determine the radiation modes, often comparable to directly calculating the sound power using the full  $\mathbf{R}$  matrix. This method of using the full  $\mathbf{R}$  matrix to compute sound power is referred to as the VBSP method [12]. Convergence for sound power results using the VBSP method can be obtained by ensuring sufficient spatial resolution when discretizing the surface of interest. Although this method utilizes the  $\mathbf{R}$  matrix, the acoustic radiation modes of simply curved plates can be obtained for other applications by performing singular value decomposition on the  $\mathbf{R}$  matrix, developed later in this work.

Previous research has established analytical expressions for the radiation resistance matrix for flat plates [2], [5], [11]-[13], fully closed cylindrical shells [10], [14]-[18], and fully closed spherical shells [1], [18], [19]. In these fully closed geometries, the acoustic pressure from one

radiator can propagate to another by traversing the surface of the structure in multiple directions as well as going around the structure several times. Many common geometries, including car door panels, windshields, aircraft fuselage panels, and engine covers do not fit these existing models. Therefore, there is a need for a validated expression for the  $\mathbf{R}$  matrix that can accurately model simply curved-plate geometries.

Bates *et al.* have shown that some baffled arbitrarily curved panels can be approximated using one of the known forms of the  $\mathbf{R}$  matrix mentioned earlier [20]. However, limitations exist in this approach, particularly regarding the radius of curvature and the coupling between radiators that exists within a certain range of frequencies. While Bates provided an analytical expression for the  $\mathbf{R}$  matrix of baffled simply curved plates, no theoretical development or validation of this expression is available in the existing literature. This knowledge gap presents a challenge for groups seeking to understand the natural acoustic radiation from these simply curved plates, whether for sound power computation or active noise control. It is crucial to address these limitations and verify the accuracy of the expression numerically or experimentally to validate this expression.

The purpose of this work is to fill this critical research gap by presenting and validating, for the first time, the theoretical development of the  $\mathbf{R}$  matrix for baffled simply curved plates. This development is based on the eigenfunction expansion and the uniform theory of diffraction to determine the distances between every elementary radiator and how the acoustic radiation is produced and transferred from these geometries. This work only considers simply curved plates with a single constant radius of curvature, deviating from fully closed geometries like cylinders and spheres.



This work then shows experimental results validating the analytical expression for this  $\mathbf{R}$  matrix and enables extension of the VBSP method to accurately account for simply curved plates. Experimental validation was conducted through comparing VBSP results with sound power measurements obtained following the ISO 3741 and ISO 3745 standards [21], [22], that are well-established sound pressure measurement-based standards. By providing a validated expression and expanding the applicability of the VBSP method, an accurate assessment of the sound radiation from simply curved plates can be facilitated, benefiting various industries and applications.

### 3.7 Curved Plate Radiation Resistance Matrix Theory

The  $\mathbf{R}$  matrix for a simply curved plate is obtained by initially deriving the  $\mathbf{R}$  matrix for a fully closed cylinder. This section begins with a concise overview of the derivation process for the  $\mathbf{R}$  matrix of the fully closed cylinder, followed by the derivation for open simply curved plates. Subsequently, the expression is further simplified for more efficient computation by using the uniform theory of diffraction.

#### 3.7.1 Simply Curved Plate Radiation Resistance Matrix

The  $\mathbf{R}$  matrix is derived from the acoustic pressure that a small vibrating element of a structure generates across the structure. The general form of the  $\mathbf{R}$  matrix for the  $pq^{\text{th}}$  element can be expressed as a function of the pressure as given by [4], [23]

$$R_{pq} = \frac{S_e}{2u_0} \text{Re}\{p_q(a, \theta_p, z_p)\}, \quad (3.2)$$

where  $S_e$  is the area of the vibrating element or radiator given by  $S_e = a\Delta\theta\Delta z$ ,  $u_0$  is the velocity amplitude of the  $q^{\text{th}}$  element,  $p_q(a, \theta_p, z_p)$  is the pressure generated at the  $p^{\text{th}}$  location by vibration

at the  $q^{\text{th}}$  location,  $a$  is the radial distance (radius of curvature) for the surface of the curved structure, and  $\theta_p$  and  $z_p$  are the physical coordinates of the  $p^{\text{th}}$  location.

Consider a rigid infinite cylinder of radius  $a$  as shown in Fig. 3.1. Assume that a small rectangular patch or radiator on the cylinder with circumferential extent  $\Delta\theta$  and height  $\Delta z$  is vibrating with a surface normal velocity  $u_0$ , such that there is effectively a simple source of strength  $u_0 a \Delta\theta \Delta z$  at  $(r, \theta, z) = (a, \theta_p, z_p)$ . This vibration creates a pressure field over the structure that can be written as [23]

$$p_q(r, \theta, z) = \sum_{m=-\infty}^{\infty} \int_{-\infty}^{\infty} A_m(k_z) e^{jk_z z} e^{jm\theta} H_m^{(2)}(k_r r) dk_z, \quad (3.3)$$

where  $A_m(k_z)$  are unknown coefficients,  $H_m^{(2)}(k_r r)$  is the  $m$ th-order Hankel function of the second kind (defined in Appendix 3A by Eqn. 3A.4),  $j = \sqrt{-1}$ ,  $m$  is an integer,  $k_z$  is the axial wavenumber, and  $k_r = \sqrt{k^2 - k_z^2}$ , where  $k$  is the acoustic wavenumber. The pressure is defined for each radiator and the pressure field is represented by a vector the length of the number of radiators. Therefore, a single subscript is used to define the pressure radiators.

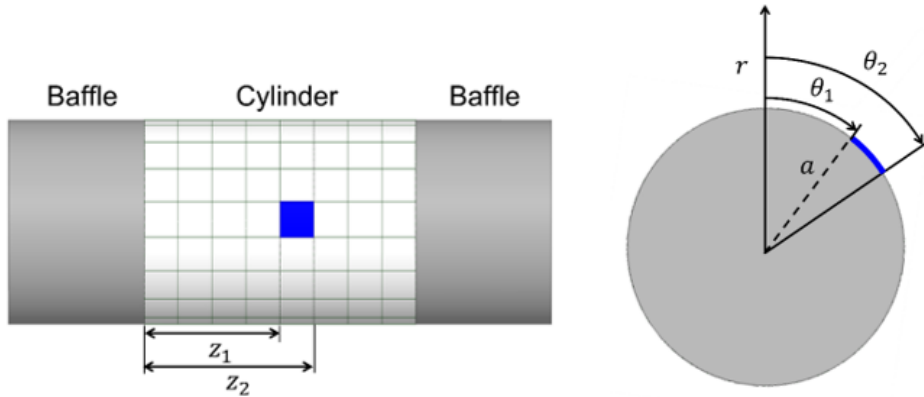


**Figure 3.1:** Schematic of the infinitely baffled cylinder geometry. The non-rigid portion of the cylinder is discretized, and the radiator described in Eqn. 3.3 is highlighted in blue (left). An end view of the cylinder of radius  $a$  shows the dimensions of an arbitrary element, represented by the length  $z_2 - z_1$  and width  $a(\theta_2 - \theta_1)$  (right).

The surface velocity may be expanded in terms of the  $\theta$  and  $z$  eigenfunctions as

$$u_q(\theta, z) = \left( \frac{u_0 \Delta \theta \Delta z}{\pi^2} \right) \sum_{m=-\infty}^{\infty} \int_{-\infty}^{\infty} e^{jk_z(z-z_q)} e^{jm(\theta-\theta_q)} dk_z, \quad (3.4)$$

from which the pressure expression coefficients may be solved for by applying the surface condition at  $r = a$ ,

$$\left. \frac{\partial p_q}{\partial r} \right|_{r=a} = -j\omega\rho_0 u_q(\theta, z). \quad (3.5)$$

Applying these steps and simplifying gives the pressure as

$$p_q(r, \theta, z) = -j \left( \frac{\omega\rho_0 u_0 \Delta \theta \Delta z}{\pi^2} \right) \sum_{m=-\infty}^{\infty} e^{jm(\theta-\theta_q)} \int_{-\infty}^{\infty} \frac{H_m^{(2)}(k_r a)}{H_m^{(2)'}(k_r a)} e^{jk_z(z-z_q)} \frac{dk_z}{k_r}, \quad (3.6)$$

where the prime denotes a derivative with respect to the argument. Using Euler's formula this can be written in terms of trigonometric functions instead of exponentials as

$$p_q(r, \theta, z) = -j \left( \frac{\omega\rho_0 u_0 \Delta \theta \Delta z}{\pi^2} \right) \sum_{m=0}^{\infty} \cos[m(\theta - \theta_j)] \int_0^{\infty} \frac{H_m^{(2)}(k_r a)}{H_m^{(2)'}(k_r a)} \cos[k_z(z - z_j)] \frac{dk_z}{k_r}. \quad (3.7)$$

The  $pq^{\text{th}}$  element of the  $\mathbf{R}$  matrix can then be expressed by substituting Eqn. 3.7 into Eqn. 3.2 as given by

$$\begin{aligned} R_{\text{cyl},pq} &= \frac{S_e}{2u_0} \text{Re}\{p_q(a, \theta_p, z_p)\} \\ &= \text{Re} \left\{ -j \left( \frac{\omega\rho_0 S_e^2}{2\pi^2 a} \right) \sum_{m=0}^{\infty} \cos[m(\theta - \theta_j)] \int_0^{\infty} \frac{H_m^{(2)}(k_r a)}{H_m^{(2)'}(k_r a)} \cos[k_z(z - z_j)] \frac{dk_z}{k_r} \right\} \\ &= \left( \frac{\omega\rho_0 S_e^2}{2\pi^2 a} \right) \sum_{m=0}^{\infty} \cos[m(\theta - \theta_j)] \int_0^{\infty} \text{Re} \left\{ -\frac{j}{k_r} \frac{H_m^{(2)}(k_r a)}{H_m^{(2)'}(k_r a)} \right\} \cos[k_z(z - z_j)] dk_z, \quad (3.8) \end{aligned}$$

which can be further simplified by recognizing that the Hankel functions ratio becomes imaginary for imaginary  $k_r$ . This simplification reduces the integration in  $k_z$  from 0 to  $k$ , giving the final form

$$R_{\text{cyl},pq} = \frac{\omega \rho_0 S_e^2}{2\pi^2 a} \sum_{m=0}^{\infty} \cos[m(\theta_p - \theta_q)] \int_0^k \frac{1}{k_r} \text{Im} \left\{ \frac{H_m^{(2)}(k_r a)}{H_m^{(2)'}(k_r a)} \right\} \cos[k_z(z_p - z_q)] dk_z. \quad (3.9)$$

In addition to this fully closed cylinder expression, eigenfunction expansion can give the  $\mathbf{R}$  matrix for a partial cylinder radiating into a partial cylindrical space as shown in Fig. 3.2. The main difference is the application of a Neumann boundary condition at  $\theta = 0$  and  $\theta = \theta_L$  where  $\theta_L$  is the angular extent of the space instead of the periodicity requirement on  $\theta$ . Making these changes results in the following expression for a partial cylinder or simply curved plate [9]

$$R_{\text{part cyl},pq} = \frac{\omega \rho_0 S_e^2}{\pi a \theta_L} \sum_{m=0}^{\infty} \cos\left(\frac{m\pi\theta_p}{\theta_L}\right) \cos\left(\frac{m\pi\theta_q}{\theta_L}\right) \int_0^k \frac{1}{k_r} \text{Im} \left\{ \frac{H_m^{(2)}(k_r a)}{H_m^{(2)'}(k_r a)} \right\} \cos[k_z(z_p - z_q)] dk_z. \quad (3.10)$$

The drawbacks to this expression are the infinite sum and the integrals which can be overcome as shown in the following section using the uniform theory of diffraction.

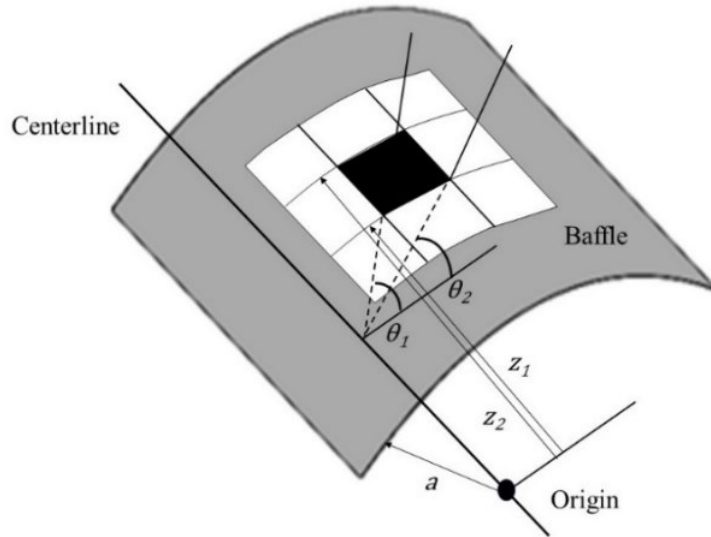


**Figure 3.2:** The geometric values and the area of an element in the baffled curved plate are shown. These elements represent the radiators that produce the pressure at the  $p$ th location in response to vibration at the  $q$ th location.

### 3.7.2 Uniform Theory of Diffraction

Although  $\mathbf{R}$  matrix formulations could be derived directly from Eqns. 3.9 and 3.10, these equations involve computationally expensive infinite sums and integrals. For cylindrical structures with large radii of curvature, Eqn. 3.9 can be further simplified by applying principles from the uniform theory of diffraction (UTD). Initially developed in electromagnetics, this approach to wave propagation around curved surfaces has had limited application in acoustics [24], [27]. The formulation can be obtained by employing an asymptotic expansion of Eqn. 3.6 for large  $ka$  values. After evaluation at  $r = a$  and substituting  $\phi = \theta - \theta_q$ , Eqn. 3.6 can be written as

$$p_q(a, \theta, z) = -j \left( \frac{\omega \rho_0 u_0 \Delta \theta \Delta z}{4\pi^2} \right) \int_{-\infty}^{\infty} dk_z \frac{e^{jk_z(z-z_q)}}{k_r} \sum_{m=-\infty}^{\infty} \frac{H_m^{(2)}(k_r a)}{H_m^{(2)'}(k_r a)} e^{jm\phi}. \quad (3.11)$$

The sum in this expression can be transformed into an integral in the complex plane by using a Watson transformation [27], [29], as follows

$$\sum_{m=-\infty}^{\infty} \frac{H_m^{(2)}(k_r a)}{H_m^{(2)'}(k_r a)} e^{jm\phi} = \frac{j}{2} \int_C \frac{e^{j\nu(\phi-\pi)} H_\nu^{(2)}(k_r a)}{\sin \nu\pi H_\nu^{(2)'}(k_r a)} d\nu, \quad (3.12)$$

where  $C$  is a contour that encircles the real axis. Then by replacing  $-\nu$  by  $\nu$  in the part of the contour above the axis, the right-hand side of Eqn. 3.12 becomes

$$\sum_{m=-\infty}^{\infty} \frac{H_m^{(2)}(k_r a)}{H_m^{(2)'}(k_r a)} e^{jm\phi} = \frac{j}{2} \int_{-\infty-j\epsilon}^{\infty-j\epsilon} \frac{\cos \nu(\phi-\pi) H_\nu^{(2)}(k_r a)}{\sin \nu\pi H_\nu^{(2)'}(k_r a)} d\nu. \quad (3.13)$$

Then, by replacing the trigonometric terms with their equivalent exponential terms yield

$$\sum_{m=-\infty}^{\infty} \frac{H_m^{(2)}(k_r a)}{H_m^{(2)'}(k_r a)} e^{jm\phi} = \frac{j}{2} \int_{-\infty-j\epsilon}^{\infty-j\epsilon} \frac{e^{-j\nu(2\pi-\phi)} + e^{-j\nu\phi}}{1 - e^{-j\nu 2\pi}} \frac{H_\nu^{(2)}(k_r a)}{H_\nu^{(2)'}(k_r a)} d\nu. \quad (3.14)$$

Next, a geometric series can be used to obtain

$$\sum_{m=-\infty}^{\infty} \frac{H_m^{(2)}(k_r a)}{H_m^{(2)'}(k_r a)} e^{jm\phi} = \frac{j}{2} \int_{-\infty-j\varepsilon}^{\infty-j\varepsilon} \frac{H_\nu^{(2)}(k_r a)}{H_\nu^{(2)'}(k_r a)} \sum_{\ell=0}^{\infty} (e^{-j\nu(2\pi-\phi)} + e^{-j\nu\phi}) e^{-j2\pi\ell\nu} d\nu. \quad (3.15)$$

Equation 3.15 can be interpreted as a summation of waves that have encircled the cylinder  $\ell$  times, composed of separate terms for waves circling in a positive direction and waves circling in a negative direction. By assuming that  $k_r a$  is large and recognizing that the greatest contribution to the integral occurs near  $\nu = k_r a$ , all but the  $\ell = 0$  terms can be neglected [25]. This simplification yields the final quantity as

$$\sum_{m=-\infty}^{\infty} \frac{H_m^{(2)}(k_r a)}{H_m^{(2)'}(k_r a)} e^{jm\phi} \approx \frac{j}{2} \int_{-\infty-j\varepsilon}^{\infty-j\varepsilon} \frac{H_\nu^{(2)}(k_r a)}{H_\nu^{(2)'}(k_r a)} (e^{-j\nu(\phi-2\pi)} + e^{-j\nu\phi}) d\nu. \quad (3.16)$$

Considering that the integral over  $\nu$  is primarily influenced by  $\nu = k_r a$ , Pathak and Wang proposed the substitution  $\nu = k_r a + \tau(k_r a/2)^{1/3}$ , with  $\tau$  as the new independent variable [25]. Following this asymptotic formulation suggested by Pathak and Wang, the sum in Eqn. 3.12 can be expressed as

$$\sum_{m=-\infty}^{\infty} \frac{H_m^{(2)}(k_r a)}{H_m^{(2)'}(k_r a)} e^{jm\phi} = -\frac{j}{2} \int_{-\infty}^{\infty} \left(\frac{k_r a}{2}\right)^{1/3} \frac{W_2(\tau)}{W_2'(\tau)} e^{-j\nu\phi} d\tau, \quad (3.17)$$

where  $W_2(\tau)$  represents one of the Airy-Fock functions [30] (defined in Appendix 3A by Eqn. 3A.5). Furthermore, it should be noted that employing  $e^{-j\nu\phi}$  in the integral accounts for a single ray traveling in one circumferential direction along the cylindrical surface. Substituting  $\nu$  and this result back into Eqn. 3.11 yields the surface pressure as [23]

$$p_q(r, \theta, z) = -\frac{\omega\rho_0 u_0 \Delta\theta\Delta z}{8\pi^2} \int_{-\infty}^{\infty} \frac{e^{j[k_z(z-z_q)+k_r a\phi]}}{k_r} dk_z \int_{-\infty}^{\infty} \left(\frac{k_r a}{2}\right)^{1/3} \frac{W_2(\tau)}{W_2'(\tau)} e^{-j\phi\left(\frac{k_r a}{2}\right)^{1/3}\tau} d\tau. \quad (3.18)$$

The first integral (over  $k_z$ ) can be evaluated using a polar transformation, resulting in the expression for the pressure from this single ray being written as

$$p_q(t) = \frac{j\omega\rho_0 u_0 S_e}{2\pi} V(\xi) \frac{e^{-jk\eta}}{\eta}, \quad (3.19)$$

where

$$V(\xi) = \left(\frac{\xi}{4\pi}\right)^{\frac{1}{2}} e^{\frac{j\pi}{4}} \int_{-\infty}^{\infty} d\tau \frac{W_2(\tau)}{W_2'(\tau)} e^{-j\xi\tau}. \quad (3.20)$$

Equation 3.20 represents a simplified version of Eqn. 3A.6 found in Appendix 3A.  $V(\xi)$  denotes the hard Fock coupling function with real argument  $\xi = \eta[k\cos^4\psi/(2a^2)]^{1/3}$ ,  $\eta = \sqrt{(\Delta z)^2 + a^2(\Delta\theta)^2}$  is the distance traversed across the curved surface, and  $\psi = \tan^{-1}\left(\frac{\Delta z}{a\phi}\right)$  is the angle between the direction of propagation and the cylinder axis.

Substitution of Eqn. 3.19 into Eqn. 3.2 gives the expression to compute the entries of the curved plate  $\mathbf{R}$  matrix as [23]

$$R_{pq} = -\frac{\omega\rho_0 S_e^2}{4\pi d_{pq}} \text{Im}\{V(\xi)e^{-jk d_{pq}}\}, \quad (3.21)$$

where  $d_{pq}$  is the distance between the  $p^{\text{th}}$  and  $q^{\text{th}}$  positions on the surface and is also substituted for  $\eta$  in  $\xi$ . It is important to note that the described radiation resistance considers only a single ray. While this approach is suitable for the scenarios addressed in this work, involving baffled curved plates, a more comprehensive treatment for a complete cylinder would require combining two or more terms from Eqn. 3.21. This would allow for the depiction of the two opposite paths around the cylinder, from the source to the field point, as well as additional paths that propagate around the cylinder multiple times.

The hard Fock coupling function  $V(\xi)$  has been characterized sufficiently, yielding useful series representations with ten or fewer terms (see Table 3A.1 in Appendix 3A). Figure 3.3 provides a plot of  $V(\xi)$ . Notably, for large curvature ( $a \gg 1$ ) and low frequency ( $k \ll 1$ ),  $\xi$  approaches zero and  $V(\xi)$  approaches unity. In this case,  $V(\xi)$  behaves like a  $\text{sinc}(kd_{pq})$  function, causing Eqn. 3.21 to collapse into the canonical expression for the  $\mathbf{R}$  matrix of a flat plate, given by [5]

$$R_{\text{flat},pq} = \frac{\rho_0 \omega^2 S_e^2}{4\pi c} \frac{\sin kd_{pq}}{kd_{pq}}. \quad (3.22)$$

Thus, the flat plate  $\mathbf{R}$  matrix serves as a good approximation for these plates. On the other hand, Fig. 3.3 also shows that the elements of the  $\mathbf{R}$  matrix for a simply curved plate, regardless of its size, tend to zero as the radius of curvature diminishes, as depicted in Eqn. 3.21. This occurs when  $V(\xi)$  approaches zero as  $\xi$  tends toward seven.

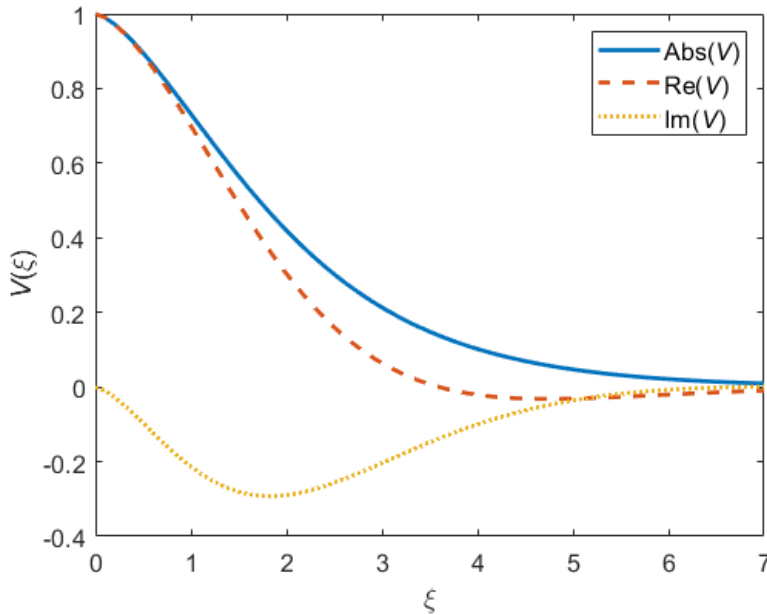


**Figure 3.3:** This plot shows the real part, imaginary part, and magnitude of the hard Fock  $V$  coupling function. As  $\xi$  approaches zero,  $V(\xi)$  behaves similarly to a  $\text{sinc}(kd_{pq})$  function and showcases the asymptotic behavior near zero for small curvature or large frequency.



## 3.8 Experimental Setups for Sound Power Measurement

To confirm the accuracy of the simply curved plate  $\mathbf{R}$  matrix expression, sound power measurements obtained through the VBSP method were compared with ISO 3741 and ISO 3745 standards. Experiments were conducted using three simply curved plates of varying radii in different acoustic environments: reverberant, anechoic, and uncontrolled. This section outlines the experimental setup, and measurement methods, and then presents the validation results.

### 3.8.1 Design and Setup of the Three Curved Plates

The three curved plates used during experimental testing were fabricated using the same materials and design, with the only distinguishing feature being the constant radius of curvature used. For simplicity, the curved plates in this work are identified according to their relative radius of curvature, as follows: tight radius (TR) (see Fig. 3.4), medium radius (MR) (see Fig. 3.5a), and wide radius (WR) (see Fig. 3.5b). The radii of curvature and other dimensions for these plates are summarized in Table 3.1.

Each structure has a thin aluminum sheet shaped into a curved plate with an approximately constant radius of curvature maintained in a rigid steel frame (see Fig. 3.4). To prevent acoustic radiation from escaping the backside of the curved plates and into the measured acoustic field, each plate is clamped on the straight edges and baffled on the curved edges using thick aluminum caps sealed to the plates with a silicone bead (see Fig. 3.4). Calibration marks were placed on the surface of each plate to enable a scanning laser Doppler vibrometer (SLDV) to virtually stitch scan section measurements.

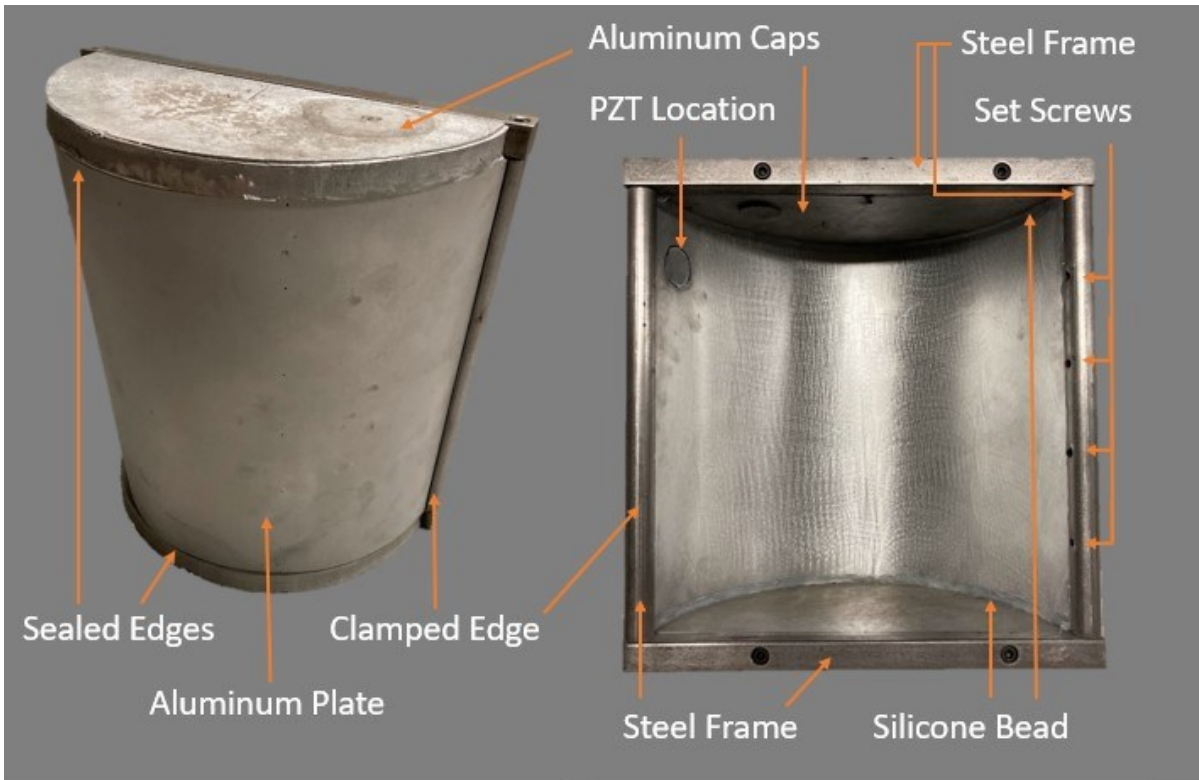


**Figure 3.4:** Annotated image of the TR curved plate, with the outer surface on the left and the inner surface on the right. The width corresponds to the clamped edges. Plate excitation was achieved through a piezoelectric transducer (PZT).

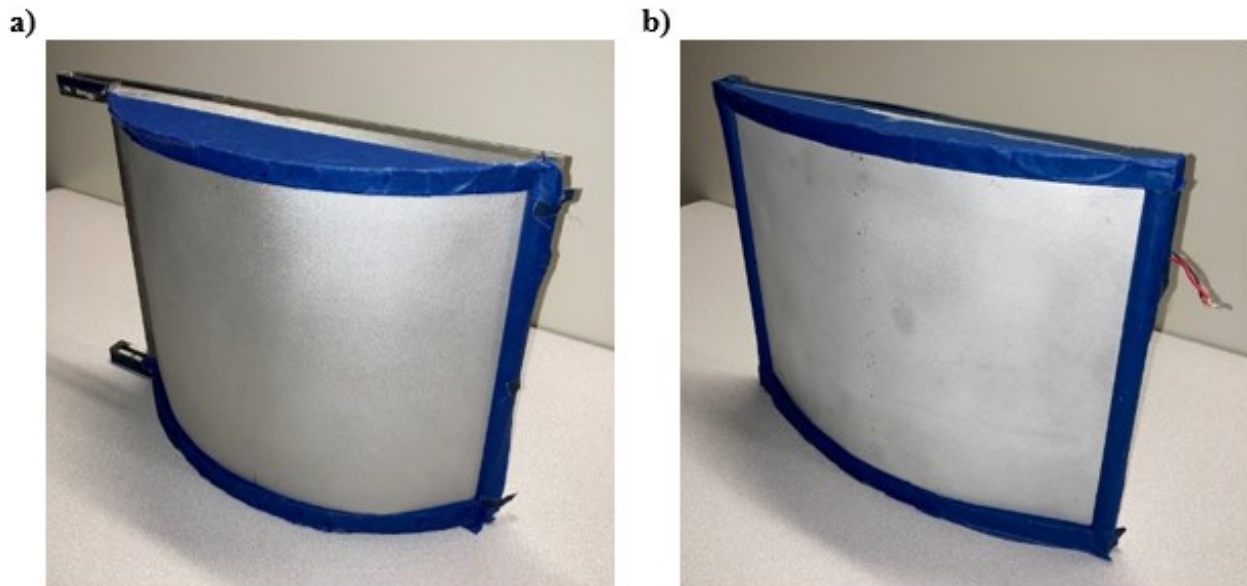


**Figure 3.5:** Images of (a) the MR curved plate and (b) the WR curved plate.

**Table 3.1:** Summary of the curved plate dimensions used for experimental testing.

<b>Object</b>	<b>Height (cm)</b>	<b>Width (cm)</b>	<b>Thickness (mm)</b>	<b>Radius of Curvature (cm)</b>
<b>TR Curved Plate</b>	30	29	1.59	15.5
<b>MR Curved Plate</b>	30	36	1.59	30
<b>WR Curved Plate</b>	30	40	1.59	51

### **3.8.2 The VBSP Method for 3D Structures**

A curved plate was mounted on the wall in the specific acoustic environment, with the wall approximating an infinite baffle. Gaff tape (thick sealing tape) was applied around the frame-to-wall interface to ensure proper sealing and eliminate any acoustic flanking paths. The vibration and standard method measurements were made for each plate while maintaining this consistent setup.

Excitation of the plates initially involved a shaker, but there were limitations in baffling behind the plate and obstructing the view of the SLDV in front of the plate. As a solution, a piezoelectric transducer (PZT) was placed on the back side of the plate in the upper right quadrant (when facing the front). This allowed flush mounting of the plates to the chamber wall while enabling measurement of the low-frequency chamber background noise.

Structural velocity measurements were made using a Polytec PSV-500-3D SLDV equipped with three independent laser scan heads for 3D measurements. Each laser head measures the velocity along the sight of the laser beam. The software uses these three measurements to compute the three orthogonal components of velocity in the predetermined laser reference coordinate system. The SLDV also measures the surface geometry of the plate from which an outward normal vector at each point can be determined. The surface normal velocity at each scan point is computed using the dot product,

$$V_n = \mathbf{V} \cdot \mathbf{N}, \quad (3.23)$$

where  $V_n$  is the surface normal velocity,  $\mathbf{V}$  is the 3D velocity vector, and  $\mathbf{N}$  is the surface normal unit vector. Due to plate curvature, separate sections of the plate were scanned and subsequently stitched together, as seen in Fig. 3.6, to obtain a complete response of each simply curved plate [31].

The frequency range of interest spanned 100 Hz to 10 kHz in one-third octave (OTO) bands (89 Hz to 11,220 Hz). The scan grid density was at least six scan points per wavelength for the shortest wavelength (5.1 mm at 11,220 Hz), ensuring a spatial resolution of approximately one wavelength between each scan point in each direction and sound power measurement accuracy. A pseudo-random signal ranging from 0 to 12.8 kHz was applied to the PZT to excite each plate.

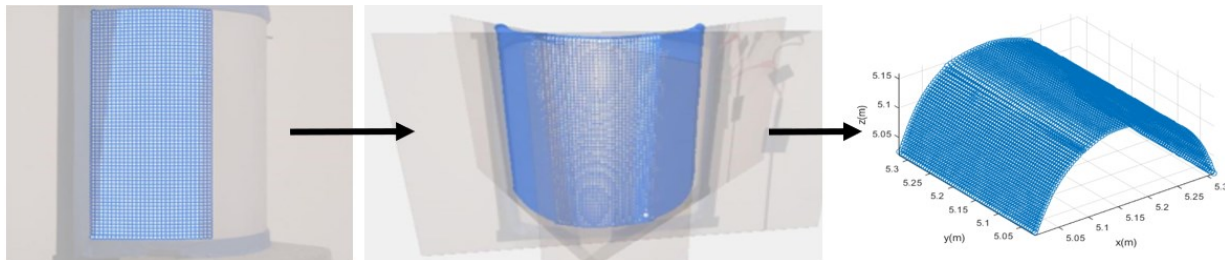


**Figure 3.6:** An example scan section taken over the surface of the TR curved plate to measure complex surface velocities. After each section is scanned and then stitched together to provide a complete response of the plate. During post-processing, the stitching is smoothed in case of any imperfect overlap of the sections.

### 3.8.3 Reverberation Chamber and the ISO 3741 Standard

The reverberation chamber employed has dimensions of approximately 5.03 m x 5.93 m x 7.01 m with a Schroeder frequency of about 385 Hz. The sound power from the curved plates was measured and then computed using the ISO 3741 standard, which is limited to frequencies above the Schroeder frequency.

An impulse response was recorded in the reverberation chamber to factor in the additional absorption attributed to the presence of the SLDV equipment and the experimental setup. Once the absorption had been accounted for, sound pressure data was recorded using six microphones placed according to the standard. The recorded pressure data was filtered into OTO bands with a frequency bandwidth resolution of 1 Hz. Then, the vibration data and the developed curved plate **R** matrix were used to calculate sound power following the VBSP method. The obtained results are reported and compared in OTO bands with the ISO 3741 standard.

### **3.8.4 Anechoic Chamber and the ISO 3745 Standard**

To assess the VBSP method's accuracy in measuring sound power below 385 Hz, VBSP measurements of the WR curved plate were compared with the measurements in an anechoic chamber according to ISO 3745. The chamber's anechoic properties extend down to approximately 80 Hz, allowing sound power measurements to be verified down to the 100 Hz OTO band center frequency, provided the excitation meets the specified sound pressure level to background noise criteria.

To minimize the potential influence of sound wrapping around the front and affecting source measurements, a 16' x 12' x ¾" thick MDF wall was constructed for mounting the WR curved plate (see Fig. 3.7). This wall served as a baffle, directing any radiated sound on the backside towards the anechoic terminations. It was specifically designed to mitigate the impact of the longest wavelength of interest at 89 Hz.

A directivity measurement system (DMS) arc array with 36 microphones evenly spaced in 5° increments [32] was used to capture frequency response functions (FRFs) around the curved plate, covering a hemisphere along a meridional path. Each recording lasted approximately 15 seconds, with an additional 15-second settling time between rotations to minimize electrical noise from the

actuator and array. The FRFs were used to calculate sound power levels from 100 Hz to 10 kHz OTO bandwidth, per the ISO 3745 standard [22].



**Figure 3.7:** Experimental setup of the DMS (arc array) and wall inside an anechoic chamber.

### **3.8.5 The VBSP Method in Uncontrolled Acoustic Environments**

To gauge the VBSP method's capability to measure radiated sound power in noisy environments outside of controlled acoustic environments, such as anechoic and reverberation chambers, experiments were conducted using the WR curved plate. The WR plate was mounted on a concrete wall at least three feet thick to baffle in two different locations: a hallway in BYU's Engineering Building (see Fig. 3.8) with moderate foot traffic, loud HVAC system, and elevator



noise, and an outdoor location (see Fig. 3.9). The outdoor setup involved challenging environmental conditions, including frequent vehicle noise, a rainstorm with thunderclaps, wind speeds up to 11 mph, and a 14°F (7.8°C) temperature change during measurement.



**Figure 3.8:** Experimental setup of the WR curved plate in a hallway inside BYU’s engineering building.



**Figure 3.9:** Experimental setup of the WR curved plate outside of BYU's engineering building.

## **3.9 Experimental Results of Sound Power Measurements**

### **3.9.1 Reverberant (Diffuse) Environment**

The Schroeder frequency was shifted down to approximately 350 Hz due to the presence of additional absorption within the reverberation chamber, placing it within the 315 Hz OTO band. Figures 3.10a and 3.10b show the sound power measurements from the TR and WR curved plates respectively using both the VBSP and ISO 3741 methods in a reverberation chamber. Excellent agreement was obtained between both methods between the 315 Hz to 10 kHz OTO bands.

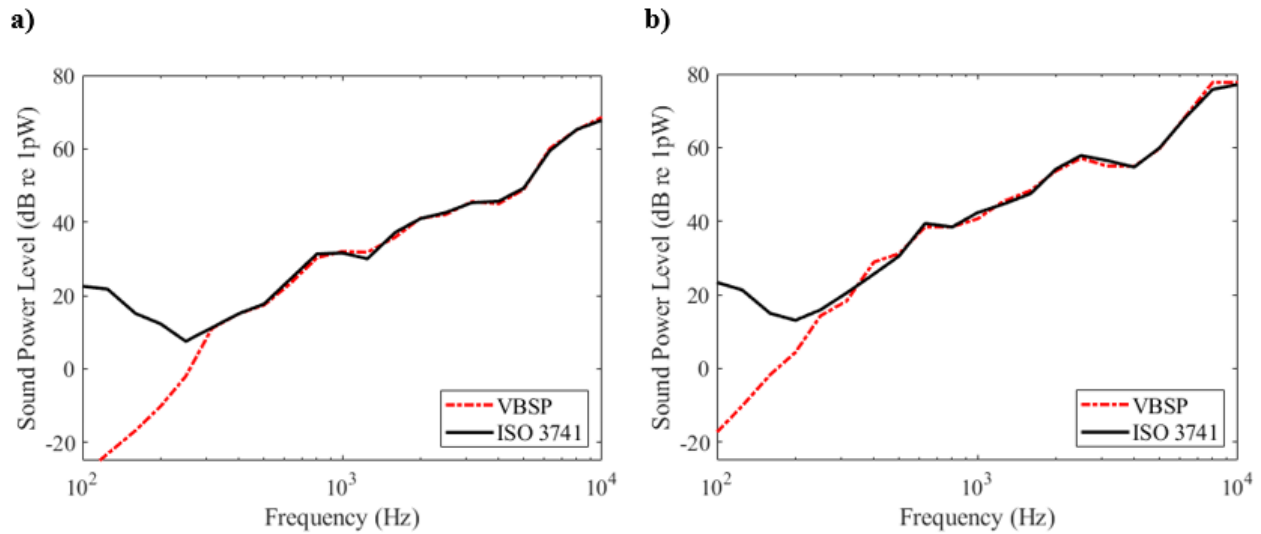


Using a reference of  $10^{-12}$  W, the overall sound power level for the TR curved plate was measured as 70.7 dB using the VBSP method and 70.2 dB using the ISO 3741 method, resulting in a difference of 0.5 dB. Similarly, for the WR curved plate, the overall sound power level was 81.0 dB using VBSP and 80.0 dB using ISO 3741, resulting in a difference of 1.0 dB.

Table 3.2 quantifies the OTO band sound power differences between the methods for these plates. The ISO 3741 method introduces significant error below the 315 Hz OTO band due to the noise floor, while the VBSP method demonstrates greater accuracy within this frequency range.

According to ISO 3741, if the noise floor is within 10 dB of the measured sound power, the results represent an upper bound on sound power [21]. The ISO 3741 standard depends on microphones to measure the acoustic pressure and is unable to distinguish between the noise produced from the curved plate and the background noise in the reverberation chamber at frequencies below the Schroeder frequency. Hence, the VBSP method is likely more accurate in measuring the sound power below the Schroeder frequency and when the noise source radiates below the noise floor of the reverberation chamber.

These results demonstrate that the VBSP method is likely able to measure sound power from specific devices in relatively noisy environments, reducing the need for specific acoustic environments such as anechoic and reverberation chambers.



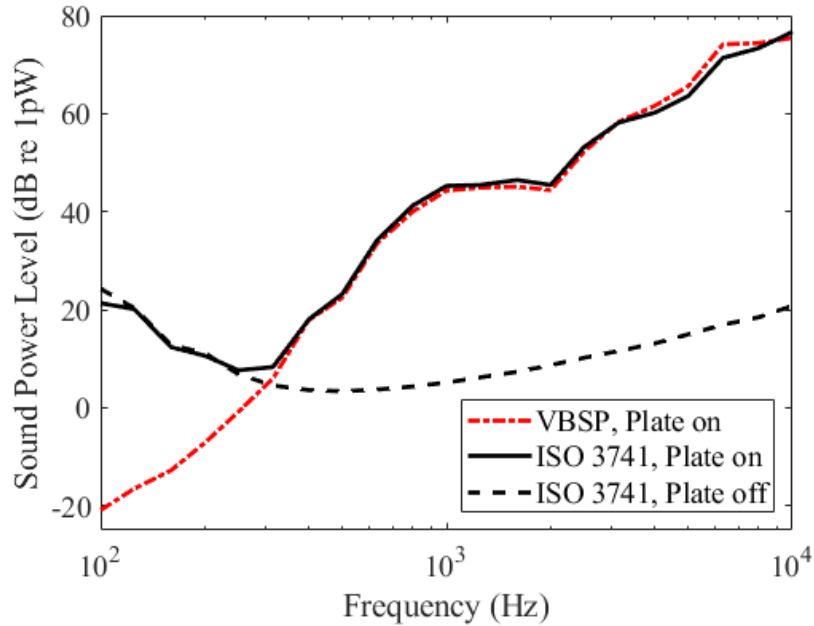
**Figure 3.10:** Results of the sound power measurements using the VBSP method compared to the ISO 3741 standard for (a) the TR curved plate and (b) the WR curved plate.

Figure 3.11 displays the sound power measured from the MR curved plate using both the VBSP and ISO 3741 methods. Initially, the plate was excited, and sound power levels were measured using both methods. Subsequently, the excitation was deactivated to measure the background noise levels in the reverberation chamber using the ISO 3741 standard (indicated by black dashed lines).

The results show favorable agreement between the sound power methods across the 315 Hz to 10 kHz OTO bands. The maximum difference between the VBSP and ISO 3741 methods across the usable bandwidth (315 Hz to 10 kHz) was 2.8 dB at the 6.3 kHz OTO band. The mean difference was 0.2 dB with a standard deviation of 1.4 dB. For the full frequency spectrum (100 Hz to 10 kHz), the overall sound power level was 79.7 dB re  $10^{-12}$  W using the VBSP method and 79.4 dB re  $10^{-12}$  W using the ISO 3741 method, resulting in a total difference of 0.3 dB.

Below the 315 Hz OTO band, the two methods diverge and there remains consistent agreement between the sound power measured from the MR curved plate using the ISO 3741 standard and the background noise in the chamber. This suggests that the ISO 3741 method

predominantly measures the background noise of the reverberation chamber below 315 Hz, which masks the relatively low sound power output from the MR curved plate within this range [31]. In contrast, the VBSP method demonstrates significantly reduced sensitivity to the chamber's background noise. Therefore, it is likely that the VBSP method is the more accurate measurement down to 100 Hz.



**Figure 3.11:** Results of the sound power measurements using the VBSP method compared to the ISO 3741 standard for the MR curved plate. Background noise results from the reverberation chamber are also included (ISO 3741, Plate off).

### 3.9.2 Anechoic and Uncontrolled Acoustic Environments

Figure 3.12 compares the results from the ISO 3745 standard in the anechoic chamber with the VBSP results in the uncontrolled environments below the 400 Hz OTO band. They show good agreement between the methods down to the 160 Hz OTO band. The deviations in the sound power methods below 160 Hz come from the inability of the PZT excitation to produce sound pressure levels above the ISO 3745 standard's background noise criterion. It is likely that the methods

would agree better with a stronger excitation below this OTO band. Further, this confirms that the VBSP method can indeed measure the sound power from baffled structures across the OTO bandwidth (160 Hz to 10 kHz).

The ISO 3741 method introduces significant error below the 315 Hz OTO band due to the noise floor, while the VBSP method demonstrates greater accuracy within this frequency range. The plate was remounted on the wall with a new PZT so these results will not be the same as the VBSP results in the reverberation chamber. A new ISO 3741 measurement was taken and included in Fig. 3.12. Table 3.2 quantifies the OTO band sound power differences between the VBSP and ISO 3741 methods for the WR curved plate. These results confirm the robustness of the VBSP method in different environments and its capability of *in situ* testing.

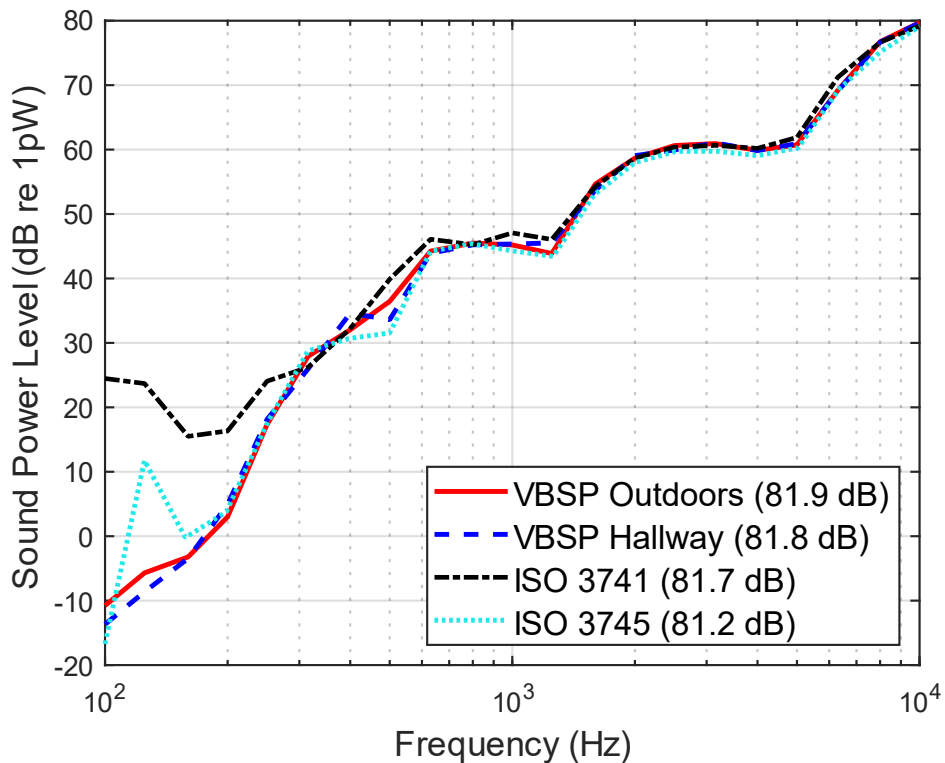


**Figure 3.12:** The VBSP results of the WR curved plate in two uncontrolled acoustic environments compared to the ISO 3741 and ISO 3745 standards.

**Table 3.2:** The absolute difference in sound power measurements for the MR, TR, and WR curved plates using the VBSP method and ISO 3741. Similarly, for the WR curved plate in two uncontrolled acoustic environments.

Curved Plate:		$\Delta L_w$ (dB re 1 pW)				
		MR	TR	WR	Hallway	Outside
OTO band frequency (Hz)	100	42.3	51.5	40.7	38.3	35.4
	125	36.6	44.9	31.5	32.0	29.1
	160	25.1	31.9	16.7	19.1	18.9
	200	17.8	22.5	8.7	11.5	13.4
	250	8.5	9.5	1.6	6.0	6.8
	315	2.3	0.2	2.2	0.3	1.7
	400	0.1	0.0	3.3	2.4	0.2
	500	0.8	0.3	0.7	6.2	3.3
	630	0.6	1.2	1.0	2.2	1.8
	800	1.2	1.0	0.1	0.0	0.2
	1000	1.0	0.4	1.7	1.7	1.8
	1250	0.5	1.8	0.7	0.5	2.2
	1600	1.4	1.3	0.9	0.6	0.4
	2000	1.1	0.1	0.5	0.4	0.1
	2500	1.0	0.5	0.7	0.4	0.3
	3150	0.2	0.3	1.5	0.4	0.3
	4000	1.4	0.7	0.2	0.3	0.3
	5000	2.0	0.3	0.2	0.9	1.1
	6300	2.8	0.6	0.3	2.1	2.0
	8000	1.0	0.1	1.9	0.1	0.1
10000	1.2	0.8	0.6	0.5	0.6	
<b>Overall</b>		<b>0.3</b>	<b>0.5</b>	<b>1.0</b>	<b>0.1</b>	<b>0.2</b>

### 3.10 Conclusions

In this study, a vibration-based sound power (VBSP) method was developed and validated for measuring sound power from baffled simply curved plates. Previous research focused on  $\mathbf{R}$  matrix expressions for baffled flat plates, fully closed cylindrical shells, and fully closed spherical shells, leaving a gap for open-curved plate geometries encountered in practical applications such as tractor cab windows, car door panels, and aircraft or marine vehicle panels.

Experimental validation was performed and involved comparing sound power obtained from the VBSP method using the new  $\mathbf{R}$  matrix expression with the pressure-based ISO 3741 and ISO 3745 standards. Three curved plates with varying radii of curvature were fabricated and tested in several environments. Excellent agreement was observed between the VBSP method and ISO 3741 standard, in a reverberation chamber, within the usable bandwidth (400 Hz to 10 kHz OTO bands). The VBSP method exhibited lower sensitivity to background noise compared to the ISO 3741 standard. Mean sound power differences for the three plates, with respective standard deviations, were 0.2 dB (1.4 dB) for the MR curved plate, 0.1 dB (0.8 dB) for the TR curved plate, and 0.1 dB (2.1 dB) for the WR curved plate, when compared to the ISO 3741 standard.

Furthermore, the VBSP method demonstrated its capability to accurately measure sound power from the WR curved plate in non-controlled acoustic environments. Tests were conducted in a hallway with moderate foot traffic, loud HVAC system, and elevator noise, as well as outdoors with high vehicle noise, a rainstorm with thunderclaps, wind speeds up to 11 mph, and temperature variations of 14°F (7.8°C), showcasing the robustness of the VBSP method.

The sound power of the WR curved plate was then measured in an anechoic chamber according to the ISO 3745 standard. The results confirm the VBSP method's ability to capture the radiated energy below the threshold frequency of 385 Hz for the ISO 3741 standard in the reverberation chamber. Previous papers on the VBSP method have not confirmed this result due to restricting the testing in a reverberation chamber with a Schroeder frequency of 385 Hz. This result supports the claim that the VBSP method is likely measuring the sound power accurately below 400 Hz OTO band.

These results highlight the potential of the VBSP method for accurately measuring sound power from baffled simply curved plates, surpassing the limitations of traditional measurement

standards in certain scenarios. The sound power from a baffled structure can be accurately measured using the VBSP method in different acoustic environments across the OTO bandwidth of interest (160 Hz to 10 kHz).

This work validates the robustness of the VBSP method in measuring sound power from baffled simply curved plates in real-world environments. The developed baffled simply curved plate  $\mathbf{R}$  matrix expression enables the natural acoustic radiation modes for these structures to be computed. These results have significant implications for accurately characterizing the sound power of curved plates in various industrial applications. The results support the practical application of the VBSP method outside of controlled acoustic environments *in situ*, allowing for accurate sound power measurements even in the presence of significant background and time-varying noise produced by the plate environment, and provide confidence in the viability of the baffled simply curved plate  $\mathbf{R}$  matrix for future use.

### **3.11 Acknowledgments**

The authors gratefully acknowledge the assistance of Jeremy Peterson and his machine shop for help with fabricating the curved plates and the wall for the anechoic chamber. Furthermore, the authors extend gratitude for the additional support from various BYU students and staff members with different aspects of the work presented here.

Funding: This work was partially supported by the National Science Foundation [grant number 1916696].

## 3.12 Appendix 3A

### 3.12.1 Introduction

A “special” function in mathematics is one that appears so often that it receives a name, and its properties are studied [23], [25]. Many special functions cannot be expressed in terms of elementary functions and therefore can only be expressed in terms of integrals and differential equations [33]. This appendix was organized using Appendices B and V from Refs. [24] and [29], respectively, to define the special functions used within this manuscript so that the manuscript is more self-contained.

### 3.12.2 Bessel and Hankel Functions

The  $\nu^{th}$ -order Bessel functions of the first and second kind are given by

$$J_\nu(x) = \sum_{m=0}^{\infty} (-1)^m \frac{x^{\nu+2m}}{m! (\nu+m)!} \quad (3A.1)$$

and

$$Y_\nu(x) = \frac{J_\nu(x) \cos(\pi\nu) - J_{-\nu}(x)}{\sin(\pi\nu)}, \quad (3A.2)$$

respectively.

The  $\nu^{th}$ -order Hankel functions of the first and second kind are given by

$$H_\nu^{(1)}(x) = J_\nu(x) + jY_\nu(x) \quad (3A.3)$$

and

$$H_\nu^{(2)}(x) = J_\nu(x) - jY_\nu(x) \quad (3A.4)$$

respectively.



### 3.12.3 Fock-type Airy Function

In electromagnetics, the Fock-type Airy function [25] is given by

$$W_2(\tau) = \frac{1}{\sqrt{\pi}} \int_{C_2} e^{-\left(\frac{z^3}{3}\right)} e^{\tau z} dz, \quad (3A.5)$$

where  $C_2$  is shown in Fig. 3A.1.

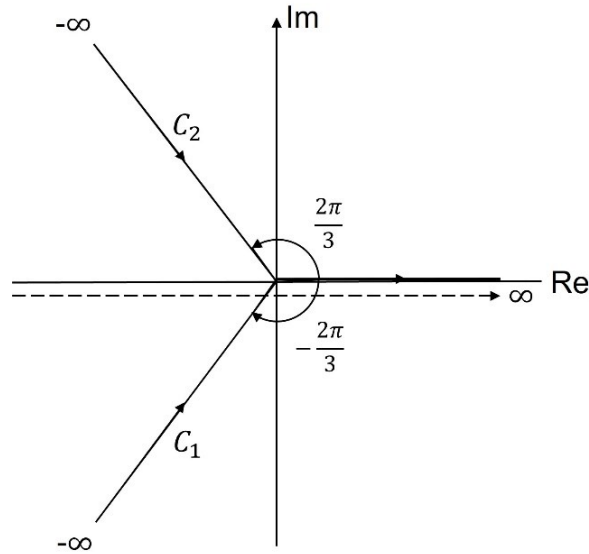


**Figure 3A.1:** Contours in the complex  $\tau$ -plane for Fock V integration.

**Table 3A.1:** The first ten zeros of  $W_2(\tau)$ :  $W_2(\tau'_n) = 0$  and  $W_2'(\tau_n) = 0$ , where  $\tau_n = |\tau_n|e^{-\frac{j\pi}{3}}$

and  $\tau'_n = |\tau'_n|e^{-\frac{j\pi}{3}}$ .

$n$	$ \tau_n $	$ \tau'_n $
1	2.33811	1.01879
2	4.08795	3.24819
3	5.52056	4.82010
4	6.78661	6.16331
5	7.94413	7.37218
6	9.02265	8.48849
7	10.0402	9.53545
8	11.0085	10.5277
9	11.9300	11.4751
10	12.8288	12.3848

### 3.12.4 The Fock V Coupling Function

The hard Fock coupling function, denoted by  $V(x)$ , was developed to give an asymptotic description of the electric current over convex surfaces [33], [35] and is given by

$$V(x) = \frac{\sqrt{x} e^{\frac{j\pi}{4}}}{2\sqrt{\pi}} \int_{\infty C_1}^{\infty} \frac{(W_2(\tau)e^{-jx\tau})}{W_2'(\tau)} d\tau. \quad (3A.6)$$

$V(x) \in \mathbb{C}$  even though  $x \in \mathbb{R}$ . The contour of integration  $C_1$  for Eqn. 3A.6 is shown in Fig. 3A.1.

Let  $\tau_n = |\tau_n|e^{-\frac{j\pi}{3}}$  and  $\tau'_n = |\tau'_n|e^{-\frac{j\pi}{3}}$ . When  $x > 0.6$ , the first ten terms are usually sufficient to approximate  $V(x)$  using the following expression [25]

$$V(x) \approx \sqrt{\pi x} e^{-\frac{j\pi}{4}} \sum_{n=1}^{10} \frac{e^{-jx\tau'_n}}{\tau'_n}, \quad (3A.7)$$

where the  $\tau'_n$  values are given in Table 3A.1. When  $x < 0.6$ , then the first four terms are usually sufficient to approximate  $v(x)$  using the following expression [25]

$$V(x) \approx 1 - \frac{\sqrt{\pi}}{4} e^{\frac{j\pi}{4}} x^{\frac{3}{2}} + \frac{7j}{60} x^3 + \frac{7\sqrt{\pi}}{512} x^{\frac{9}{2}}. \quad (3A.8)$$

### 3.13 References

- [1] G.V. Borgiotti, “The power radiated by a vibrating body in an acoustic fluid and its determination from boundary measurements,” *J. Acoust. Soc. Am.* **88**(4), 1884-1893 (1990). doi: 10.1121/1.400211
- [2] S. J. Elliot and M. E. Johnson, “Radiation modes and the active control of sound power,” *J. Acoust. Soc. Am.* **94**(4), 2194-2204 (1993). doi: 10.1121/1.407490
- [3] A. Sarkissian, “Acoustic radiation from finite structures,” *J. Acoust. Soc. Am.* **90**, 574-578 (1991). doi: 10.1121/1.401231
- [4] K. A. Cunefare and M. N. Currey, “On the exterior acoustic radiation modes of structures,” *J. Acoust. Soc. Am.* **96**(4), 2302-2312 (1994). doi: 10.1121/1.410102
- [5] F. Fahy and P. Gardonio, *Sound and Structural Vibration: Radiation, Transmission and Response*, 2nd ed. (Academic Press, Oxford, UK, 2007), pp. 165-175.
- [6] J. P. Arenas and M. J. Crocker, “Sound radiation efficiency of a baffled rectangular plate excited by harmonic point forces using its surface resistance matrix,” *Int. J. Acoust. Vib.* **7**(4), 217-229 (2002). doi: 10.20855/ijav.2002.7.4120
- [7] A. Loghmani, M. Danesh, M. K. Kwak, and M. Keshmiri, “Active control of radiated sound power of a smart cylindrical shell based on radiation modes,” *Appl. Acoust.* **114**, 218-229 (2016). doi: 10.1016/j.apacoust.2016.07.027
- [8] J. Liu, Y. Liu, and J. S. Bolton, “Acoustic source reconstruction and visualization based on acoustic radiation modes,” *J. Sound Vib.* **437**, 358-372 (2018). doi: 10.1016/j.jsv.2018.08.030

- [9] C. B. Goates, S. D. Sommerfeldt, and J. D. Blotter, "Frequency trends of acoustic radiation modes for cylindrical structures," *Proc. Mtgs. Acoust.* **35**(1), 065003 (2018). doi: 10.1121/2.0001020
- [10] C. B. Goates, C. B. Jones, S. D. Sommerfeldt, and J. D. Blotter, "Sound power of vibrating cylinders using the radiation resistance matrix and a laser vibrometer," *J. Acoust. Soc. Am.* **148**(6), 3553-3561 (2020). doi: 10.1121/10.0002870
- [11] C. B. Jones, C. B. Goates, J. D. Blotter, and S. D. Sommerfeldt, "Experimental validation of determining sound power using acoustic radiation modes and a laser vibrometer," *Appl. Acoust.* **164**, 107254 (2020). doi: 10.1016/j.apacoust.2020.107254
- [12] I. C. Bacon, S. D. Sommerfeldt, and J. D. Blotter, "Developing an indirect vibration-based sound power method to determine the sound power radiated from acoustic sources," *Proc. Mtgs. Acoust.* **50**(1), 065003 (2022). doi: 10.1121/2.0001732
- [13] M. R. Bai and M. Tsao, "Estimation of sound power of baffled planar sources using radiation matrices," *J. Acoust. Soc. Am.* **112**, 876-883 (2002). doi: 10.1121/1.1499133
- [14] W. R. Johnson, P. Aslani, S. D. Sommerfeldt, J. D. Blotter, and K. L. Gee, "Acoustic radiation mode shapes for control of plates and shells," *Proc. Mtgs. Acoust.* **19**(1), 065036 (2013). doi: 10.1121/1.4799718
- [15] G. V. Borgiotti and K. E. Jones, "Frequency independence property of radiation spatial filters," *J. Acoust. Soc. Am.* **96**(6), 3516-3524 (1994). doi: 10.1121/1.411407
- [16] Y. Sun, T. Yang, and Y. Chen, "Sound radiation modes of cylindrical surfaces and their application to vibro-acoustics analysis of cylindrical shells," *J. Sound Vib.* **424**, 64-77 (2018). doi: 10.1016/j.jsv.2018.03.004

- [17] D. M. Photiadis, “The relationship of singular value decomposition to wave-vector filtering in sound radiation problems,” *J. Acoust. Soc. Am.* **88**(2), 1152-1159 (1990). doi: 10.1121/1.399811
- [18] H. Wu, W. Jiang, and Y. Zhang, “A method to compute the radiated sound power based on mapped acoustic radiation modes,” *J. Acoust. Soc. Am.* **135**, 679 (2014). doi: 10.1121/1.4861242
- [19] K. A. Cunefare, M. N. Currey, M. E. Johnson, and S. J. Elliott, “The radiation efficiency grouping of free-space acoustic radiation modes,” *J. Acoust. Soc. Am.* **109**, 203-215 (2001). doi: 10.1121/1.1323236
- [20] T. P. Bates, I. C. Bacon, J. D. Blotter, and S. D. Sommerfeldt, “Vibration-based sound power measurements of arbitrarily curved panels,” *J. Acoust. Soc. Am.* **151**, 1171-1179 (2022). doi: 10.1121/10.0009581
- [21] ISO 3741:2010, *Acoustics – Determination of sound power levels and sound energy levels of noise sources using sound pressure — Precision methods for reverberation test rooms*, (International Organization for Standardization, Geneva, Switzerland), (2010).
- [22] ISO 3745:2012, *Acoustics – Determination of sound power levels and sound energy levels of noise sources using sound pressure – Precision methods for anechoic rooms and hemi-anechoic rooms*, (International Organization for Standardization, Geneva, Switzerland), (2012).
- [23] C. B. Goates, *Analytical Expressions for Acoustic Radiation Modes of Simple Curved Structures*, Master’s Thesis, Brigham Young University, Provo, UT, 2019.

- [24] D. A. McNamara, J. A. G. Malherbe, and C. W. Pistorius, *Introduction to the uniform geometrical theory of diffraction*, (Artech House, Boston, 1990), pp. 422-433.
- [25] P. H. Pathak and N. N. Wang, "Ray analysis of mutual coupling between antennas on a convex surface," *IEEE Trans. Ant. Prop.* **29**(6), 911-922 (1981). doi: 10.1109/TAP.1981.1142682
- [26] T. A. Pitts, R. H. Selfridge, D. M. Bhabries, "Solution of the Euler field equations for plane-wave scattering by an end-capped cylinder via the uniform geometrical theory of diffraction," *J. Acoust. Soc. Am.* **94**(6), 3437-3447 (1993). doi: 10.1121/1.407197
- [27] B. R. Levy and B. J. Keller, "Diffraction by a smooth object," *Comm. Pur. Appl. Math.* **12**(1), 159-209 (1959). doi: 10.1002/cpa.3160120108
- [28] A. S. Fokas and E. A. Spence, "Synthesis, as Opposed to Separation, of Variables," *SIAM Review*, **54**(2), 291-324 (2012). doi: 10.1137/100809647
- [29] G. N. Watson, "The diffraction of electric waves by the earth," *Proc. R. Soc. Lond. A.* **95**, 83-99 (1918). doi: 10.1098/rspa.1918.0050
- [30] P. H. Pathak and N. N. Wang, "An analysis of the mutual coupling between antennas on a smooth convex surface," *Tech. Report 784583-7*, Ohio State Univ. Columbus Electroscience Lab (1978).
- [31] T. P. Bates, I. C. Bacon, C. B. Goates, S. D. Sommerfeldt and J. D. Blotter, "Experimental sound power from curved plates using the radiation resistance matrix and a scanning vibrometer," *InterNoise21*, 2755-2766 (2021). doi: 10.3397/IN-2021-2221

- [32] T. W. Leishman, S. Rollins, H. M. Smith, “An experimental evaluation of regular polyhedron loudspeakers as omnidirectional sources of sound,” *J. Acoust. Soc. Am.* **120**(3), 1411-1422 (2006). doi: 10.1121/1.2221552
- [33] S. Hassani, *Mathematical Physics: A Modern Introduction to Its Foundations*, 2<sup>nd</sup> ed. (Cham: Springer, 2013), pp. 437. doi: 10.1007/978-3-319-01195-0
- [34] T. Bird, “Accurate asymptotic solution for the surface field due to apertures in a conducting cylinder,” in *IEEE Transactions on Antennas and Propagation*, **33**(10), 1108-1117 (1985). doi: 10.1109/TAP.1985.1143497
- [35] S. Bird, “Appendix D: Properties of Surface Fock Functions,” in *Mutual Coupling Between Antennas*, 429-432 (2021). doi: 10.1002/9781119565048.app4

## Chapter 4 Application to Baffled Arbitrarily Curved Plates

### 4.1 Introduction

This chapter was published as a peer-reviewed article in the *Journal of the Acoustical Society of America*. Trent Bates and I worked together on this as co-authors. This article represents a significant advancement in the application of the VBSP method across various geometries. It challenged the prevailing notion maintained over 35 years within the acoustical community—that each unique structure requires a unique radiation resistance matrix. The findings demonstrate that approximating arbitrarily curved plates with a single radius of curvature allows the use of radiation resistance matrices derived from simpler geometries, such as flat plates, cylinders, and simply curved plates, for more complex structures. This breakthrough enhances the practicality and application of the VBSP method.

*\*\* My contributions to this paper were primarily on the experimental testing of arbitrarily curved plates. The stitching process was instrumental in connecting the datasets for each section of the structure, enabling comprehensive and accurate analyses. I contributed equally with the first author on the experimental work, but I was not the primary author of this document. \*\**



## 4.2 Required Copyright Notice

The following article appeared in the Journal of the Acoustical Society of America and may be found at <https://doi.org/10.1121/10.0009581> under the title “Vibration-based sound power measurements of arbitrarily curved panels.” It is reproduced in its original published format here by rights granted in the JASA Transfer of Copyright document, item 3.

<https://pubs.aip.org/DocumentLibrary/files/publications/jasa/jascpyrt.pdf>


Citation:

T. P. Bates, I. C. Bacon, J. D. Blotter, and S. D. Sommerfeldt, “Vibration-based sound power measurements of arbitrarily curved panels,” *J. Acoust. Soc. Am.* **151**(2), 1171–1179 (2022).

I hereby confirm that the use of this article is compliant with all publishing agreements.

FEBRUARY 18 2022

## Vibration-based sound power measurements of arbitrarily curved panels

Trent P. Bates; Ian C. Bacon; Jonathan D. Blotter; Scott D. Sommerfeldt 

 Check for updates

*J. Acoust. Soc. Am.* 151, 1171–1179 (2022)  
<https://doi.org/10.1121/10.0009581>



19 June 2024 07:32:46



 **ASA**

Advance your science and career as a member of the  
**Acoustical Society of America**

[LEARN MORE](#)

## Vibration-based sound power measurements of arbitrarily curved panels

Trent P. Bates,<sup>1</sup> Ian C. Bacon,<sup>2</sup> Jonathan D. Blotter,<sup>1,a)</sup> and Scott D. Sommerfeldt<sup>2</sup>

<sup>1</sup>Department of Mechanical Engineering, Brigham Young University, Provo, Utah 84602, USA

<sup>2</sup>Department of Physics and Astronomy, Brigham Young University, Provo, Utah 84602, USA

### ABSTRACT:

Vibration-based sound power (VBSP) measurement methods are appealing because of their potential versatility in application compared to sound pressure and intensity-based methods. It has been understood that VBSP methods have been reliant on the acoustic radiation resistance matrix specific to the surface shape. Expressions for these matrices have been developed and presented in the literature for flat plates, simple-curved plates (constant radius of curvature in one direction), and cylindrical- and spherical-shells. This paper shows that the VBSP method is relatively insensitive to the exact form of the radiation resistance matrix and that computationally efficient forms of the radiation resistance matrix can be used to accurately approximate the sound power radiated from arbitrarily curved panels. Experimental sound power measurements using the VBSP method with the simple-curved plate radiation resistance matrix and the ISO 3741 standard method are compared for two arbitrarily curved panels and are shown to have good agreement. The VBSP method based on the simple-curved plate form of the radiation resistance matrix is also shown to have excellent agreement with numerical results from a boundary element model, which inherently uses the appropriate form of the radiation resistance matrix. © 2022 Acoustical Society of America.

<https://doi.org/10.1121/10.0009581>

(Received 14 August 2021; revised 14 December 2021; accepted 28 January 2022; published online 18 February 2022)

[Editor: Nickolas Vlahopoulos]

Pages: 1171–1179

### I. INTRODUCTION

Sound power is a standard metric commonly used to evaluate the amount of noise radiated from a source. The International Organization for Standardization (ISO) has published ten standards and two technical specifications describing methods for measuring sound power. The accuracy of the results from these ISO methods are rated as precision (Grade 1), engineering (Grade 2), and survey (Grade 3).<sup>1</sup> The ten ISO standards are pressure or intensity-measurement based and the two technical specifications are vibration measurement based. The vibration-based technical specifications only provide engineering (Grade 2) or survey (Grade 3) results. Vibration-based measurements are of interest if significant background noise is present, other methods are difficult to apply, and/or sound power measurements for a specific or partial source are required in the presence of other noise sources. Because of the potential versatility, the development of a vibration-based sound power (VBSP) measurement method that can provide precision (Grade 1) results is desirable. The motivation of this work is to further develop and validate a practical method for measuring sound power, based on vibration-based measurements, that could provide accurate *in situ* measurements of sound power.

VBSP methods are based on the theory of elementary radiators that was developed in the early 1990s.<sup>2–8</sup> In the

past, volume velocity methods and lumped parameter models have also been used for computing sound power.<sup>9–11</sup>

More recently, development of a VBSP method that has enabled sound power from flat plates, simple-curved plates (constant radius of curvature in one direction), and cylindrical-shells to be accurately measured has been presented in the literature.<sup>12–14</sup> As many commercial products and useful devices that radiate noise have more complex geometries than these simple shapes, the VBSP method needs to be extended to account for arbitrarily curved surfaces. This extension of the VBSP method is the focus of this paper.

The basic equation for computing sound power using the VBSP method is given by

$$P(\omega) = \mathbf{v}_e^H(\omega) \mathbf{R}(\omega) \mathbf{v}_e(\omega), \quad (1)$$

where  $\mathbf{v}_e$  is a vector of the surface normal velocity of each elementary radiator,  $(\cdot)^H$  is the Hermitian transpose,  $\mathbf{R}$  is the acoustic radiation resistance matrix, and  $\omega$  is the frequency.<sup>8</sup> Previous work has established specific forms of the radiation resistance matrix for basic surface shapes, but a specific form for arbitrarily curved surfaces has not yet been developed. However, work presented here indicates that a specific form of the radiation resistance matrix that closely matches the geometry for every useful surface shape may not be required to obtain accurate results.

In this paper, the sensitivity of sound power results to specific forms of the radiation resistance matrix is explored

<sup>a)</sup>Electronic mail: jblotter@byu.edu, ORCID: 0000-0001-8783-5243.

to support using an existing, computationally efficient form of the radiation resistance matrix to provide sound power results for arbitrarily curved panels. This exploration specifically compares the radiation resistance matrix expressions for flat plates, simple-curved plates, and cylindrical-shells. The results show that errors in the calculated sound power can be small when using any form of the radiation resistance matrix for many cases. Experimental sound power measurement results from two arbitrarily curved panels, obtained using the VBSP and ISO 3741<sup>15</sup> methods, show excellent agreement despite using the simple-curved plate form of the radiation resistance matrix in the VBSP calculations.

To further support the use of simple and computationally efficient forms of the radiation resistance matrix for arbitrarily curved panels, numerical models of the experimental arbitrarily curved-panels were created. The elemental velocities computed by the numerical models were used in the VBSP method to compute the sound power with the simple-curved plate radiation resistance matrix. These results were compared to the sound power computed directly from the numerical boundary element model (BEM), which inherently computes the appropriate radiation resistance matrix for the structure. Results from the two numerical data-based approaches show excellent agreement.

## II. SOUND POWER SENSITIVITY TO BASIS FUNCTION

The VBSP method uses the radiation resistance matrix and surface normal velocity measurements to compute sound power. Previous research has established the form of the radiation resistance matrix for flat plates, cylindrical- and spherical-shells, and simple-curved plates.<sup>8,12-14</sup> After presenting the radiation resistance matrix expressions for these simple geometries, this section investigates the differences in sound power obtained using these expressions.

### A. Radiation resistance matrix expressions

For simple flat plates, the radiation resistance matrix is given by

$$R_{\text{flat},ij} = \frac{\rho_0 \omega^2 S_e^2 \text{sinc}kd_{ij}}{4\pi c kd_{ij}}, \quad (2)$$

where  $\rho_0$  is the density of the surrounding fluid,  $\omega$  is the angular frequency,  $S_e$  is the area of a single discrete element,  $c$  is the speed of sound in the fluid,  $k$  is the acoustic wavenumber, and  $d_{ij}$  is the distance from the  $i$ th to the  $j$ th element.<sup>8</sup> This form of the radiation resistance matrix is relatively simple and computationally efficient, providing a useful basis function to apply the VBSP method for flat plates.<sup>12</sup>

The form of the radiation resistance matrix, or basis function, for cylindrical-shells has been recently derived and validated.<sup>13</sup> This expression is given by

$$R_{\text{cyl},ij} = \frac{S_e^2 \omega \rho_0}{a\pi^2} \sum_{m=0}^{\infty} \cos[m(\theta_i - \theta_j)] \times \int_0^k \frac{1}{k_r} \text{Im} \left\{ \frac{H_m^{(2)}(k_r a)}{H_m^{(2)'}(k_r a)} \right\} \cos[k_z(z_i - z_j)] dk_z, \quad (3)$$

where  $S_e = a\Delta\theta\Delta z$  is the area of a single discrete element,  $a$  is the radius of curvature,  $\theta_i, \theta_j, z_i, z_j$  are the physical coordinates of the  $i$ th and  $j$ th elements, as shown in Fig. 1,  $k$  is the acoustic wavenumber,  $k_r = \sqrt{k^2 - k_z^2}$ ,  $k_z$  is the axial wavenumber, and  $H_m^{(2)}(x)$  is the  $m$ th-order Hankel function of the second kind. This form of the radiation resistance matrix is more computationally expensive than the flat plate expression.

Using eigenfunction expansion and the uniform theory of diffraction the cylindrical shell radiation resistance matrix can be modified to model simple-curved plates as given by

$$R_{ij} = -\frac{\rho_0 \omega S_e^2}{4\pi d_{ij}} \text{Im} \{ V(\xi) e^{-jk d_{ij}} \}, \quad (4)$$

where  $V(\xi)$  is the hard Fock V coupling function with argument  $\xi = t [k \cos^4 \psi / (2a^2)]^{1/3}$ ,  $t = \sqrt{(z_i - z_j)^2 + a^2 \phi^2}$  is the distance traversed across the curved surface,  $\psi = \tan^{-1}(z_i - z_j / a\phi)$  is the angle between the direction of propagation and the cylinder axis,  $\phi = \theta_i - \theta_j$ , and the non-subscripted  $j = \sqrt{-1}$ .<sup>14</sup> The hard Fock V coupling function,  $V(\xi)$ , has been sufficiently characterized to produce useful series representations with ten terms or less, with these terms given in an Appendix in Ref. 16. This form of the radiation resistance matrix is still relatively complex but is less computationally expensive than the form for cylindrical-shells and is useful for applying the VBSP method to simple-curved plates.

Computational efficiency is an important consideration in the development of VBSP methods. Given that the forms of the radiation resistance matrix are relatively complex for geometries with curvature, computation of the cylindrical-shell and simple-curved plate forms are less efficient than the flat plate form. If the specific form of the radiation

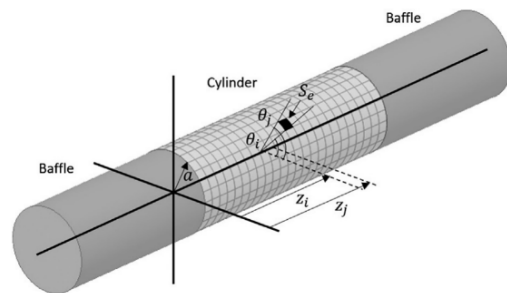


FIG. 1. A diagram of the infinitely baffled cylinder geometry with a discretization of the non-rigid portion of the cylinder shown. Variables of interest from Eq. (3) are illustrated with a single element of the discretized surface highlighted in black.



resistance matrix does not significantly affect the accuracy of the sound power results, it may be preferable to use a computationally efficient form of the radiation resistance matrix.

**B. Sensitivity of sound power computation to form of radiation resistance matrix**

The sensitivity of the sound power calculations to the form of the radiation resistance matrix was investigated by comparing computational sound power results from the forms provided in Eqs. (2)–(4). The theoretical structure under test was a 2 mm thick, 31.5 cm × 31.5 cm, aluminum plate curved to various constant radii of curvature in one direction. Each plate was discretized with a 21 × 21 point grid. The velocity at each grid point was calculated with respect to frequency using the expression,

$$v_n(\theta, z) = \tilde{v}_{pq} \sin(p\pi\theta/\theta_{\max}) \sin(q\pi z/h), \tag{5}$$

where  $\tilde{v}_{pq}$  is the input amplitude,  $p$  and  $q$  are mode numbers,  $\theta = x/a$  and  $\theta_{\max} = w/a$  where  $x$  is the coordinate arc length along the width and  $a$  is the radius of curvature,  $w$  and  $h$  are the width and height of the plate when flat, and  $z$  is the coordinate location along the height of the plate. Equation (5) is a modified form of the surface velocity expression for simply supported flat plates. Figure 2 illustrates an example of the theoretical test structure and how the radius was applied, with other variables shown for clarity. Sound power was computed using the radiation resistance matrix for flat plates, cylindrical-shells, and simple-curved plates to apply the VBSP method based on the above theoretical inputs.

The differences between the various forms of the radiation resistance matrix are best observed by plotting the differences in calculated radiated sound power (in dB) between each of the matrices. This was done over the frequency range from 100 Hz to 2 kHz.

Figure 3 shows the results from comparing the sound power calculated using the simple-curved plate and flat-plate formulations of the radiation resistance matrix. The difference in sound power was computed by subtracting the flat plate result from the simple-curved plate result. As any difference shown is positive, the results indicate that the flat

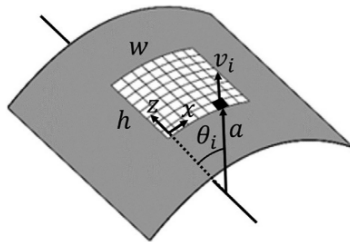


FIG. 2. A diagram of a simply supported curved plate with partial discretization of the surface shown and element  $i$  highlighted in black. This is an example of the theoretical structure applied, with various radii of curvature and surface velocity from Eq. (5), to produce the results in Figs. 3–5.

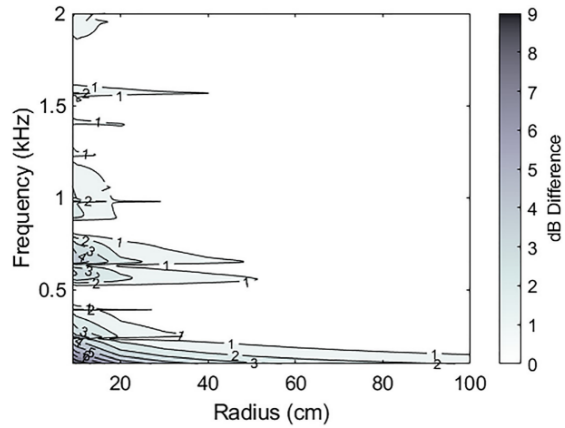


FIG. 3. (Color online) Difference in sound power between the simple-curved plate and flat plate formulations of the radiation resistance matrix using the VBSP method.

plate results represent a lower bound on sound power. The results show that there is little difference in using either formulation for larger radii of curvature and higher frequencies. There are larger differences in the sound-power results when the curvature is tight (below 20 cm) and the frequency is below 700 Hz but otherwise the differences are at most 2 dB and very often essentially zero. Figure 4 shows similar results from comparing the cylindrical-shell and flat-plate formulations of the radiation resistance matrix. Figure 5 shows the comparison between the simple-curved plate and cylindrical-shell formulations of the radiation resistance matrix. The basic trend of the largest difference in sound power results occurring only when the curvature is tight and the frequency is below 700 Hz holds for all three comparisons presented.

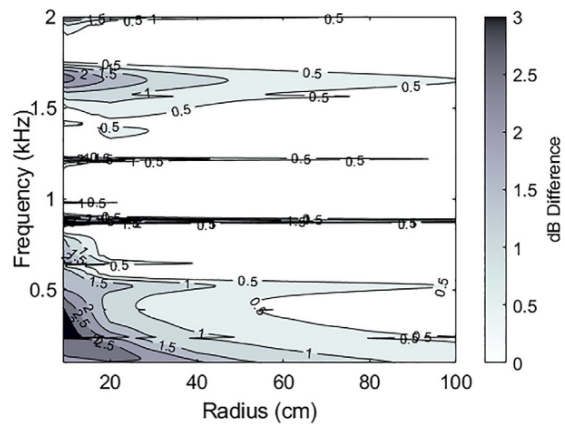


FIG. 4. (Color online) Difference in sound power between the cylindrical-shell and flat plate formulations of the radiation resistance matrix using the VBSP method.

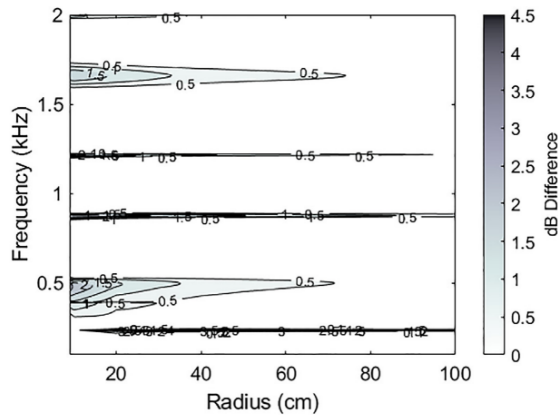


FIG. 5. (Color online) Difference in sound power between the curved-plate and cylindrical-shell formulations of the radiation resistance matrix using the VBSP method.

### III. EXPERIMENTAL VERIFICATION OF SOUND POWER CALCULATIONS

To explore computing the sound power for arbitrarily curved plates using the simple-curved plate radiation resistance matrix, experimental results from the VBSP and ISO 3741 methods were compared. Two arbitrarily curved panels with significantly different shapes were used in the comparison. The experimental results are reported in one-third octave bands as per ISO 3741.

#### A. Experimental setup and measurement of two arbitrarily curved panels

The two arbitrarily curved panels used to obtain the experimental results presented in this work have similar boundary conditions but significantly different shapes of curvature. The arbitrarily curved panels are identified as the S-curved panel and M-curved panel, based on their basic curvature shape. These panels were shaped with a non-constant radius of curvature and are thus considered

arbitrarily curved, but like a simple-curved plate, they have curvature in only one direction.

Each arbitrarily curved panel is composed of a thin aluminum panel formed in a curvature that is clamped along each straight edge in a heavy steel frame and baffled with solid aluminum caps along each curved edge (see Fig. 6). A silicone sealant bead was applied on the inside of the panel along the curved edges to prevent any sound radiation from the back of the panel escaping into the measured field (see Fig. 7). The basic dimensions of each arbitrarily curved panel are summarized in Table I.

The arbitrarily curved panels were mounted flush against one wall of a reverberation chamber with approximate dimensions  $5\text{ m} \times 6\text{ m} \times 7\text{ m}$ . An infinite baffle was approximated by mounting the panels on the wall of the reverberation chamber. The edges of the frame holding the arbitrarily curved panels were sealed to the wall using Gaff tape to prevent acoustic radiation from the back of the panels escaping into the measured field. A piezoelectric transducer was attached to the inside surface of each panel within 4 cm of one corner. The piezoelectric transducer was activated with a pseudo random signal from 0 to 12.8 kHz.

A Polytec PSV-500-three-dimensional (3D), scanning laser Doppler vibrometer (SLDV), was used to measure the velocity response of the arbitrarily curved panels. One advantage of using an SLDV is that a large number of measurement points can be easily used to measure a surface. To enable the 3D features of the SLDV, precise registration points with known spatial locations with respect to a global coordinate system were placed on each panel using a 3D coordinate measurement arm. Each arbitrarily curved panel was scanned in three or four sections and then each section was stitched together to form a complete surface velocity response. The spatial resolution of scan points for each panel was a maximum of 6.7 mm, which gives a minimum of six scan points per structural wavelength for frequencies up to 10 kHz. The VBSP method requires the magnitude of the normal component of the surface velocity to compute sound power. The SLDV was also used to measure the

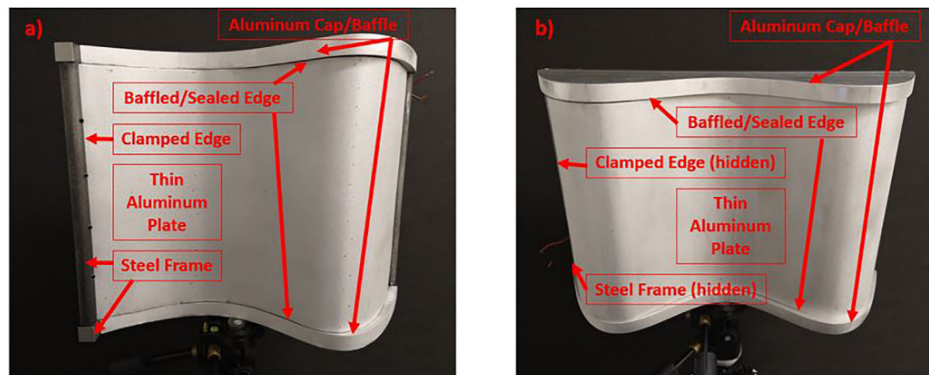


FIG. 6. (Color online) Images of the outside surfaces of the (a) S-curved panel and (b) M-curved panel to illustrate the general build of the arbitrarily curved plates used in this work. Coordinate frame included in (a) for reference, see Fig. 8.

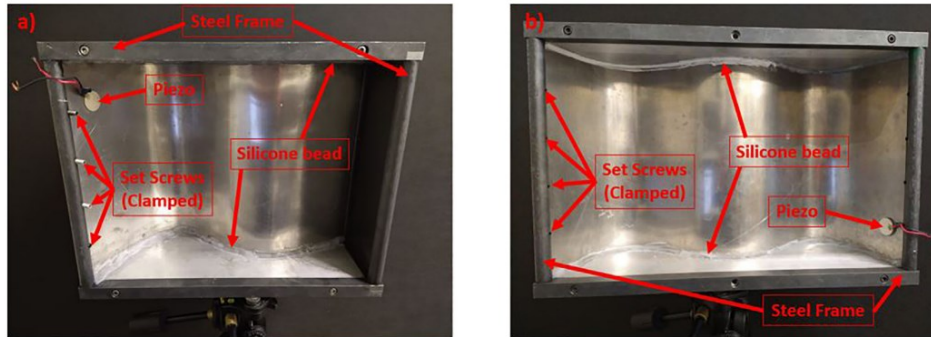


FIG. 7. (Color online) Images of the inside surfaces of the (a) S-curved panel and (b) M-curved panel to illustrate the general build of the arbitrarily curved panels used in this work.

surface geometry, from which the normal direction at each scan point was determined and then used to compute the normal component of velocity.

Experimental sound-power results were computed using the VBSP (SLDV velocity and geometry data) and ISO 3741 (microphone sound-pressure data) methods. These results are presented and compared in the following section. Both sets of results are presented and compared in one-third octave bands as per ISO 3741. The VBSP method was employed using the simple-curved plate radiation resistance matrix given by Eq. (3).

**B. Sound power results of two arbitrarily curved panels**

**1. Applying the simple-curved plate radiation resistance matrix**

The form of the simple-curved plate radiation resistance matrix assumes a constant radius of curvature,  $a$ , and also includes an angle  $\phi$  that is determined using this constant radius of curvature [see Eq. (4)]. When applying the simple-curved plate form of the radiation resistance matrix to arbitrarily curved panels an appropriate constant radius value must be determined. This was done by applying a constant-radius curve fit to the basic curvature of each panel, constraining the width to match the width of the actual panels (see Fig. 8 for an example using the S-curved panel). The resulting radius of curvature for each panel was used in computing the radiation resistance matrix. The rest of the computations proceeded using the experimental data as measured and with no further modifications.

It was found that sound power computed using the simple-curved plate form of the radiation resistance matrix

is not highly sensitive to the radius of curvature. Figure 9 shows results from investigating the impact of the radius on sound power using the same theoretical setup presented in Sec. II B. A radius of 50 cm was selected as the base comparison radius. Sound power was then calculated using the simple-curved plate form of the radiation resistance matrix for a range of radius values from 5 to 100 cm. The results are shown as sound power difference in dB between each radius case and the comparison radius case of 50 cm. These results indicate that sound power calculated using the simple-curved plate form of the radiation resistance matrix is not highly sensitive to the constant radius value except at low frequency (below 200 Hz) and when the radius is tight (below 20 cm).

**2. S-curved panels**

Figure 10 presents the sound power results comparison between the VBSP and ISO 3741 methods for the S-curved panel. The results show excellent agreement between the two methods for the center band frequency range from

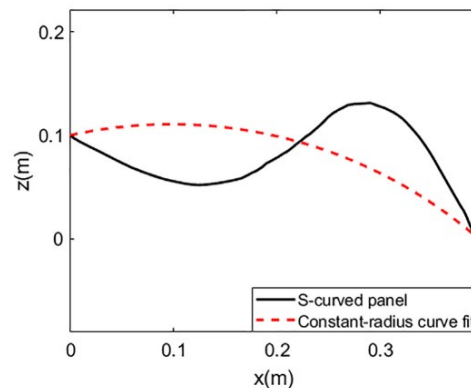


FIG. 8. (Color online) Plot of a constant-radius curve fit applied to the curvature of the S-curved panel, to compute a resultant radius to use in applying the simple-curved plate form of the radiation resistance matrix. The curvatures are shown with  $x$  and  $z$  coordinates, with  $y$  normal to the page, see Fig. 6.

TABLE I. Dimensions of the S and M arbitrarily curved panels.

Panel	Height (cm)	Width (cm)	Thickness (mm)	Range of radius of curvature (cm)
S-Curved	30	40	1.59	6–63
M-Curved	30	48	1.59	6–51



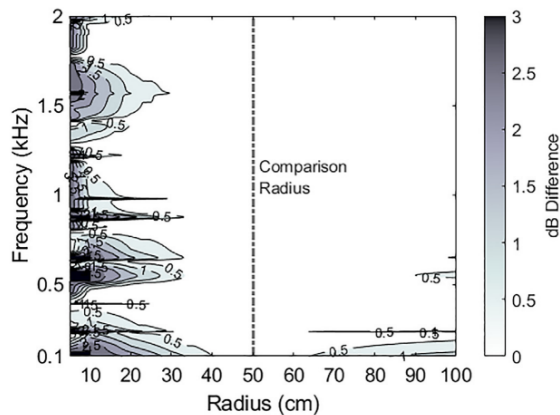


FIG. 9. (Color online) Difference in sound power between different radius value cases and the base comparison radius case of 50 cm (dash and dot vertical line). Sound power was computed using the simple-curved plate form of the radiation resistance matrix and the same theoretical setup presented in Sec. II B.

400 Hz to 10 kHz. In this frequency range, the mean difference was 0.4 dB with a standard deviation of 1.3 dB, and the maximum absolute difference was 3.2 dB at center band frequency 8 kHz. For the full frequency spectrum from 100 Hz to 10 kHz, the total sound-power level based on the VBSP method was 77.9 dB re  $10^{-12}$  W and, based on ISO 3741, the sound power was measured as 79.9 dB re  $10^{-12}$  W for a total absolute difference of 2.0 dB. At frequencies below 400 Hz, the noise floor of the reverberation chamber introduces significant error in the ISO 3741 results. This is due to the piezoelectric transducer not exciting the S-curved plate significantly at these lower frequencies, resulting in the plate not radiating above the background noise in the reverberation chamber. In this low frequency regime, it is likely that the VBSP method provides more accurate results than the ISO 3741 method because the background noise has less effect on the VBSP method.

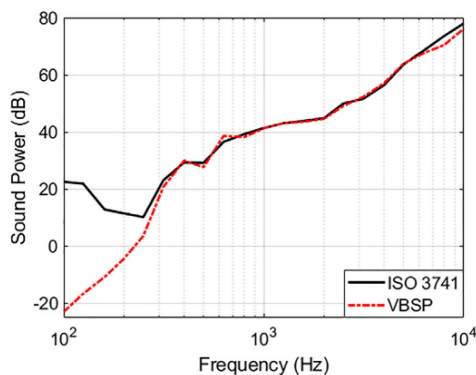


FIG. 10. (Color online) Results of the sound-power measurements of the S-curved panel using the VBSP and ISO 3741 methods.

### 3. M-curved panel

Figure 11 shows the comparison between the VBSP and ISO 3741 sound power results for the M-curved panel. Again, the results show excellent agreement for the one-third octave center band frequency range from 400 Hz to 10 kHz. In this frequency range, the mean difference was 0.3 dB with a standard deviation of 1.2 dB, and with a maximum absolute difference of 3.0 dB at center band frequency 4 kHz. For the full frequency spectrum from 100 Hz to 10 kHz, the total sound power level based on the VBSP method was 72.2 dB re  $10^{-12}$  W and based on ISO 3741 was 71.8 dB re  $10^{-12}$  W, for a total absolute difference of 0.4 dB. The sound power results below 400 Hz again indicate that there is significant error introduced into the ISO 3741 results due to the presence of background noise in the chamber.

Table II provides a summary of the difference in the sound-power results between the VBSP and ISO 3741 methods for both arbitrarily curved panels. The results in this table are presented with one-third octave band frequencies and the sound power difference in dB, with a total difference for each arbitrarily curved panel presented on the bottom row.

## IV. COMPUTATIONAL VERIFICATION OF SOUND POWER CALCULATIONS

To provide additional evidence that supports the use of the simple-curved plate radiation resistance matrix to calculate sound power from arbitrarily curved panels, a BEM computational model was created for each arbitrarily curved panel presented above. Each model was setup for coupled analysis with structural finite elements and a fluid boundary element mesh. Sound power results from the BEM models were determined by applying data recovery surfaces around the radiating surface of each model. The surface velocity of each element of the radiating surface was exported from the models to compute sound power using the VBSP method. The VBSP results are based on the simple-curved plate radiation resistance matrix and BEM computed velocities and compared with numerical results for the sound power from

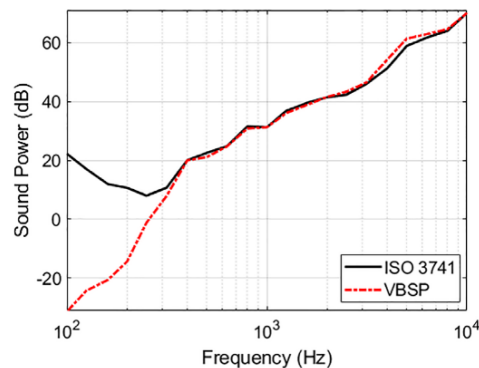


FIG. 11. (Color online) Results of the sound power measurements of the M-curved panel using the VBSP and ISO 3741 methods.



TABLE II. Differences in sound power measurements between the VBSP and ISO 3741 methods for the S- and M- curved panels.

Arbitrarily curved panel:	Sound power difference (dB)		
	S	M	
Third octave band by center	100	45.5	53.6
band frequency (Hz)	125	38.5	41.3
	160	23.7	32.6
	200	15.9	25.0
	250	6.6	9.2
	315	2.3	2.8
	400	-0.6	0.0
	500	1.5	1.5
	630	-2.1	0.1
	800	1.1	0.7
	1000	0.1	0.0
	1250	0.0	0.8
	1600	0.3	0.6
	2000	0.2	-0.2
	2500	0.8	-1.0
	3150	-0.7	-0.5
	4000	-0.6	-3.0
	5000	-0.3	-2.5
	6300	0.9	-1.2
	8000	3.2	-0.5
	10 000	1.9	0.0
Total	2.0	-0.4	

the BEM models, which inherently uses the correct radiation resistance matrix. The same S- and M-surface shapes used in the experimental measurements were used in the numerical models. The numerical models were developed using VA One™, a commercial software package produced by the ESI Group.

The comparison was performed for each arbitrarily curved panel (S-curved panel then M-curved panel) with a setup that was similar to that used in the experimental testing. An infinite baffle was applied to simulate the rigid wall of the reverberation chamber. Rigid plates were modeled at the edges of the radiating surface such that the back side of the radiating surface was sealed against the infinite baffle and could not radiate. A 0.1% damping loss factor was assumed and applied to the radiating surface. The straight edges of the radiating surface were set to a clamped boundary condition and the curved edges were set to a simply supported boundary condition. A constant point force was applied in a similar location to that used in the experimental testing setup. The spacing between nodes applied for each model was a maximum of 13 mm, which is sufficient to resolve the response up to 4 kHz. For reference, the S-curved model was meshed with a total 10 082 triangle elements and 10 903 nodes. The M-curved model was meshed in the same way with triangle elements and a similarly refined mesh. The highest frequency was limited to 4 kHz, with a spacing of 2 Hz, as this was considered sufficient evidence and higher frequency models require increased nodal density that greatly increases the time to solve the models.

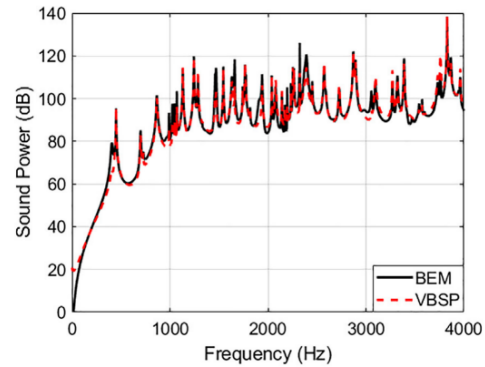


FIG. 12. (Color online) Numerically derived sound power of the S-curved panel using the VBSP and BEM methods.

The BEM models were used to compute the sound power for the panels and to compute the surface velocity at each node. The surface velocity and geometry data were then used to apply the VBSP method, which was based on the simple-curved plate radiation resistance matrix. The results are presented for the sound power (in dB) over the narrow band frequency range from 0 to 4 kHz.

The results of the S-curved panel model are presented in Fig. 12 and show good agreement. The total sound power computed from the BEM results was 141.7 dB and the total sound power computed from the VBSP method based on the simple-curved plate radiation resistance matrix was 141.3 dB, for a total absolute difference of 0.4 dB. The results from each method do not agree perfectly with respect to a number of specific frequencies but the overall sound power levels do indicate that the approximation of using the simple-curved plate formulation of the radiation resistance matrix is accurate enough to produce useful sound power results in practice.

The sound power results of the M-curved panel model are presented in Fig. 13 and also show good agreement. The total sound power result computed by the BEM was 141.8 dB and the total sound power result computed by the

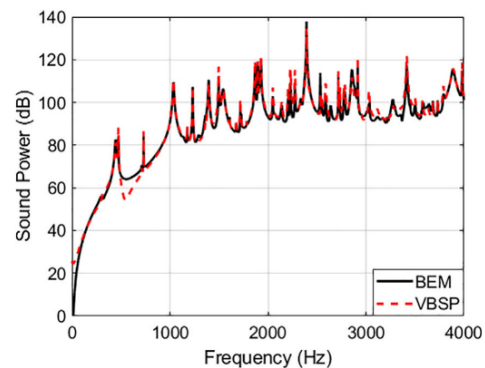


FIG. 13. (Color online) Numerically derived sound power of the M-curved panel using the VBSP and BEM methods.

VBSP method was 141.1 dB, for a total absolute difference of 0.7 dB. As noted above, these results do not show perfect agreement at every discrete frequency but the total results do indicate the likelihood that the use of the simple-curved plate radiation resistance matrix for the VBSP method for arbitrarily curved panels is accurate enough to produce useful sound power results in practice.

## V. CONCLUSIONS

The VBSP method is a useful tool for measuring sound power from acoustically radiating surfaces. Critical to the VBSP method is the use of the acoustic radiation resistance matrix. Previous work has established the form of the radiation resistance matrix for flat plates, cylindrical- and spherical-shells, and simple-curved plates. There is no established form of the radiation resistance matrix for arbitrarily curved panels, such as the panels experimentally tested and presented in this paper.

The sound power sensitivity of the VBSP method to different forms of the radiation resistance matrix was explored to assess whether established, computationally efficient forms could be used to approximate sound power results for arbitrarily curved panels. For numerical model-based test cases where the radius of curvature is greater than 20 cm and the frequency is above 500 Hz, there is less than 1 dB difference in the sound power results computed using the flat plate, simple-curved plate, and cylindrical-shell radiation resistance matrices.

Experimental results showing excellent agreement between the VBSP and ISO 3741 methods were also presented. For the VBSP method, surface velocity measurements were obtained using a SLDV. Surface shape geometry data were also obtained using the SLDV and were used to calculate the normal velocity components. The experimental results showed good agreement over the 400 Hz to 10 kHz one-third octave band spectrum for both arbitrarily curved panels measured. The mean sound power difference in third-octave bands was 0.4 dB with a standard deviation of 1.3 dB for the S-curved panel, and 0.3 dB with a standard deviation of 1.2 dB for the M-curved panel. Below 400 Hz, the lack of good agreement was due to background noise in the reverberation chamber and that the arbitrarily curved panels radiated relatively little noise in this low frequency range. The VBSP method was less sensitive to background noise than the ISO 3741 method, and in this case, may likely be more accurate in the low frequency range.

To further investigate the use of the simple-curved plate radiation resistance matrix to compute the sound power for arbitrarily curved panels, numerical BEM and VBSP results were compared. The BEM is capable of providing computationally correct radiation resistance matrices for arbitrarily curved panels and computing the correct sound power. Surface velocity results from the BEM models were used to compute sound power using the VBSP method with the simple-curved plate radiation resistance matrix. The results

showed that the total sound power difference between the BEM and VBSP methods was less than 1 dB. These results indicate that useful sound power results may be obtained from arbitrarily curved panels using a form of the radiation resistance matrix that is not specific to the arbitrarily curved surface.

The results presented in this paper have shown validation for extending the VBSP method to accurately measure sound power from arbitrarily curved panels and continue to establish the potential usefulness of the method. Furthermore, the results indicate that an approximate and or general form of the radiation resistance matrix could be used for many different cases and basic shapes of acoustically radiating surfaces. In considering more complex systems, such as ribbed plates, the sound power would still be given by Eq. (1) since the radiation resistance matrix is primarily dependent on the geometry of the radiating surface and the physical properties of the fluid surrounding the surface. This indicates that the VBSP method is applicable for more complex systems. With the form of the radiation resistance matrix being available for several ideal geometries, a user can choose the radiation resistance matrix form that most closely approximates the general geometry being considered. The capability of utilizing a single form of the radiation resistance matrix for many cases would greatly simplify the VBSP method in further applications and extension to more complex acoustically radiating surfaces of interest, perhaps ultimately leading to establishing a standardized VBSP method.

## ACKNOWLEDGMENTS

The authors gratefully acknowledge funding for this work provided by the National Science Foundation, Grant No. 1916696. We also gratefully acknowledge the work of Professor Eric McKell of the BYU Manufacturing Engineering department for providing precision calibration marks on each arbitrarily curved panel and the fabrication work performed by the BYU Physics Machine Shop to produce the arbitrarily curved panels.

<sup>1</sup>ISO 12001:1996, *Acoustics—Noise Emitted by Machinery and Equipment—Rules for the Drafting and Presentation of a Noise Test Code* (International Organization for Standardization, Geneva, Switzerland, 1996).

<sup>2</sup>G. V. Borgiotti, "The power radiated by a vibrating body in an acoustic fluid and its determination from boundary measurements," *J. Acoust. Soc. Am.* **88**, 1884–1893 (1990).

<sup>3</sup>D. M. Photiadis, "The relationship of singular value decomposition to wave-vector filtering in sound radiation problems," *J. Acoust. Soc. Am.* **88**, 1152–1159 (1990).

<sup>4</sup>A. Sarkissian, "Acoustic radiation from finite structures," *J. Acoust. Soc. Am.* **90**, 574–578 (1991).

<sup>5</sup>S. J. Elliot and M. E. Johnson, "Radiation modes and the active control of sound power," *J. Acoust. Soc. Am.* **94**(4), 2194–2204 (1993).

<sup>6</sup>K. A. Cunefare and M. N. Currey, "On the exterior acoustic radiation modes of structures," *J. Acoust. Soc. Am.* **96**, 2302–2312 (1994).

<sup>7</sup>K. A. Cunefare and M. N. Currey, "The radiation efficiency grouping of free-space acoustic radiation modes," *J. Acoust. Soc. Am.* **109**, 203–215 (2001).

- <sup>8</sup>F. Fahy and P. Gardonio, "Sound radiation by vibrating structures," in *Sound and Structural Vibration: Radiation, Transmission and Response*, 2nd ed. (Academic Press, Oxford, UK, 2007).
- <sup>9</sup>J. B. Fahline and G. H. Koopmann, "A lumped parameter model for the acoustic power output from a vibrating structure," *J. Acoust. Soc. Am.* **100**, 3539–3547 (1996).
- <sup>10</sup>J. B. Fahline and G. H. Koopmann, "Numerical implementation of the lumped parameter model for the acoustic power output of a vibrating structure," *J. Acoust. Soc. Am.* **102**, 179–192 (1997).
- <sup>11</sup>D. Fritze, S. Marburg, and H. J. Hardtke, "Estimation of radiated sound power: A case study on common approximation methods," *Acta Acust. united Ac.* **95**(5), 833–842 (2009).
- <sup>12</sup>C. B. Jones, C. B. Goates, J. D. Blotter, and S. D. Sommerfeldt, "Experimental validation of determining sound power using acoustic radiation modes and a laser vibrometer," *Appl. Acoust.* **164**, 107254 (2020).
- <sup>13</sup>C. B. Goates, C. B. Jones, S. D. Sommerfeldt, and J. D. Blotter, "Sound power of vibrating cylinders using the radiation resistance matrix and a laser vibrometer," *J. Acoust. Soc. Am.* **148**(6), 3553–3561 (2020).
- <sup>14</sup>C. B. Goates, "Analytical expressions for acoustic radiation modes of simple curved structures," Master's thesis, BYU, Provo, UT (2019).
- <sup>15</sup>ISO 3741:2010. "Acoustics – Determination of sound power levels and sound energy levels of noise sources using sound pressure – Precision methods for reverberation test rooms," (International Organization for Standardization, Geneva, 2010).
- <sup>16</sup>D. A. McNamara, J. A. G. Malherbe, and C. W. Pistorius, *Introduction to the Uniform Geometrical Theory of Diffraction* (Artech House, Norwood, MA, 1990).

## Chapter 5 Expansion for Thin Unbaffled Flat Plates

This chapter presents the foundation of a journal article intended for publication in *The Journal of the Acoustical Society of America*. The work detailed here includes a literature review, the development of the distance matrix and radiation resistance matrix for thin unbaffled flat plates, and initial contributions from COMSOL Multiphysics™ modeling.

The key finding of this research is the demonstration that a plate's sound power can be effectively modeled using the sound power equation for two out-of-phase point sources. This model accounts for the interaction between the front and back sides of the plate, capturing the dipole nature of the plate when acoustic wavelengths exceed the plate dimensions and its monopole behavior when wavelengths are much smaller.

This contribution is particularly significant for the VBSP method, because it extends its applicability to unbaffled radiating structures. This advancement paves the way for broader and more accurate sound power estimations for many unbaffled radiating structures of interest.

## 5.1 Introduction

Sound radiation from un baffled flat plates poses significant challenges in acoustics due to their intricate boundary conditions and complex radiation characteristics. Accurately predicting the acoustic response is complicated because, unlike baffled plates—where the velocity distribution is well-defined and assumed to be zero at the baffle, allowing for calculations using the Rayleigh integral [1]—un baffled plates require solving a Robin boundary condition. In this case, the velocity is only known at the surface of the plate, while the pressure is zero in the same plane outside the plate. Both the velocity and pressure are essential for accurately solving the problem.

The reliance on a Robin boundary condition adds to the complexity of the acoustic analysis. This complexity has led to the creation of various analytical, semi-analytical, and numerical methods, each with its own strengths and limitations. These methods are crucial because un baffled plates are widely used in fields like aerospace engineering to architectural acoustics, where accurate acoustic modeling is essential for improving designs and effective noise control.

Various strategies have been employed by researchers to address the complexities of sound radiation from un baffled plates. For example, Atalla *et al.* [2] utilized the Kirchhoff-Helmholtz Integral Equation (KHIE) [3] to model sound radiation of un baffled plates, simplifying their analysis by disregarding the pressure jump across the plate's boundary. While this model facilitated the analytical derivation of boundary conditions, it also resulted in numerical inaccuracies, particularly at high frequencies due to convergence problems linked to the singular behavior of Green's functions.

A more comprehensive KHIE model was developed by Laulagnet [4], incorporating the pressure jump and plate displacement by using a series of plate modes. This model analyzed the

radiation resistance by numerically calculating a matrix of cross-modal coupling coefficients to capture the acoustic behavior of the plates. Although the method showed strong agreement with theoretical predictions tested in air and water, its application to complex boundary conditions and fluid interactions demands significant computational resources.

In another study, Williams [5], [6] applied an FFT-based iterative method to numerically evaluate the acoustic pressure and velocity for un baffled thin plates vibrating in air. While effective in certain scenarios, this method also faces convergence issues at lower frequencies due to singularities occurring when sample points align with the radiation circle  $k_x^2 + k_y^2 = k^2$ .

Fahy and Thompson [1], [7], introduced a wavenumber domain technique that uses matrix inversion to evaluate acoustic pressure in perforated plates, which can also be adapted for un baffled configurations. Their method relates acoustic pressure to acoustic impedance, addressing mixed boundary conditions beyond the plate surface and facilitating acoustic power calculations. However, challenges such as singularities in the matrix inversion can impact result accuracy. This understanding informs my work on developing a more efficient radiation resistance (**R**) matrix for thin un baffled flat plates to mitigate these issues.

In addition to the analytical and semi-analytical approaches, empirical methods have also been applied. For example, Oppenheimer and Dubowsky [8] explored simpler empirical corrections for baffled plates to approximate un baffled behavior. These empirical models are tailor made for specific cases and, therefore, lack generality.

In addition to the analytical and semi-analytical approaches mentioned earlier, numerical techniques, like the Boundary Element Method (BEM) and Finite Element Method (FEM), have also been extensively used. These methods are beneficial in analyzing the dynamic characteristics and acoustic response of un baffled plates in diffuse fields, especially for plates with arbitrary

shapes and boundary conditions. Some examples of how these techniques have been applied illustrate the effectiveness and limitations of this approach.

FEM/BEM can be applied for vibrating structures radiating in different fluids. Nelisse *et al.* [9], [10] examined un baffled vibrating plates in air, water, and diffuse sound fields, showing how fluid-structure interactions can alter radiation impedance of these plates using a Rayleigh-Ritz approach with the BEM. A combined FEM-BEM model was employed by Nolte and Gaul [11] to analyze sound radiation in underwater environments. However, both models often require considerable computational resources and can be impractical for large structures or high-frequency scenarios.

FEM/BEM models are also often used in aerospace engineering applications. García-Fogeda *et al.* developed a fluid-structure interaction model for predicting the dynamic response of un baffled plates subjected to high acoustic loads [12]. By combining FEM and BEM, the approach effectively handles arbitrary plate shapes and complex boundary conditions and has been validated against experimental data, demonstrating its accuracy. However, the method is computationally intensive, especially for near-field radiation modeling, and requires careful consideration of mutual impedance effects to ensure reliable predictions.

A different approach is to model the surface using simple radiators. Fahnlne and Koopman [13] used a lumped parameter model for various un baffled geometries, representing the elements using multipoles. While this method has shown promise, it can become cumbersome for more complex geometries or high-frequency ranges. Hashimoto [14] used a discrete calculation method (DCM) that simplifies radiation impedance analysis by breaking down the radiating surface into smaller piston-like elements but is only applicable for baffled structures.

Considering these different approaches and recognizing the need for an efficient and accurate way to understand the acoustic radiation from un baffled plates, this chapter introduces a new approach focused on developing a simpler  $\mathbf{R}$  matrix for thin un baffled flat plates. By utilizing the method of elementary radiators and incorporating symmetry principles (refer to Unit 3), this research aims to balance computational efficiency and accuracy, with the potential to perform measurements of un baffled flat plates *in situ*. The proposed solution not only reduces computational costs but also extends the capabilities of the Vibration-Based Sound Power (VBSP) method, making it applicable to both baffled and un baffled configurations. This advancement provides a precise and practical tool for sound power estimation that can be effectively used in real-world situations where traditional methods are insufficient.

## 5.2 The Un baffled Distance Matrix

This section focuses on how the distances,  $d_{ij}$ , between any two elements on the front and back of the flat plate are computed for the un baffled distance matrix,  $\mathbf{d}$ , to aid the construction of the  $\mathbf{R}$  matrix. First, the two-sided flat plate was conceptually “un folded,” as illustrated in Fig. 5.1. This approach simplifies the calculation of the shortest distance between a source element on the front side of the plate and a receiver element on the back side, considering the paths around all four edges of the plate (see Fig. 5.2). In this calculation, the shortest path, which is the most influential for the mutual interaction between any two elements, was identified. For each pair of elements, the shortest path  $d_{ij}$  is included in the un baffled distance matrix.



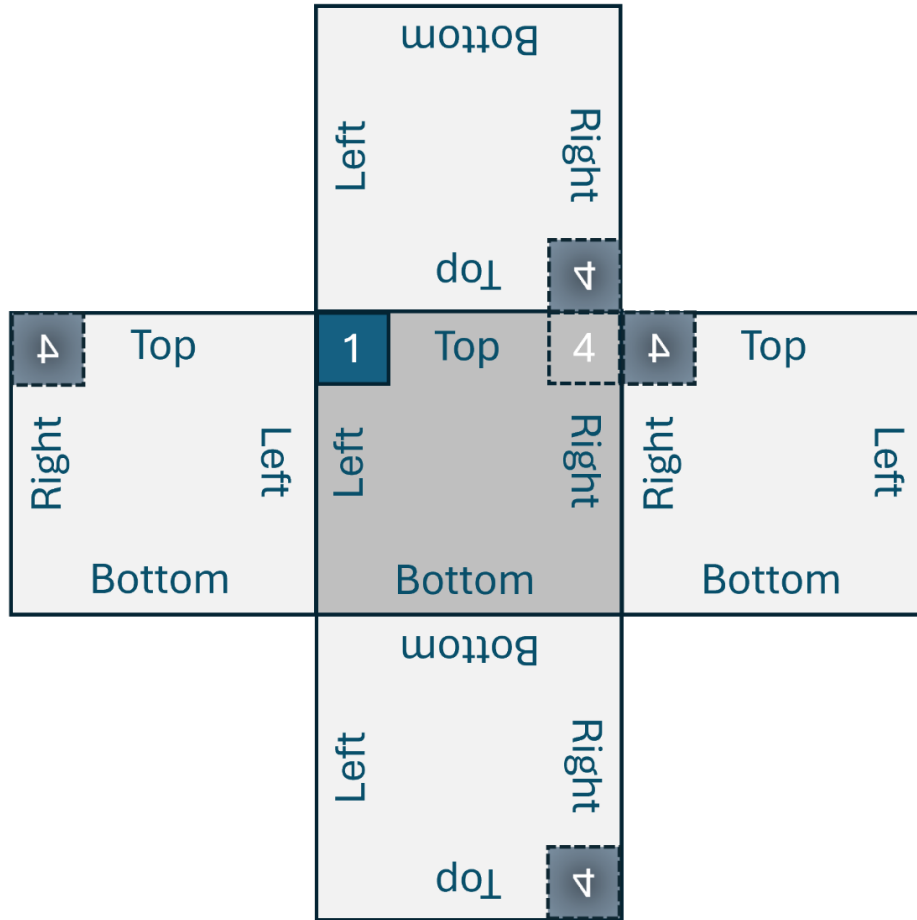


**Figure 5.1:** The front of the unbaffled flat plate (dark gray) and the back (light gray) are shown in an “unfolded” view. Elements “1” on the front and “4” on the back are used for illustration. The shaded element “4” represents the element is now on the same side of the plate as element “1.”

Initially, the methodology assumed a single shortest path when in some cases, multiple paths could be equivalently the shortest. This early approach focused on scenarios where the computation considered only one path out of several potential shortest paths. This could potentially introduce errors in the  $\mathbf{R}$  matrix calculations, as certain paths, though equally short, might influence the acoustic interactions differently. The implications of this scenario will be further explored and addressed in Sec 5.5.

The elements on the plate are organized such that the upper left corner on the front side of the plate is designated as the first element, and the lower right element on the back as the last element. To provide insight into what the  $\mathbf{d}$  matrix looks like, an example is provided in Fig. 5.3. The variation in  $d_{ij}$  can be understood by returning to Fig. 5.3, where it is evident that the first element on the front of the plate and the last element on the back of the plate have the largest separation distance.

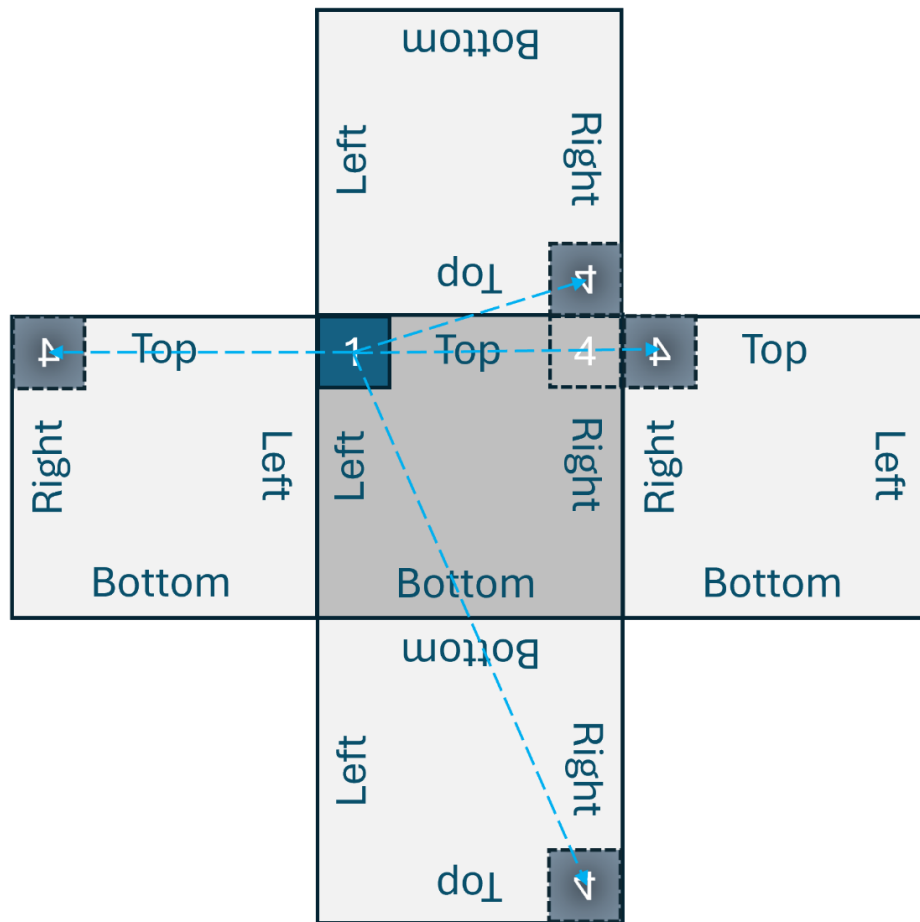


**Figure 5.2:** The distances between the front element “1” and the back element “4” are indicated by blue arrows connecting the element centers. The shortest path is selected for the corresponding  $d_{ij}$  entry.

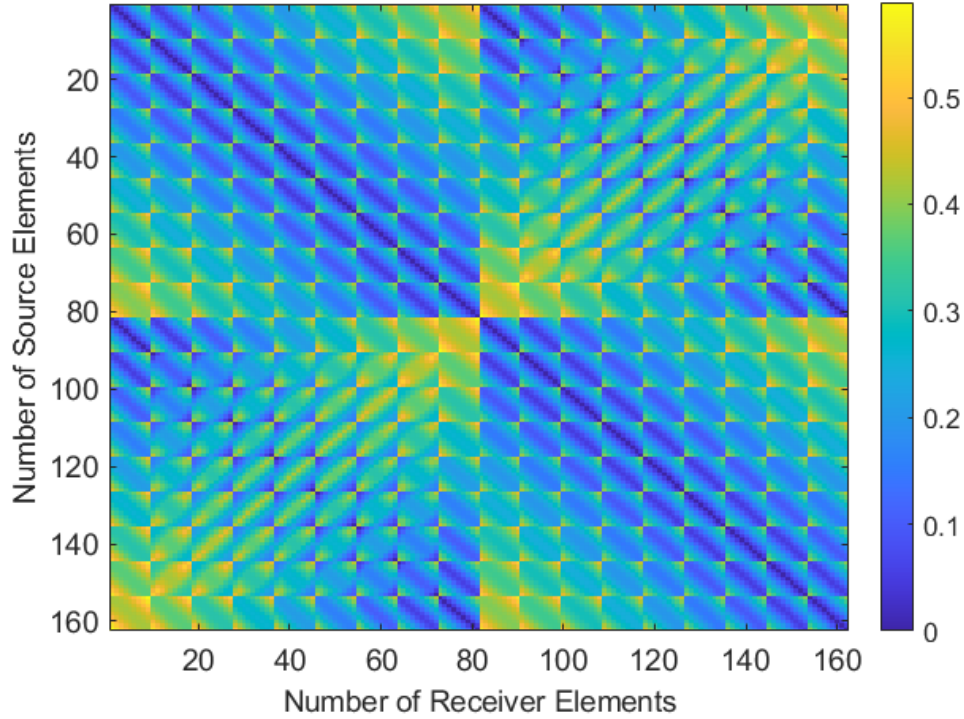


**Figure 5.3:** An example distance matrix,  $\mathbf{d}$ , for a thin un baffled flat plate with a 9 x 9 element grid on the front and back of a thin un baffled flat plate. This includes all combinations of elements on the front with itself, front and back, back and front, and back with itself.

### 5.3 Un baffled Flat Plate $\mathbf{R}$ Matrix

An un baffled thin flat plate involves a two-sided radiation problem, resulting in a more complex  $\mathbf{R}$  matrix compared to the simpler forms used for baffled structures in Chs. 3 and 4. This section examines the specific structure of the  $\mathbf{R}$  matrix for thin un baffled plates, which must account for interactions between the front and back surfaces. The front-to-front and back-to-back interactions are captured by the matrices  $\mathbf{R}_{\mathbf{FF}}$  and  $\mathbf{R}_{\mathbf{BB}}$ , respectively, which use the half-space Green's function and take the form of Eqn. 1.1 for the baffled flat plate. Additionally, the  $\mathbf{R}$  matrix incorporates cross-interactions between the front and back surfaces around the plate edges, represented by the  $\mathbf{R}_{\mathbf{FB}}$  and  $\mathbf{R}_{\mathbf{BF}}$  matrices.

These four  $\mathbf{R}$  matrices compose the total radiation resistance matrix for a thin un baffled flat plate, represented as:

$$\mathbf{R}_{\text{unbaffled}}(\omega) = \begin{bmatrix} \mathbf{R}_{\text{FF}}(\omega) & \mathbf{R}_{\text{FB}}(\omega) \\ \mathbf{R}_{\text{BF}}(\omega) & \mathbf{R}_{\text{BB}}(\omega) \end{bmatrix}. \quad (5.1)$$

An example of  $\mathbf{R}_{\text{unbaffled}}$  for a thin un baffled flat plate is shown in Fig. 5.4

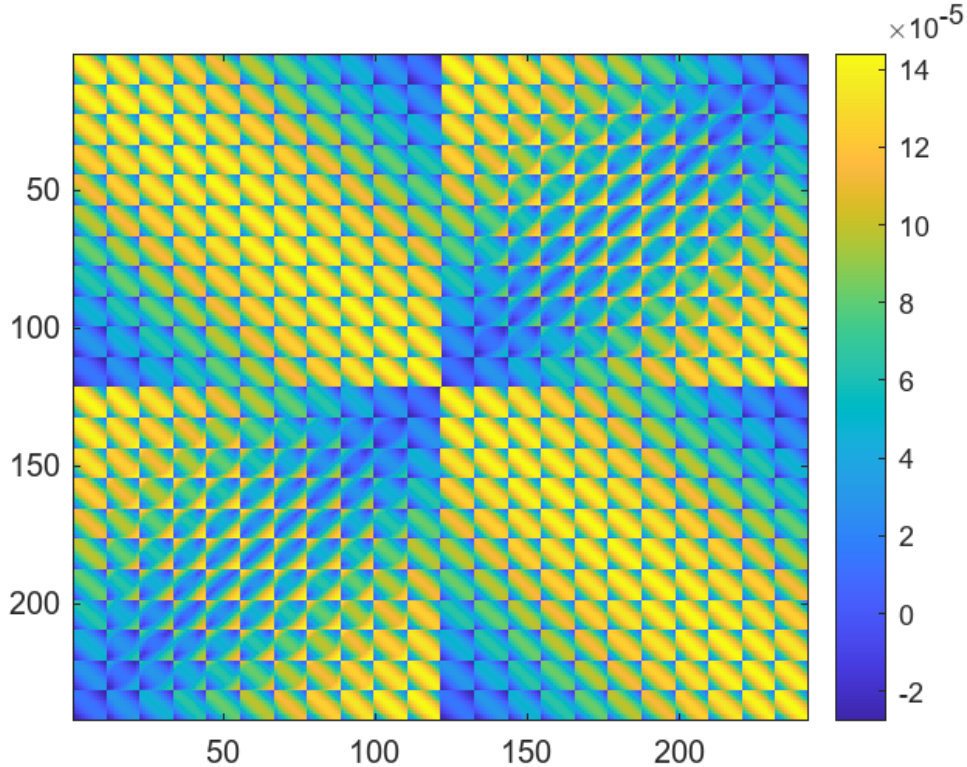


**Figure 5.4:** A 242 x 242  $\mathbf{R}_{\text{unbaffled}}$  matrix displaying the four 121 x 121  $\mathbf{R}$  matrices from Eqn. 5.1 for an 11 x 11 scan grid of an un baffled flat plate. The submatrices are normalized to illustrate the double-layered Toeplitz and centrosymmetric symmetries better. The computation of sound power using Eqn. 5.1 employs this form of the  $\mathbf{R}$  matrix.

The only unknowns in Eqn. 5.1 are the  $\mathbf{R}_{\text{FB}}$  and  $\mathbf{R}_{\text{BF}}$  matrices. These matrices are based on the discretization of the vibrating structure (refer to Sec. 1.3). Because the elements are designed to be smaller than an acoustic wavelength, each element radiates as an acoustic monopole source.

The complex sound pressure exerted by one monopole source on another source a distance  $d$  away is:

$$\hat{p}(d) = \pm \frac{j\rho_0ck\hat{Q}}{4\pi d} e^{-jkd}, \quad (5.2)$$

where the  $\pm$  signs correspond to in-phase or out-of-phase sources, respectively  $c$  is the speed of sound in the surrounding fluid,  $d_{ij}$  is the distance between the two sources,  $k$  is the acoustic wavenumber,  $\rho_0$  is the fluid density surrounding the vibrating surface, and  $\hat{Q}$  is the complex strength of the monopole source [1]. Each monopole source radiates power independently, given by:

$$\Pi_{\text{monopole}} = \frac{1}{2} \text{Re}\{\hat{Q} \cdot \hat{p}^*\} = \frac{\omega^2 \rho_0 |\hat{Q}|^2}{8\pi c}, \quad (5.3)$$

where  $\hat{p}^*$  denotes the complex conjugate of the pressure.

In addition to monopole power, mutual coupling between monopoles must be accounted for. Fahy expresses the sound power generated by mutual coupling each source as

$$\Pi_{ij} = \frac{1}{2} \text{Re}\{\hat{Q}_i \cdot \hat{p}_j^*\} = \pm \frac{1}{2} \frac{\omega^2 \rho_0 |\hat{Q}|^2}{4\pi c} \text{sinc}(kd_{ij}) = \pm \Pi_{\text{monopole}} * \text{sinc}(kd_{ij}). \quad (5.4)$$

Thus, the total radiated power from each source is:

$$\Pi_{\text{tot},i} = \Pi_{\text{monopole}} \pm \sum_{j \neq i} \Pi_{\text{monopole}} * \text{sinc}(kd_{ij}) = \Pi_{\text{monopole}} * \left[ 1 \pm \sum_{j \neq i} \text{sinc}(kd_{ij}) \right]. \quad (5.5)$$

The self-power of a volume source (Eqn. 5.3) increases with the square of the frequency. However, the mutual coupling between two sources (Eqn. 5.4) introduces a  $\text{sinc}(kd_{ij})$  term. The pressure from a non-coincident source is linearly dependent on frequency. The variation with distance arises from the effect of hemispherical spreading of the pressure exerted by one source on another. As  $kd_{ij}$  increases, source  $i$  radiates independently of source  $j$ .

On the other hand, the  $kd_{ij} \ll 1$  condition indicates a large amount of coupling in two ways. First, when regions of a vibrating surface are close together, Eqn. 5.5 shows how the sound power can decrease due to out-of-phase coupling; their mutual acoustic interaction significantly reduces the amount of sound power each region can generate. Second, at low frequencies, where the wavelength exceeds the dimensions of the plate, the two sides of the plate vibrate out-of-phase, causing the plate to act like an un baffled piston with dipole characteristics.

These  $kd_{ij}$  regimes provide insights to how the front-back interactions should be included in the  $\mathbf{R}$  matrix. Because the sound power is  $\Pi = \mathbf{v}_e^H \mathbf{R} \mathbf{v}_e$ , the factor  $1 - \text{sinc}(kd_{ij})$  needs to be included in the  $\mathbf{R}_{\text{FB}}$  and  $\mathbf{R}_{\text{BF}}$  matrices reflecting the impact of spatial and frequency-dependent interactions between the out-of-phase monopole sources. Therefore,

$$\mathbf{R}_{\text{FB}} = \mathbf{R}_{\text{BF}} = \frac{\omega^2 \rho_0 A_e^2}{4\pi c} \frac{1}{2} [1 - \text{sinc}(kd_{ij})], \quad (5.6)$$

where  $d_{ij}$  represents the distance between an element on one side of the plate to the opposite side of the plate around the surface without going through the plate. This looks similar to Eqn. 1.1 for the baffled plate. However, the factor of 1/2 is necessary because the free-space Green's function must be used when the monopole sources are not baffled.

Combining all four resistance matrices from Eqns. 1.1 and 5.6, the  $\mathbf{R}_{\text{unbaffled}}$  matrix in Eqn. 5.1 becomes

$$\mathbf{R}_{\text{unbaffled}}(\omega) = \frac{\omega^2 \rho_0 A_e^2}{4\pi c} \begin{bmatrix} \text{sinc}(kd_{ij}) & \frac{1}{2} [1 - \text{sinc}(kd_{ij})] \\ \frac{1}{2} [1 - \text{sinc}(kd_{ij})] & \text{sinc}(kd_{ij}) \end{bmatrix}. \quad (5.7)$$

The sound power expression from Eqn. 1.2 for an unbaffled plate is

$$\Pi(\omega) = \begin{bmatrix} \mathbf{v}_{\text{e,FF}}(\omega) \\ \mathbf{v}_{\text{e,BB}}(\omega) \end{bmatrix}^H \begin{bmatrix} \mathbf{R}_{\text{FF}}(\omega) & \mathbf{R}_{\text{FB}}(\omega) \\ \mathbf{R}_{\text{BF}}(\omega) & \mathbf{R}_{\text{BB}}(\omega) \end{bmatrix} \begin{bmatrix} \mathbf{v}_{\text{e,FF}}(\omega) \\ \mathbf{v}_{\text{e,BB}}(\omega) \end{bmatrix}. \quad (5.8)$$

The velocity vectors,  $\mathbf{v}_{e,FF}$  and  $\mathbf{v}_{e,BB}$ , represent the velocities of the front and back sides of the plate, respectively. The  $\mathbf{v}_{e,FF}$  are obtained using the SLDV (as described in Sec. 1.3). The  $\mathbf{v}_{e,BB}$  are derived by inverting  $\mathbf{v}_{e,FF}$  by  $180^\circ$ , effectively changing the phase. Using Eqn. 5.7, the sound power expression for the thin unbaffled flat plate becomes

$$\Pi(\omega) = \frac{\omega^2 \rho_0 A_e^2}{4\pi c} \begin{bmatrix} \mathbf{v}_{e,FF}(\omega) \\ \mathbf{v}_{e,BB}(\omega) \end{bmatrix}^H \begin{bmatrix} \text{sinc}(kd_{ij}) & \frac{1}{2}[1 - \text{sinc}(kd_{ij})] \\ \frac{1}{2}[1 - \text{sinc}(kd_{ij})] & \text{sinc}(kd_{ij}) \end{bmatrix} \begin{bmatrix} \mathbf{v}_{e,FF}(\omega) \\ \mathbf{v}_{e,BB}(\omega) \end{bmatrix}. \quad (5.9)$$

## 5.4 Experimental Setup

Two thin flat plates, each measuring 16 3/8" (0.416 m) square, were used for this test: an aluminum plate with a thickness of 0.0215" (0.000546 m) and a steel plate with a thickness of 0.0475" (0.00121 meters). A piezoelectric transducer affixed near a corner of a plate generated a broadband pseudorandom signal up to 12.8 kHz with a 2 Hz frequency resolution excited the plates. To approximate free boundary conditions, the plates were suspended 40" above the ground using speaker stands, each corner of a plate supported by 3/4" surgical tubing to maintain these conditions.

The microphone-based ISO 3741 standard was used in the reverberation chamber to measure sound power first. Due to the additional material in the chamber such as tables, speaker stands, and carts, the reverberation ( $T_{60}$ ) time was measured to account for the absorption in the chamber so the ISO standard could be applied correctly.

The experimental configuration used is shown in the following figures. Figure 5.5 shows the positioning of the SLDV above the plate to scan the vibrational response. Figure 5.6 displays the density of the scan grid used for the SLDV measurement, designed to improve the accuracy of the

VBSP method at higher frequencies. Figures 5.7 and 5.8 illustrate several operational deflection shapes of the plate under free-free-free-free boundary conditions, demonstrating that the plate was scanned properly, and that the experimental data should be accurate enough for the VBSP method.



**Figure 5.5:** Flat plate setup for an SLDV scan in a reverberation chamber.





**Figure 5.6:** SLDV scan of the thin flat plate illustrating a 63x63 grid (~6.6 mm spacing).

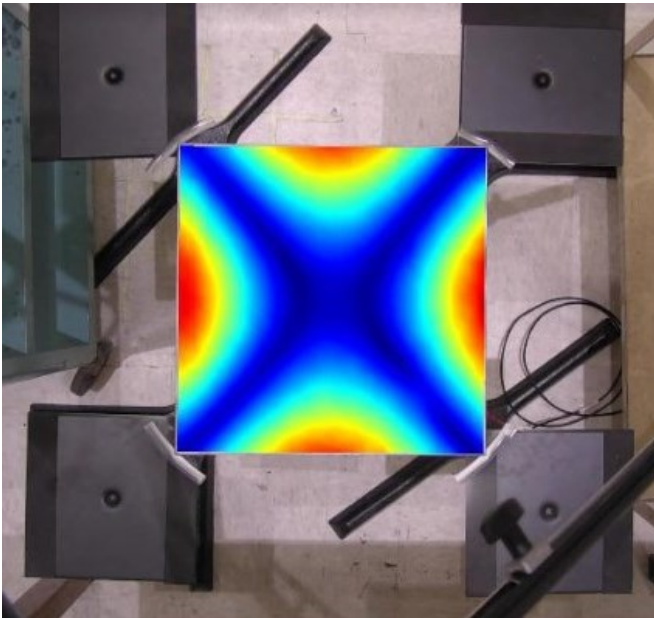


**Figure 5.7:** Fundamental mode of the thin flat plate with free boundary conditions from the SLDV.

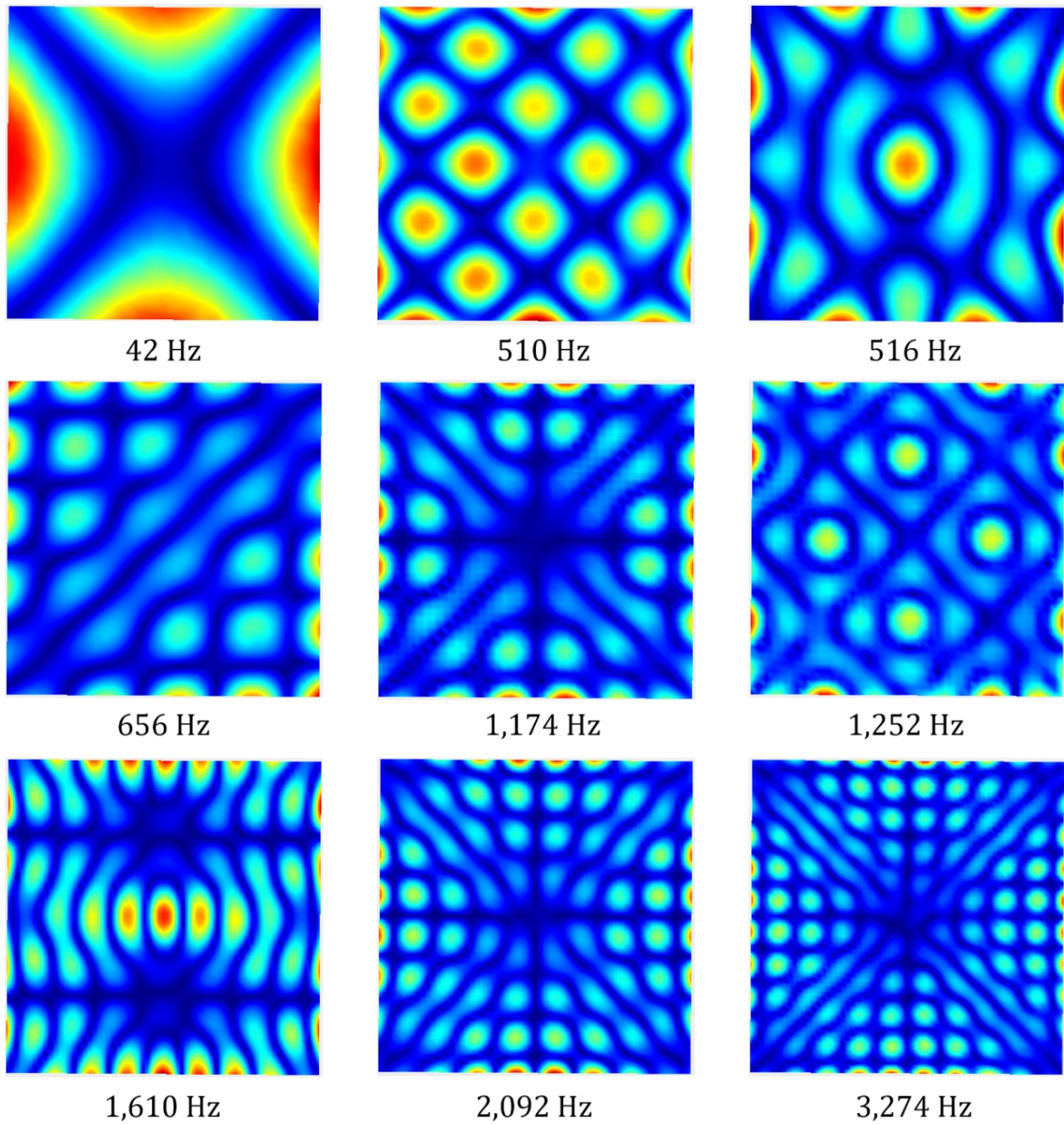


**Figure 5.8:** Nine of the structural modes of the un baffled flat plate with free boundary conditions obtained from the SLDV scan.

## 5.5 VBSP Results

The accuracy of the  $\mathbf{R}_{\text{unbaffled}}$  and  $\mathbf{d}$  matrices in estimating the sound power from unbaffled plates is demonstrated experimentally. A comparison is done using an unbaffled aluminum plate. The VBSP results are compared with ISO 3741 measurements for two cases: with the SLDV on and off. This comparison demonstrates that the additional background noise from the SLDV fan does not bias the VBSP results for this unbaffled plate, whereas the ISO 3741 results are dramatically impacted by the presence of the fan below 800 Hz (see Fig. 5.9). The VBSP method accurately estimates the sound power levels of the aluminum plate for the 315 Hz and 630 Hz one-third octave (OTO) bands and from 1 kHz to 10 kHz OTO bands using the current  $\mathbf{R}_{\text{unbaffled}}$  matrix. The 400, 500, and 800 Hz OTO bands need additional work.

A second comparison is made using an unbaffled steel plate with ISO 3741 as shown in Fig. 5.10. The VBSP results (blue) are again compared with ISO 3741 measurements (red). This comparison demonstrates the accuracy of the current  $\mathbf{R}_{\text{unbaffled}}$  matrix and  $\mathbf{d}$  matrix in estimating the sound power from these plates. The VBSP results agree with the ISO 3741 standard within 1 to 2 dB at the 500 Hz OTO band and from 800 Hz to 10 kHz, which is the frequency range over which the ISO 3741 standard applies in the reverberation chamber used.

The current  $\mathbf{R}_{\text{unbaffled}}$  matrix performs well for mid-to-high frequencies based on the experimental VBSP results. However, for low frequencies, adjustments are needed. When the acoustic wavelength is significantly larger than the plate's characteristic dimension, the  $\mathbf{R}_{\text{unbaffled}}$  matrix should be modified as

$$\hat{\mathbf{R}}_{\text{unbaffled}}(\omega) \approx 2 * \frac{\omega^2 \rho_0 A_e^2}{4\pi c} [1 - \text{sinc}(kd_{ij})]. \quad (5.10)$$



This modified matrix, like  $\mathbf{R}_{FF}$  and  $\mathbf{R}_{BB}$ , only considers interactions on a single side of the plate. It was derived in Sec. 5.3 using the dipole relationship  $1 - \text{sinc}(kd_{\text{baffled}})$  for two out-of-phase sources. The factor of 2 accounts for the identical contributions from both the front and back sides of the plate, while  $d_{ij}$  represents the shortest distance between elements on a single side. This adjustment better captures the dipole nature of the plate's radiation behavior at low frequencies. The VBSP results using Eqn. 5.10 (black) show improved accuracy for the aluminum plate in the 250 Hz to 1,630 Hz OTO bands (see Fig. 5.10) and for the steel plate in the 250 Hz to 500 Hz OTO bands (see Fig. 5.11).

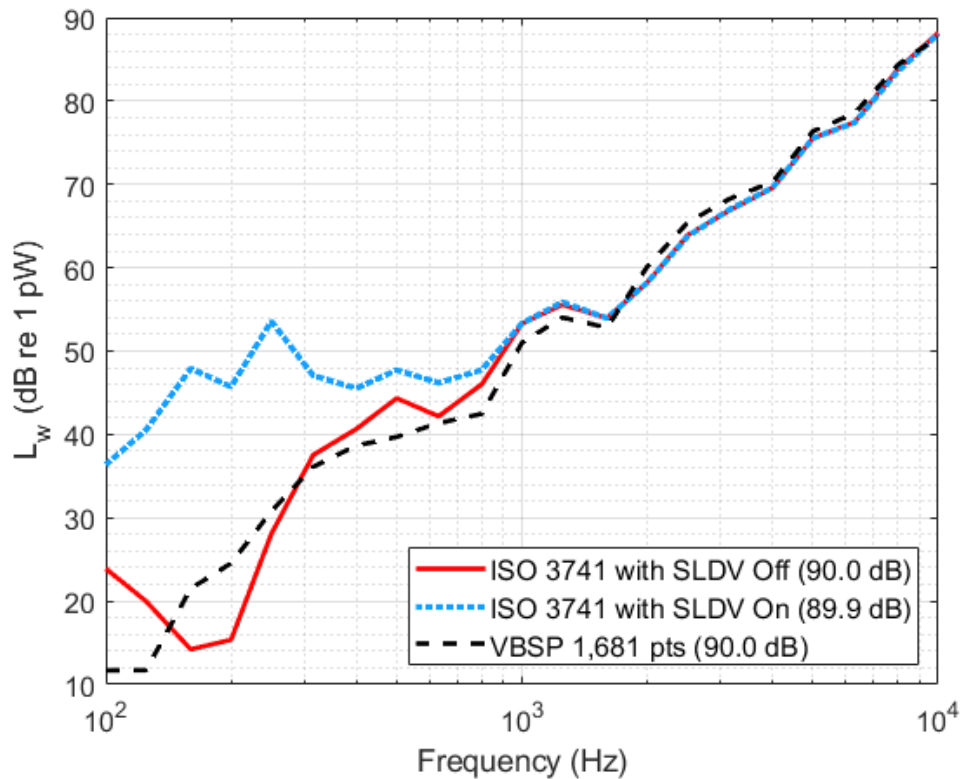


**Figure 5.9:** Sound power levels ( $L_w$ ) of the thin un baffled aluminum plate, showing the ISO 3741 standard results (red) and the VBSP results using  $\mathbf{R}_{\text{unbaffled}}$  (black). An additional ISO 3741 measurement with the SLDV active (blue) indicates that the extra noise did not bias the VBSP results.

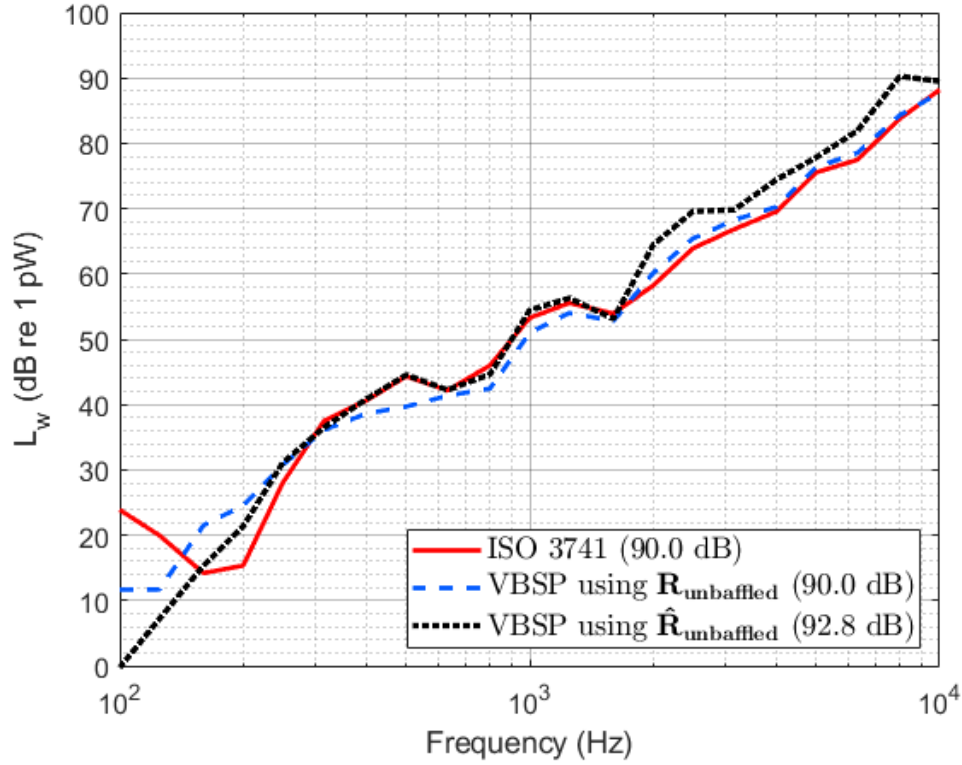


**Figure 5.10:** Sound power levels ( $L_w$ ) of the thin unbaffled aluminum plate, comparing results from the ISO 3741 standard (red), the VBSP method using the  $\mathbf{R}_{\text{umbaffled}}$  matrix (Eqn. 5.7) (blue), and the VBSP method using the  $\hat{\mathbf{R}}_{\text{umbaffled}}$  matrix (Eqn. 5.10) (black). The  $\hat{\mathbf{R}}_{\text{umbaffled}}$  matrix was derived using the dipole relationship  $1 - \text{sinc}(kd_{\text{baffled}})$  for two out-of-phase sources. The overall sound power level differences between the ISO 3741 and the VBSP methods are 0 dB and 2.8 dB, respectively.

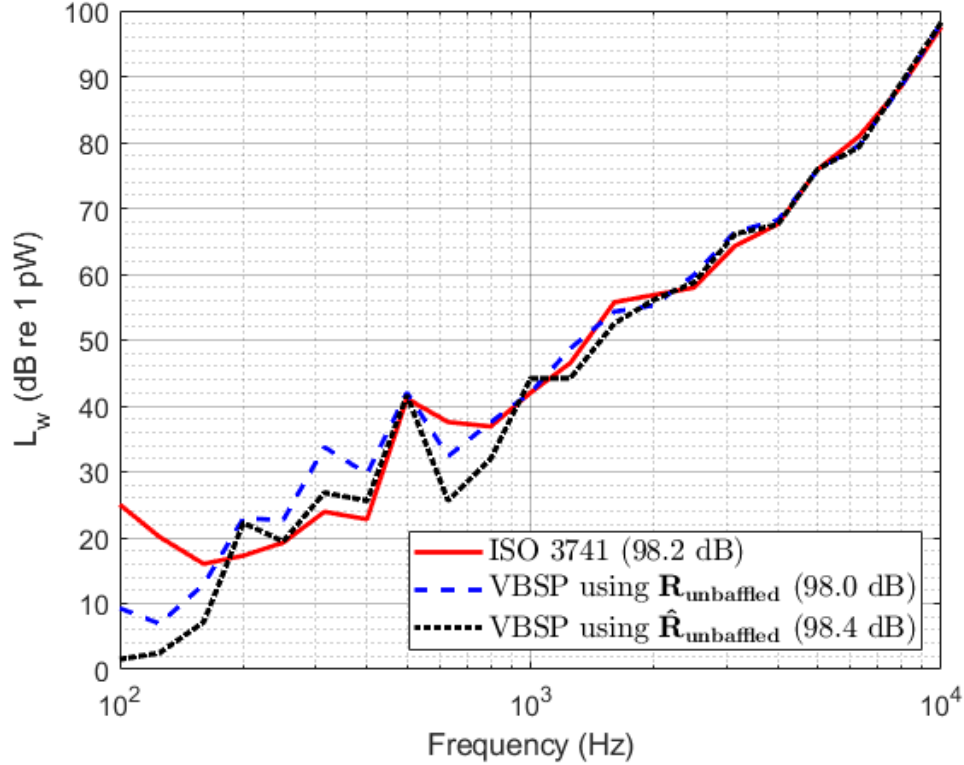


**Figure 5.11:** Sound power levels ( $L_w$ ) of the thin unbaffled steel plate, comparing results from the ISO 3741 standard (red), the VBSP method using the  $\mathbf{R}_{\text{unbaffled}}$  matrix (Eqn. 5.7) (blue), and the VBSP method using the  $\hat{\mathbf{R}}_{\text{unbaffled}}$  matrix (Eqn. 5.10) (black). The  $\hat{\mathbf{R}}_{\text{unbaffled}}$  matrix was derived using the dipole relationship  $1 - \text{sinc}(kd_{\text{baffled}})$  for two out-of-phase sources. The overall sound power level differences between the ISO 3741 and both VBSP methods is 0.2 dB.

## 5.6 Computational Model

This section presents ongoing work to validate the current  $\mathbf{R}_{\text{unbaffled}}$  matrix across three frequency regimes:  $kd \ll 1$  (when the plate behaves like a dipole),  $kd \approx 1$  (the transition region), and  $kd \gg 1$  (where elements radiate more independently, exhibiting a “baffled” effect). Any boundary element method (BEM) software, such as COMSOL®, can be used to model the

unbaffled plate, analyze the diffracted pressure around it, and compute the corresponding  $\mathbf{R}_{\text{unbaffled}}$  matrix.

Preliminary results in Figs. 5.12 and 5.13 demonstrate the initial development of a COMSOL® BEM model, aligned with the same 41x41 element mesh used in the VBSP analysis from Sec. 5.5. Figure 5.12 shows the pressure distribution on the front face of a thin unbaffled steel plate at 1,600 Hz to verify the model's functionality. Due to the small gaps between elements relative to their size and the plate's thin profile, the BEM model is highly sensitive to gap handling.

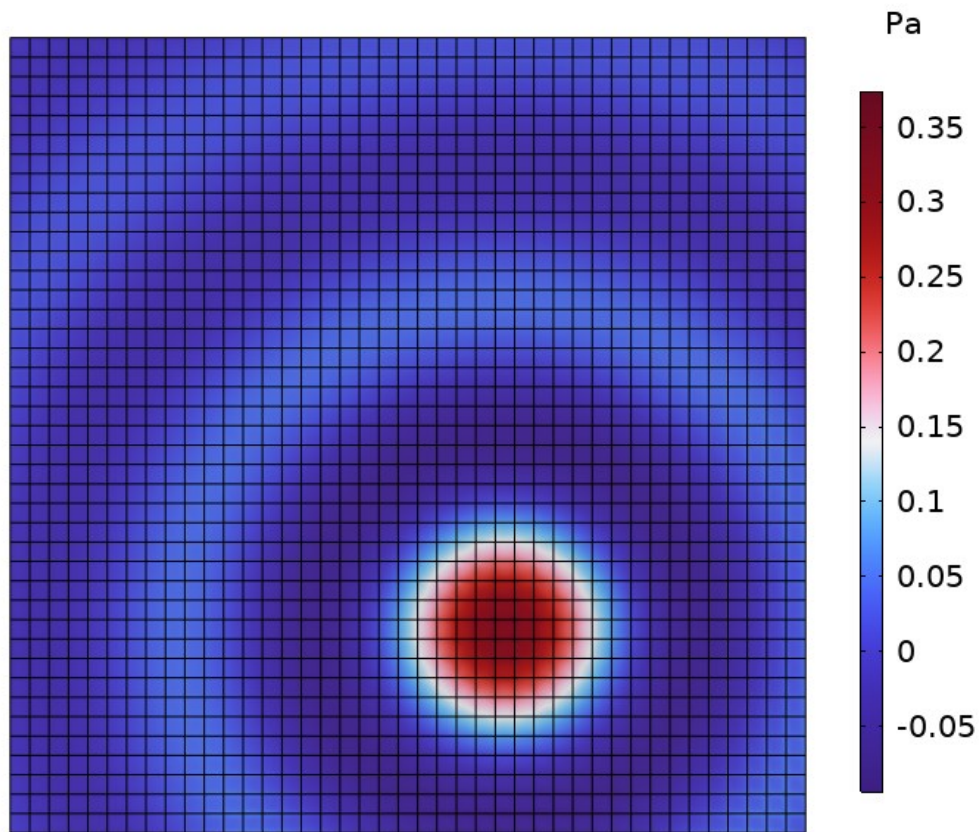


**Figure 5.12:** The thin unbaffled steel flat plate used in this work, created in COMSOL®. The 41x41 element grid shown matches the grid used for the VBSP method. The complex acoustic pressure produced by a single element excited at 2,475 Hz is shown across the front of the plate. 2,475 Hz is about three times the acoustic wavelength of the plate's characteristic dimension.

To mitigate this, COMSOL®’s thin-gap handling feature is used to prevent pressure leakage through the plate, as seen in Fig. 5.13b, where leakage effects are illustrated. Once leakage is resolved, the  $\mathbf{R}$  matrix can be computed by determining the pressure at each element on both faces due to a single element vibrating at a constant unit velocity. This procedure is repeated for each element, and then a frequency sweep is conducted to build the  $\mathbf{R}$  matrices for each frequency.

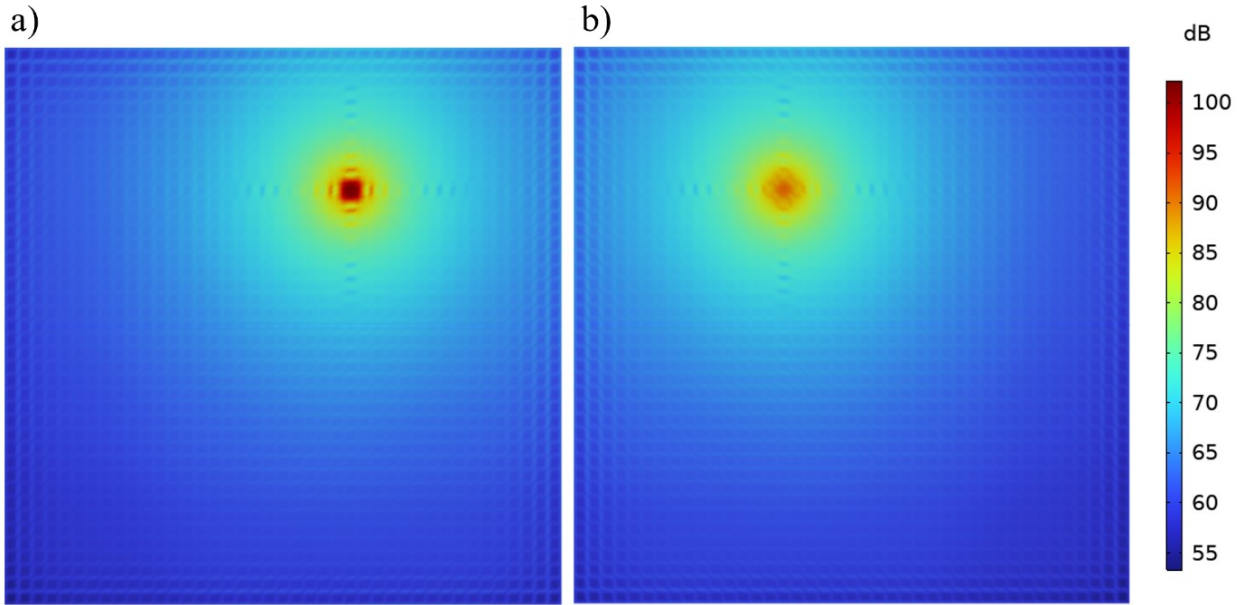


**Figure 5.13:** a) Sound pressure level (SPL) distribution on the front side of a thin unbaﬄed flat plate in COMSOL® when a corner element is excited, with the remaining elements acting as receivers. b) SPL distribution on the back side of the same plate, where a significant drop in pressure compared to the front is expected.

The  $\mathbf{R}$  matrices obtained using the BEM model can then serve as a tool to potentially establish a smoother connection between the  $\mathbf{R}_{\text{unbaﬄed}}$  matrices for thin unbaﬄed flat plates for  $kd \gg 1$  in Eqn. 5.7 and  $kd \ll 1$  in Eqn. 5.10. The insights gained from the BEM model may assist with the goal of developing a single  $\mathbf{R}_{\text{unbaﬄed}}$  matrix that works for all  $kd$ .



## 5.7 Conclusions

An initial  $\mathbf{R}$  matrix is developed to estimate the sound power for thin un baffled flat plates, which relies on a distance matrix that chooses the shortest path on the surface between any two elements. The shortest path is the greatest contributor to the acoustic pressure. The VBSP method is fairly accurate through the mid and high frequencies.

In this frequency regime, the overall sound power levels obtained from the ISO 3741 standard and the VBSP method agreed for both an aluminum and steel plate above 800 Hz. Although there were large differences below 800 Hz, the VBSP method's estimate was unaffected by the presence of the SLDV fan when it was active. Whereas the ISO 3741 result changed below 800 Hz due to the SLDV fan and other background noise.

For low frequencies, the VBSP method yielded better estimates when representing a single side of the plate using the sound power equation for two out-of-phase sources. However, further improvements are required for the low-frequency regime. Conducting tests in an anechoic chamber using the ISO 3745 standard would provide a more precise understanding of low-frequency behaviors and enable the acquisition of free-field results for the VBSP method. Additionally, exploring BEM models could serve as a numerical benchmark, offering insights into linking frequency regimes for a unified  $\mathbf{R}$  matrix applicable to thin un baffled flat plates.

To validate the un baffled  $\mathbf{R}$  matrix more broadly, it is advisable to test additional flat plates varying in thickness, material, and dimensions. Currently, the shortest distance is used for the  $\mathbf{R}$  matrix calculations. Further research should explore scenarios where two or more paths are equally the shortest, as considering only one path might lead to inaccuracies in the sound power estimates as highlighted by Eqn. 5.7.

## 5.8 References

- [1] F. Fahy and P. Gardonio, *Sound and Structural Vibration: Radiation, Transmission and Response*, 2nd ed. (Academic Press, Oxford, UK, 2007), pp. 165-175.
- [2] N. Atalla, J. Nicolas, and C. Gauthier, “Acoustic radiation of an un baffled vibrating plate with general elastic boundary conditions,” *J. Acoust. Soc. Am.* **99**(3), 1484-1494, (1996). doi: 10.1121/1.414727
- [3] A. D. Pierce, *Acoustics: An Introduction to Its Physical Principles and Applications*, (Springer, Cham, Switzerland, 2019).
- [4] B. Laulagnet, “Sound radiation by a simply supported un baffled plate,” *J. Acoust. Soc. Am.* **103**(5), 2451-2462, (1998). doi: 10.1121/1.422765
- [5] E. G. Williams and J. D. Maynard, “Numerical evaluation of the Rayleigh integral for planar radiators using the FFT,” *J. Acoust. Soc. Am.* **72**(6), 2020-2030, (1982). doi: 10.1121/1.388633
- [6] E. G. Williams, “Numerical evaluation of the radiation from un baffled, finite plates, using the FFT,” *J. Acoust. Soc. Am.* **74**(1), 343-347, (1983). doi: 10.1121/1.389683
- [7] F. J. Fahy and D. J. Thompson, “The effect of perforation on the radiation efficiency of vibrating plates,” *Proc. Institute Acoust.* **26**, (2004).
- [8] C. H. Oppenheimer and S. Dubowski, “A radiation efficiency for un baffled plates with experimental validation,” *J. Sound Vib.* **199**(3), 473-489, (1997). doi: 10.1006/jsvi.1996.0609
- [9] H. Nelisse, O. Beslin, and J. Nicolas, “A generalized approach for the acoustic radiation from a baffled and un baffled plate with arbitrary boundary conditions, immersed in a light or heavy fluid,” *J. Sound Vib.* **211**(2), 207-225, (1998). doi: 10.1006/jsvi.1997.1359

- [10] O. Beslin and J. Nicolas, “A hierarchical functions set for predicting very high order plate bending modes with any boundary conditions,” *J. Sound Vib.* **202**(5), 633-655, (1997). doi: 10.1006/jsvi.1996.0797
- [11] B. Nolte and L. Gaul, “Sound energy flow in the acoustic near field of a vibrating plate,” *Mech. Sys. Signal Process.* **10**(3), 351-364, (1996). doi: 10.1006/mssp.1996.0025
- [12] P. García-Fogeda, F. de la Iglesia, K. Salehi, “Acoustic and Dynamic Response of Unbaffled Plates of Arbitrary Shape,” *Appl. Sci.* **11**(17), 8019, (2021). doi: 10.3390/app11178019
- [13] G. H. Koopmann and J. B. Fahline, *Designing quiet structures: A sound power minimization approach* (Academic Press, 1997).
- [14] N. Hashimoto, “Measurement of sound radiation efficiency by the discrete calculation method,” *Appl. Acoust.* **62**(4), 429-446 (2001). doi: 10.1016/S0003-682X(00)00025-6

## Chapter 6 Vibroacoustic Response of Pickleball Paddles

This chapter presents a journal article intended for publication in *The Journal of the Acoustical Society of America* in Fall 2024. It demonstrates the practical application of the vibration-based sound power (VBSP) method by analyzing the vibroacoustic response of pickleball paddles. The chapter details the experimental procedures, including impact testing and vibrometry, and discusses findings in the context of product design and noise control. This work is particularly relevant to the dissertation's objective of developing a robust VBSP method, as it extends the unbaffled plate work from Ch. 5 to a real-world application. By applying the VBSP method to pickleball paddles, this chapter aims to verify the sound power estimation for more complex, unbaffled structures. Although obtaining an ISO 3741 measurement for the paddle was unsuccessful due to ongoing campus construction, the insights gained significantly contribute to understanding how the VBSP method can be adapted and validated across different types of radiating structures. Initial sound power predictions using the VBSP method and the thin unbaffled flat plate model to estimate the sound power from three paddles are provided.

*\*\*I conducted the experimental testing, analysis, and writing for the manuscript. My contributions included performing impact testing and vibrometry measurements for thirteen pickleball paddles, analyzing their vibroacoustic responses, and identifying the vibration mode that primarily contributes to the noise produced during paddle-to-ball impact. I also obtained the velocity data needed to compute the sound power using the VBSP method for both the paddle blade and handle using the developments found in Ch. 5 and provided initial sound power predictions. \*\**

## 6.1 Title

Characterizing the vibroacoustic response of pickleball paddles through impact testing and laser Doppler vibrometry

## 6.2 Authors and Affiliations

Ian C. Bacon,<sup>1a</sup> Corey E. Dobbs<sup>1</sup>, Matt S. Allen<sup>2</sup>, and Brian D. Patchett<sup>3</sup>

<sup>1</sup> *Department of Physics and Astronomy, Brigham Young University, Provo, Utah 84602.*

[icbacon@byu.edu](mailto:icbacon@byu.edu), [cedobbs@byu.edu](mailto:cedobbs@byu.edu)

<sup>2</sup> *Department of Mechanical Engineering, Brigham Young University, Provo, Utah 84602.*

[matt.allen@byu.edu](mailto:matt.allen@byu.edu)

<sup>3</sup> *Department of Physics, Utah Valley University, Orem, Utah 84058.*

[brian.patchett@uvu.edu](mailto:brian.patchett@uvu.edu)

## 6.3 Abstract

This study investigates the vibroacoustic behavior of pickleball paddles, focusing on identifying the vibrational modes that most significantly contribute to noise during gameplay. Thirteen paddles from ten different brands, made from materials such as wood, graphite, composite, and hexcore, were analyzed using experimental modal analysis and scanning laser Doppler vibrometry. Acoustic testing was conducted in an anechoic chamber to correlate these vibrational modes with the audible noise produced by paddle impact. Findings indicate that while the dominant structural vibration modes vary across brands, the primary contributor to acoustic noise is the “membrane mode,” typically occurring within the 980 to 1,477 Hz range. Graphite paddles exhibited higher fundamental frequencies and lower damping ratios, leading to prolonged vibrations. In contrast, wooden paddles displayed lower frequencies and higher damping ratios, resulting in quicker vibration decay. These findings highlight the critical role of material properties and paddle design in influencing both the acoustic and vibrational performance of pickleball paddles, offering valuable insights for manufacturers seeking to optimize paddle design for improved player experience and noise reduction.

Keywords: Experimental Modal Analysis, Noise, Pickleball, SLDV

## 6.4 Introduction

Pickleball has seen explosive growth in the United States with the number of players skyrocketing from 8.9 million in 2022 [1] to 13.6 million in 2023 [2]. An increase in noise complaints from communities across the country driven by the distinct “pop-pop-pop” sound characteristic of pickleball gameplay has accompanied this surge in popularity. This noise has even led to legal disputes, with the New York Times [3] highlighting the absence of a clear solution to the issue. Some of the factors causing the acoustic challenges in pickleball, including smaller court size than, say, a tennis court, the higher resonant pitch of the pickleball compared to a tennis ball, and the more frequent occurrence of the hits during gameplay [4].

The study of vibroacoustics in sports equipment is crucial for understanding how the design and material properties of equipment like paddles, rackets, and bats influence both performance and noise generation. While extensive research has been conducted on the vibroacoustic behavior of tennis rackets and ping pong paddles, the literature on pickleball paddle dynamics remains sparse.

Research on the vibroacoustics of sports equipment has shown that the vibration modes of paddles and rackets play a significant role in the sound produced during play. For example, a comprehensive study by Dan Russell at Penn State explored the vibroacoustic properties of ping pong paddles and balls. Russell’s research [5] demonstrated that the racket displays a variety of structural vibration patterns similar to those found in elliptical plates. Two of these modes, specifically the (0,2) and (1,2) membrane modes primarily influence the sound produced when the paddle strikes the ball. This study is particularly relevant to this investigation, since the vibration modes in ping pong paddles may exhibit similarities to those in pickleball paddles due to the comparable shapes of equipment used in both sports.

Research in tennis has shown that factors such as string tension and material composition of the stringbed influence a racket's vibration response. Banwell *et al.* [6] conducted a thorough analysis of the vibrational mode shapes of tennis rackets, revealing how these modes impact a player's control during gameplay. These findings underscore the importance of understanding the relationship between equipment vibration and player experience, a theme that is central to the study of pickleball paddles.

While there is limited specific research on the vibroacoustics of pickleball paddles, some studies consider the time signature of the paddle to ball impact to address noise pollution [4], [7], though these do not delve into the specific vibrational modes that contribute to noise generation. The unique construction and shape of pickleball paddles, which differ from those of ping pong paddles and tennis rackets (see Fig. 6.1), suggest that their vibration responses could vary significantly, highlighting the need for a dedicated investigation.

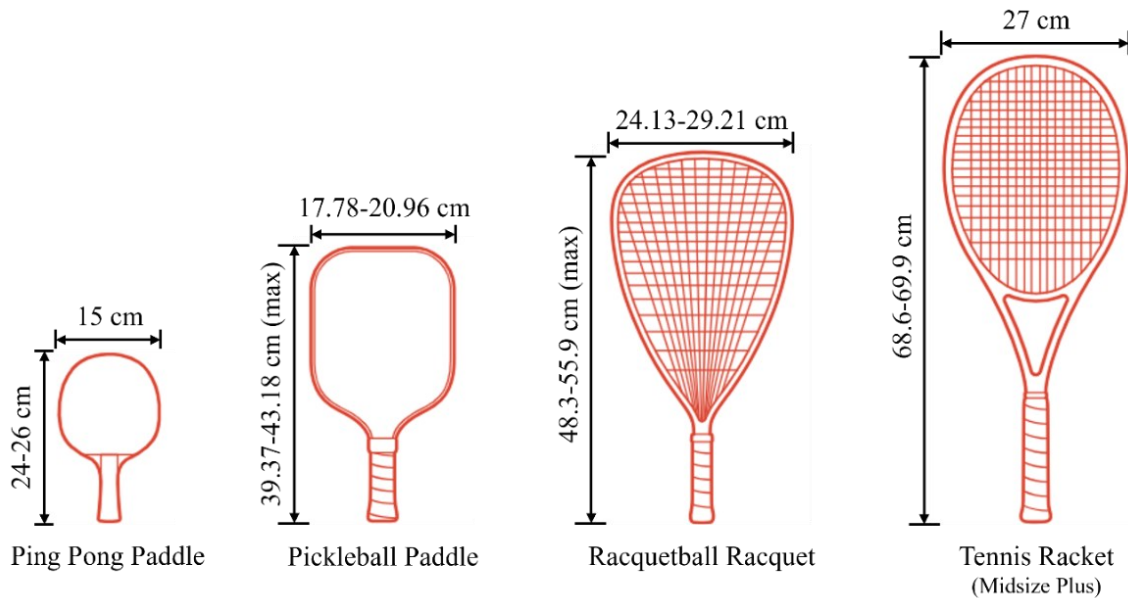


**Figure 6.1:** (*color online*) The relative size and shapes of different paddles and rackets used in sports with average dimensions and individual graphics obtained from dimensions.com.



This study intends to fill the gap in literature by conducting an in-depth analysis of the vibroacoustic behavior of pickleball paddles. An examination of 13 paddles from ten different brands, constructed of a variety of materials including wood, composite, and graphite, priced from \$15 to \$480 USD (as of May 20, 2024) and chosen to represent the diversity of paddles available on the market. This research seeks to identify the vibrational modes that contribute most significantly to noise during gameplay.

This research uses experimental modal analysis and scanning laser Doppler vibrometry to determine the vibrational mode shapes and frequencies that are significant in sound radiation. Acoustic testing was then conducted to correlate these vibrational modes with the audible noise produced by paddle impact. Comparing the vibration responses across different paddle brands established a link among modal analysis, paddle performance, and noise generation, ultimately offering insights into how these factors influence player experience and community noise concerns.

The modal analysis was conducted using a roving hammer test with accelerometers and Siemens SimCenter™ Impact Testing software (Leuven, Belgium) to determine the frequency response of the different paddles. This was supplemented by using a scanning laser Doppler vibrometer (SLDV) to provide a more detailed and repeatable assessment of the vibrational mode shapes. Additionally, acoustic data was collected in an anechoic chamber using a ZOOM H6 Handy Recorder (Hauppauge, USA) and analyzed using custom software developed in LabView® (Austin, USA). The resulting data in turn identified correlations between the vibrational modes and the noise generated during gameplay.

This study thus offers a comprehensive investigation into the vibroacoustic behavior of pickleball paddles. By bridging the gap between laboratory modal analysis and real-world

gameplay, this research improves the understanding of pickleball paddle dynamics and contributes to the development of quieter and better performing equipment.

## **6.5 Hammer Testing**

### **6.5.1 Pickleball Paddles**

The vibrational mode shapes and frequencies of 13 pickleball paddles from ten different brands constructed from wood, graphite, or a composite mix of different materials were investigated using a roving-hammer experimental modal analysis, as shown in Figs. 6.2a and 6.2b. Another interesting case is paddles advertised to be built with a hexcore structure within the blade of the paddle that are different from the wooden paddles.

### **6.5.2 Experimental Setup**

To determine the frequency range of interest, a preliminary acoustical test was conducted by tapping a pickleball repeatedly with three different paddles. A spectrogram analysis revealed that most of the significant resonance frequencies were primarily below 2 kHz. Based on this information, an initial 10-point grid, with points approximately 7 cm apart, was established on the paddles to serve as impact locations. Three accelerometers were mounted on the backside of each paddle, using wax positioned directly behind three of the impact points, a setup hereafter referred to as the coarse configuration.

The paddles were suspended using bungee cords to simulate free boundary conditions, a common method for testing hand-held sports equipment [5] (see Fig. 6.2b). The coarse setup quickly estimated resonance frequencies of the paddles so that the acoustic testing could be performed to isolate the mode that primarily contributes to the sound produced by the paddles.

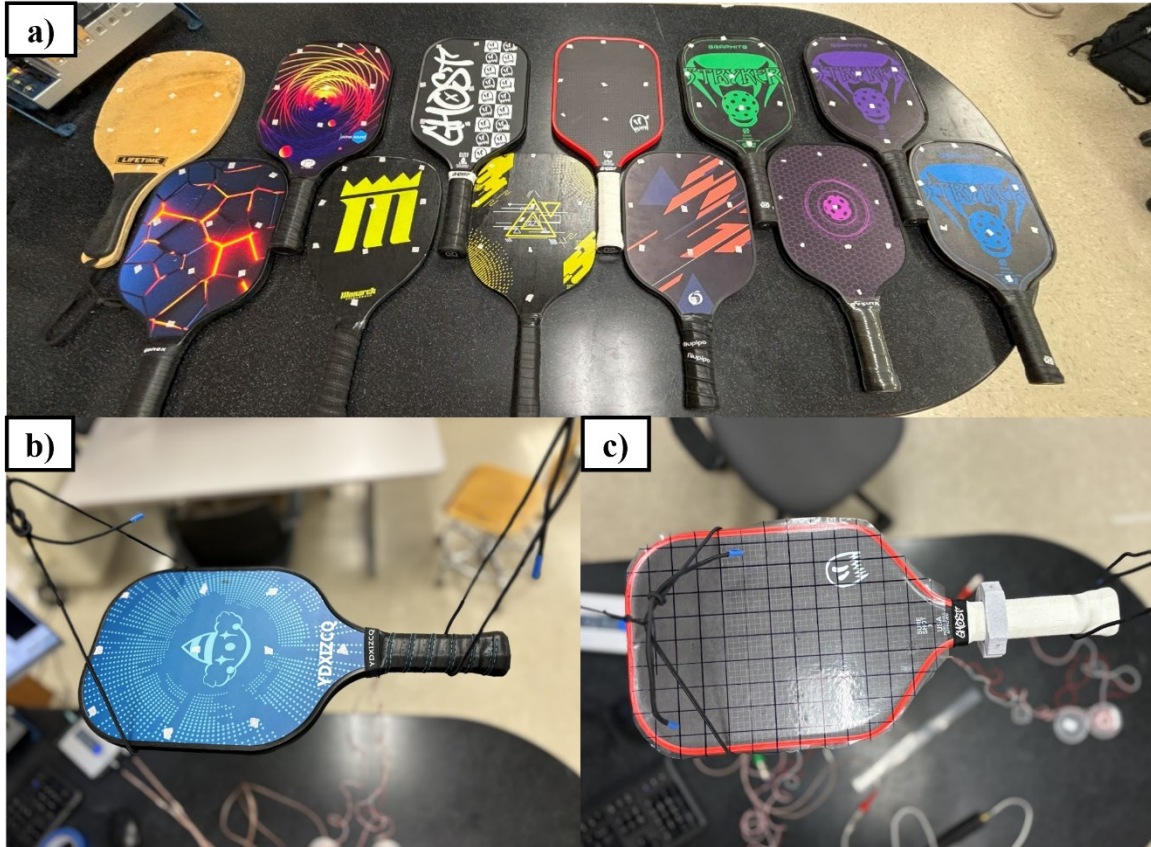


**Figure 6.2:** (color online) a) Twelve pickleball paddles used for testing, identified by brand name and color/pattern (left to right): Lifetime, Gonex, Panel Sound, Monarch, checkered Ghost, Triangle, red Ghost, Niupipo, green Stryker, Bykuta, purple Stryker, and blue Stryker. b) The 13th paddle, labeled YDXIZCQ, resting on bungee cords in preparation for impact testing, showing the coarse grid. c) The red Ghost paddle is set up for impact testing with the fine grid, indicating the impact locations at the grid intersections.

Hammer testing was performed using the Siemens SimCenter™ Impact Testing software using a frequency bandwidth of 2,048 Hz with 8,192 FFT lines, yielding a frequency resolution of 0.25 Hz. Additional settings included a scope time of 6.4 seconds, a trigger level of 15 mV, an input range of 10 V, a pre-trigger of 0.01 seconds, and an average of five readings per impact location.

During testing, the accelerometers recorded the paddle's response to a manual hammer excitation at each impact point. Analyzing the ratio of acceleration response to force input using a four-channel frequency analyzer generated Frequency Response Functions (FRFs) in the Impact Testing software. Assuming reciprocity between the hammer and the accelerometer positions, 30 FRFs were measured for each paddle face.

The resulting FRF data were combined into a composite FRF matrix in Matlab© to provide a holistic view of how the entire paddle face behaves across the bandwidth of interest. Figure 6.3 shows an example of the composite FRF for one of the paddles, the purple Stryker. The composite FRF was fitted to a modal model which was then curve-fitted to better resolve the accuracy. A single-input-multi-output (SIMO) extension of a modal identification algorithm by Allen *et al.* [8] was used to process the FRFs for all response points simultaneously. This algorithm takes the composite FRF and fits it to a modal model to obtain the global estimates for the natural frequencies and damping modes of each paddle face.

Using SimCenter™ Impact Testing software, data were mapped to the paddle geometry and post-processing produced animated mode shapes that visually depicted the relative vibration amplitudes at the natural frequencies of each paddle.

In addition to the 10-point coarse configuration, a finer grid of 102 points with 2 cm spacing was also employed. Due to the longer measurement time, the finer hammer testing was performed on only three of the paddles – the red Ghost, Triangle, and Bykuta models, made of hexcore, wood, and composite, respectively. The same process was applied for the 10-point measurement resulting in 306 reciprocal FRF measurements (see Fig. 6.2c) to improve the resolution of the modes of the paddle faces, hence referred to as finer configuration.

### 6.5.3 Hammer Test Data

The average FRFs generated from this data provided detailed insights into the natural frequencies and damping ratios of the paddles up to 2 kHz (see Fig. 6.3). Figure 6.4 shows six of the vibrational modes common to each of the paddles. The out-of-plane bending modes are where the paddle bends or flexes along its length, with the first two bending modes being the most prominent. Torsion modes are observed as the paddle blade twists about its central axis. Additionally, membrane-like modes are also present, resembling circular membranes or drumheads with distinct regions where the blade moves upward and adjacent regions where it moves downward, separated by nodal lines where the vibration amplitude is zero.

Table 6.1 shows the name of each paddle tested and compares the fundamental frequencies between them with their corresponding damping ratios.

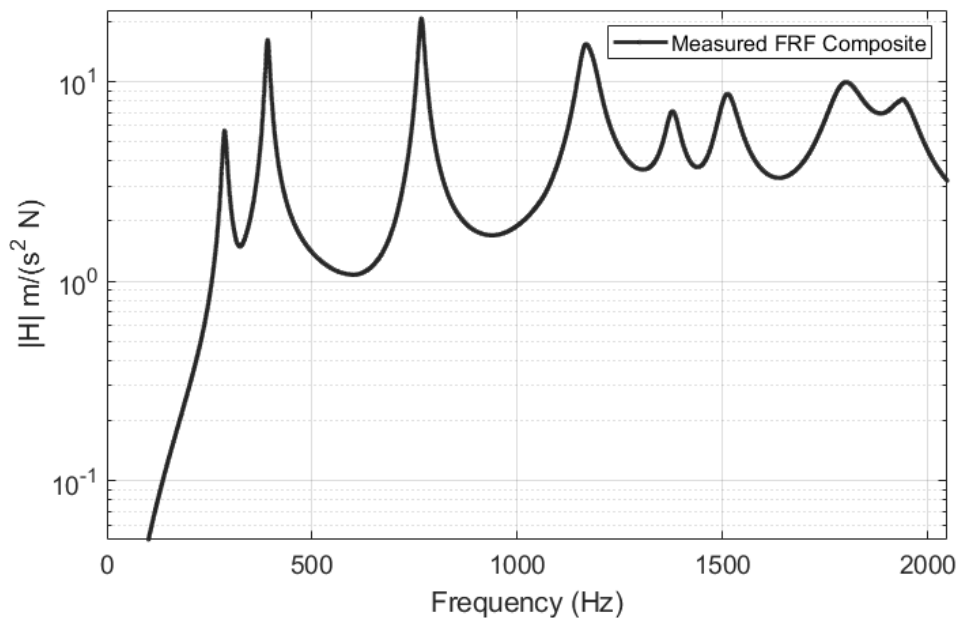


**Figure 6.3:** The average FRF for the purple Stryker paddle using the coarse configuration measured through impact testing showing the natural frequencies of the paddle, as recorded by accelerometers in the coarse configuration.

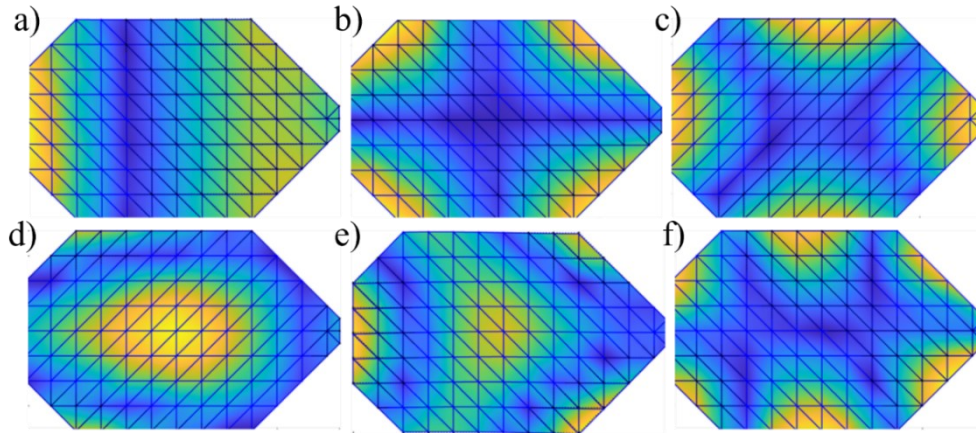


**Figure 6.4:** (*color online*) An example of six of the vibrational modes common to the paddles. These images came from the red Ghost model, but other paddles showed similar shapes, though at different frequencies. (a) lengthwise bending, (b) first torsion, (c) torsion about diagonal, (d) first membrane, (e) second bending, (f) second torsion about axis.

**Table 6.1:** (*color online*) The names of the 13 paddles with their corresponding fundamental frequencies and damping ratios.

Paddle Name	Frequency (Hz)	Damping Ratio
Lifetime	111.25	0.030
Monarch	171.53	0.041
Triangle	173.72	0.038
Red Ghost	197.22	0.032
Checkered Ghost	200.06	0.034
YDXIZCQ	201.00	0.027
Panel Sound	201.99	0.034
Gonex	204.57	0.025
Niupipo	205.01	0.026
Bykuta	262.65	0.039
Purple Stryker	286.93	0.021
Green Stryker	292.00	0.018
Blue Stryker	298.18	0.014

#### **6.5.4 Pickleballs**

Impact analysis of a pickleball was conducted using a suspended setup, where the ball hung from a thin string to simulate free boundary conditions (see Fig. 6.5). This method was chosen to ensure that the ball's natural frequencies and damping ratios could be accurately measured without interference from external constraints.

Testing parameters were set to a bandwidth of 6 kHz with a frequency resolution of 1.46 Hz across 4,096 spectral lines and a data acquisition time of 0.68 seconds, with an average of five readings taken per impact location to ensure reliable results. The ball was subjected to impacts at ten different locations with response measurements recorded using three accelerometers placed at strategic points on the ball, which captured the ball's vibrational response to hammer excitation, similar to the method used for the paddles. Placing the accelerometers on the ball would likely cause mass loading and change the resonance frequencies from the true values.

Resulting FRFs were analyzed to determine the ball's natural frequencies and identified the primary peak frequency at approximately 1,330 Hz. The next section compares this result with acoustic data obtained from the paddles.

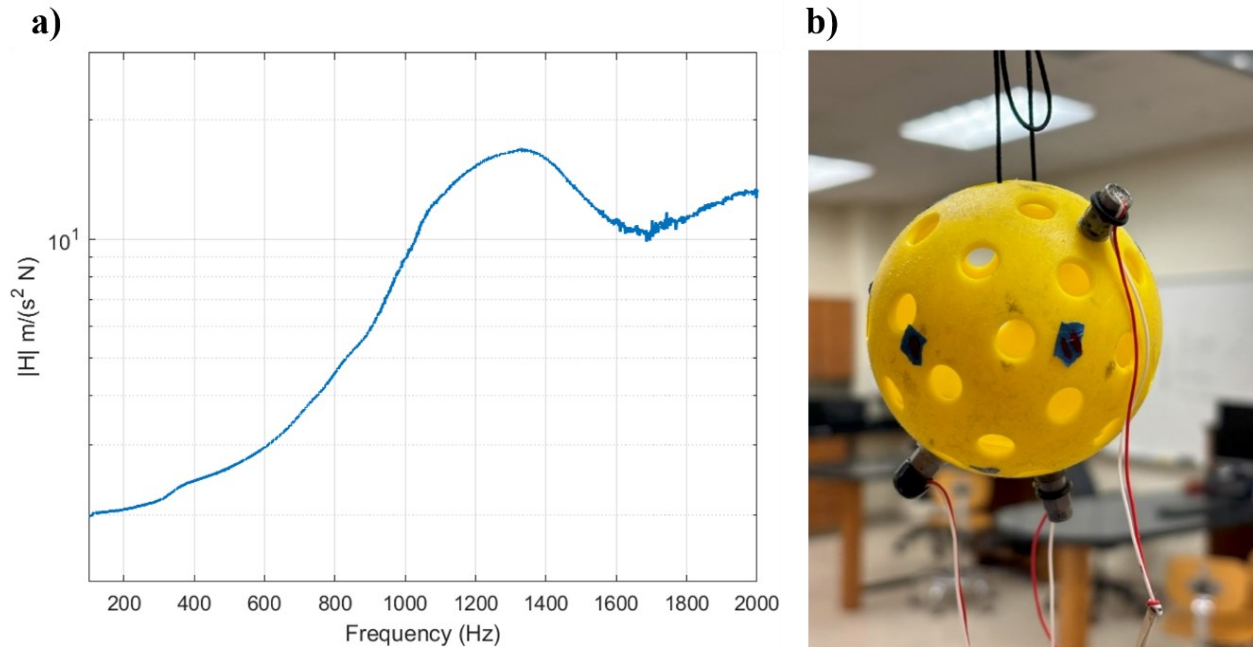


**Figure 6.5:** (color online) a) The average FRF for the pickleball using 30 measured FRFs (obtained from ten input locations and the three accelerometer locations as outputs). b) A Niupipo brand pickleball set up for impact testing.

## 6.6 Vibrometer Testing

To verify that the mass loading of the accelerometers and bungee cord damping did not dramatically affect the resonance frequencies, an SLDV was employed (see Fig. 6.6). As a non-contact method, the SLDV allows a comparison of the resulting resonance frequencies between measurement techniques.

SLDV testing was also performed to obtain a detailed view of the mode shapes for the paddles with handles included. Each paddle was scanned to confirm the mode shapes found using the hammer test method with higher resolution and to evaluate the response in the handle. The paddles stood on the edge of a rigid table, with a piezoelectric transducer attached to the back of the paddle



faces to excite them with a broadband pseudorandom signal up to 4,096 Hz at a 0.5 Hz resolution. The paddles had a mostly free boundary condition on the handle (see Fig. 6.6), which is different from the hammer tests. Six complex FFT averages, taken for each scan point, identified six to eleven distinct modes below 2 kHz, depending on a paddle's material properties and size.



**Figure 6.6:** (*color online*) The SLDV experimental set up for the pickleball paddles.

Figure 6.7 captures eight of the operational deflection mode shapes of the paddle blade and handle, showcasing various vibrational behaviors similar to the hammer results. The 62.5 Hz shape is a rigid body mode.

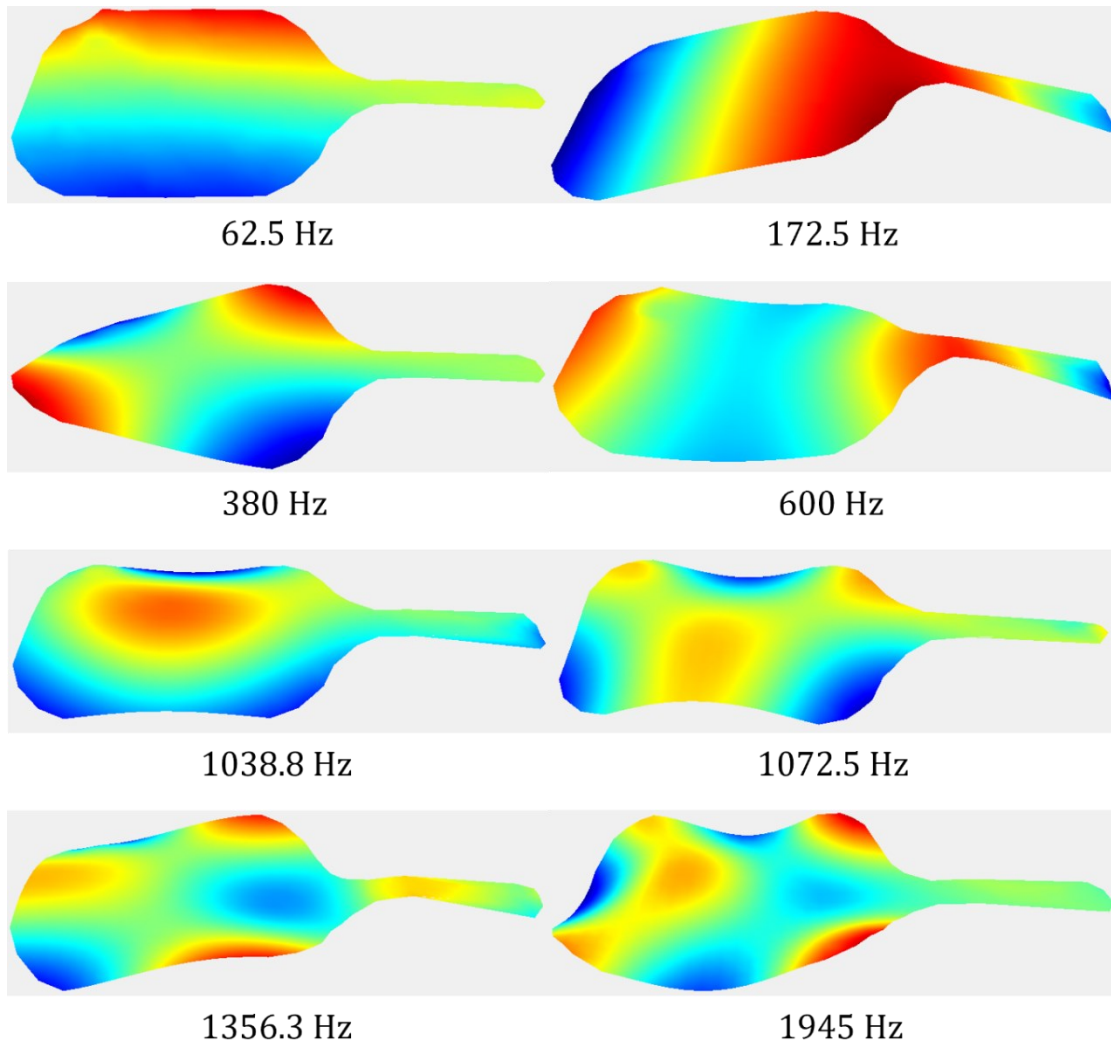


**Figure 6.7:** (*color online*) Eight operational deflection shapes of the Triangle pickleball paddle obtained from the SLDV.

## 6.7 Acoustic Testing

To identify which vibrational modes of the pickleball paddle contribute the most to sound radiation during gameplay, acoustic testing of the paddles was conducted in an anechoic chamber, reducing the external noise interference down to 85 Hz and ensuring the capture of all critical information. A ZOOM H6 Handy Recorder was employed, utilizing two built-in stereo

microphones and an external 1/8" microphone to capture comprehensive acoustic data. Each paddle underwent a series of taps and serves with a pickleball, while the paddle to ball impact sound was recorded, allowing for a thorough assessment of its acoustic behavior in typical gameplay scenarios.

This acoustic response was then overlaid on top of the vibrational response of the paddle to identify the vibrational mode contributing the greatest to the sound produced by the paddle. Figure 6.8 shows this plot for the purple Stryker paddle. Table 6.2 illustrates the difference between the frequency of the first membrane mode and that of the greatest acoustic response for ten of the paddles. The remaining three paddles needed to be returned to their owners before the testing could be performed. However, the other ten paddles confirm that the first membrane mode is the primary contributor to the noise generated by the paddle to ball impact.

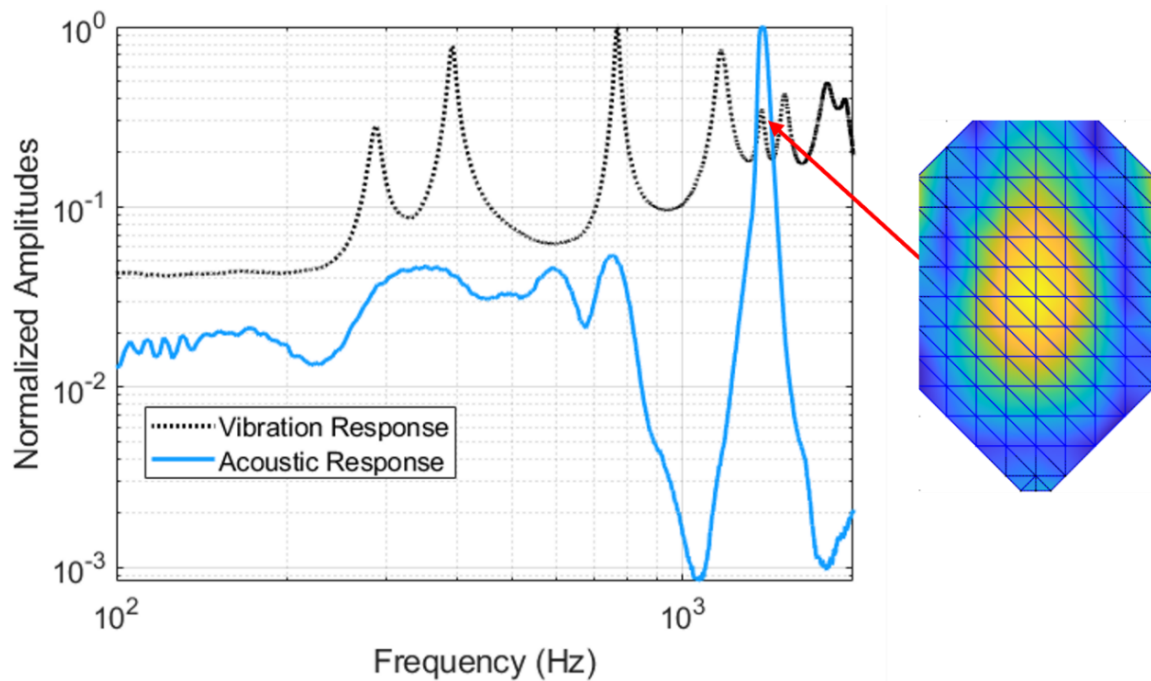


**Figure 6.8:** (*color online*) The acoustic response (blue) overlaying the vibrational response of the purple Stryker paddle (black) highlighting this vibrational mode as the primary contributor to the sound the paddle produces.

**Table 6.2:** The peak acoustic frequency compared to the frequency of the first membrane mode for ten paddles shows that the first membrane mode is responsible for the primary noise signature produced by each paddle. The table also illustrates the damping ratios of the first membrane mode and the percent difference between vibration and acoustic frequencies.

Paddle	Acoustic Peak Frequency (Hz)	1 <sup>st</sup> Membrane Mode Frequency (Hz)	Damping Ratio	Percent Difference (%)
Niupipo	1002.0	980.4	0.029	2.1
Lifetime	1010.0	1003.5	0.022	0.6
Bykuta	1010.4	994.8	0.030	1.6
YDXIZCQ	1024.8	987.9	0.032	3.6
Triangle	1065.6	1068.6	0.014	0.3
Red Ghost	1144.8	1103.7	0.042	3.6
Checkered Ghost	1166.4	1150.0	0.045	1.4
Purple Stryker	1384.8	1378.6	0.014	0.4
Blue Stryker	1459.2	1446.4	0.019	0.9
Green Stryker	1481.8	1476.7	0.026	0.3

## 6.8 Sound Power Prediction

This section utilizes vibration measurements from Sec 6.6 to predict the sound power for three paddle models: Bykuta, Red Ghost, and Triangle, made from composite materials, hexcore, and wood, respectively. Due to the unavailability of a reverberation chamber for Precision (Grade 1) sound power measurements per the ISO 3741 standard, this section presents the vibration-based sound power (VBSP) predictions for these three paddles.

The sound power of a pickleball paddle is modeled using the sound power equation (Eqn. 1.2) with three different **R** matrices. First, the paddle is approximated as a baffled flat plate, using the monopole-based **R** matrix defined by Eqn. 1.1. Second, a more realistic model treats the paddle as

a thin, un baffled flat plate, applying the dipole-based  $\mathbf{R}$  matrix from Eqn. 5.10. Third, the combination  $\mathbf{R}$  matrix from Eqn. 5.7 is applied. A comparison of these three methods is provided.

The scan positions for all three paddles are identical, with horizontal and vertical spacings of 8.6 mm and 10.1 mm, respectively. Figure 6.9 illustrates the scan positions for the Red Ghost paddle, where positions are numbered column-wise from left to right. The front side positions are shown in Fig. 6.9a, followed by the backside positions in Fig. 6.9b. The corresponding distance matrix,  $\mathbf{d}$ , is presented in Fig. 6.10. Within each block of the  $\mathbf{d}$  matrix, Toeplitz symmetry, centrosymmetry, and bisymmetry are observed. However, these symmetries do not appear between the blocks.

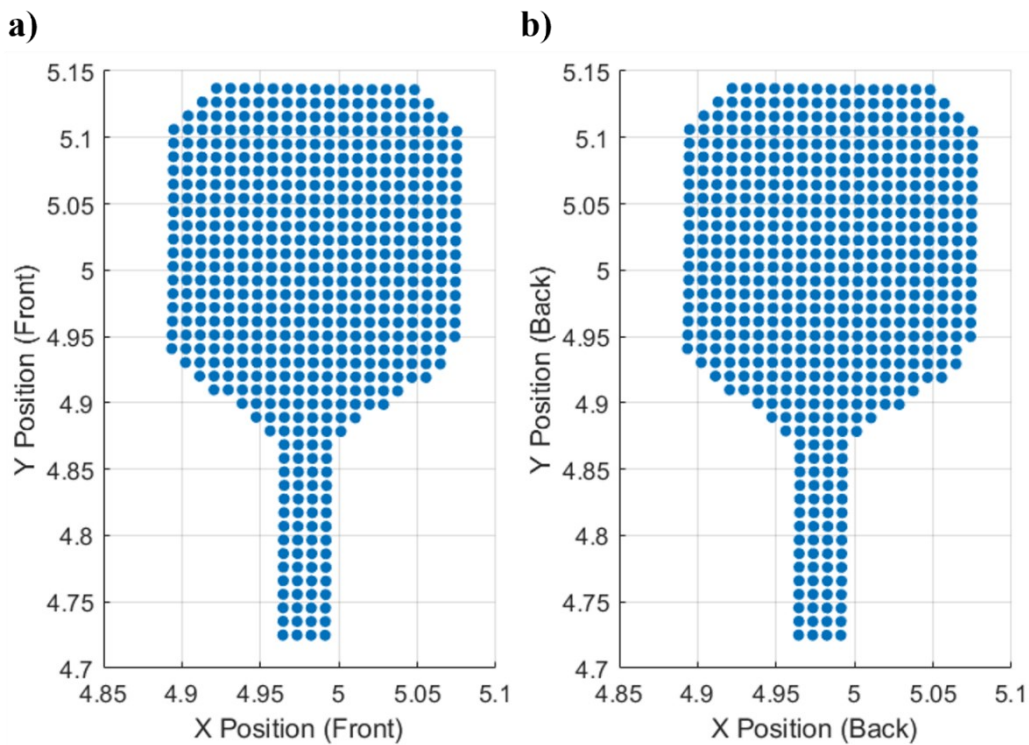


**Figure 6.9:** SLDV scan locations on the Red Ghost paddle used to measure vibration response, with horizontal and vertical spacings of 8.6 mm and 10.1 mm, respectively. (a) Front side scan locations. (b) Backside scan locations aligned identically in the xy-plane but offset in the z-direction by the paddle thickness, as used in sound power calculations.



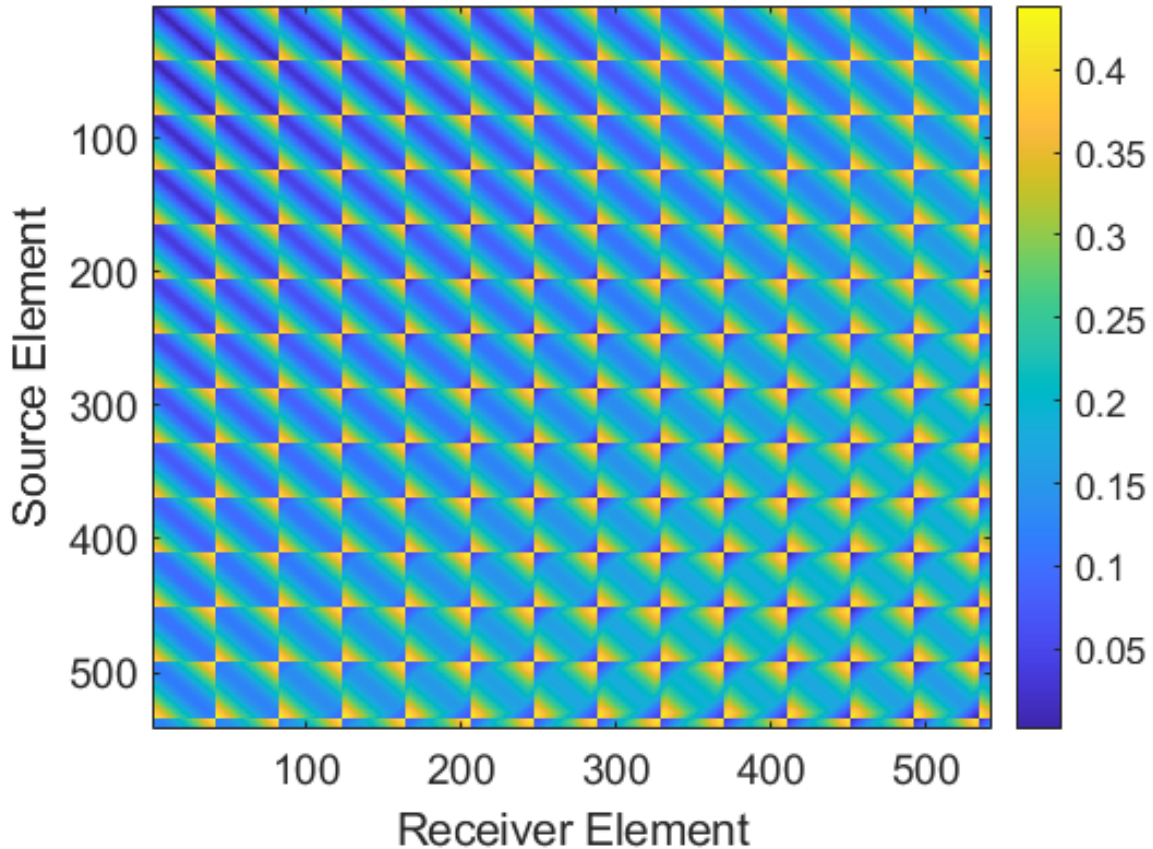


**Figure 6.10:** Distance matrix produced from the Red Ghost paddle scan data.

Sound power predictions using the three different  $\mathbf{R}$  matrices are shown in Figs. 6.11-6.13 for the Bykuta, Red Ghost, and Triangle paddles, respectively. For the Bykuta paddle, sound power is computed up to the 10 kHz one-third octave (OTO) band to assess its broadband response, while for the Red Ghost and Triangle paddles, calculations are limited to 2 kHz, aligning with other tests in this chapter.

Examining the broadband response up to 10 kHz reveals two distinct regimes. At higher frequencies, excitation appears stronger, likely due to the frequency response of the piezoelectric transducer (PZT). Below the 2 kHz OTO band, the Bykuta paddle displays modal behavior, with peaks in sound power that indicate more efficient sound radiation in these bands. Above 2 kHz,

this modal behavior dissipates. Based on this observation, sound power for the other paddles was computed only up to the 2 kHz OTO band.

Looking at the broadband response up to 10 kHz, two regimes are evident. First, higher frequencies are more strongly excited, likely due to the frequency response of the piezoelectric transducer (PZT). Second, below the 2 kHz OTO band, the Bykuta paddle displays modal behavior, with peaks in sound power indicating more efficient sound radiation in these frequency bands. Above 2 kHz, this modal behavior diminishes. Based on this observation, sound power for the other paddles was computed only up to the 2 kHz OTO band.

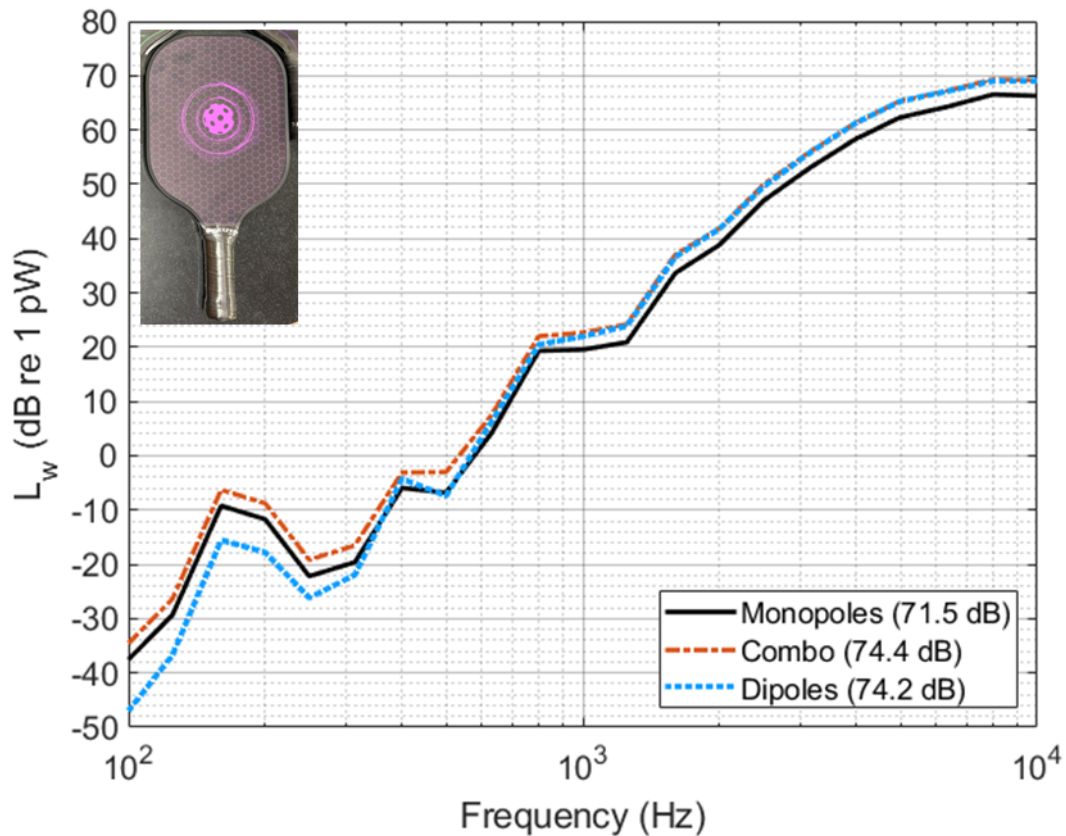


**Figure 6.11:** Comparison of sound power predictions for the Bykuta paddle using the VBSP method, calculated with three  $\mathbf{R}$  matrix models: the monopole-based model (Eqn. 1.1, black), the dipole-based model (Eqn. 5.10, blue), and the combination model (Eqn. 5.7, burnt orange).

The differences between the three sound power models across the figures reflect how each model captures the vibrational behavior of the paddles at different frequency ranges, influenced by their material and structural properties. At low frequencies, the dipole-based model often predicts lower sound power, as observed below 315 Hz for the Bykuta paddle and below 200 Hz for the Triangle paddle. This reduction aligns with the dipole model's sensitivity to phase variations and its representation of opposing directional forces, which are less effective at radiating sound at low frequencies. The cutoff frequency where this drop-off becomes evident varies based on the paddle's material and construction (e.g., composite, hexcore, wood); for example, composite and hexcore paddles show this drop-off at a slightly higher frequency cutoff than wood, likely due to differences in mass, stiffness, and damping properties across these materials.

At higher frequencies, the monopole model tends to underestimate sound power, particularly above the 1 kHz OTO band, as seen in Figs. 6.11-6.13. In this range, the dipole and combination models generally yield higher estimates due to their ability to model the interactions across the paddle surface better than the monopole-based model generally for baffled structures. The monopole-based model appears to be about 3 dB lower than the combined model indicating a factor of two less in the pressure.

In the mid-frequency range, from about 315 Hz to 1 kHz, the monopole and dipole models are often close in their estimates, as shown in Figs. 6.11-6.13. This convergence suggests that, at mid-frequencies, both models effectively capture the paddle's acoustic radiation behavior, making them reasonably accurate approximations. The combination model, however, remains slightly higher, likely due to its inclusion of both monopole and dipole components in mid-frequency bands.



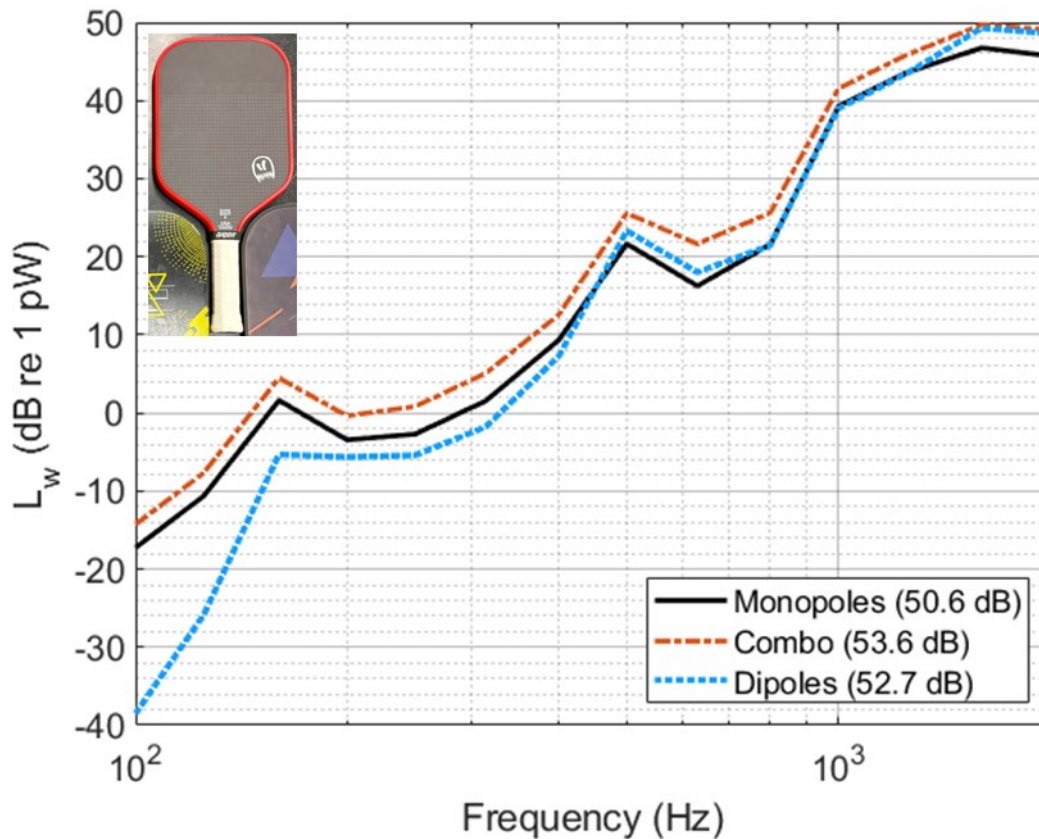


**Figure 6.12:** Comparison of sound power predictions for the Red Ghost paddle using the VBSP method, following the same approach as in Fig. 6.11.

The observed resonance frequencies—appearing in specific OTO bands across Figs. 6.11-6.13—indicate how the material and structural properties of each paddle influence sound power behavior. For instance, the resonance bands at 160 Hz, 200 Hz, 400 Hz, 800 Hz, and 1,600 Hz in Fig. 6.11; 160 Hz, 500 Hz, 1,000 Hz, and 1,600 Hz in Fig. 6.12; and 160 Hz, 400 Hz, 630 Hz, and 1,000 Hz in Fig. 6.13 highlight these modal characteristics and higher radiation efficiency.

The earlier onset of resonance modes in the Triangle paddle, as observed in Fig. 6.13, is likely attributable to its higher mass, as structures with greater mass tend to have more pronounced vibrational responses at lower frequencies. This characteristic contrasts with the composite and

hexcore paddles, where resonances appear more spaced out, aligning with their respective material damping and structural design.

However, these resonance frequencies do not align perfectly with those identified in other tests. This discrepancy may stem from slight differences in boundary conditions and excitation points during measurements, which can shift resonance points and excite only certain modes.

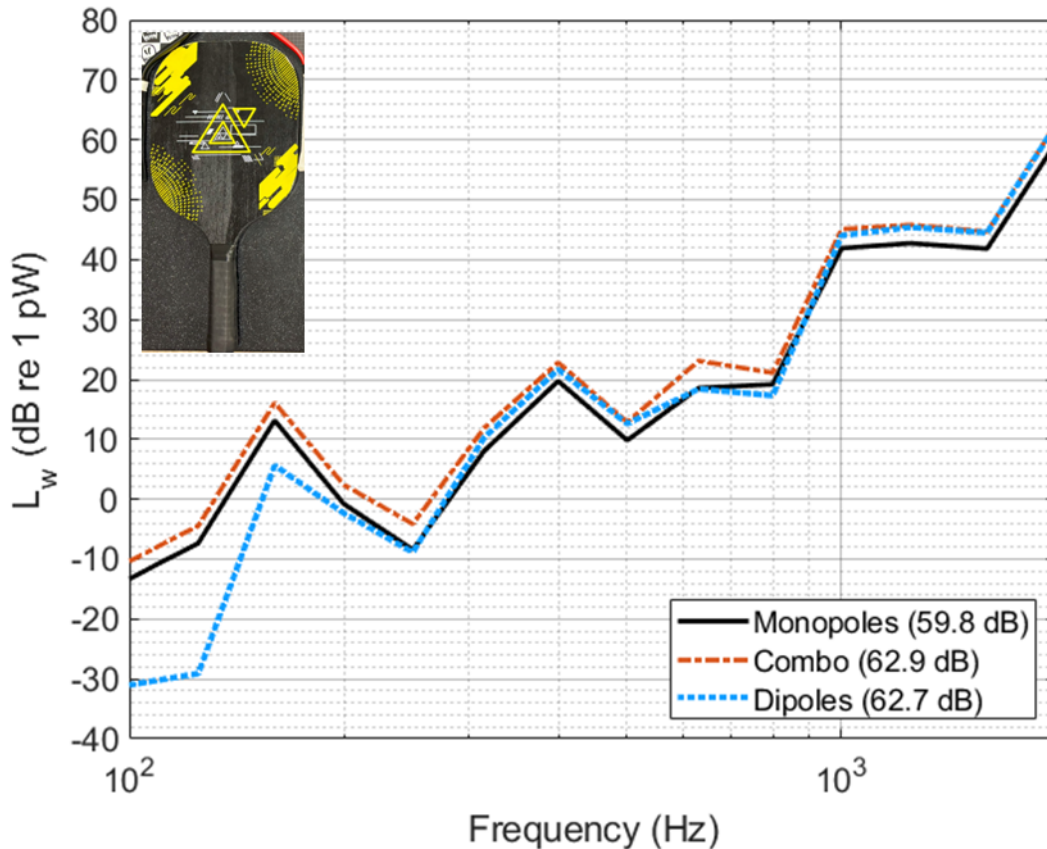


**Figure 6.13:** Comparison of sound power predictions for the Triangle paddle using the VBSP method, following the same approach as in Fig. 6.11.

Figure 6.14 compares the sound power of the Red Ghost and Triangle paddles using the combined  $\mathbf{R}$  matrix model. The Bykuta paddle, which was tested differently at 12.8 kHz, is therefore not included in this comparison. According to the VBSP method, the Triangle paddle is predicted to have higher sound power levels than the Red Ghost paddle across the 100 Hz to 200

Hz, 400 Hz, 1 kHz, and 2 kHz OTO bands, likely due to its higher mass contributing to stronger low-frequency sound radiation. Conversely, the Red Ghost paddle shows higher sound power levels at the 250 Hz, 500 Hz, 800 Hz, and 1,600 Hz OTO bands, with both paddles producing similar sound power levels at the 630 Hz OTO band. The Red Ghost paddle’s relatively lower sound power output at high frequencies aligns with the noticeable audible difference at higher frequencies, where the Red Ghost sounds more muted compared to the Triangle paddle, particularly around the 2 kHz band.

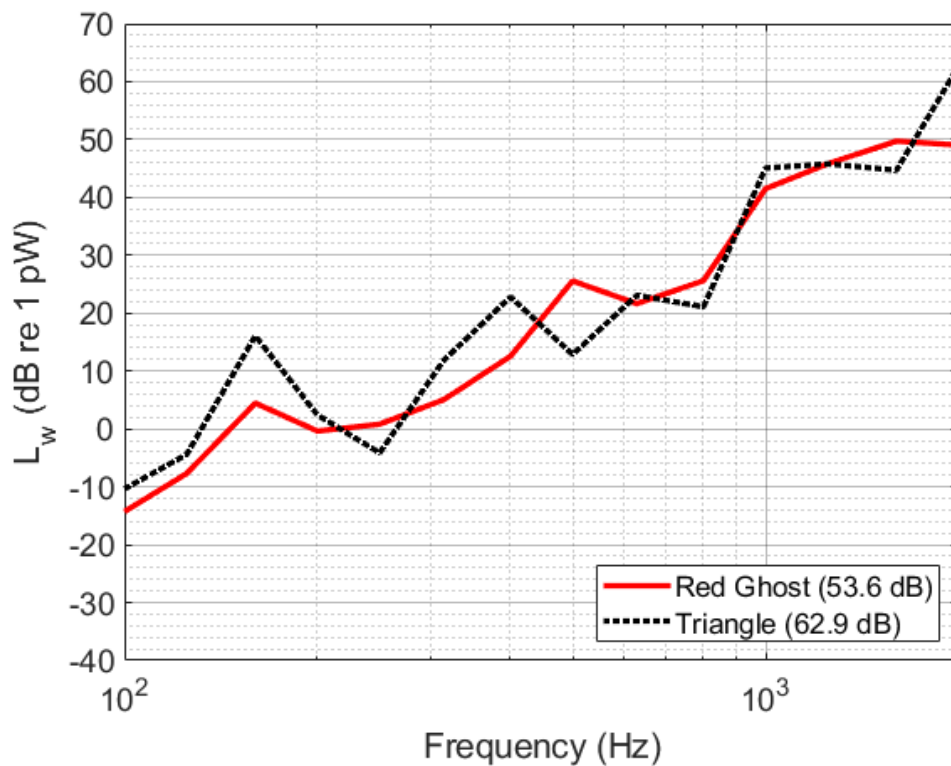


**Figure 6.14:** Sound power comparison of the Red Ghost and Triangle pickleball paddles using the combined  $\mathbf{R}$  matrix (Eqn. 5.7) to assess relative loudness across OTO bands. Both paddles were excited at the upper corner.

## 6.9 Results

Impact testing of 13 pickleball paddles revealed clear trends in fundamental frequencies and damping ratios, emphasizing the role of material properties and design in paddle performance. Fundamental frequencies ranged from 111.25 Hz to 298.18 Hz, with consistent results observed within the same brands, such as the Ghost and Stryker series. Damping ratios at these frequencies varied from 0.014 to 0.041. Graphite paddles, like those in the Stryker series, exhibited higher fundamental frequencies and lower damping ratios than wooden paddles, including the Monarch, Triangle, and Lifetime brands. The heavier weight and lower stiffness of wooden paddles contributed to their lower frequencies and higher energy dissipation, distinguishing them acoustically and vibrationally.

Comparisons of the acoustic peak frequencies and first membrane mode frequencies showed strong correlations, with percentage differences ranging between 0.3% and 3.6%. These results indicate that the first membrane mode is the primary contributor to the sound produced during paddle-to-ball impact. Despite three paddles being unavailable for acoustic testing, the trend observed in the remaining ten paddles supports this conclusion.

Stryker paddles demonstrated very low percentage differences (under 1%), showing strong alignment between acoustic and vibrational data. First membrane mode frequencies ranged from 980 Hz to 1,477 Hz, with damping ratios varying across paddle designs. The purple Stryker paddle had the lowest damping ratio (0.014), while the checkered Ghost paddle exhibited the highest (0.045). Paddles such as the Niupipo and Triangle had damping ratios of 0.029 and 0.014, respectively, with percent differences of 2.1% and 0.3%. The close relationship between acoustic and vibrational frequencies was consistent across different materials, with acoustic peak frequencies generally slightly higher than first membrane mode frequencies. This discrepancy may

stem from the increased stiffness imparted by gripping the handle during acoustic testing compared to the more flexible bungee cord setup used in hammer testing.

The sound power levels were predicted for three pickleball paddles—Bykuta, Red Ghost, and Triangle—using the VBSP method and the **R** matrices developed in this study. Peaks in the sound power curves appear near the 1 kHz OTO band, corresponding to the first membrane mode for each paddle. This study compares sound power predictions for these three paddles using the VBSP method with three distinct **R** matrices, revealing how each model captures acoustic behavior across low, mid, and high frequencies, shaped by material and structural characteristics.

In the low-frequency range, the Triangle paddle consistently demonstrates higher sound power levels due to its greater mass, enhancing low-frequency sound radiation. Mid-frequency comparisons show convergence between the monopole and dipole models, while the combination model yields slightly higher predictions, suggesting its added sensitivity to interactions across both sides of the paddle. At high frequencies, the monopole model underestimates sound power, while the dipole and combination models align more closely, particularly above 1 kHz.

The VBSP method, applied with different **R** matrices, effectively identifies where each paddle radiates sound most efficiently, highlighting distinctions unique to each paddle's design and material composition. Observed resonances occur at predictable bands, with mass and material stiffness influencing resonance distribution across paddles. Although slight deviations in resonance frequencies compared to hammer testing suggest the effect of boundary conditions and different excitation locations, the VBSP method's detailed sound power predictions provide valuable insights into the vibrational dynamics of each paddle.

## 6.10 Conclusions

This study provides a comprehensive analysis of the vibroacoustic behavior of a variety of pickleball paddles, focusing on the relationship between vibrational modes and noise generated during paddle-to-ball impact. Testing identified the “membrane mode,” typically occurring within the 980 Hz to 1,477 Hz range, as the primary contributor to the noise produced during gameplay. Consistent patterns in mode shapes and frequencies were observed across paddles, particularly within the same brand, highlighting the significant influence of material properties and design on vibroacoustic behavior. Graphite paddles exhibited higher fundamental frequencies and lower damping ratios, resulting in prolonged vibrations. In contrast, wooden paddles showed lower fundamental frequencies and higher damping ratios, leading to faster vibration decay.

These findings emphasize the importance of understanding the vibroacoustic characteristics of pickleball paddles for both manufacturers and players. By optimizing paddle design and material selection, manufacturers can enhance player performance while potentially reducing noise impacts in communities. This research establishes a foundation for future studies aimed at improving the acoustic properties of pickleball paddles through targeted design modifications.

This study also demonstrates the VBSP method’s effectiveness in predicting sound power for pickleball paddles, presenting it as a robust alternative to traditional acoustic chamber testing. Once validated against a standard like ISO 3741, the VBSP approach could become a reliable tool for paddle evaluation, enabling the determination of relative loudness and frequency-specific behaviors for various designs. Notably, the method’s ability to capture sound power differences across materials and structures allows for precise assessment of paddles based on sound characteristics. This capability is instrumental in guiding paddle design improvements, whether aimed at reducing sound output to mitigate noise or enhancing acoustics for player feedback.

Overall, the VBSP method's adaptability to different materials and structural properties suggests broader applications in acoustically evaluating consumer products. By providing an efficient and accurate means of sound power estimation across complex geometries and frequency ranges, the VBSP method holds promise for advancing acoustic design beyond paddle manufacturing, supporting the development of quieter, more acoustically refined products.

## **6.11 Acknowledgments**

The authors gratefully acknowledge the support of the Provo, UT community for providing pickleball paddles for testing and Dan Russell and Adam Kingsley as consultants.

## 6.12 References

- [1] E. Nash, “The real pickleball wars are off the court,” *The New York Post*, 2023.
- [2] 2024 Sports & Fitness Industry Association (SFIA) Topline Participation Report.
- [3] A. Keh, “Shattered nerves, sleepless nights: pickleball noise is driving everyone nuts,” *The New York Times*, 2023.
- [4] Z. Weiss, J Komrower, “Pickleball Noise & Political Ploys: A Cape Cod Case Study,” *Institute of Noise Control Engineering*, **12**, 443-454 (2023). doi: 10.3397/NC\_2023\_0067
- [5] D. A. Russell, “Vibroacoustic analysis of table tennis rackets and balls: The acoustics of ping pong,” *J. Sports Sci.* **36**(23), 2644-2652 (2018). doi: 10.1080/02640414.2018.1462578
- [6] G. H. Banwell, J. R. Roberts, B. J. Halkon, S. J. Rothberg, and S. Mohr, “Understanding the dynamic behaviour of a tennis racket under play conditions,” *Exp. Mech.* **54**(4), 527–537 (2014). doi: 10.1007/s11340-013-9803-9
- [7] B. Wyerman and R. Unetich, “Pickleball sound 102 - time history and spectral analysis of pickleball sound,” *INTER-NOISE and NOISE-CON Congress and Conference Proceedings*, NOISE-CON23, **12**, 31-42 (2023). doi: 10.3397/NC\_2023\_0008
- [8] M. S. Allen and J. H. Ginsberg, “A global, single-input–multi-output (SIMO) implementation of the algorithm of mode isolation and application to analytical and experimental data,” *Mech. Syst. Signal Process.* **20**(5), 1090-1111 (2006). doi: 10.1016/j.ymsp.2005.09.007



## Chapter 7 A Generalized Radiation Resistance Matrix

This chapter is an initial development of a generalized radiation resistance ( $\mathbf{R}$ ) matrix, built on the work presented in Chs. 3 and 4. The analytical  $\mathbf{R}$  matrices established for simple geometries serve as a foundation for approximating more complex structures. The chapter demonstrates how these established  $\mathbf{R}$  matrices can effectively approximate complex structures due to the similarities in their acoustic radiation modes (ARMs).

The similarity of acoustic radiation modes across different geometries suggests that sound power could potentially be estimated using a generalized  $\mathbf{R}$  matrix. The primary goal is to design this generalized  $\mathbf{R}$  matrix, which can be adapted for any surface once the distances between elements are determined.

As proof of concept, the chapter provides an example of using  $\mathbf{R}$  matrices for a flat plate to approximate a simply curved plate. The VBSP method, as demonstrated in Ch. 4, effectively utilizes this approach. Initially, the curvature in radiating structures complicates the basis functions used to describe acoustic radiation, leading to increased computational time for generating each  $\mathbf{R}$  matrix entry.

Finally, this chapter addresses these challenges by exploring methods to reduce computational demands and extend the applicability of the VBSP method to more complex radiating structures. Further strategies for reducing computational demands in constructing the  $\mathbf{R}$  matrix is discussed later in Unit 3.

## 7.1 Introduction

The Vibration-Based Sound Power (VBSP) method relies on the accurate computation of sound power radiated from vibrating structures. A crucial component of this method is the acoustic  $\mathbf{R}$  matrix, which quantifies the real part of the interaction between a vibrating surface and the acoustic pressure produced at the surface. While established forms of the  $\mathbf{R}$  matrix exist for simpler geometries like flat plates, cylindrical shells, and simply curved plates, no specific matrix has been standardized for arbitrarily curved panels.

This chapter revisits the numerical modeling process discussed in Ch. 4 and explores how existing  $\mathbf{R}$  matrices for simpler geometries can approximate the sound radiation from arbitrarily curved panels. Furthermore, it delves into the concept of ARMs, their similarities across different geometries, and how these similarities justify the use of  $\text{sinc}(kd_{ij})$  functions from baffled flat plates to approximate the radiation for more complex structures.

## 7.2 Numerical Model Process

Bates [1] designed a numerical modeling process to test the applicability of the flat plate, cylinder, and simply curved plate  $\mathbf{R}$  matrices for approximating the sound power radiated by arbitrarily curved panels. The process began by creating Boundary Element Method (BEM) models for different arbitrarily curved panels, including S-curved and M-curved panels, for use in experimental measurements. These models allowed for the calculation of surface velocities and corresponding sound power, using the exact  $\mathbf{R}$  matrix that can be obtained from the BEM solution.

To compare these results with approximations made using simpler  $\mathbf{R}$  matrices, Bates applied the flat plate, cylindrical, and simply curved plate  $\mathbf{R}$  matrices to the same panels, which revealed

that these simpler  $\mathbf{R}$  matrices could indeed approximate the sound radiation from arbitrarily curved panels, particularly at higher frequencies (above 400 Hz).

Bates discussed possible approaches for reducing low frequency discrepancies. The approximation at low frequencies could have been improved if the arbitrarily curved panels had been excited using a shaker rather than a small piezoelectric transducer. Shakers are more effective at exciting low frequencies, which would have raised the sound pressure level produced by the structure above the noise floor of the reverberation chamber, resulting in more accurate measurements. Furthermore, if the measurements had been conducted in an anechoic chamber following the ISO 3745 standard, measurement errors below 400 Hz could have been minimized, providing a more reliable comparison with the VBSP measurements.

### **7.3 Acoustic Radiation Modes**

In contrast to Bates' numerical model, this work focuses on analyzing the vibration via acoustic radiation modes (ARMs). ARMs are specific patterns of surface movement on a vibrating structure that independently influence the sound it produces. Unlike vibration modes, which describe overall motion based on a structure's shape and boundary conditions, ARMs focus on how these movements translate into sound radiation. Each ARM represents a unique vibration pattern that converts motion into sound energy [2].

A continuous system, such as a plate, can exhibit an infinite number of vibrational modes, each defined by its own frequency and shape [3]. According to the superposition principle, complex vibration patterns can be represented by combining these modes. Consequently, exciting a single mode triggers several other modes to a lesser extent, complicating analysis due to their overlapping nature.

In contrast, for a single frequency, ARMs are derived through singular value decomposition (SVD) of the  $\mathbf{R}$  matrix [4]. The eigenvectors obtained from this process correspond to ARMs of the structure at that frequency, which are orthogonal and independent. The associated eigenvalues indicate the efficiencies of these radiation modes and their contributions to the overall sound field. This orthogonality ensures that ARMs do not interfere with one another, facilitating a clearer understanding of sound radiation [5]. By studying ARMs, engineers and researchers can gain insights into the noise generated by various structures, enabling more effective noise control strategies.

## 7.4 Radiation Resistance Approximation

The radiation modes of baffled flat plates, cylinders, and simply curved plates exhibit notable similarities. An example of 3D ARMs of a curved plate is shown in Fig. 7.1. A 2D projection for the ARMs of flat and simply curved plates is shown in Fig. 7.2. The primary distinction among these ARMs lies in the stretching (dilation) or compressing (contraction) of the shapes of the sixth and twelfth modes in Fig. 7.2. For example, Goates [6] illustrated that the radiation modes of cylindrical or curved plates can be viewed as dilated or contracted versions of those observed in flat plates. However, he did not explicitly connect this observation to why their  $\mathbf{R}$  matrices could approximate those of other geometries, as discussed in Ch. 4 (see Figs. 3-2 and 4-2 in his thesis).

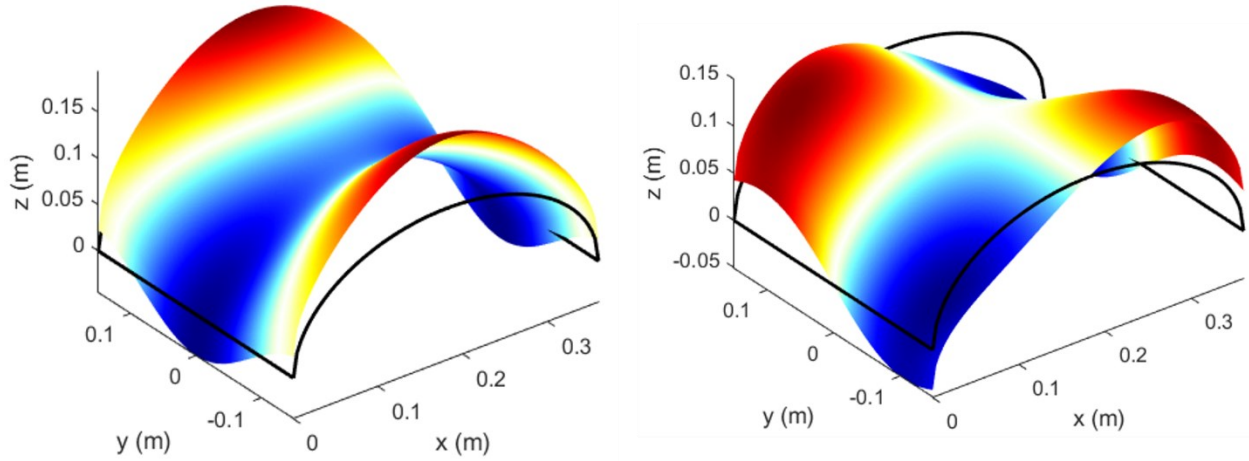


**Figure 7.1:** Two generated simply curved plate ARMs illustrated in 3D.

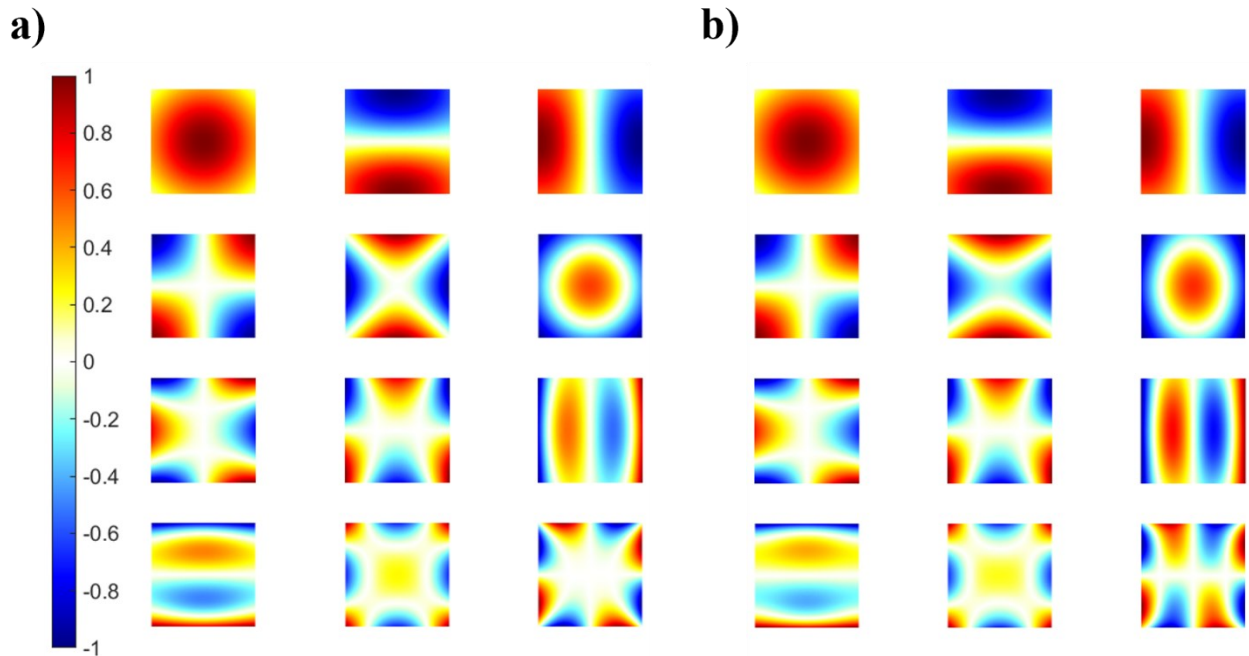


**Figure 7.2:** ARMs for a 0.5 m square plate at 480 Hz. a) Flat plate ARMs. b) Simply curved plate ARMs with a 1 cm radius of curvature, both mapped to the same square plate dimensions.

When the ARMs for a given frequency are similar for different geometries, their  $\mathbf{R}$  matrices must also be similar. The first few ARMs dominate the acoustic radiation produced by a vibrating structure at a given frequency. For example, the first few arms of the flat plate in Fig. 7.2 look

similar to those for the curved plate. Thus, even though higher-order ARMs for a curved plate do not appear exactly related to those of a flat plate, the focus should remain on the primary ARMs.

The observed contraction and dilation of the ARMs for the flat plate and cylinder/curved plate suggest a scaling factor difference between the  $\mathbf{R}$  matrices. This observation likely explains the effectiveness of sinc functions in approximating sound power from baffled flat plates and arbitrarily curved structures, as discussed in Ch. 4.

The sinc function, defined as

$$\text{sinc}(kd_{ij}) = \frac{\sin(kd_{ij})}{kd_{ij}}, \quad (7.1)$$

is important in understanding the mutual interaction between the pressure produced by any two elements on the surface of a vibrating structure. This function represents the Fourier transformation of a rectangular window and illustrates how the distance between elements  $i$  and  $j$ ,  $d_{ij}$ , influences the mutual coupling. The frequency also influences the sound pressure generated by another element as represented by the wavenumber  $k$ .

Given the similarity of the ARMs for flat plates, cylinders, and curved plates, the entries of the  $\mathbf{R}$  matrix can be effectively approximated by adjusting the  $\text{sinc}(kd_{ij})$  functions according to the unique distance values between surface elements. This approach was validated through successful applications of the  $\mathbf{R}$  matrices from flat plates, cylinders, and simply curved plates to arbitrarily curved panels in both numerical models and experimental measurements in Ch. 4. To support the work in Ch. 4, this chapter explains how the observed similarity between the ARMs for different geometries are used to identify a generalized  $\mathbf{R}$  matrix.

The  $\mathbf{R}$  matrix of a structure is influenced significantly by whether it is baffled or unbaffled, as well as by the relationship between the wavelength and the characteristic dimensions of the

structure. For un baffled structures, different expressions for the  $\mathbf{R}$  matrix apply depending on the relative sizes of the wavelength and the structure.

For a thin un baffled flat plate (refer to Ch. 5), when the wavelength is much larger than the characteristic dimension of the structure ( $kd \ll 1$ ), the  $\mathbf{R}$  matrix is given by:

$$\hat{\mathbf{R}}_{\text{unbaffled}}(\omega) \approx 2 * \frac{\omega^2 \rho_0 A_e^2}{4\pi c} [1 - \text{sinc}(kd_{ij})]. \quad (7.2)$$

In this equation,  $d_{ij}$  considers only the shortest distances between elements on one side of the plate. The factor of 2 is included to represent contributions from both the front and back sides of the flat plate, as the distances are considered separately for each side. These are the same for the flat plate (Eqn. 5.10).

In scenarios where the wavelengths are comparable to the characteristic dimensions of the structure ( $kd \approx 1$ ) or smaller than the structure ( $kd \gg 1$ ), the expression changes to:

$$\mathbf{R}_{\text{unbaffled}}(\omega) \approx \frac{\omega^2 \rho_0 A_e^2}{4\pi c} \begin{bmatrix} \text{sinc}(kd_{ij}) & \frac{1}{2} [1 - \text{sinc}(kd_{ij})] \\ \frac{1}{2} [1 - \text{sinc}(kd_{ij})] & \text{sinc}(kd_{ij}) \end{bmatrix}. \quad (7.3)$$

Here, the  $d_{ij}$  accounts for the shortest distances between elements on both sides of the plate. The  $\text{sinc}(kd_{ij})$  terms reflect the baffled nature of the structure for high frequencies, while the  $\frac{1}{2} [1 - \text{sinc}(kd_{ij})]$  components address the un baffled characteristics of the plate.

For wavelengths that are much smaller than the characteristic dimension ( $kd \gg 1$ ), the  $\mathbf{R}_{\text{unbaffled}}$  matrix approaches the  $\mathbf{R}_{\text{baffled}}$ :

$$\mathbf{R}_{\text{unbaffled}}(\omega) \approx \frac{\omega^2 \rho_0 A_e^2}{4\pi c} [\text{sinc}(kd_{ij})] = \mathbf{R}_{\text{baffled}}(\omega). \quad (7.4)$$

## 7.5 Conclusions

In summary, the acoustic radiation modes of flat plates, cylinders, and simply curved plates at a specific frequency reveal similarities in their radiation characteristics. This resemblance allows for the application of established forms of radiation resistance matrices to effectively estimate the sound power of structures with unknown  $\mathbf{R}$  matrices, as discussed in Ch. 4. By focusing on the shortest distances between elements, these similarities can be leveraged to simplify the analysis of complex geometries in acoustic radiation. Initial  $\mathbf{R}$  matrices for both baffled and unbaffled structures have been proposed, but further validation work is needed.



## 7.6 References

- [1] T. P. Bates, I. C. Bacon, J. D. Blotter, and S. D. Sommerfeldt, “Vibration-based sound power measurements of arbitrarily curved panels,” *J. Acoust. Soc. Am.* **151**(2), 1171-1179 (2022). doi: 10.1121/10.0009581
- [2] J. Liu, Y. Liu, and J. S. Bolton, “Acoustic source reconstruction and visualization based on acoustic radiation modes,” *J. Sound Vib.* **437**, 358-372 (2018). doi: 10.1016/j.jsv.2018.08.030
- [3] R. P. Feynman, R. B. Leighton, and M. Sands. *The Feynman Lectures on Physics*, (Basic Books, New York, 2011), Vol. 1, Chapter 49.
- [4] G.V. Borgiotti, “The power radiated by a vibrating body in an acoustic fluid and its determination from boundary measurements,” *J. Acoust. Soc. Am.* **88**(4), 1884–1893 (1990). doi: 10.1121/1.400211
- [5] C. B. Goates, S. D. Sommerfeldt, and J. D. Blotter, “Frequency trends of acoustic radiation modes for cylindrical structures,” *Proc. Mtgs. Acoust.* **35**(1), 065003 (2018). doi: 10.1121/2.0001020
- [6] C. B. Goates, *Analytical Expressions for Acoustic Radiation Modes of Simple Curved Structures*, Master’s Thesis, Brigham Young University, Provo, UT, 2019.

# Unit 3

## Symmetry Enhancements for Sound Power Computation

This unit addresses methods for efficiently constructing radiation resistance ( $\mathbf{R}$ ) matrices by leveraging symmetries present in the acoustic reciprocity of Green's functions. The primary goal is to reduce the computational demand, particularly as the basis functions become more complex or as scans become denser to accommodate larger structures or higher frequencies.

Currently, the temporal demand,  $\tau$ , for constructing  $\mathbf{R}$  matrices vary depending on the geometry:

$$\tau_{\text{flat}} < \tau_{\text{curved}} < \tau_{\text{cylinder}}$$

$\tau_{\text{flat}}$  is relatively low because  $\mathbf{R}_{\text{flat}}$  requires a single sinc function computation.  $\tau_{\text{curved}}$  is longer, requiring up to ten terms (or less) due to the asymptotic expansion discussed in Ch. 3 for  $\mathbf{R}_{\text{curved}}$ .  $\tau_{\text{cylinder}}$  is significantly longer, as each entry of  $\mathbf{R}_{\text{cylinder}}$  requires summing an infinite series of Hankel functions.

One approach for reducing computational time is through symmetry. Since the  $\mathbf{R}$  matrix is symmetric, these symmetries can simplify matrix construction. Chapters 8 and 9 discuss different types of symmetries found in these  $\mathbf{R}$  matrices and their practical implications. These advancements have broader potential applications in other areas of acoustics that rely on the Kirchoff-Helmholtz integral theorem (KHIT).

## Chapter 8 Symmetry in Baffled $\mathbf{R}$ Matrices

### 8.1 Introduction

This chapter is based on a peer-reviewed manuscript published in the *Journal of the Acoustical Society of America Express Letters*. This research began with Trent Bates and John Ebeling's initial work, which used color-coding to highlight patterns within the square symmetric  $\mathbf{R}$  matrix from experimental data. Building on these preliminary efforts, I identified these patterns as Toeplitz symmetry. This crucial discovery simplifies the computational process by requiring only a single line of the  $\mathbf{R}$  matrix rather than the entire matrix to be computed, and then using symmetry to enhance the efficiency of sound power computations significantly, achieving excellent results.

This research marks a significant advancement in the VBSP method, particularly by enabling higher density scans of large, baffled structures and those involving higher frequencies, through the efficient processing capabilities provided by the discovered Toeplitz symmetry.

*\*\* As co-first author, I was deeply involved in drafting the manuscript. My key contribution was identifying the Toeplitz symmetry within the  $\mathbf{R}$  matrix, which was essential for simplifying the computational process. Additionally, I obtained the experimental data used in this work. After Ebeling's initial draft, I took the lead following his graduation—completing the revisions, enriching the literature review, and successfully guiding the paper to publication. \*\**

## 8.2 Required Copyright Notice

The following article appeared in the *Journal of the Acoustical Society of America Express Letters* and can be found at <https://doi.org/10.1121/10.0015355> under the title “Improved efficiency of vibration-based sound power computation through multi-layered radiation resistance matrix symmetry.” It is reproduced in its original published format here by rights granted in the JASA Transfer of Copyright document, item 3.

<https://pubs.aip.org/DocumentLibrary/files/publications/jasa/jascpyrt.pdf>


Citation:

J. C. Ebeling, I. C. Bacon, T. P. Bates, S. D. Sommerfeldt and J. D. Blotter, “Improved efficiency of vibration-based sound power computation through multi-layered radiation resistance matrix symmetry,” *JASA Express Lett.* **2**(12), 125601 (2022).

I hereby confirm that the use of this article is compliant with all publishing agreements.

DECEMBER 02 2022

## Improved efficiency of vibration-based sound power computation through multi-layered radiation resistance matrix symmetry

John C. Ebeling; Ian C. Bacon; Trent P. Bates; Scott D. Sommerfeldt ; Jonathan D. Blotter

 Check for updates

JASA Express Lett. 2, 125601 (2022)  
<https://doi.org/10.1121/10.0015355>



19 June 2024 07:30:54




 **ASA**

Advance your science and career as a member of the  
**Acoustical Society of America**

[LEARN MORE](#)

# Improved efficiency of vibration-based sound power computation through multi-layered radiation resistance matrix symmetry

John C. Ebeling,<sup>1</sup> Ian C. Bacon,<sup>2,a)</sup> Trent P. Bates,<sup>3</sup>  
 Scott D. Sommerfeldt,<sup>2</sup>  and Jonathan D. Blotter<sup>3</sup>

<sup>1</sup>Department of Mathematics, Brigham Young University, Provo, Utah 84602, USA

<sup>2</sup>Department of Physics and Astronomy, Brigham Young University, Provo, Utah 84602, USA

<sup>3</sup>Department of Mechanical Engineering, Brigham Young University, Provo, Utah 84602, USA

[jcebeling@gmail.com](mailto:jcebeling@gmail.com), [ianbacon24@gmail.com](mailto:ianbacon24@gmail.com), [tbateslefty24@gmail.com](mailto:tbateslefty24@gmail.com), [scott\\_sommerfeldt@byu.edu](mailto:scott_sommerfeldt@byu.edu), [jblotter@byu.edu](mailto:jblotter@byu.edu)

**Abstract:** Computing sound power using complex-valued surface velocities involves using a geometry-dependent acoustic radiation resistance matrix multiplied by a velocity vector to compute sound power for a given frequency range. Using a laser scan grid with constant spacing and a scalar radiator area approximation, a multi-layered Toeplitz symmetry exists in the radiation resistance matrix. An innovative approach was developed to exploit this Toeplitz symmetry. This approach preserved accuracy and resulted in a maximum of ~1300% computation time reduction for curved plate calculations and a ~9600% computation time reduction for cylindrical shell sound power calculations. © 2022 Author(s). All article content, except where otherwise noted, is licensed under a Creative Commons Attribution (CC BY) license (<http://creativecommons.org/licenses/by/4.0/>).

[Editor: Nickolas Vlahopoulos]

<https://doi.org/10.1121/10.0015355>

**Received:** 1 September 2022 **Accepted:** 11 November 2022 **Published Online:** 2 December 2022

## 1. Introduction

Sound power has become an increasingly important metric in the field of acoustics. Three main approaches exist for measuring the sound power of a source. First, pressure microphone measurements within a controlled acoustic environment can be converted to power. Second, by using an acoustic intensity probe, a surface surrounding a source can be scanned to measure the sound intensity and then converted to power. Third, vibration measurements can be used in conjunction with geometric data to calculate sound power by utilizing the acoustic radiation impedance. This paper explores how to optimize the computation for this third approach.

The radiation resistance matrix provides knowledge of how the acoustic field couples with a structure vibrating in one of its fundamental modes. It is fundamental in analyzing and understanding the structural response to noise, acoustic fatigue, sound transmission, and radiation efficiency and is responsible for the radiation of sound from noise sources.<sup>1,2</sup>

Since the early 1990s, researchers have used radiation modes to compute sound power.<sup>3-7</sup> This method involves using singular value decomposition (SVD) and functional analysis to obtain the eigenvectors, or radiation modes, and eigenvalues of the radiation resistance matrix from which the sound power can be computed. However, as more frequencies of interest are included, many more radiation modes are required to capture the full sound power, and the efficiencies gained by using SVD are curtailed. For this reason, alternative numerical methods are desirable to determine sound power while minimizing the computational expense.<sup>8</sup>

Several recent papers,<sup>9-13</sup> both computational and experimental, have verified the use of a radiation resistance matrix in conjunction with complex-valued surface velocity measurements to calculate sound power. Using the radiation resistance matrix,  $\mathbf{R}$ , and the surface velocity vector,  $\mathbf{v}_e$ , (consisting of all the measured element velocities arranged in vector form), the sound power,  $P$ , at a given frequency,  $\omega$ , is given as<sup>13,14</sup>

$$P(\omega) = \mathbf{v}_e^H(\omega)\mathbf{R}(\omega)\mathbf{v}_e(\omega). \quad (1)$$

As an example, a baffled flat plate with  $N$  elements has an  $\mathbf{R}$  matrix given as<sup>11</sup>

<sup>a)</sup>Author to whom correspondence should be addressed.

$$\mathbf{R}(\omega) = \frac{\omega^2 \rho_0 A_e^2}{4\pi c} \begin{bmatrix} 1 & \frac{\sin kd_{12}}{kd_{12}} & \dots & \frac{\sin kd_{1N}}{kd_{1N}} \\ \frac{\sin kd_{21}}{kd_{21}} & 1 & \ddots & \vdots \\ \vdots & \vdots & \ddots & \vdots \\ \frac{\sin kd_{N1}}{kd_{N1}} & \dots & \dots & 1 \end{bmatrix} \quad (2)$$

with the distance matrix,  $d_{ij}$ , given as

$$d_{ij} = \sqrt{(x_{j,1} - x_{i,1})^2 + (x_{j,2} - x_{i,2})^2} = \|\mathbf{x}_j - \mathbf{x}_i\|, \quad (3)$$

where  $x_{j,1}$  and  $x_{j,2}$  represent the  $x$  and  $y$  coordinates of the  $j$ th point on the scan grid, respectively,  $\omega$  is a given frequency,  $\rho_0$  is the fluid density surrounding the vibrating surface,  $A_e$  is the area of a single radiator [assumed constant in Eq. (2)],  $c$  is the speed of sound in the surrounding fluid, and  $k$  is the acoustic wavenumber. This radiation resistance matrix accounts for the influence of each radiator on every other radiator, which is primarily discriminated through distance. In addition to flat plates, prior research has developed the  $\mathbf{R}$  matrix to encode these acoustic radiation modes for two additional geometries, which have been tested with promising results. These geometries correspond to curved plate and cylindrical shell geometries, respectively. In each of these cases, the formulation of  $\mathbf{R}$  includes using some version of a distance matrix. Preliminary research shows that these radiation formulations may be used for some arbitrarily curved structures as well.<sup>13</sup>

At this point, it is instructive to consider the size of the matrices at play to give an idea of why the computation is considered “heavy,” which in turn will motivate the work done in this paper. For example, a  $5 \times 5$  scan grid will yield a  $25 \times 25$   $\mathbf{R}$  matrix that must be calculated for each frequency of interest. In most of the experimental work done in this paper, scans typically involved at least 20 scan points in each Euclidean direction, which created much larger  $\mathbf{R}$  matrices and, thus, severely increase the computation time for each individual frequency of interest. Furthermore, a general rule of thumb when considering the size of the scan grid is to have about six scan points per wavelength to capture the sound power at the corresponding frequency.<sup>15</sup> Therefore, denser scan grids are needed to achieve the resolution needed to examine higher frequencies, again adding to the size of the  $\mathbf{R}$  matrix. One can easily see how these calculations become computationally expensive quite quickly, especially when these computations are performed for curved plates and cylindrical shells, where the basis functions become much more complex.

## 2. Symmetry in the distance matrix

Assuming a plate modeled with  $N$  radiators, a clear symmetry in the distance matrix is seen. First, it follows trivially that

$$d_{ij} = d_{ji} \quad (4)$$

from the fact that distance is calculated using a mathematical norm, which implies the classical matrix symmetry of the distance matrix. However, additional symmetries in the matrix exist given the assumption that all points of the scan grid are equally spaced in the  $x$  direction by a factor,  $dx$ , and all points are also equally spaced in the  $y$  direction by a factor,  $dy$ , not necessarily equal to  $dx$ . Indeed, this assumption yields a distance matrix having two layers of Toeplitz<sup>16</sup> matrix symmetry. A visual description of a  $5 \times 5$  scan grid with 25 radiators is presented in Fig. 1. In this figure, the various

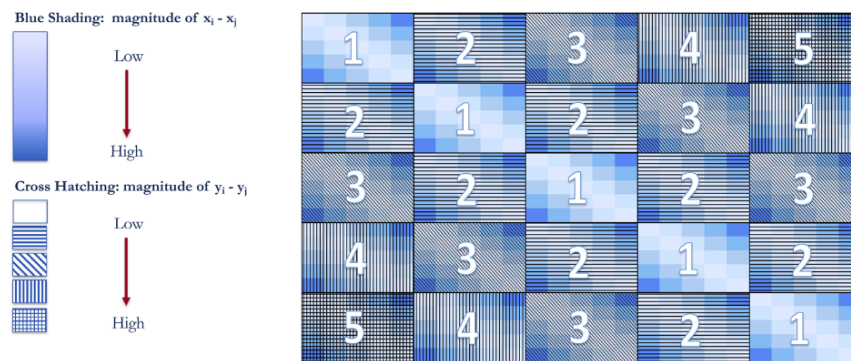


Fig. 1. The Toeplitz pattern found in a  $5 \times 5$  flat plate scan grid’s corresponding radiation resistance matrix, given the assumption of constant spacing. Every shade of blue corresponds to a specific distance between  $x$  coordinates of two radiators, and each fill pattern corresponds to a specific distance between  $y$  coordinates of two radiators. These reveal two sets of Toeplitz symmetries present in the radiation resistance matrix. Careful inspection shows that each unique color-shading combination appears on the first row of the matrix.



matrix elements are coded by color and fill pattern to easily visualize elements in the matrix that have the same value, thereby making the double-layered Toeplitz symmetry more identifiable.

The large numbers shown in Fig. 1 showcase a Toeplitz symmetry made of submatrices. However, within each large-numbered submatrix, another Toeplitz symmetry appears. Thus, the distance matrix and, by relation, the radiation resistance matrix both exhibit a double-layered Toeplitz symmetry, given the assumption of constant spacing in the  $x$  and  $y$  directions. Note that the number of scan points need not be equal in either direction. The real assumption is that the spacing of scan grid points is constant.

More importantly, due to the distance matrix's intimate connection with the radiation resistance matrix, as seen in Eq. (2), all but the  $A_e$  term share this symmetry. After observation, it also becomes clear that all the unique values of the resulting radiation resistance matrix are actually present in just the first row of that matrix, as can be seen by looking at Fig. 1. Thus, the heavy computation using complex-valued basis functions (or other necessary approximations) may be performed on the first row of the radiation resistance matrix, after which a careful expansion of the first row, using the double-layered Toeplitz symmetry as a guide, yields an equivalent radiation resistance matrix for sound power computation.

### 2.1 The importance of scan grid spacing

The aforementioned symmetries rely on the assumption of equally spaced points in the  $x$  and  $y$  directions, respectively. The sensitivity of the output of the algorithm due to the strictness of this assumption is not explored in the scope of this paper. However, the results in Sec. 3 assure that at least for most cases, even though the scan grid spacing may not have exactly constant spacing, the method still delivers an accurate reading of sound power. This assumption could be investigated in future research to establish bounds on the accuracy that can be achieved for scan grid spacing that is not completely uniform.

### 2.2 Radiator area optimization

As presented in Eq. (2), the  $A_e$  term is an integral part of the formulation of the radiation resistance matrix. That formulation is adequate for flat plate geometry; however, when curvature is introduced, the assumption of uniform radiator areas across the plate no longer holds, as projecting a two-dimensional (2D) laser scan grid with uniform spacing onto a three-dimensional (3D) surface creates differences in radiator area. To account for these differences, Bates *et al.* experimented with using an  $A_e$  matrix with the  $ij$ th element in the matrix corresponding to the product of the  $i$ th radiator's area with the  $j$ th radiator's area.<sup>17</sup> This matrix was then elementwise multiplied by the radiation resistance matrix in the sound power computation before the velocity vector multiplication to weight each of the radiator areas more accurately. The results showed an improved accuracy over using just a single  $A_e$  term average. More specifically, the improvement correlated positively with the curvature of the structure.

However, as discussed in their work, large oscillations in specific radiator areas were present in the matrix version of the  $A_e$  term, though these were mostly localized to the seam that stitched together two scans from the laser head to get a full reading of a curved surface, something necessary when the radius of curvature of the plate is sufficiently small. Even though a matrix version of the  $A_e$  term can increase the accuracy of the sound power calculation in general, for some cases, the large amplitude of noise in this matrix that can result from variations that occur along scanning seams can lead to inaccuracies.

As a result, a new approach was formulated to mitigate the problems from the seams: first, approximating the plate geometry with a perfectly spaced and seam-free scan grid and then taking the average of the matrix version of the  $A_e$  term for this new smooth geometry and using this in the sound power calculation. Note that the matrix version of the  $A_e$  term was calculated using the same method that Bates *et al.* used, taking the product of the  $i$ th radiator's area with

Table 1. A comparison of the temporal costs for computing the sound power for all frequencies between 100 and 10 000 Hz with 2 Hz frequency resolution using the vibration-based sound power (VBSP) method with and without using the Toeplitz symmetry. Note that the complexity of the basis function positively correlates with the speed up ratio, with the Hankel function computation gaining the most efficiency.

Shape	Radius of curvature (m)	Basis function	No. of elements in $\mathbf{R}$	Computation time: Control (min)	Computation time: Toeplitz (min)	Speed up ratio
Flat plate	$\infty$	Sinc	275 625	0.55	0.57	0.97
Curved plate	0.51	Fock V (Ref. 19)	3 956 121	88	8	11.01
Curved plate	0.51	Fock V (Ref. 19)	21 316 689	608	53	11.48
Curved plate	0.30	Fock V (Ref. 19)	19 263 321	569	46	12.38
Curved plate	0.16	Fock V (Ref. 19)	28 676 025	944	73	12.94
Cylinder	0.08	Hankel	3 556 996	$\sim 2000$	10	$\sim 200$





Fig. 2. An example of the 3D SLDV set up in a reverberation chamber prepared to scan a curved aluminum panel with a 0.16 m radius of curvature mounted in a steel frame and sealed to the wall acting as a baffle.

the  $j$ th radiator's area.<sup>17</sup> Results proved to retain accuracy and, in some cases, speed up computation time, due to element-wise matrix multiplication for large matrices being minimized. Experimental results are presented in Sec. 3.

As an example of a data set for which this approximation is optimal, a curved aluminum plate of length 0.3 m, width 0.4 m, and thickness of 1.59 mm was considered. The radius of curvature for the plate was 0.51 m, and the percent difference in average radiator area for the scanned plate was about 9.5%. Thus, in investigating the use of a single term average, the smooth geometric approximation average was used, rather than the average from the highly oscillatory matrix version of  $A_e$ . Results from experimental data indicate that using the single term average from the geometric approximation yields a result that better matches the sound power measurement using the ISO 3741 standard.<sup>18</sup> These results are presented in Sec. 3. Furthermore, this effectively reduced the  $A_e$  matrix to a single term, and the efficiency gains based on experimental data are also presented in Sec. 3.

### 3. Experimental verification

Exploiting this symmetry has led to meaningful efficiency gains in computation time with the calculation of sound power for curved plate and cylindrical shell structures, as shown in Table 1. The data sets were obtained using a Polytec (Baden-Württemberg, Germany) PSV-500 3D scanning laser doppler vibrometer with the experimental setup depicted in Fig. 2.

The hard Fock V coupling function has been sufficiently characterized to produce useful series representations with ten terms or fewer, which are given in an appendix of Pathak and Wang<sup>19</sup> and in McNamara *et al.*<sup>20</sup> At very large curvature and low frequency, the Fock V function behaves like a sinc function, and Eq. (2) approximates the radiation resistance matrix for these cases of curved plates.

The results are very encouraging. Notice the speed up ratio increases as the radius of curvature decreases. Translating the ratios into percentages, we obtain a  $\sim 1300\%$  maximum efficiency gain for curved plate computations and a stunning  $\sim 9600\%$  maximum efficiency gain for cylindrical geometry.

Table 2. Temporal savings using a single term  $A_e$  approximation. The computation time comes from processing curved plate data sets for all frequencies between 100 and 10 000 Hz with 2 Hz resolution and shows marginal efficiency gains by employing the  $A_e$  approximation.

Radius of curvature (m)	No. of elements in $\mathbf{R}$	Old areas (min)	New areas (min)	Speed up (%)
0.51	21 316 689	41.34	40.39	2.29
0.30	19 263 321	38.00	35.46	6.69
0.16	28 676 025	57.64	52.29	9.28
0.51	3 956 121	7.05	6.26	11.14

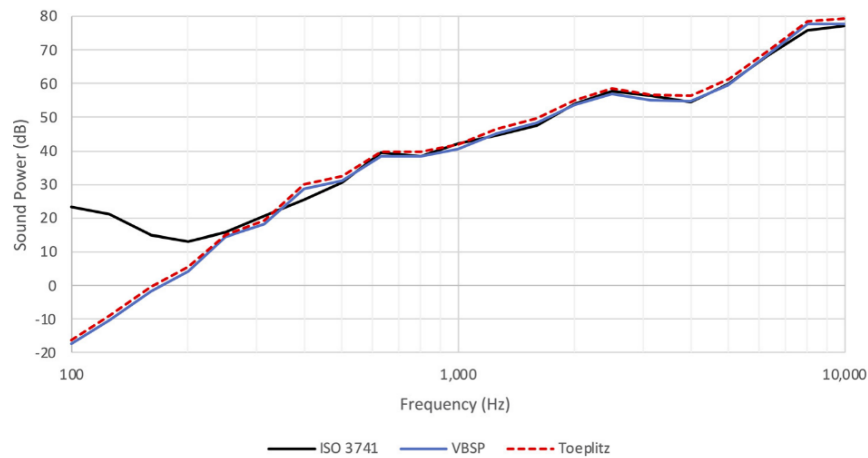


Fig. 3. The ISO 3741 standard, the original VBSP method, and the Toeplitz VBSP method are compared for a curved plate excited with a piezoelectric transducer. The results show that employing the Toeplitz method sacrifices very little in terms of the accuracy of the computation, with the Toeplitz result matching the traditional VBSP within roughly 1 dB throughout the spectrum.

Calculation is further optimized by smoothing the radiator area matrix using a normalized geometric approximation and using its average value in the calculation. This reduced the  $A_e$  term in Eq. (2) to simply a constant value for all geometries. The results are shown in Table 2. Please note that these results were calculated with a machine slightly different from the one used to calculate the previous results; hence, the emphasis on speed up ratios and percentages rather than actual calculation speeds.

Regarding accuracy, the Toeplitz method and single area approximation are no worse than the traditional VBSP method. Figures 3 and 4 are representative of our data sets.

The ISO 3741 standard does not provide precision grade results below the Schroeder frequency of the reverberation chamber used, which was about 385 Hz, leading to the large discrepancy between sound power methods. It is likely that the noise floor of the chamber is masking the true energy produced from the vibrating panels below the 400 Hz one-third octave (OTO) band. Thus, it is possible that the VBSP/Toeplitz results may be a more accurate representation of the energy produced by those frequency bands. In addition, Fig. 4 shows that the single term area average method can be employed without sacrificing the accuracy of the computation. Also, note that the computation time per frequency is approximately constant.

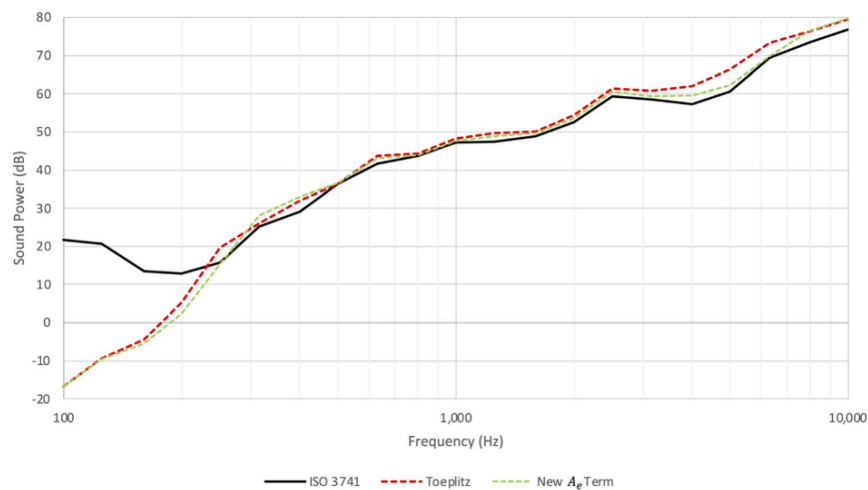


Fig. 4. The ISO 3741 standard, VBSP Toeplitz, and VBSP Toeplitz with a single term well-informed element area average (new  $A_e$  term) are compared for a specific data set. The single term average area approximation stays within one dB of the Toeplitz (and thus VBSP) method up until around 2.6 kHz, at which point it follows ISO more closely, indicating a more accurate result at higher frequency.

#### 4. Conclusion

As seen from the experimental data, allowing the assumption of constant spacing to take full advantage of the radiation resistance matrix's Toeplitz symmetry dramatically speeds up sound power computation time without significant loss of accuracy, compared to both ISO and previous VBSP methods. Approximating the surface and then using a well-informed single average area radiator term also preserves the integrity of the result and yields further speed improvement. Future areas to research include using a tensor or hypermatrix and/or multithreading to compute all frequencies simultaneously. Such improvements could continue to dramatically expand the number of applications of the VBSP method.

#### Acknowledgments

This work was funded by National Science Foundation Grant No. 1916696.

#### References and links

- <sup>1</sup>C. E. Wallace, "Radiation resistance of a rectangular panel," *J. Acoust. Soc. Am.* **51**, 946–952 (1972).
- <sup>2</sup>A. C. García, N. Dauchez, and G. Lefebvre, "Radiation efficiency of a distribution of baffled pistons with arbitrary phases," *J. Acoust. Soc. Am.* **152**, 1135–1145 (2022).
- <sup>3</sup>G. V. Borgiotti, "The power radiated by a vibrating body in an acoustic fluid and its determination from boundary measurements," *J. Acoust. Soc. Am.* **88**, 1884–1893 (1990).
- <sup>4</sup>D. M. Photiadis, "The relationship of singular value decomposition to wave-vector filtering in sound radiation problems," *J. Acoust. Soc. Am.* **88**, 1152–1159 (1990).
- <sup>5</sup>A. Sarkissian, "Acoustic radiation from finite structures," *J. Acoust. Soc. Am.* **90**, 574–578 (1991).
- <sup>6</sup>S. J. Elliot and M. E. Johnson, "Radiation modes and the active control of sound power," *J. Acoust. Soc. Am.* **94**, 2194–2204 (1993).
- <sup>7</sup>K. A. Cunefare and M. N. Currey, "On the exterior acoustic radiation modes of structures," *J. Acoust. Soc. Am.* **96**, 2302–2312 (1994).
- <sup>8</sup>J. P. Arenas, "Numerical computation of the sound radiation from a planar baffled vibrating surface," *J. Comp. Acoust.* **16**, 321–341 (2008).
- <sup>9</sup>D. Fritze, S. Marburg, and H. J. Hardtke, "Estimation of radiated sound power: A case study on common approximation methods," *Acta Acust. Acust.* **95**, 833–842 (2009).
- <sup>10</sup>P. Aslani, S. D. Sommerfeldt, and J. D. Blotter, "Analysis of external radiation from circular cylindrical shells," *J. Sound Vib.* **408**, 154–167 (2017).
- <sup>11</sup>C. B. Jones, C. B. Goates, J. D. Blotter, and S. D. Sommerfeldt, "Experimental validation of determining sound power using acoustic radiation modes and a laser vibrometer," *Appl. Acoust.* **164**, 107254 (2020).
- <sup>12</sup>C. B. Goates, C. B. Jones, S. D. Sommerfeldt, and J. D. Blotter, "Sound power of vibrating cylinders using the radiation resistance matrix and a laser vibrometer," *J. Acoust. Soc. Am.* **148**, 3553–3561 (2020).
- <sup>13</sup>T. P. Bates, I. C. Bacon, J. D. Blotter, and S. D. Sommerfeldt, "Vibration-based sound power measurements of arbitrarily curved panels," *J. Acoust. Soc. Am.* **151**, 1171–1179 (2022).
- <sup>14</sup>F. Fahy and P. Gardonio, "Sound radiation by vibrating structures," in *Sound and Structural Vibration: Radiation, Transmission and Response*, 2nd ed. (Academic, Oxford, UK, 2007), pp. 165–175.
- <sup>15</sup>S. Marburg, "Six boundary elements per wavelength: Is that enough?," *J. Comp. Acoust.* **10**, 25–51 (2002).
- <sup>16</sup>Bini, D. "Toeplitz matrices, algorithms and applications," ECRIM News Online Ed. **22** (1995), available at [www.ercim.eu/publication/Ercim\\_News/enw22/toeplitz.html](http://www.ercim.eu/publication/Ercim_News/enw22/toeplitz.html).
- <sup>17</sup>T. P. Bates, "Experimental validation of a vibration-based sound power method," master's thesis, Brigham Young University, Provo, UT, 2022.
- <sup>18</sup>ISO 3741:2010. "Acoustics—Determination of sound power levels and sound energy levels of noise sources using sound pressure—Precision methods for reverberation test rooms" (International Organization for Standardization, Geneva, 2010).
- <sup>19</sup>P. H. Pathak and N. N. Wang, "An analysis of the mutual coupling between antennas on a smooth convex surface," Report No. ESI-784583-7, Ohio State University Columbus Electroscience Lab, Columbus, OH, 1978, pp. 89–92.
- <sup>20</sup>D. A. McNamara, J. A. G. Malherbe, and C. W. Pistorius, *Introduction to the Uniform Geometrical Theory of Diffraction* (Artech House, Norwood, MA, 1990), pp. 417–433.

## Chapter 9 Symmetry in Unbaffled R Matrices and KHIT

This work presents advancements in computational analysis of acoustic radiation problems involving the Kirchhoff-Helmholtz integral theorem and Green's functions using matrix symmetry. Radiation resistance matrices for both baffled and unbaffled flat plates are used to showcase these symmetries. By identifying and utilizing symmetries such as translational (Toeplitz), reflection (bissymmetry), and rotational (centrosymmetry), the number of unique computations required is drastically reduced, enhancing efficiency. For unbaffled flat plates, four layers of symmetry are identified, reducing the computational cost to compute the full matrix. Practical applications are demonstrated with different discretization methods for circular plates, highlighting trade-offs between computational efficiency and geometric accuracy. The impact of element selection and arrangement in baffled circular plates reveals the benefits and complexities of using voussoirs versus a rectangular element mesh. An approach to extend the rectangular mesh beyond the circular plate to create a double-layered Toeplitz matrix is proposed, further simplifying computations. These symmetries enable efficient compression and subsequent reconstruction of the resistance matrix. High-performance computing and parallelization techniques are suggested to further optimize acoustic simulations.

## 9.1 Introduction

Green's functions are essential tools in acoustics for describing the response of an acoustic system to a monopole source. These functions play a crucial role in the Kirchhoff-Helmholtz integral theorem (KHIT), a powerful theorem applicable to arbitrary surfaces with extensive applications in acoustics. The KHIT can represent the total pressure field, accounting for boundary surfaces that contribute to the field as a vibrational boundary condition.

The KHIT has several applications, including acoustic radiation problems, scattering and reflection, mutual interaction between acoustic sources and enclosed spaces, and fluid loading effects on vibrating structures. KHIT is also used to determine the resonance frequencies and mode shapes of arbitrarily enclosed fields, near-field acoustical holography (NAH) for arbitrary geometries, in the Boundary Element Method (BEM) for numerical analysis of systems, and the equivalent sources method [19], [20], [24], [31].

KHIT is based on Green's function in free space:

$$G_{\omega}(\mathbf{r}|\mathbf{r}_0) = \frac{e^{jk|\mathbf{r}-\mathbf{r}_0|}}{4\pi|\mathbf{r}-\mathbf{r}_0|}, \quad (9.1)$$

where  $|\mathbf{r}-\mathbf{r}_0|$  is the distance between the source location  $\mathbf{r}_0$  and the receiver location  $\mathbf{r}$  and  $k$  is the acoustic wavenumber. The superposition principle enables the use of Green's functions to determine the sound field solutions for multiple point sources of varying amplitudes [29], thus requiring a matrix of source/receiver distances. The distance matrix is clearly an integral part of general computations using the free-space Green's function. This distance metric is also fundamental in constructing the radiation resistance matrix, which allows the computation of acoustic pressure and sound power radiated by vibrating structures.

Regardless of the characteristics of a surrounding medium, a fundamental property of Green's functions is the reciprocity relation

$$G_{\omega}(\mathbf{r}|\mathbf{r}_0) = G_{\omega}(\mathbf{r}_0|\mathbf{r}), \quad (9.2)$$

which reflects the symmetry in the distance between the source and receiver locations [29], [37], [38].

Many KHIT applications can be computationally demanding due to factors such as high dimensionality, matrix inversion, complex geometries, discretization, and coupling between elements. To reduce computation time while preserving accuracy researchers have employed high-performance computing (HPC) techniques and leveraged physical symmetry. Czuprynski [13] identified a block circulant symmetry that arises when the boundary surface is rotationally symmetric. Additional symmetry can also be found in the distance matrix due to the reciprocity requirement. For example, Ebeling *et al.* [17] revealed a layer of symmetry arising from the reciprocity relationship in the Green's functions, which is manifest in the radiation resistance matrix.

This chapter explores types of symmetries that can be found in KHIT applications due to acoustic reciprocity, with a focus on the radiation resistance matrix for various geometries. This chapter also demonstrates how these symmetrical patterns can be utilized to simplify computations and enable efficient compression and reconstruction of the matrix. In the context of KHIT, exploiting these symmetrical properties enhances our ability to predict sound fields accurately. For the example of a baffled circular plate, the impact of element selection and arrangement of the resistance matrix is also discussed, along with how the choice of elements can introduce different symmetry considerations, thereby simplifying or complicating a problem.

By understanding these symmetries, their implications, and potential pitfalls, researchers can optimize their analyses and enhance their understanding of complex systems. This chapter aims to highlight the practical benefits of these symmetries, demonstrating how they can lead to significant computational efficiencies in acoustics.

## 9.2 Review of $\mathbf{R}$ Matrices and the Role of Symmetry

The radiation resistance matrix ( $\mathbf{R}$ ) is a mathematical tool that captures the real part of the relationship between structural vibrations and the resulting sound pressures produced [2], [5]. This matrix serves as a bridge, mapping the surface normal velocities, which describe the motion of different points on a structure, to the acoustic pressures they generate. The  $\mathbf{R}$  matrices encode the specific set of orthogonal basis functions that describe the acoustic radiation produced from each of these geometries.

The  $\mathbf{R}$  matrix has practical applications in radiation problems. For instance, it is used in the vibration-based sound power (VBSP) method [6], which involves complex surface vectors,  $\mathbf{v}_e$ , containing all the measured element velocities from the vibrating structure. The frequency-dependent sound power  $\Pi(\omega)$  can be calculated using the following expression [19]

$$\Pi(\omega) = \mathbf{v}_e^H(\omega)\mathbf{R}(\omega)\mathbf{v}_e(\omega), \quad (9.3)$$

where the italicized characters denote scalars and bold-faced characters denote matrices.

For reference, a baffled flat plate discretized into  $N$  element radiators have a  $\mathbf{R}$  matrix given by:

$$\mathbf{R}(\omega) = \frac{\omega^2 \rho_0 A_e^2}{4\pi c} \begin{bmatrix} 1 & \frac{\sin kd_{12}}{kd_{12}} & \dots & \frac{\sin kd_{1N}}{kd_{1N}} \\ \frac{\sin kd_{21}}{kd_{21}} & 1 & \ddots & \vdots \\ \vdots & \ddots & \ddots & \vdots \\ \frac{\sin kd_{N1}}{kd_{N1}} & \dots & \dots & 1 \end{bmatrix}, \quad (9.4)$$

where  $\omega$  is a given frequency,  $\rho_0$  is the fluid density surrounding the vibrating surface,  $A_e$  is the area of a single radiator,  $c$  is the speed of sound in the surrounding fluid, and  $k$  is the acoustic wavenumber [7], [18], [28].

As demonstrated in Eqn. 9.4, the distance matrix  $\mathbf{d}$  is a crucial role in the formation of the  $\mathbf{R}$  matrix, which is derived from the analytical Green's function. This matrix,  $\mathbf{d}$ , connects the pressures across the surface of each geometrical shape to the radiating elements. While these elements are approximations, they become exact when limited to a point source [19]. Equal-sized elements are created around each scan point where the velocity was measured, with the scan points lying at the center of each element.

Comparison of the  $\mathbf{R}$  matrices for three geometries illustrates how symmetry originates from  $\mathbf{d}$ . First, the entries for  $\mathbf{d}$  in the baffled flat plate are computed using the Euclidean distance metric:

$$d_{ij} = \sqrt{(x_{j,1} - x_{i,1})^2 + (x_{j,2} - x_{i,2})^2} = \|\mathbf{x}_j - \mathbf{x}_i\| \quad (9.5)$$

where  $x_{i,1}$  and  $x_{i,2}$  represent the x- and y-coordinates of the center of the  $i^{\text{th}}$  element, respectively, and  $x_{j,1}$  and  $x_{j,2}$  represent the x- and y-coordinates of the center of the  $j^{\text{th}}$  element, respectively [17]. The symmetric property of the  $\mathbf{d}$  matrix leads to symmetry  $\mathbf{R}$  matrix (Eqn. 9.4).



The entries for the radiation resistance matrix for a full cylinder are given by [3], [23]:

$$R_{\text{cyl},pq} = \frac{\omega\rho_0 S_e^2}{2\pi^2 a} \sum_{m=0}^{\infty} \cos[m(\theta_p - \theta_q)] \int_0^k \frac{1}{k_r} \text{Im} \left\{ \frac{H_m^{(2)}(k_r a)}{H_m^{(2)'}(k_r a)} \right\} \cos[k_z(z_p - z_q)] dk_z, \quad (9.6)$$

where the entries for the  $\mathbf{d}$  matrix come from the angular distance  $\Delta\theta_{pq} = \theta_p - \theta_q$  and the axial distance  $\Delta z_{pq} = z_p - z_q$  as  $d_{pq} = \sqrt{(\Delta z_{pq})^2 + a^2(\Delta\theta_{pq})^2}$  between any two points along the surface of the cylinder at  $r = a$ .

The entries for the  $\mathbf{R}$  matrix for a partial cylinder or simply curved plate similarly depend on the path between points along the surface. The distance traversed across the curved surface is  $\eta_{pq} = \sqrt{(\Delta z_{pq})^2 + a^2(\Delta\theta_{pq})^2}$  and the angle between the direction of propagation and the cylinder axis is  $\psi = \tan^{-1} \left( \frac{\Delta z_{pq}}{a\phi} \right)$  [5]. For the partial cylinder or simply curved plate, where  $a$  is the plate's radius. The effects of the curved surface geometry and the propagation direction on the pressure are encapsulated in the hard Fock coupling function  $V(\xi)$ , where the real argument  $\xi_{pq} = \eta_{pq} [k \cos^4 \psi / (2a^2)]^{1/3}$ . More information on the hard Fock coupling function can be found in Sec. 3.12. The path also impacts the phase delay and amplitude decay as  $\frac{e^{-jk\eta_{pq}}}{\eta_{pq}}$  due to the distance  $\eta_{pq}$  traversed across the curved surface. The entries of the resistance matrix for a curved plate are given by

$$R_{pq} = -\frac{\omega\rho_0 S_e^2}{4\pi} \text{Im} \left\{ V(\xi_{pq}) \frac{e^{-jk\eta_{pq}}}{\eta_{pq}} \right\}. \quad (9.7)$$

Once a  $\mathbf{d}$  matrix is chosen and the form of  $\mathbf{R}$  is established for the chosen geometry, the high computational costs of estimating the  $\mathbf{R}$  matrix depend on the selected grid. Firstly, the  $\mathbf{R}$  matrix must be computed for every frequency of interest. The number of elements increases the size of the  $\mathbf{d}$  matrix and, therefore, the  $\mathbf{R}$  matrix. For example, a  $n \times n$  grid of elements would yield a

$n^2 \times n^2$   $\mathbf{d}$  matrix to account for the effect of each element radiator on every other element radiator. When time is a constraint, the element grid size is a limit not only for the VBSP method but also for any KHIT application.

The number of elements varies according to the size and shape of the structure along with the frequency of interest, the acceptable tolerance or uncertainty level, and the appropriate order for interpolating polynomials or elements. Marburg's study [32] highlights two key factors in determining the right number of elements per wavelength: setting an acceptable tolerance or uncertainty level and choosing the appropriate order for interpolating polynomials or elements. After careful consideration, it was found that six elements per wavelength worked well for this research, especially for achieving Precision (Grade 1) sound power measurements from a flat plate using linear elements [5], [8], [17]. Because the requirement is in terms of elements per wavelength, higher frequencies require a denser grid for accurate estimation, which increases both the size of the  $\mathbf{d}$  matrix and computation time.

One approach to improve computational efficiency is to exploit symmetry of the system. As a fundamental characteristic of many objects [44], symmetry serves as a pre-attentive feature [4]. For example, symmetry guides visual attention as a person focuses on and identifies the fundamental components that cannot be decomposed into simpler features [43]. Symmetry enhances the recognition and reconstruction of shapes and objects. By choosing symmetry as the feature of interest for vibrating structures, radiation resistance matrices,  $\mathbf{R}$ , may be constructed more efficiently. This approach allows  $\mathbf{R}$  to be represented with fewer entries, effectively reducing its dimensionality and, thus, reducing its computation time [44].

In the next sections, three specific types of symmetries are discussed—bissymmetry, centrosymmetry, and Toeplitz symmetry—that are often encountered in physical systems and have

significant implications for simplifying mathematical analysis and computational modeling. These symmetries can simplify KHIT applications involving Green's functions and acoustic reciprocity.

### 9.3 Reflection Symmetry and Bisymmetric Matrices

Bisymmetry refers to the presence of two planes or axes of symmetry within a structure. Bisymmetry means that the object or system remains invariant under reflection across two orthogonal planes or rotation about two perpendicular axes. Bisymmetric matrices are very useful in engineering and statistics [9] and numerical analysis [33], and others. These matrices can be particularly relevant when analyzing the physical symmetry of a vibrating structure or the vibrational patterns and sound radiation of certain structures [13].

A classic example of bisymmetry is the rectangular flat plate, which exhibits symmetry about both its horizontal and vertical centerlines. When such a plate vibrates, its motion and the resulting sound radiation patterns are influenced by this dual symmetry. Each half of the plate mirrors the other across the central axes, leading to predictable and repeatable patterns of acoustic radiation.

The presence of bisymmetry simplifies the mathematical analysis and computational modeling of these structures. In a bisymmetric structure, the properties and behavior of one quadrant can be used to infer the properties and behavior of the other three quadrants. This symmetry significantly reduces the computational effort required to analyze the entire system. For instance, in the computation of the  $\mathbf{d}$  matrix, recognizing bisymmetry allows for the reduction in the number of unique computations needed. Instead of calculating the entire matrix from scratch, only the elements in one quadrant need to be determined, and the remaining elements can be derived by applying the symmetry transformations.

By leveraging these symmetries, the computational burden is greatly reduced, making it feasible to conduct high-fidelity acoustic analyses with fewer resources. To explicitly state the condition for bisymmetry, consider a square matrix  $\mathbf{B}$  of order  $n$ .  $\mathbf{B}$  is bisymmetric if the entries  $B_{ij}$  satisfy the condition:

$$B_{ij} = B_{ji} \text{ and } B_{ij} = B_{n+1-j, n+1-i} \forall i, j. \quad (9.8)$$

Thus,  $\mathbf{B}$  must be symmetric with respect to both its main diagonal and its anti-diagonal [41].

While bisymmetry specifically pertains to two planes of symmetry, other forms of symmetry also contribute to computational efficiencies in different geometries:

- A rectangular plate typically requires 1/4 of the elements on one side to compute the distances in the distance matrix.
- A square plate, due to its equal major and minor axes, may require only 1/8 of the elements for the same purpose.
- A circular plate necessitates only a single radius of elements to obtain the unique entries of the distance matrix due to its radial symmetry.

These reductions in computation, although not strictly due to bisymmetry, reflect the broader advantages of symmetrical properties in various structures, as illustrated in Fig. 9.1. Symmetry not only simplifies the analysis but also allows for significant computational savings, enabling more complex and realistic simulations to be performed.

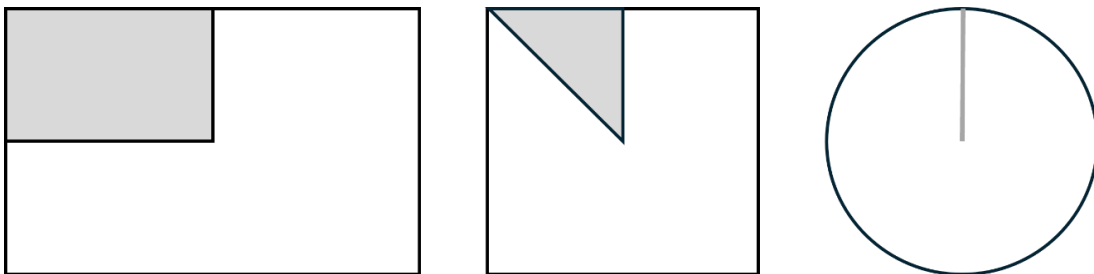


**Figure 9.1:** An illustration depicting the unique portion of a rectangle, square, and circle.

## 9.4 Rotational Symmetry and Centrosymmetric Matrices

The reflection symmetry in the previous section was only considering the physical structure. When considering the acoustic signature from vibrating flat plates, the radiation may appear baffled or unbaffled depending on frequency of interest. For the case of unbaffled radiation, the flat plate now becomes a two-sided radiation problem making its  $\mathbf{d}$  matrix more complex. The unbaffled flat plate has an additional symmetry within the distance matrix that helps reduce computation time.

This section investigates the mutual influence between the front and back sides of both square and rectangular plates. Regardless of the plate geometry, the  $\mathbf{d}$  matrix is a square symmetric matrix. This symmetry arises from considering all possible combinations between elements across the surface. The  $\mathbf{d}$  matrix now accounts for paths around all four sides of the unbaffled flat plate, selecting the shortest path between any two points as the most influential within the  $\mathbf{d}_{\text{FB}}$  and  $\mathbf{d}_{\text{BF}}$  matrices. Here, the subscripts “FB” and “BF” denote the front-on-back and back-on-front cases, respectively.

Rotational symmetry of the unbaffled plate appears as centrosymmetry in the  $\mathbf{R}$  matrix. Centrosymmetry or “inversion” symmetry [36], means the matrix remains unchanged when inverted through a central point, as illustrated in Fig. 9.2. Equation 9.9 provides examples of centrosymmetric matrices with both even and odd numbers of entries [42]:

$$\begin{bmatrix} a & b \\ b & a \end{bmatrix} \quad \text{and} \quad \begin{bmatrix} a & b & c \\ d & e & d \\ c & b & a \end{bmatrix}. \quad (9.9)$$

To explicitly state the condition that checks if a matrix is centrosymmetric, consider a square matrix  $\mathbf{C}$  of order  $n$ .  $\mathbf{C}$  is centrosymmetric if the entries  $C_{ij}$  satisfy the condition:

$$C_{ij} = C_{n-i+1, n-j+1} \quad \forall 1 \leq i, j \leq n. \quad (9.10)$$

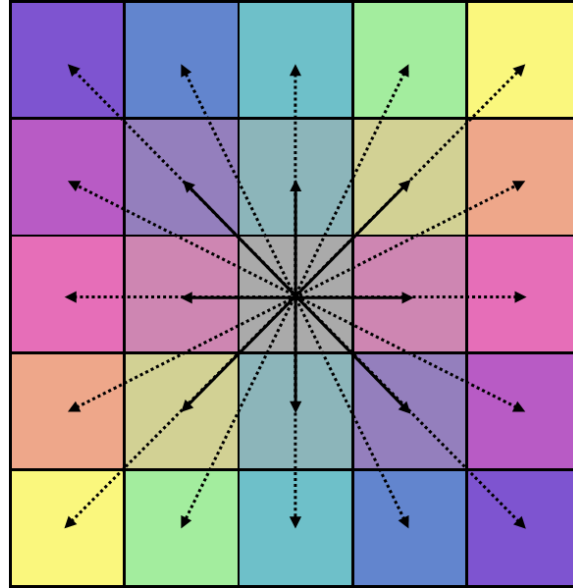


**Figure 9.2:** An illustration depicting the centrosymmetry or inversion symmetry about the central element. (Author generated; image inspired by Quartl, CC BY-SA 3.0 <<https://creativecommons.org/licenses/by-sa/3.0>>, via Wikimedia Commons)

For the un baffled plate  $\mathbf{R}$  matrix, there are two layers of rotational symmetry in the  $\mathbf{d}$  matrix. This multi-layer centrosymmetry within the  $\mathbf{d}_{\mathbf{FB}}$  and  $\mathbf{d}_{\mathbf{BF}}$  matrices are illustrated in Fig. 9.3. The first layer of symmetry within each block of the  $\mathbf{d}$  matrix reveals the rotational symmetry around the center of oscillation. The center of oscillation is either the vertical or horizontal centerline of the flat plate, depending on the way the user indexes the discretized elements. The second layer of symmetry within the entire  $\mathbf{d}$  matrix highlights the rotational symmetry of the elements around the center of the plate.

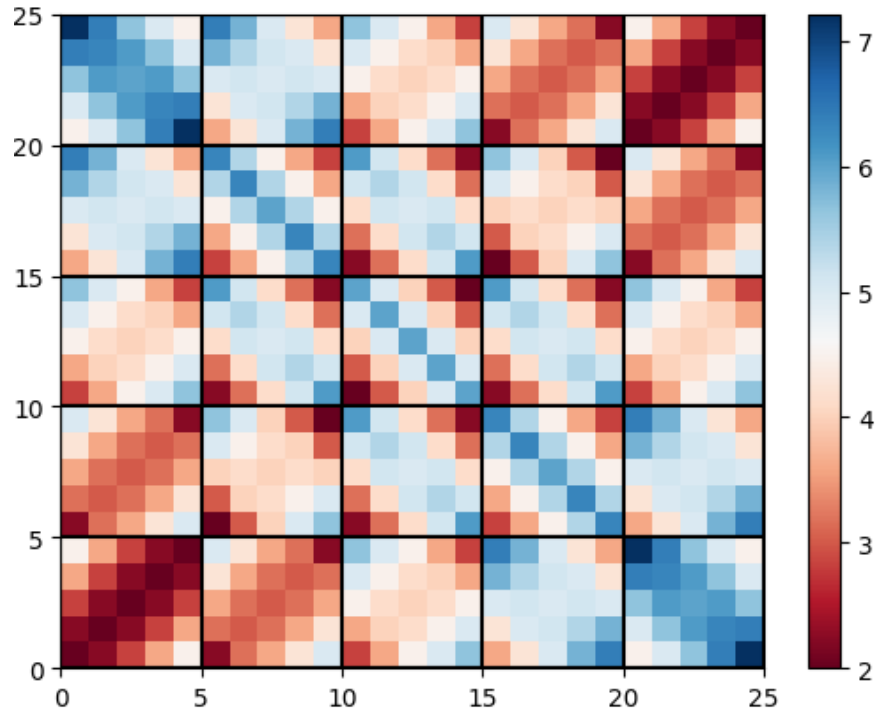


**Figure 9.3:** A double-layered centrosymmetric pattern is observed in the 25 x 25  $\mathbf{d}_{\text{FB}}$  and  $\mathbf{d}_{\text{BF}}$  matrices for a square flat plate, assuming constant grid spacing. The first layer of symmetry within the blocks indicates symmetry about the vertical centerline of the flat plate. The second layer of symmetry within the entire matrix shows inversion symmetry around the central element of the plate. The symmetries are evident when any element or block in the matrix is visually rotated by  $180^\circ$  around the central element or block, resulting in identical configurations.

Centrosymmetry is characteristic of systems with rotational invariance, where structures maintain symmetry about their equilibrium positions (e.g., beams, plates, and shells). This symmetry is observed in various fields such as linear least-squares problems [11], time series analysis [40], quantum mechanics [25], optics [45], and Markov processes [14]. In addition to this work on acoustic radiation resistance matrices, other acoustic examples include underwater acoustic arrays [35] and power transfer matrices [19].

When the un baffled flat plate vibrates, it displaces from its equilibrium position and oscillates around this central position. Since the structure exhibits symmetry about the center of the plate and the center of oscillation, the matrix describing its motion possesses centrosymmetry. This symmetry arises from the structure's balanced geometry, ensuring that the matrix remains unchanged when its elements are mirrored across the equilibrium point. Therefore, the distance relationships between the elements exhibit centrosymmetric properties, meaning the **d** matrix itself is centrosymmetric.

Centrosymmetric matrices have useful properties that are particularly important in the study of structural vibration and acoustic radiation problems. They have real eigenvalues and orthogonal eigenvectors, which can be used to analyze the motion and acoustic radiation of a structure, helping to understand its behavior under different conditions.

There are many numerical methods for solving centrosymmetric matrices, making them easier to analyze and solve in practice than a brute force method that requires computation of the entire matrix. For example, since this un baffled flat plate exhibits centrosymmetry, the number of degrees of freedom needed to describe its motion can be significantly reduced. Specifically, the number of degrees of freedom can be cut in half, as the plate has two lines of symmetry that intersect at its center. Half as many variables is needed to describe the plate's motion, simplifying the analysis and making it easier to identify key features of the plate's behavior. A set of two-dimensional coordinates can describe the motion of one quadrant, and the plate's symmetry can be used to infer the motion of the other three quadrants.

The implications of centrosymmetric matrices are substantial. For one layer of symmetry, the total number of computations needed is potentially reduced by up to 50%. For the case of double-layer symmetry, a reduction of up to 75% of the total number of computations is achieved [16].



## 9.5 Translational Symmetry and Toeplitz Matrices

Toeplitz symmetry has been applied to accelerate acoustic computations in various contexts. Jelich *et al.* [26] used block Toeplitz symmetry for efficient problem-solving with multiple right-hand sides. Ebeling *et al.* [17] explored Toeplitz symmetry within the  $\mathbf{R}$  matrix for baffled plates, finding that these structures exhibit a Toeplitz symmetry when the number of elements is consistent across rows and columns. This symmetry significantly reduced computational requirements for acoustic radiation analysis and  $\mathbf{R}$  matrix construction. However, despite efficiency gains for curved structures, baffled flat plates showed no appreciable computational savings, as the time needed for matrix reconstruction was comparable to that required for computing  $\text{sinc}(x)$  basis functions [17].

Building on Ebeling’s work [17], this section focuses on unbaffled plates where the influence of elements on the front and back sides of a square or rectangular plate must be accounted for. The distance between any two points on either side of the plate is determined by Eqn. 9.5 which implies the classical matrix symmetry of the  $\mathbf{d}$  matrix [39]. This holds true between any two x-coordinates and any two y-coordinates. As a result, there are two layers of translational invariant symmetries—one vertical and one horizontal—leading to Toeplitz symmetry in the  $\mathbf{d}_{\mathbf{FF}}$  and  $\mathbf{d}_{\mathbf{BB}}$  matrices. The subscripts “FF” and “BB” denote the front-on-front element and back-on-back element cases, respectively.

Toeplitz symmetry features matrices where each diagonal has the same value, as shown in Fig. 9.4. This symmetry arises in systems with translational invariance and is a special case that is both bisymmetric and centrosymmetric. To explicitly state the matrix equation that checks if a

matrix is Toeplitz, consider a square matrix  $\mathbf{T}$  of order  $n$ .  $\mathbf{T}$  is Toeplitz if and only if the entries  $T_{ij}$  satisfy the condition:

$$T_{ij} = T_{i+1,j+1} \quad \forall i, j. \quad (9.11)$$

Toeplitz matrices are widely used in fields such as pattern recognition, speech analysis, antenna theory, linear prediction, communication theory, linear systems, and convolutional neural networks [10], [15], [21], [34]. Their repetitive structure, where all unique information can be found in a single row or column of the matrix, allows for efficient algorithms that exploit these symmetries, significantly speeding up computations like matrix inversion and leading to substantial performance improvements [22].

For radiation resistance matrices, every unique value of the  $n^2 \times n^2$   $\mathbf{d}$  matrix is present on the first row of that matrix (refer to Fig. 9.4) [17]. Thus, only the first row needs to be computed and stored; the rest of the matrix can be reconstructed using the double-layered Toeplitz symmetry, reducing the number of computations from  $n^4$  to  $n^2$ . This significantly decreases the computational effort required for high-fidelity acoustic analysis of vibrating structures. Similar applications of these symmetries can be found in other KHIT applications.

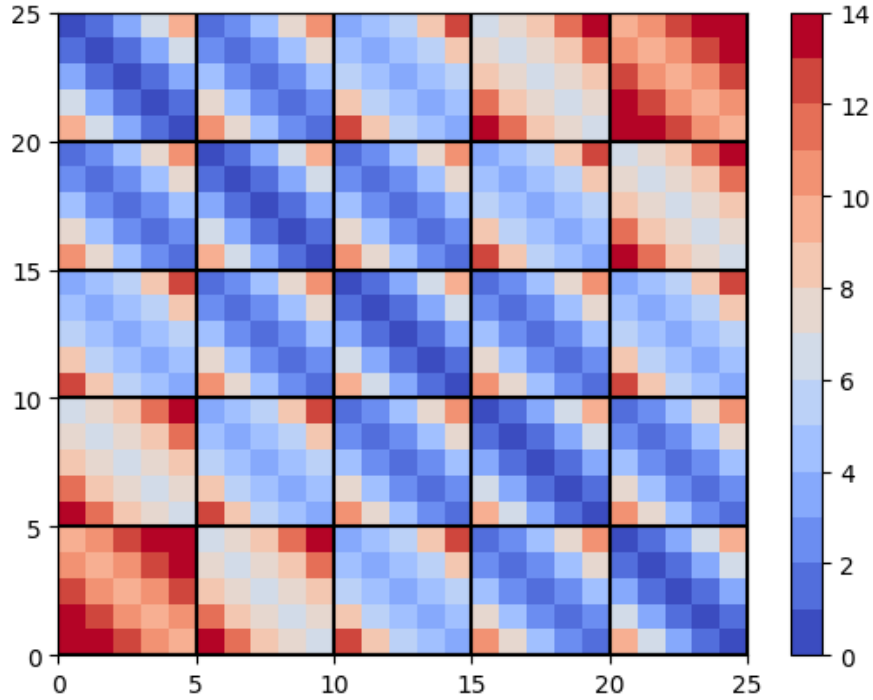


**Figure 9.4:** A double-layered Toeplitz pattern is found within the 25 x 25  $\mathbf{d}_{FF}$  and  $\mathbf{d}_{BB}$  matrices for a square flat plate, assuming constant grid spacing. The x-coordinate distances between any two element radiators exhibit Toeplitz symmetry within each block (constant values along each diagonal), while the y-coordinate distances reveal Toeplitz symmetry between blocks in the entire matrix (constant values along each block diagonal).

## 9.6 Unbaffled Flat Plate Radiation Resistance Matrix

The previous three sections have described the reflection (Sec. 9.3), rotational (Sec. 9.4), and translational (Sec. 9.5) symmetries. This section combines the effects of all symmetries to obtain the radiation resistance matrix. These symmetries are directly tied to the distances between all

elements on the plate. The complete distance matrix for an unbaffled flat plate can take the form of

$$\mathbf{d}_{\text{unbaffled}}(\omega) = \begin{bmatrix} \mathbf{d}_{\text{FF}}(\omega) & \mathbf{d}_{\text{FB}}(\omega) \\ \mathbf{d}_{\text{BF}}(\omega) & \mathbf{d}_{\text{BB}}(\omega) \end{bmatrix}. \quad (9.12)$$

Figure 9.5 illustrates an example of  $\mathbf{d}_{\text{unbaffled}}$  for an unbaffled flat plate.

The SLDV measurements yield velocity vectors which include the velocities of the front side of the plate,  $\mathbf{v}_{\text{e,FF}}$ , and the velocities of the back side of the plate,  $\mathbf{v}_{\text{e,BB}}$ . The velocity vector,  $\mathbf{v}_{\text{e,FF}}$ , is obtained by measuring the surface velocity of only the front side of the structure. The velocity vector,  $\mathbf{v}_{\text{e,BB}}$ , is obtained by taking  $\mathbf{v}_{\text{e,FF}}$  and multiplying it by -1, thus inverting the phase by 180°.

The sound power expression to be solved for every frequency using these velocity vectors. Using the matrix in Eqn. 9.12, Eqn. 9.3 becomes

$$\Pi(\omega) = \begin{bmatrix} \mathbf{v}_{\text{e,FF}}(\omega) \\ \mathbf{v}_{\text{e,BB}}(\omega) \end{bmatrix}^H \begin{bmatrix} \mathbf{R}_{\text{FF}}(\omega) & \mathbf{R}_{\text{FB}}(\omega) \\ \mathbf{R}_{\text{BF}}(\omega) & \mathbf{R}_{\text{BB}}(\omega) \end{bmatrix} \begin{bmatrix} \mathbf{v}_{\text{e,FF}}(\omega) \\ \mathbf{v}_{\text{e,BB}}(\omega) \end{bmatrix}. \quad (9.13)$$

Eqn. 9.13 holds for any unbaffled plate and can be used to understand the advantages of symmetry that come from acoustic reciprocity and the Euclidean distance. As an example, for a  $n \times n$  grid of elements, the total number of computations to construct  $\mathbf{d}_{\text{unbaffled}}$  for a single frequency is  $4n^4$ . Utilizing the Toeplitz symmetry,  $n^2$  unique computations are required for both  $\mathbf{d}_{\text{FF}}$  and  $\mathbf{d}_{\text{BB}}$ . The centrosymmetry reduces the number of unique computations for both  $\mathbf{d}_{\text{FB}}$  and  $\mathbf{d}_{\text{BF}}$  to  $\frac{1}{2}(n^2 + n\%2)$ , where the modulo operator (%) yields the remainder after division of  $n$  by 2. Altogether, these symmetries reduce the number of computations for  $\mathbf{d}_{\text{unbaffled}}$  from  $4n^4$  to  $2[n^2 + \frac{1}{2}(n^2 + n\%2)]$ , which simplifies to  $3n^2 + n\%2$ . This approach reduces quartic growth with increasing  $n$  to quadratic growth when constructing the  $\mathbf{R}$  matrix.

Finally, if the same element mesh is used for a band of frequencies, the  $\mathbf{d}$  matrix only needs to be computed once. This matrix can then be used for constructing the  $\mathbf{R}$  matrix for any of the frequencies in the bandwidth instead of redundant computing.

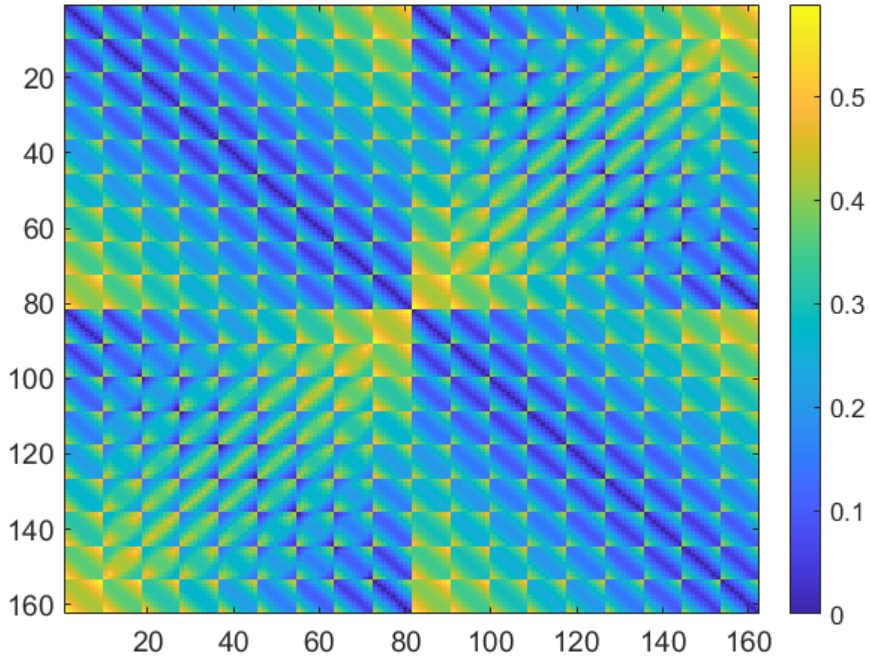


**Figure 9.5:** A 162 x 162  $\mathbf{d}_{\text{unbaffled}}$  matrix displaying the four 81 x 81  $\mathbf{d}$  matrices from Eqn. 9.12 for a 9 x 9 grid of elements used for an unbaffled flat plate. This form of the  $\mathbf{d}$  matrix was used to compute sound power using Eqn. 9.13.

To illustrate an additional benefit, consider the lumped-parameter model developed by Fahnlne and Koopman [30] to compute sound power. When an unbaffled flat plate is modeled using dipole sources, their lumped parameter formulation produces a Toeplitz radiation resistance matrix. The application of the symmetry as described in this section, would reduce the number of computations required to construct the  $\mathbf{R}$  matrix from Ref. [30].

## 9.7 Impact of Element Selection and Arrangement

The previous sections have been developed for a flat rectangular plate. For rectangular plates, the element selection can either be column-wise or row-wise and yield the same  $\mathbf{R}$  matrix. For a baffled circular plate, however, the selection and arrangement of elements in the discretization significantly impacts the form and computational complexity of the  $\mathbf{R}$ . Different discretization schemes introduce varying symmetrical considerations that can either simplify or complicate the problem. This section examines the impact of these choices, focusing on voussoirs with equal-area elements and rectangular elements in a lattice form.

When discretizing a circular plate using voussoirs or rings with equal-area elements [1], the number of elements grows in each concentric ring, leading to a unique structure in the  $\mathbf{d}$  matrix as seen in Fig. 9.6a. This approach ensures an even distribution of elements across the plate's surface, closely approximating its geometry. However, the growing number of elements in each ring alters the matrix's form as seen in Fig. 9.6b.

The overall  $\mathbf{d}$  matrix remains square and symmetric. The diagonal blocks exhibit Toeplitz symmetry due to the equidistance of elements in the same ring, where each diagonal has the same value. The size of these blocks increases with the number of elements in each ring. Off-diagonal blocks display a combination of bisymmetry, centrosymmetry, and varying degrees of block circulant symmetry, depending on the relative positions of the source and receiver elements in different rings. These single-layer symmetries within the blocks can significantly reduce the number of unique computations required to construct the  $\mathbf{d}$  matrix. However, the complexity of managing these symmetries increases as the number of rings grows.

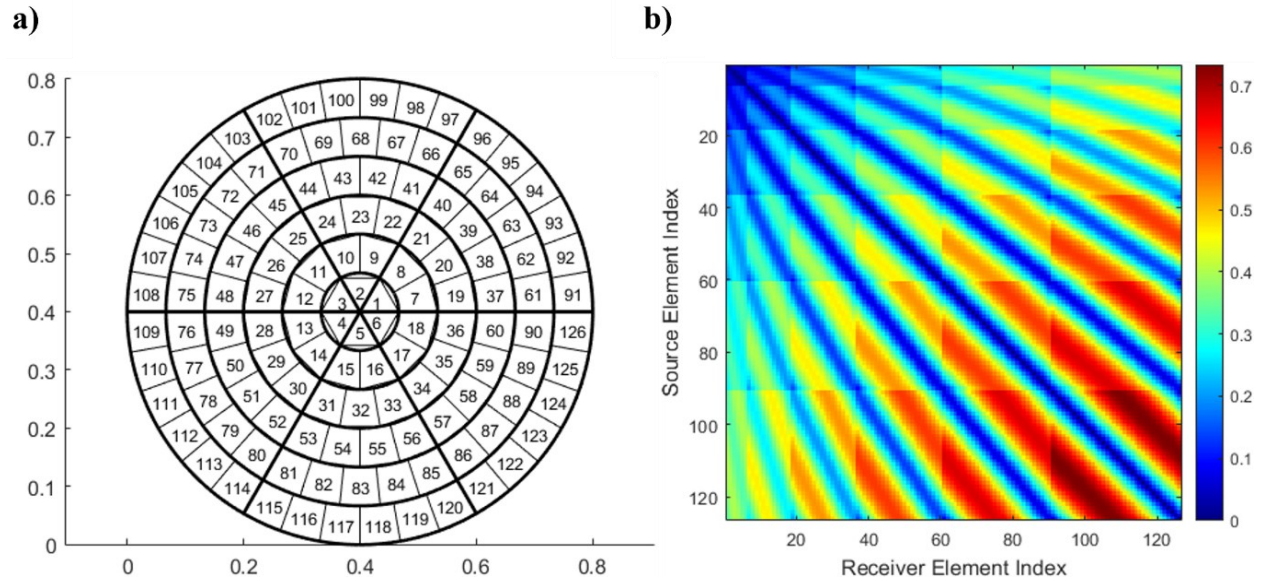


**Figure 9.6:** (a) A circular plate discretized into 126 voussoir elements. The numbers are used to identify the number of elements within each ring. (b) The  $126 \times 126$   $\mathbf{d}$  matrix for this circular plate. The diagonal blocks are Toeplitz due to the symmetry within each ring. The off-diagonal blocks have centrosymmetry, bisymmetry, and block-circulant symmetry within them.

Alternatively, discretizing the circular plate using rectangular elements [27] in a lattice form offers a different set of advantages and trade-offs. Although this method does not fill the circular area as accurately as the voussoir approach, it introduces a more manageable symmetry as seen in Fig. 9.7a. The resulting  $\mathbf{d}$  matrix shown in Fig. 9.7b exhibits double-layered centrosymmetry, reducing the number of computations by approximately 75%. This symmetry simplifies the placement of elements within the matrix. The rectangular elements can be made smaller to better fit the circular area, balancing computational savings and approximation accuracy. The reduction in unique entries allows for more elements to be included, so smaller rectangular elements can be used to better fill the circular plate.

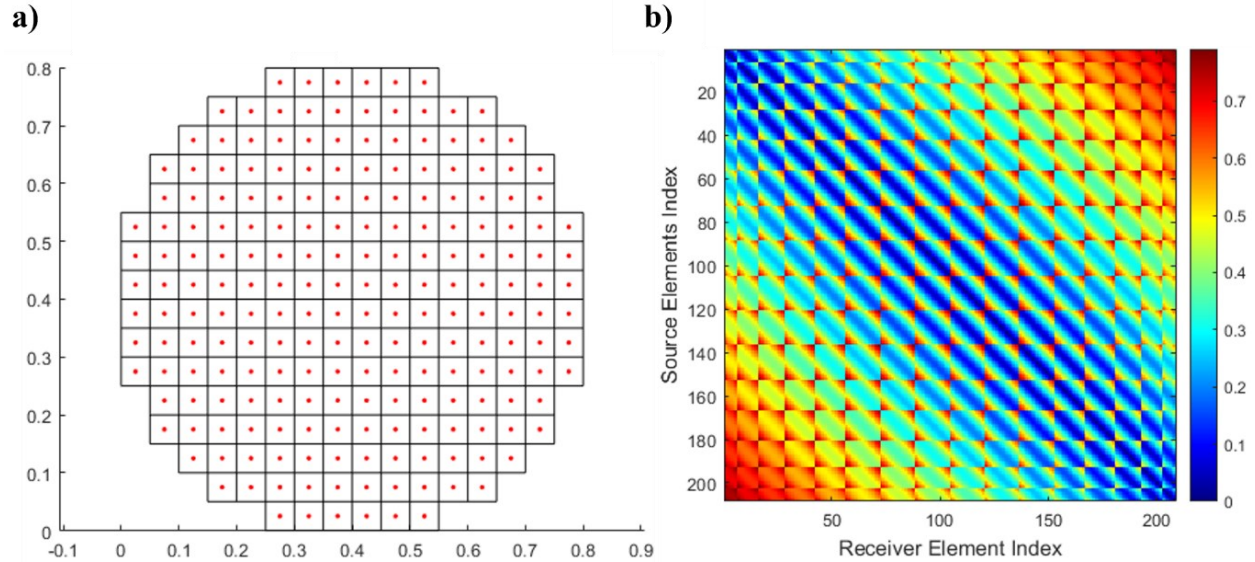


**Figure 9.7:** (a) A circular plate discretized into 210 rectangular elements. The dots represent the element centers. (b) The 210 x 210  $\mathbf{d}$  matrix for this circular plate using the rectangular discretization. The diagonal blocks are Toeplitz due to the symmetry within each row or column. This  $\mathbf{d}$  matrix now has double-layered centrosymmetry. This symmetry comes from the centerline and central point of the plate.

The choice between voussoirs and rectangular elements depends on the specific requirements of the analysis. The double-layered centrosymmetry of the rectangular element array provides substantial computational savings, making it a suitable choice for scenarios where computational resources are limited. The voussoir method offers a more accurate representation of the circular plate's geometry, which may be critical for high-fidelity simulations, but introduces more complex symmetry considerations that can complicate the computational process. Managing the symmetries within the voussoir-based  $\mathbf{d}$  matrix requires careful handling of multiple layers of symmetry, while the simpler symmetry of the rectangular element array makes it easier to implement and exploit.



Another option is to allow the rectangular grid of elements to exceed the circular plate creating a square grid around the circular plate, where the elements outside the plate have an associated area but zero velocities since they are not on the vibrating plate. This approach enables the construction of an entirely double-layered Toeplitz  $\mathbf{R}$  matrix, simplifying the computational process. This approach works well when dealing with elements on the plate, as the zero velocities for elements off the plate ensure their contributions to the power equation  $\mathbf{v}_e^H \mathbf{R} \mathbf{v}_e$  are nullified. However, special care must be taken when handling the coupling terms between elements on the plate with a velocity and elements off the plate with an area.

For the elements located off the plate, the velocities can be set to zero, effectively removing the influence of their self-resistance from the power computation. The challenge arises due to the mutual impedance with elements on the plate, which are still included in the  $\mathbf{R}$  matrix. Specifically, the off-plate elements still possess an area, leading to non-zero coupling terms when considering the pressure produced by elements on the plate.

To handle the mutual impedances, the contributions of these off-plate elements must be systematically omitted from the calculations. One effective way to achieve this is to zero out the corresponding entries in the  $\mathbf{R}$  matrix relating to these off-plate elements. This ensures that no coupling pressure from on-plate elements to off-plate elements is included in the computation, maintaining the integrity of the double-layered Toeplitz symmetry while accurately representing the physical scenario.

By carefully managing these entries, the computational benefits of the Toeplitz symmetry can be fully leveraged without compromising the accuracy of the acoustic analysis. This method allows for a more streamlined and efficient construction of the  $\mathbf{R}$  matrix, ensuring that only relevant

contributions are considered in the sound power computations. A similar approach can be taken for elliptical plates, using a square or rectangular grid with similar results.

The impact of element selection and arrangement on the baffled circular plate  $\mathbf{R}$  matrix highlights the trade-offs between computational efficiency and geometric accuracy. Voussoirs provide a closer approximation of the circular geometry but introduce complex symmetry considerations, while square elements offer significant computational savings through double-layered centrosymmetry. Depending on the acceptable degree of tolerance and the specific goals of the analysis, one method may be more advantageous than the other. By understanding these trade-offs and leveraging the appropriate symmetries, researchers can optimize the construction of the  $\mathbf{R}$  matrix to achieve accurate and efficient acoustic simulations.

## 9.8 Conclusions

Computational analysis of radiation resistance matrices for baffled and unbaffled flat plates has been significantly advanced by identifying and leveraging various symmetries. The research highlights the use of Toeplitz, bisymmetry, and centrosymmetry within these matrices to drastically reduce the number of unique computations required. The practical applications of these symmetries were demonstrated using different discretization methods for circular plates, revealing the trade-offs between computational efficiency and geometric accuracy.

In the case of an unbaffled flat plate, four layers of symmetry were identified within the  $\mathbf{R}$  matrix. These symmetries reduced the computational burden from  $4n^4$  to  $3n^2 + n\%2$  for a single frequency, showcasing a remarkable improvement in efficiency. This foundational work paves the way for more advanced techniques, such as high-performance computing and parallelization, to further optimize acoustic simulations.

The impact of element selection and arrangement in baffled circular plates was also explored. Discretizing a circular plate with voussoirs offers a precise geometric approximation but introduces complex symmetries, including Toeplitz and block circulant symmetries, within the matrix's diagonal and off-diagonal blocks. While these symmetries reduce the number of unique computations, they also increase the complexity of managing the matrix as the number of elements grows.

Alternatively, using rectangular elements in lattice form results in a double-layered centrosymmetric matrix. This method does not fill the circular area as accurately but simplifies the computational process by reducing the number of required computations by approximately 75%. The trade-off between computational efficiency and geometric accuracy becomes evident, with the choice depending on the specific requirements of the analysis.

One approach allowed the rectangular grid to exceed the circular plate, assigning zero velocities to elements outside the plate. This creates an entirely double-layered Toeplitz matrix, simplifying computations while accurately representing the physical scenario by systematically omitting off-plate elements' contributions.

In conclusion, the work underscores the importance of understanding and exploiting symmetries within general radiation problems to enhance computational efficiency. These symmetries can be found in any KHIT application. By carefully selecting element arrangements and leveraging appropriate symmetries, researchers can achieve accurate and efficient acoustic simulations. Future research will involve temporal comparison tests using experimental data to quantify efficiency gains, and the exploration of advanced computing techniques to further expand the applicability of these findings in real-time scenarios.

## 9.9 Acknowledgments

The authors gratefully acknowledge John Fahline for providing support with his power.f script Ref. [30] to validate the symmetries present in the un baffled flat plate, and Emily Cook-Bacon for using hexadecimal color codes to identify similar elements within the numerical  $\mathbf{R}$  matrix so that the centrosymmetry could be found as seen in Fig. 9.3. This work was partially funded by the National Science Foundation, grant number 1916696.

## 9.10 References

- [1] J. P. Arenas, “On the Sound Radiation from a Circular Hatchway,” *International Journal of Occupational Safety and Ergonomics (JOSE)* **15**(4), 401-407, (2009). doi: 10.1080/10803548.2009.11076819
- [2] J. P. Arenas and M. J. Crocker, “Sound radiation efficiency of a baffled rectangular plate excited by harmonic point forces using its surface resistance matrix,” *Int. J. Acoust. Vib.* **7**(4), 217-229, (2002). doi: 10.20855/ijav.2002.7.4120
- [3] P. Aslani, S. D. Sommerfeldt, and J. D. Blotter, “Analysis of external radiation from circular cylindrical shells,” *J. Sound Vib.* **408**, 154-167, (2017). doi: 10.1016/j.jsv.2017.07.021
- [4] F. Attneave, “Symmetry, information, and memory for patterns,” *Am. J. Psychol.* **68**(2), 209-222, (1955). doi: 10.2307/1418892
- [5] I. C. Bacon, T. P. Bates, C. B. Goates, M. R. Shepherd, J. D. Blotter, and S. D. Sommerfeldt, “Radiation resistance matrix for baffled simply curved plates for sound power applications,” *Noise Control Eng. J.* **72**(2), 65-78, (2024). doi: 10.3397/1/37728
- [6] I. C. Bacon, S. D. Sommerfeldt, and J. D. Blotter, “Developing an indirect vibration-based sound power method to determine the sound power radiated from acoustic sources,” *Proc. Mtgs. Acoust.* **50**(1), 065003, (2022). doi: 10.1121/2.0001732
- [7] M. R. Bai and M. Tsao, “Estimation of sound power of baffled planar sources using radiation matrices,” *J. Acoust. Soc. Am.* **112**, 876–883, (2002). doi: 10.1121/1.1499133
- [8] T. P. Bates, I. C. Bacon, J. D. Blotter, and S. D. Sommerfeldt, “Vibration-based sound power measurements of arbitrarily curved panels,” *J. Acoust. Soc. Am.* **151**, 1171-1179, (2022). doi: 10.1121/10.0009581

- [9] A. Cantoni and P. Butler, "Eigenvalues and eigenvectors of symmetric centrosymmetric matrices," *Linear Algebra Appl.* **13**, 275–288, (1976). doi: 10.1016/0024-3795(76)90101-4
- [10] A. Cantoni and P. Butler, "Properties of the eigenvectors of persymmetric matrices with applications to communication theory," *IEEE Trans. Commun.* **24**(8), 804-809, (1976), doi: 10.1109/TCOM.1976.1093391.
- [11] H. C. Chen, "Generalized reflexive matrices: Special properties and applications," *SIAM. J. Matrix. Anal. Appl.* **19**(1), 140-153, (1998). doi: 10.1137/S0895479895288759
- [12] K. A. Cunefare and M. N. Currey, "On the exterior acoustic radiation modes of structures," *J. Acoust. Soc. Am.* **96**, 2302-2312, (1994). doi: 10.1121/1.410102
- [13] K. D. Czuprynski, J. B. Fahnlne, and S. M. Shontz, "Parallel boundary element solutions of block circulant linear systems for acoustic radiation problems with rotationally symmetric boundary surfaces," *Proc. of the Internoise 2012/ASME NCAD Meeting*, (2012). doi: 10.1115/NCAD2012-0445
- [14] E. B. Dagum, L. Guidotti, and A. Luati, *Some Statistical Applications of Centrosymmetric Matrices*, (Springer, Berlin, Heidelberg, 2005), pp. 97-104, doi: 10.1007/3-540-27373-5\_12.
- [15] L. Datta and S. D. Morgera, "On the reducibility of generalized centrosymmetric matrices – Applications in engineering problems," *Int. J. Circuits Syst.* **8**, 71–96, (1989). doi: 10.1007/BF01598746
- [16] L. Datta and S. D. Morgera, "Some results on matrix symmetries and a pattern recognition application," *IEEE Trans. Acoust., Speech, Signal Process.* **34**(4), 992-994, (1986). doi: 10.1109/TASSP.1986.1164890

- [17] J. C. Ebeling, I. C. Bacon, T. P. Bates, S. D. Sommerfeldt, and J. D. Blotter, “Improved efficiency of vibration-based sound power computation through multi-layered radiation resistance matrix symmetry,” *JASA Express Lett.* **2**(12), 125601, (2022). doi: 10.1121/10.0015355
- [18] S. J. Elliot and M. E. Johnson, “Radiation modes and the active control of sound power,” *J. Acoust. Soc. Am.* **94**, 2194-2204, (1993). doi: 10.1121/1.407490
- [19] F. Fahy and P. Gardonio, *Sound and Structural Vibration: Radiation, Transmission and Response*, 2nd ed. (Academic Press, Oxford, UK, 2007), pp. 165-175, 408-427, 503-519.
- [20] P. J. T. Filippi, “Layer potentials and acoustic diffraction,” *J. Sound Vib.* **54**(4), 473-500, (1977). doi: 10.1016/0022-460X(77)90607-1
- [21] Fok Hing Chi Tivive and A. Bouzerdoun, “Efficient training algorithms for a class of shunting inhibitory convolutional neural networks,” *IEEE Trans. Neural Netw.* **16**(3), 541-556, (2005). doi: 10.1109/TNN.2005.845144
- [22] G. O. Glentis and N. Kalouptsidis, “Efficient algorithms for the solution of block linear systems with Toeplitz entries,” *Linear Algebra Appl. J.* **179**, 85-104, (1993). doi: 10.1016/0024-3795(93)90322-F
- [23] C. B. Goates, C. B. Jones, S. D. Sommerfeldt, and J. D. Blotter, “Sound power of vibrating cylinders using the radiation resistance matrix and a laser vibrometer,” *J. Acoust. Soc. Am.* **148**, 3553–3561, (2020). doi: 10.1121/10.0002870
- [24] W. Gordon, “Far-field approximations to the Kirchoff-Helmholtz representations of scattered fields,” *IEEE Trans. Antennas Propag.* **23**(4), 590-592, (1975). doi: 10.1109/TAP.1975.1141105

- [25] S. Han, H. W. Lee, and K. W. Kim, “Orbital Dynamics in Centrosymmetric Systems,” *Phys. Rev. Lett.* **128**(17), 176601, (2022). doi: 10.1103/PhysRevLett.128.176601
- [26] C. Jelic, M. Karimi, N. Kessissoglou, and S. Marburg, “Efficient solution of block Toeplitz systems with multiple right-hand sides from a periodic boundary element formulation,” *Eng. Anal. Bound. Elem.* **130**, 135-144, (2021). doi: 10.1016/j.enganabound.2021.05.003
- [27] W. R. Johnson, P. Aslani, S. D. Sommerfeldt, J. D. Blotter, and K. L. Gee, “Acoustic radiation mode shapes for control of plates and shells,” *Proc. Mtgs. Acoust.* **19**, 065036, (2013). doi: 10.1121/1.4799718
- [28] C. B. Jones, C. B. Goates, J. D. Blotter, and S. D. Sommerfeldt, “Experimental validation of determining sound power using acoustic radiation modes and a laser vibrometer,” *Appl. Acoust.* **164**, (2020). doi: 10.1016/j.apacoust.2020.107254
- [29] M. Junger and D. Feit, *Sound, Structures, and Their Interaction*, 2nd ed. (The MIT Press, Cambridge, MA, 1986), pp. 75-90, 313-341.
- [30] G. H. Koopmann and J. B. Fahline, *Designing quiet structures: A sound power minimization approach* (Academic Press, 1997), pp. 227-237.
- [31] S. Lee, “Review: The Use of Equivalent Source Method in Computational Acoustics,” *J. Comp. Acoust.* **25**(1), 1630001 (2017). doi: 10.1142/S0218396X16300012
- [32] S. Marburg, “Six boundary elements per wavelength: is that enough?” *J. Comput. Acoust.* **10**, 25-51, (2002). doi: 10.1142/S0218396X02001401
- [33] A. Melman, “Symmetric centrosymmetric matrix–vector multiplication,” *Linear Algebra Appl.* **320**, 193–198, (2000). doi: 10.1016/S0024-3795(00)00232-9



- [34] S. D. Morgera, “On the reducibility of finite Toeplitz matrices – Applications in speech analysis and pattern recognition,” *Signal Process.* **4**(5), 425-443, (1982). doi: 10.1016/0165-1684(82)90057-3
- [35] X. Pei, X. Ma, X. Li, and Y. Fu, “Underwater reverberation suppression method by the symmetry of signal and centrosymmetric arrays,” *Appl. Acoust.* **221**, 109986, (2024). doi: 10.1016/j.apacoust.2024.109986
- [36] K. Pelzer, N. Schwarz, and R. Harder, “Removal of spurious data in Bragg coherent diffraction imaging: an algorithm for automated data preprocessing,” *J. Appl. Cryst.* **54**, 523-532, (2021). doi: 10.1107/S1600576721000819
- [37] A. D. Pierce, *Acoustics: An Introduction to Its Physical Principles and Applications*, (Springer, Cham, Switzerland, 2019), pp. 222-229.
- [38] J. W. B. S. Rayleigh, *The Theory of Sound*, 2nd. ed. (Dover Publications, New York, 1896), pp. 143-148.
- [39] R. S. Strichartz, *The Way of Analysis*, 2nd ed. (Jones & Bartlett Learning, Oxford, UK, 2007), pp. 357.
- [40] W. F. Trench, “Numerical solution of the inverse eigenvalue problem for real symmetric Toeplitz matrices,” *SIAM, J. Sci. Comput.* **18**, 1722-1736, (1997). doi: 10.1137/S1064827595280673
- [41] Y. Wang, F. Lü, and W. Lü, “The inverse of bisymmetric matrices,” *Linear Multilinear A.* **67**(3), 479-489, (2019). doi: 10.1080/03081087.2017.1422688
- [42] J. R. Weaver, “Centrosymmetric (cross-symmetric) matrices, their basic properties, eigenvalues, and eigenvectors,” *Am. Math. Mon.* **92**(10), 711-717, (1985). doi: 10.2307/2323222

- [43] J. M. Wolfe and I. S. Utochkin, "What is a preattentive feature?" *Curr. Opin. Psychol.* **29**, 19-26, (2019). doi: 10.1016/j.copsyc.2018.11.005
- [44] H. Zabrodsky, S. Peleg and D. Avnir, "Symmetry as a continuous feature," *IEEE TPAMI* **17**(12), 1154-1166, (1995). doi: 10.1109/34.476508
- [45] H. Zhang, X. Li, H. Ma, M. Tang, H. Li, and Y. Cai, "Centrosymmetric optical vortex," *Appl. Sci.* **9**, 1429, (2019). doi: 10.3390/app9071429

# Unit 4

## Development of the Indirect Vibration-Based Sound Power (I-VBSP) Method

This unit focuses on enhancing the VBSP method to address noise sources commonly encountered in daily life, such as electric drone motors, kitchen appliances, and vehicles, where internal noise generation cannot be captured through surface velocity measurements alone. To accommodate these sources, the development of an indirect method, known as the I-VBSP method, began.

The I-VBSP method involves using a rectangular enclosure, acting as an ‘acoustic tent’ over the noise source. The enclosure features a flexible panel that links surface laser Doppler vibrometry (SLDV) measurements to the radiated sound power of the encased source, enabling the VBSP method to be applied effectively. This unit focuses on the initial stages of I-VBSP development, particularly for compact sources that fit within the enclosure and exhibit constant volume velocity, ensuring minimal interference from the enclosure itself due to their high internal impedance.

# Chapter 10 Method Development for Cube Enclosures

## 10.1 Introduction

This chapter contains a paper published in the Acoustical Society of America's *Proceedings of Meetings on Acoustics*, which introduces a new method for using vibration measurements to determine the sound power produced by an internal source accurately. The study includes the design and fabrication of an enclosure that demonstrated the ability to calibrate the effects of the enclosure within  $\pm 1$  dB for frequencies above 1 kHz and  $\pm 3$  dB below this threshold.

*\*\* In addition to writing this manuscript, I designed the enclosure and assisted with the fabrication. I was responsible for the experiments, data processing, calibration, validation, and all aspects of this work. \*\**

## 10.2 Required Copyright Notice

The following article was published in the *Proceedings of Meetings on Acoustics* and is available at <https://doi.org/10.1121/2.0001663> under the title “Determination of radiated sound power from acoustic sources using the VBSP method and a mylar boundary.” It is reproduced here in its original published format by rights granted in the JASA Transfer of Copyright document, item 3.

<https://pubs.aip.org/DocumentLibrary/files/publications/jasa/jascpyrt.pdf>

### Citation:

I. Bacon, S. D. Sommerfeldt, and J. D. Blotter, “Determination of radiated sound power from acoustic sources using the VBSP method and a mylar boundary,” *Proc. Mtgs. Acoust.* **46**(1), 065003 (2022).

I hereby confirm that the use of this article is compliant with all publishing agreements.

DECEMBER 28 2022

## Determination of radiated sound power from acoustic sources using the VBSP method and a mylar boundary **FREE**

Ian Bacon; Scott D. Sommerfeldt ; Jonathan D. Blotter

 Check for updates

*Proc. Mtgs. Acoust.* 46, 065003 (2022)  
<https://doi.org/10.1121/2.0001663>



19 June 2024 07:03:30



LEARN MORE

Advance your science and career as a member of the  
**Acoustical Society of America**



---

## 182nd Meeting of the Acoustical Society of America

Denver, Colorado

23-27 May 2022

### Structural Acoustics and Vibration: Paper 4aSAb3

---

## Determination of radiated sound power from acoustic sources using the VBSP method and a mylar boundary

**Ian Bacon and Scott D. Sommerfeldt**

*Department of Physics & Astronomy, Brigham Young University, Provo, UT, 84602;  
ianbacon24@gmail.com; scott.sommerfeldt@byu.edu*

**Jonathan D. Blotter**

*Department of Mechanical Engineering, Brigham Young University, Provo, UT, 84602; jblotter@byu.edu*

The development of an “acoustic tent” for measuring the radiated sound power from devices with complex or hidden geometries using a vibration-based sound power (VBSP) method is presented. The VBSP method is based on spatially dense velocity measurements of the vibrating structure and has previously been validated for flat plates, cylindrical-shells, simple-curved panels, and arbitrarily curved panels. However, many acoustic sources, such as electric drone motors, kitchen appliances, and vehicles have sound power contributions from components where the velocity is difficult to measure. To overcome this challenge, a rectangular box with four high impedance walls, one rigid side, and one thin mylar side was used to enclose the noise source, forming an acoustic tent around the device. The acoustic tent was able to be calibrated to within 1-3 dB of the free-field sound power measurements for several different sources. Limitations of the VBSP acoustic tent are also presented and discussed.

## INTRODUCTION

The International Standard for Organization (ISO) indicates that the sound power level is an important parameter in product design as it characterizes the airborne noise emitted from acoustic sources. It is desirable for many applications and must be determined by measurement.<sup>1</sup> Furthermore, vibration-based measurements are becoming desirable when the background noise, testing environment, and application limit the current sound power methods.<sup>2</sup>

The vibration-based sound power (VBSP) method used in this paper relies on a 3D scanning laser Doppler vibrometer (SLDV) to obtain the components of the velocity at every location on a scan grid across the surface of a vibrating structure from which the complex normal velocities can be computed. From a discrete form of the Rayleigh integral, the sound power,  $\Pi$ , can be computed for a given frequency,  $\omega$ , using a column vector of the surface normal velocities,  $\mathbf{v}_e$ , in conjunction with a radiation resistance matrix,  $\mathbf{R}$ , as:

$$\Pi(\omega) = \{\mathbf{v}_e(\omega)\}^H [\mathbf{R}(\omega)] \{\mathbf{v}_e(\omega)\} \quad (1)$$

where  $(\cdot)^H$  denotes a Hermitian transpose.<sup>3,4</sup>

This method works well for vibrating structures such as flat plates, cylindrical shells, and simple-curved panels. Recent work has shown that this VBSP method can even obtain accurate sound power levels for arbitrarily curved panels by employing a known form of the radiation resistance matrix that approximates these structures.<sup>2,4-8</sup> A previous result of a curved aluminum panel with a 0.51 m radius of curvature is shown in Fig. 1 to illustrate the accuracy of the results that have been obtained with this VBSP method.

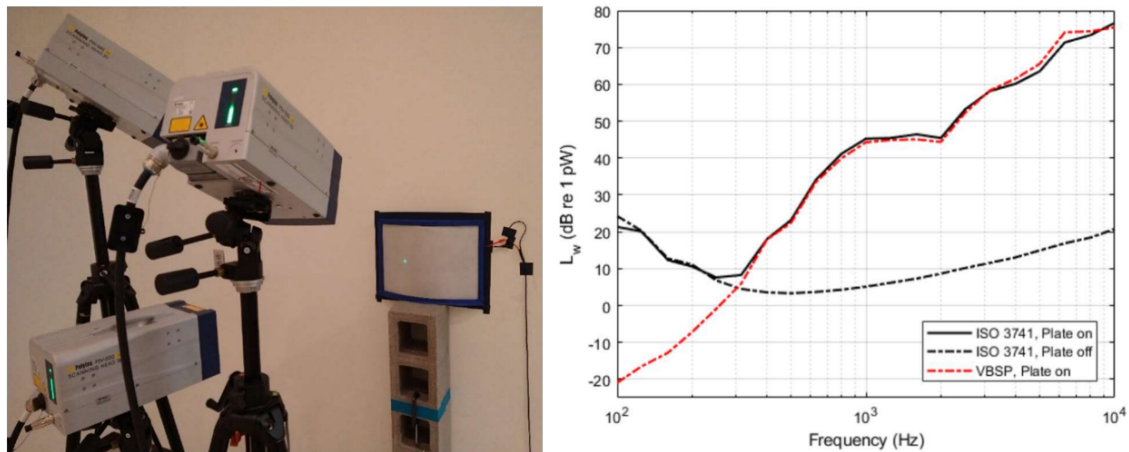


**Figure 1. a)** The 3D SLDV setup in a reverberation chamber prepared to scan a curved aluminum panel having a radius of curvature of 0.51 m mounted in a steel frame and sealed to the wall acting as a baffle. **b)** A result of this VBSP method applied to the simple-curved panel in (a) using Eq. (1). The sound power levels measured using the ISO 3741 standard (black curves) against the VBSP method (red) are compared.<sup>5,8</sup>



There are many sources of interest that radiate sound where the user cannot scan the source to obtain the sound power radiated from the vibration, so this raises the need to develop an extension of the VBSP method to determine the sound power for such sources. Examples include sources with internal fans, gears, etc. that have contributors to the sound power, but cannot be scanned properly. The purpose of this paper is to present an adapted VBSP method to accommodate these sources and lay out some of the challenges and potential solutions to the previously mentioned limitation.

## ADAPTED VBSP METHOD

This section outlines an indirect way to extend the VBSP method to account for the numerous sources that cannot be scanned properly. For this to happen, the source radiation needs to produce something that vibrates that can be scanned properly. Placing the source inside an enclosure where all sides are acoustically transparent and vibrate would be ideal. However, such materials, like mylar, are transparent only for a limited range of low frequencies. This means that a correction will be needed to obtain the true sound power of these sources. To simplify the problem, a rectangular enclosure was fabricated, as seen in Fig. 2, where four sides on the perimeter are made up of 1 1/2" thick MDF, the top face has a mylar membrane secured to the structure, and the base is open so that the rigid floor will seal off the bottom of the enclosure.

This enclosure is placed over the sources of interest, acting as an “acoustic tent.” The rigid floor and four high impedance walls direct nearly all the acoustic energy from the source to excite the mylar membrane. Its vibration behaves as a flexible membrane, which can be scanned by an SLDV. Even though the mylar is acoustically transparent for a limited low-frequency band, the enclosure significantly affects the way each source radiates. Nevertheless, the sound power radiated from the enclosure can be measured and then calibrated to match the free-field sound power.

To better understand and calibrate the effect of the enclosure, the free-field sound power was measured for an individual source in a reverberation chamber using the ISO 3741 standard.<sup>9</sup> The source was then placed at nine distinct locations on the floor inside the enclosure, from which the sound power was measured for each location using the ISO 3741 standard. This process was repeated for multiple sources to see the potential variation between sources. By averaging the nine ISO measurements for each enclosed source and comparing these to their corresponding free-field results, a calibration curve was obtained to remove the influence of the enclosure to obtain each source’s true radiated power. (See Fig. 5 for the calibration curve for several sources)

The adapted VBSP approach can be outlined as follows: first, the ISO 3741 standard is used in a reverberation chamber to obtain the sound power for multiple unique sources. Next, each source can be placed into the enclosure described above which has a mylar face that can be scanned using an SLDV. The ISO 3741 standard can be used to determine how much sound power the enclosure radiates into the larger space due to each source. Then, using the free-field ISO results, along with the enclosure ISO results, a calibration curve can be found to remove the radiation effects the enclosure has on the sources. Once this curve is established, the VBSP method can be used to obtain the sound power from the mylar face upon which the calibration can be applied to compare this method to the ISO standard. Finally, the adjusted VBSP results can be compared with the free-field ISO 3741 measurements of these sources to verify precision.

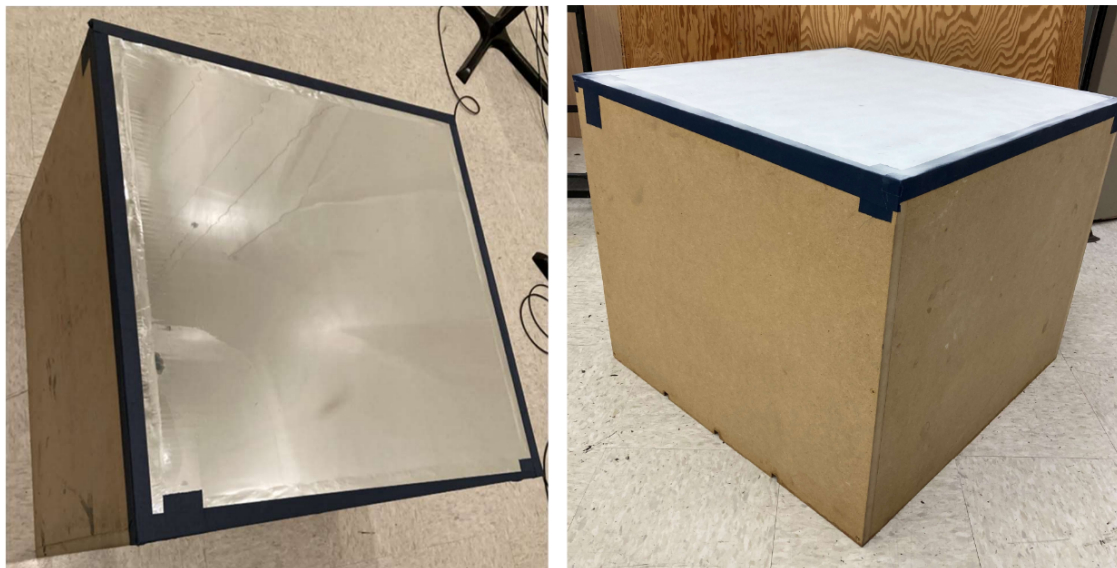


**Figure 2.** A visual of the enclosure used to simplify the problem. a) The mylar stretched across the MDF enclosure. b) A side view of the enclosure showing a developer spray used to make the mylar membrane easier to scan by the SLDV and the three ports drilled in the bottom left to feed the source cabling.

## CALIBRATION

The purpose of this section is to verify that each of the tested sources leads to the same correction and to figure out if these sources can be moved internally on the floor without significantly impacting the radiated power. Kleiner and Tichy state “The sound radiation into a room depends on the source, its properties and location, and on the properties of the room such as its size, shape, and sound absorption.”<sup>10</sup> Small enclosures have acoustic properties that are largely determined by the individual eigenfrequencies below the Schroeder frequency.<sup>11</sup> Due to the effect of the small enclosure on the radiation, it is desirable to obtain a calibration curve that could be used to hopefully remove the influence of the enclosure on the sources, including absorption, radiation impedance loading, and significant pressure differences that occur with resonances of the enclosure.

Initially, a class of sources will be used that should experience fewer effects on the way they radiate inside the enclosure. When a driving source is coupled with the acoustic waves present inside the enclosure, the radiation impedance can potentially be altered. The radiation impedance is defined as the ratio of the total force on the surface of a radiator that is needed to move the surrounding medium over the particle velocity of the radiator surface.<sup>10,12</sup> Therefore, nominally constant volume velocity sources will be considered for this method because they have a higher internal impedance and therefore the volume velocity of each source will be affected similarly. As a result, the sound power change due to the enclosure should be mostly attributable to the radiation impedance change and the absorption of the enclosure, both of which can be corrected for with an appropriate calibration curve.

Another consideration is to what extent these sources can be moved around within the enclosure without significantly altering the radiated sound power. This was done by performing an ISO 3741 measurement of each source in a reverberation chamber to obtain the free-field sound power result for every source. This was followed by placing each source within the enclosure at various locations on the floor as seen in Fig. 3a and then measuring the sound power using the ISO 3741 standard in a reverberation chamber. The result

for a blender is shown in Fig. 3b.

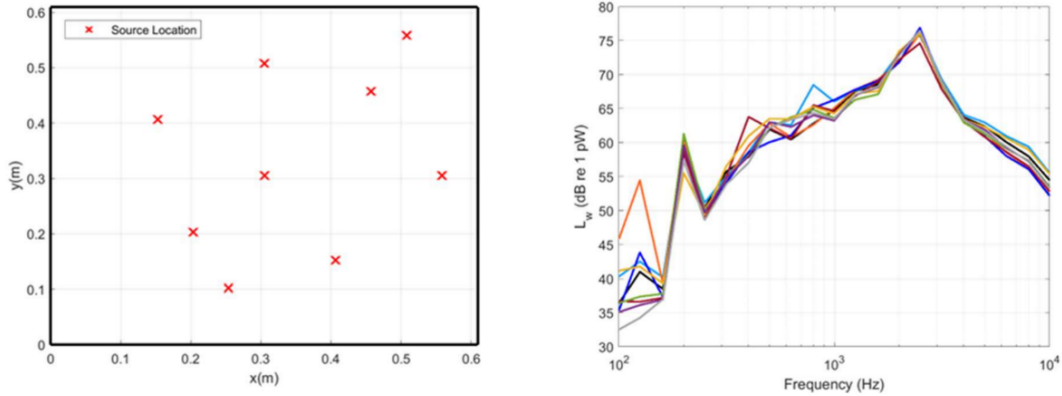


**Figure 3.** a) The floor map within the enclosure with the nine locations where each source was placed shown by a red “x.” b) The nine sound power results obtained for a blender within the enclosure using ISO 3741 measurements.

Fig. 4 shows the average ISO 3741 curve from the data in Fig. 3b, and the blender’s actual sound power measured using ISO 3741 without the enclosure present. The difference between these curves will identify a one-third octave (OTO) band correction for the blender.

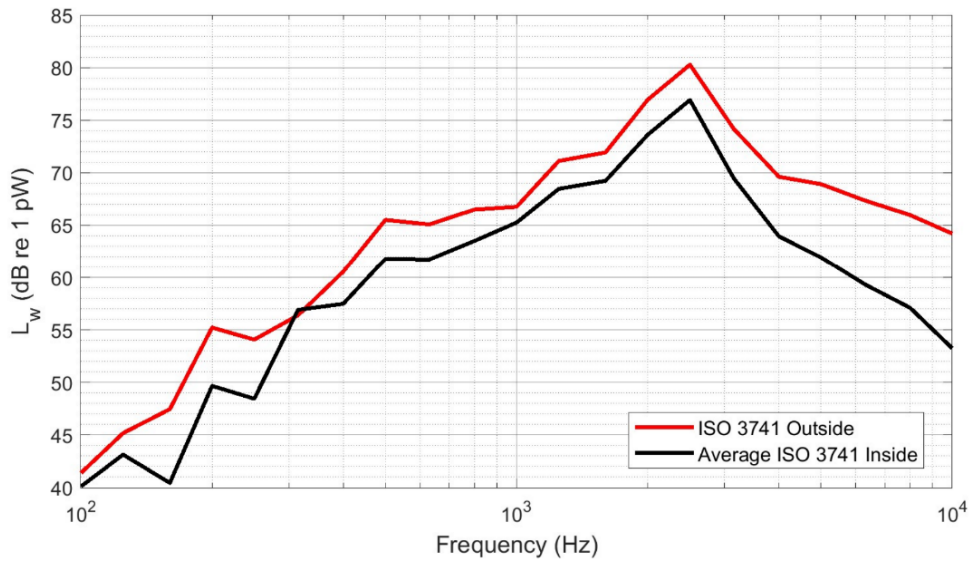
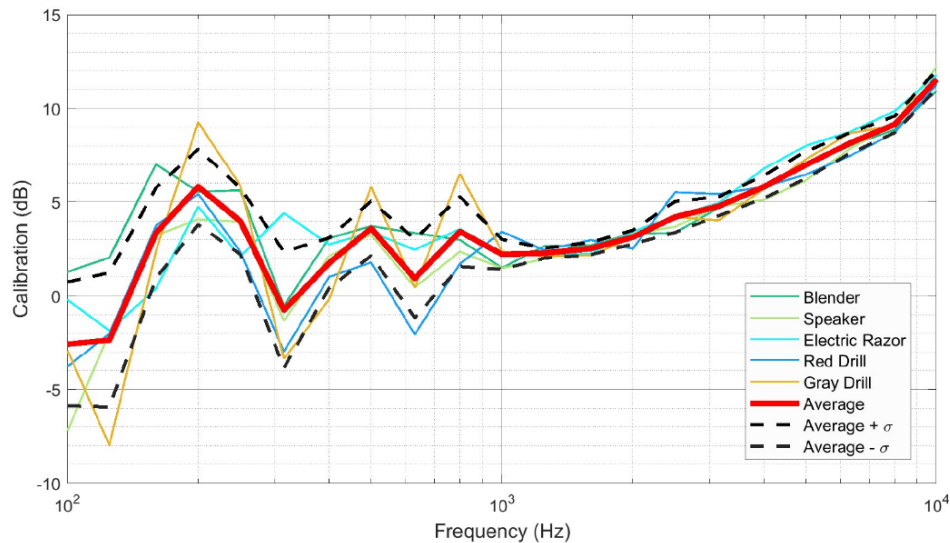


**Figure 4.** The free-field sound power result of a blender (red) is compared against the average of all nine ISO 3741 measurements of the blender within the enclosure (black).

Fig. 5 shows the OTO band correction curve that needs to be applied to the blender’s sound power inside the enclosure to obtain the free-field sound power of the blender. The Schroeder frequency of the reverberation chamber used for testing is about 385 Hz so the ISO 3741 results below this frequency are not compliant with the standard’s requirements and will not be considered. The energy is reduced across the bandwidth above the 400 Hz band due to the presence of the enclosure. This correction curve was



obtained for multiple sources. For simplicity, five of them are shown in this figure. The average of these correction curves is shown in red. The calibration is within  $\pm 1$  dB above the 1 kHz OTO band. Below that band the calibration is within  $\pm 2-3$  dB in most areas. The acoustic field inside the enclosure is becoming diffuse above 1 kHz due to the reduced variation in sound power for each source over nine different areas within the enclosure. On the other hand, the modal region below 1 kHz significantly affects the pressure radiated from the sources due to the low modal density – leading to large pressure differences



throughout the enclosure depending on the source's location.

**Figure 5.** This OTO band calibration curve was obtained for multiple sources. The correction curves for five of the sources are shown here. The average of these correction curves is shown in red. A standard deviation is included to show that the average calibration is within  $\pm 1$  dB above 1 kHz and within 2-3 dB below 1 kHz.

Recognizing that axial modes carry more energy than tangential and oblique modes, the frequencies of the enclosure's first couple of axial modes may significantly affect the output of the source, depending on its location.<sup>10</sup> This idea was investigated by identifying the significant resonances of the enclosure in the low frequency region to find better and poorer locations for each source within the enclosure that would lead to more consistency across ISO measurements.

Considering the modal behavior of the enclosure below 1 kHz, only modal indices up to 2 in each Cartesian direction are present. These are shown by the orange and blue lines in Fig. 6a. Strategically placing the blender in eight of these new locations and taking ISO 3741 measurements minimized much of the variation in the sound power obtained from the blender within the enclosure, as seen in Fig. 6b. This shows that the accuracy of the calibration developed previously can be improved below 1 kHz. In addition, these results support the findings in Fig. 5. Further work will be done to confirm this for multiple sources.

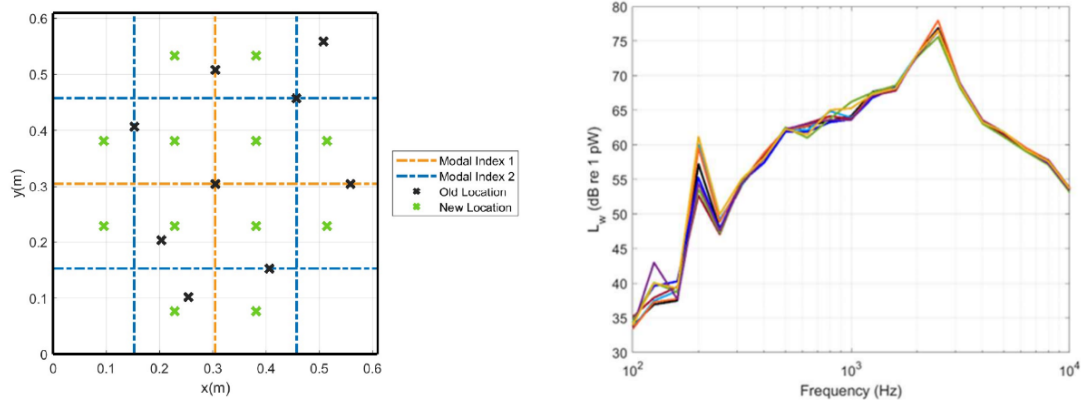


**Figure 6.** a) The pressure node lines for the first two mode indices of the enclosure in the  $x$ -,  $y$ -cartesian directions and the updated source locations (green 'x') against the earlier source locations (black 'x') relative to these node lines. b) Eight ISO 3741 measurements for the blender were made using the new source locations which tightened up all the curves better than before.

## CONCLUSION

It has been shown that a high-impedance source can be placed into an enclosure with four high impedance walls and a mylar face, and the sound power results obtained can be corrected by a calibration process to obtain the free-field sound power. A calibration curve was developed to remove the radiation effects of the enclosure on each source to obtain the free-field radiated sound power of nominal constant velocity sources within  $\pm 1$  dB above the 1 kHz OTO band and  $\pm 3$  dB below that band. These results indicate that each source can be moved anywhere along the floor except directly in the corners of the enclosure to be within this uncertainty for the true free-field sound power result. In addition, locations were found that would lead to more consistent results for the sound power radiated from the enclosure and reduce the uncertainty associated with the calibration curve. Current efforts focus on obtaining an accurate calibration curve for a wide range of sources and then applying the VBSP method to confirm the radiated sound power can accurately be obtained by applying the calibration curve to the VBSP results. The current work shows promise in developing an extended VBSP method that can be used to obtain the sound power from structures that cannot be scanned effectively using vibration-based measurements.

## ACKNOWLEDGEMENTS

John C. Ebeling and Gibson H. Campbell contributed to the ISO 3741 measurements for many of the sources within the enclosure. Added support was provided by the BYU College of Physical and Mathematical Sciences Wood Shop. This project was funded by the National Science Foundation, grant number 527136.

## REFERENCES

- <sup>1</sup> ISO 3740:2019. “Acoustics – Determination of sound power levels of noise sources – Guidelines for the use of basic standards” (International Organization for Standardization, Geneva, 2019).
- <sup>2</sup> Trent P. Bates, Ian C. Bacon, Jonathan D. Blotter, and Scott D. Sommerfeldt, "Vibration-based sound power measurements of arbitrarily curved panels," *J. Acoust. Soc. Am.* 151, 1171-1179 (2022), <https://doi.org/10.1121/10.0009581>.
- <sup>3</sup> F. Fahy and P. Gardonio, “Sound radiation by vibrating structures,” in *Sound and Structural Vibration, in Radiation, Transmission and Response*, 2nd ed. (Academic Press, Oxford, UK, 2007), pp. 165-175.
- <sup>4</sup> C. B. Jones, C. B. Goates, J. D. Blotter, and S. D. Sommerfeldt, “Experimental validation of determining sound power using acoustic radiation modes and a laser vibrometer,” *Applied Acoustics*, 164, Jul. 2020, doi: 10.1016/j.apacoust.2020.107254.
- <sup>5</sup> T. P. Bates, “Experimental validation of a vibration-based sound power method,” Master’s Thesis, Brigham Young University, Provo, UT (2022).
- <sup>6</sup> P. Aslani, S. D. Sommerfeldt, and J. D. Blotter, “Analysis of external radiation from circular cylindrical shells,” *J. Sound Vib.* 408, 154-167 (2017).
- <sup>7</sup> C. B. Goates, C. B. Jones, S. D. Sommerfeldt, and J. D. Blotter, “Sound power of vibrating cylinders using the radiation resistance matrix and a laser vibrometer,” *J. Acoust. Soc. Am.*, 148, 3553–3561 (2020), doi: 10.1121/10.0002870.

---

<sup>8</sup> T. P. Bates, I. C. Bacon, S. D. Sommerfeldt, J. D. Blotter, “Measuring sound power from curved plates using the radiation resistance matrix,” submitted for review to *Applied Acoustics*, (August 2022).

<sup>9</sup> ISO 3741:2010. “Acoustics – Determination of sound power levels and sound energy levels of noise sources using sound pressure – Precision methods for reverberation test rooms” (International Organization for Standardization, Geneva, 2010).

<sup>10</sup> M. Kleiner and J. Tichy, “Acoustics of Small Rooms,” (CRC, New York, 2017), pp. 28-32, 37-48, 64-71.

<sup>11</sup> H. Kuttruff, “Room acoustics,” 5th ed. (CRC Press LLC, 2009), pp. 83-91.

<sup>12</sup> L. E. Kinsler, A. R. Frey, A. B. Coppens, & J. V. Sanders, “Fundamentals of acoustics,” 4th ed., (John Wiley & Sons, New York, 2000), pp. 286-291.

# Chapter 11 Source Placement and VA One Validation

## 11.1 Introduction

The following chapter contains a paper published in the Acoustical Society of America's *Proceedings of Meetings on Acoustics*, which presents a study focused on identifying specific locations within a mylar enclosure that would minimize the variance in calibration measurements essential for the I-VBSP method. Additionally, the paper includes the design of a VA One model of the mylar enclosure to facilitate this study.

The results of this work, aligned with boundary element method (BEM) modeling conducted using VA One, confirm that the **R** matrix for a baffled flat plate accurately approximates the energy radiated from the enclosure at frequencies above the 630 Hz one-third octave (OTO) band. This theoretical validation is further supported by practical experimental measurements, with the sound power of a blender, as determined by the I-VBSP method, showing agreement within  $\pm 1$  to 2 dB of the free-field sound power measurements conducted in a reverberation chamber from 1.63 to 10 kHz.

*\*\* In addition to writing this manuscript, I identified specific locations within a mylar enclosure to minimize the variance in calibration measurements, which is essential for the I-VBSP method. I also designed a VA One model of the mylar enclosure to support this study. My work played a key role in the theoretical validation of the **R** matrix for a baffled flat plate to approximate the energy radiated from the enclosure accurately. I also conducted experimental work and validated the I-VBSP method for a blender. \*\**



## 11.2 Required Copyright Notice

The following article appeared in the Acoustical Society of America's *Proceedings of Meetings on Acoustics* and may be found at <https://doi.org/10.1121/2.0001732> under the title "Developing an indirect vibration-based sound power method to determine the sound power radiated from acoustic sources." It is reproduced in its original published format here by rights granted in the JASA Transfer of Copyright document, item 3.

<https://pubs.aip.org/DocumentLibrary/files/publications/jasa/jascpyrt.pdf>

### Citation:

I. C. Bacon, S. D. Sommerfeldt, and J. D. Blotter, "Developing an indirect vibration-based sound power method to determine the sound power radiated from acoustic sources," *Proc. Mtgs. Acoust.* **50**(1), 065003 (2023).

I hereby confirm that the use of this article is compliant with all publishing agreements.

APRIL 07 2023

## Developing an indirect vibration-based sound power method to determine the sound power radiated from acoustic sources **FREE**

Ian C. Bacon; Scott D. Sommerfeldt ; Jonathan D. Blotter



*Proc. Mts. Acoust.* 50, 065003 (2022)  
<https://doi.org/10.1121/2.0001732>



19 June 2024 07:22:26



LEARN MORE

Advance your science and career as a member of the  
**Acoustical Society of America**



## 183rd Meeting of the Acoustical Society of America

Nashville, Tennessee

5-9 December 2022

### Structural Acoustics and Vibration: Paper 4aSAa3

## Developing an indirect vibration-based sound power method to determine the sound power radiated from acoustic sources

**Ian C. Bacon and Scott D. Sommerfeldt**

*Department of Physics & Astronomy, Brigham Young University College of Physical and Mathematical Sciences, Provo, UT, 84602; [ianbacon24@gmail.com](mailto:ianbacon24@gmail.com); [scott\\_sommerfeldt@byu.edu](mailto:scott_sommerfeldt@byu.edu)*

**Jonathan D. Blotter**

*Department of Mechanical Engineering, Brigham Young University, Provo, UT, 84602; [jblotter@byu.edu](mailto:jblotter@byu.edu)*

An indirect vibration-based sound power (I-VBSP) method is in development to be used to measure noise from the numerous sources that radiate energy that cannot be captured effectively using surface vibration measurements. These sources are placed inside a rectangular enclosure with four high impedance sides, a single rigid side, and a single mylar side, inducing a vibration on the mylar membrane. A scanning laser Doppler vibrometer (SLDV) is used to scan the vibrating mylar to determine the sound power radiated through the mylar and this sound power result is then calibrated to obtain the free-field radiated sound power. A boundary element method (BEM) model showed that using the baffled flat plate form of the radiation resistance matrix approximates well the energy radiated from the enclosure above the 630 Hz one-third octave (OTO) band, enabling the indirect method to work above that frequency for this enclosure. The experimental sound power measurement of a blender obtained from the I-VBSP method agreed with the free-field sound power obtained in a reverberation chamber using the ISO 3741 standard within +/- 1 to 2 dB from 1.63-10 kHz. Other challenges are discussed that will be addressed in future research.

## 1. INTRODUCTION

The sound power level characterizes airborne noise emitted from acoustic sources. It is an important parameter in product design, is desirable for many applications, and must be determined by measurement.<sup>1</sup> For some applications, the background noise or testing environment limits the current sound power methods, making an alternate method for determining this valuable quantity desirable. Recent work has shown that a vibration-based sound power (VBSP) method is finding success in overcoming these limitations while maintaining the same level of precision.<sup>2-6</sup>

The VBSP method relies on a 3D scanning laser Doppler vibrometer (SLDV) to measure the components of the velocity at every location spanning the surface of a vibrating structure from which the complex normal velocities can be computed. From a discrete form of the Rayleigh integral, the sound power,  $\Pi$ , can be computed for a given frequency,  $\omega$ , using a column vector of the surface normal velocities,  $\mathbf{v}_e$ , in connection with the radiation resistance matrix,  $\mathbf{R}$ , as:

$$\Pi(\omega) = \mathbf{v}_e^H(\omega)\mathbf{R}(\omega)\mathbf{v}_e(\omega) \quad (1)$$

where  $(\cdot)^H$  denotes a Hermitian transpose.<sup>6-8</sup>

This method works well for vibrating structures such as flat plates, cylindrical shells, and simple-curved panels.<sup>3-6</sup> This VBSP method can even obtain accurate sound power levels for arbitrarily curved panels by employing a known form of the  $\mathbf{R}$  matrix that approximates these structures.<sup>2</sup> A previous result of a curved aluminum panel with a 0.51 m radius of curvature is shown in Fig. 1 to illustrate the accuracy of the results that have been obtained with this method.

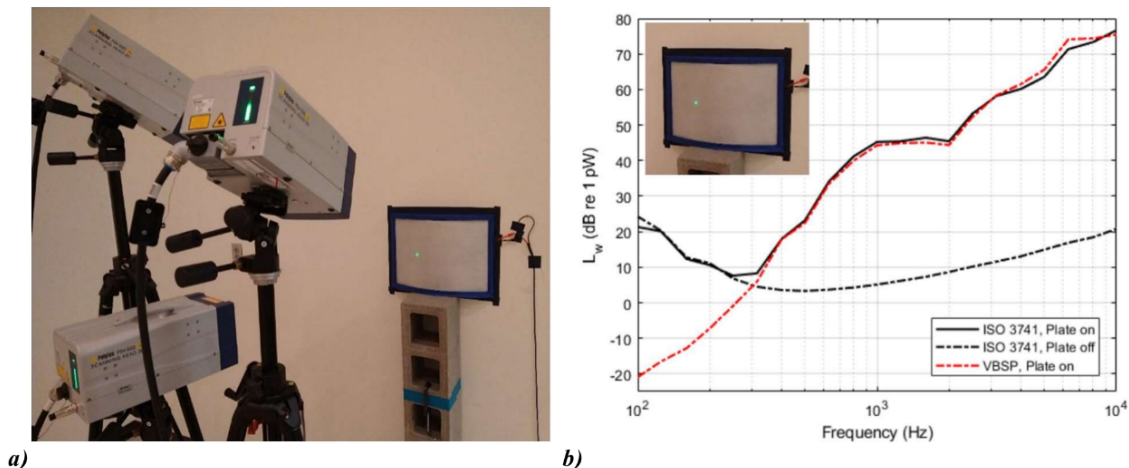


**Figure 1. a)** The 3D SLDV setup in a reverberation chamber prepared to scan a curved aluminum panel having a radius of curvature of 0.51 m mounted in a steel frame and sealed to the wall acting as a baffle.<sup>8</sup> **b)** A result of the VBSP method applied to the simple-curved panel shown in the corner using Eq. (1). The sound power levels measured using the ISO 3741 standard (black curves) against the VBSP method (red) are compared.<sup>3</sup>

There are numerous products used on a daily basis with sound power levels that a user may want to quantify. Many of these sources, such as a blender, Bluetooth speaker, and electric drill, have internally generated noise that cannot be captured using surface velocity measurements. A new indirect method is being developed to extend the VBSP method to quantify many of these sources.<sup>8</sup> The purpose of this paper is to present further developments for this adapted VBSP method to measure these sources and lay out some of the challenges and potential solutions to the previously mentioned limitation.

---

## 2. INDIRECT VBSP METHOD

This section outlines an indirect method to extend the VBSP method to account for the numerous sources that cannot obtain the sound power from direct surface vibration measurements. For this method to work, the source radiation needs to vibrate something that can be scanned directly. A 0.61 m (2 ft) cube enclosure was fabricated for this purpose, as seen in Fig. 2. The four sides on the perimeter are made up of 1 1/2" thick medium-density fiberboard (MDF), the top face has a mylar membrane that is stretched taut over the MDF enclosure, and the base is open so that the rigid floor will seal off the bottom of the enclosure. The mylar was glued to the MDF, adhered using gaff tape, and shrink-wrapped using a heat gun to increase surface tension of the membrane. Furthermore, the mylar is coated with a developer spray making it easier for the SLDV to scan.

This enclosure is placed over the sources of interest, acting as an “acoustic tent.” During measurements, the ports and base are sealed off with putty and Gaff tape to reduce energy leaking through the bottom of the enclosure. The rigid floor and four high impedance walls direct nearly all the acoustic energy from the source to excite the mylar membrane. Its vibration behaves as a flexible membrane, which can be scanned by an SLDV. Even though the mylar is acoustically transparent for a limited low-frequency band, the enclosure significantly affects the way each source radiates over most of the frequency range. Nevertheless, the sound power radiated from the enclosure can be measured and then calibrated to match the free-field sound power.<sup>8</sup>

The presence of the enclosure introduces absorption and can affect the radiation impedance of the internal sources. The radiation impedance is defined as the ratio of the total force on the surface of a radiator that is needed to move the surrounding medium to the particle velocity of the radiator surface.<sup>9,10</sup> Constant volume velocity sources have high internal impedances and therefore will experience little change to the volume velocity inside the enclosure. As a result, the change in sound power due to the enclosure will be attributed to the absorption and/or radiation impedance change, which can be corrected with a suitable calibration. It will be necessary to show that each of the sources will lead to the same calibration curve and that the sources can be moved internally in the enclosure without significantly affecting the radiated power. This will be the focus of the next section.

The I-VBSP method is outlined as follows: first, place the source into a small enclosure that ideally has five rigid sides and a single mylar face that can be scanned using an SLDV. Next, develop a calibration curve to remove the influence of the enclosure on the source using ISO 3741 measurements<sup>11</sup> to obtain the sound power for multiple sources to see how the enclosure radiates into the larger space. Then, obtain the sound power from the mylar face using the VBSP method. Apply the calibration to the VBSP results to obtain the free-field sound power of the source of interest. Finally, compare the free-field ISO 3741 result with the corrected VBSP result to verify accuracy and precision between measurements.





*Figure 2. The mylar and MDF enclosure for I-VBSP measurements. There are three ports drilled in the bottom left to feed the source cabling. The bottom face is open so that the source can be enclosed on the floor where the source will then excite the mylar membrane acoustically.<sup>8</sup>*

### 3. CALIBRATION

This section identifies a calibration curve for five tested sources (a blender, a speaker, an electric razor, and two different electric drills) and shows whether these nominally constant volume velocity sources can be moved within the enclosure without significantly impacting the radiated power. Kleiner and Tichy<sup>9</sup> state, “The sound radiation into a room depends on the source, its properties and location, and on the properties of the room such as its size, shape, and sound absorption.” Small enclosures have acoustic properties that are largely determined by the individual eigenfrequencies below the Schroeder frequency.<sup>12</sup> It is desirable to obtain a calibration curve to remove the effects of the small enclosure on the source radiation. These effects are mostly attributable to absorption, enclosure resonances, radiation impedance loading, and significant pressure differences that occur internally.

ISO 3741 measurements were used to better understand these effects and calibrate the enclosure. The free-field sound power was measured for an individual source in a reverberation chamber following the ISO 3741 procedure.<sup>11</sup> The source was then placed at nine distinct locations on the floor inside the enclosure (see Fig. 5 for where those locations were chosen from), from which the sound power was measured for each location following the ISO 3741 procedure. Figure 3 shows the average of these nine enclosed ISO measurements for a blender and compares it against the blender’s free-field ISO measurement. As expected, by enclosing the noise source with the constructed enclosure described above, the acoustic energy measured by the microphone-based standard is reduced. A one-third octave (OTO) band calibration curve for each source was obtained by taking the difference of the free-field ISO measurement and the average of the enclosed ISO measurements. This process was repeated for multiple sources to see the variation between sources (see Fig. 4 for the calibration curve for several sources). The calibration curve for each source was then averaged to obtain an effective calibration curve to remove the influence of this enclosure to obtain each source’s true radiated power.

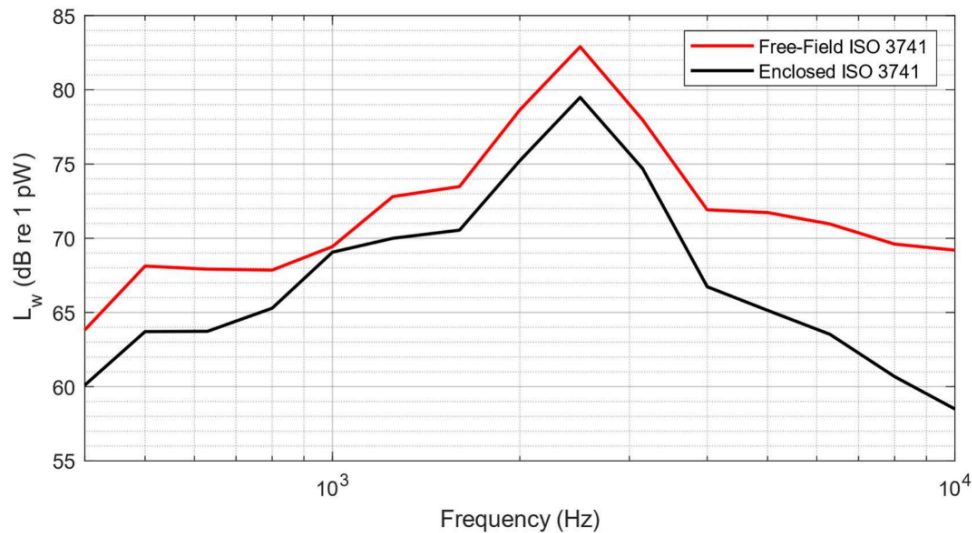


**Figure 3.** The free-field sound power level,  $L_w$ , spectrum of a blender (red) compared to the average of all nine ISO 3741 measurements of the blender within the enclosure (black). The difference between these two curves will identify an OTO band calibration curve for this source.<sup>8</sup>

Figure 4 shows an OTO band correction curve obtained using five sources, which were applied to the enclosed sound power of a blender to correct for the enclosure effects and obtain the free-field sound power of the blender. This calibration curve was obtained by averaging the individual calibration curves for the five sources. Above the 1 kHz OTO band, the calibration is about  $\pm 1$  dB. Between the 400 Hz and 1 kHz OTO bands, the calibration is about  $\pm 2$  to 3 dB. The reverberation chamber used for testing has a Schroeder frequency of 385 Hz, so the ISO 3741 results below this frequency do not meet the standard's requirements and will not be considered. The reduced variation in the sound power output above 1 kHz for each source over the nine different locations within the enclosure indicates that the acoustic field is becoming diffuse. On the other hand, below 1 kHz, the modal region significantly impacts the radiated pressure from the sources due to the low modal density. This leads to large pressure differences throughout the enclosure depending on the source location.

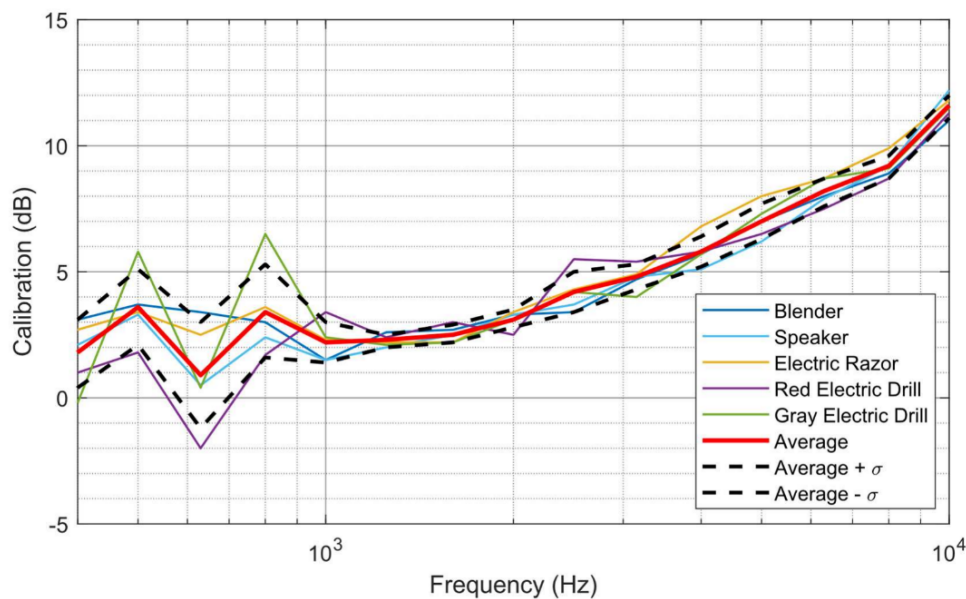


**Figure 4.** OTO band calibration curves obtained from multiple sources. The calibration curves for five of the sources are shown. The average of these calibration curves is shown in red. A standard deviation is included (black dashed) to show that the average calibration is within  $\pm 1$  dB above 1 kHz and within 2 to 3 dB below 1 kHz. Note: The abscissa for this figure starts at 400 Hz – the usable bandwidth for the ISO 3741 standard measurements made.

Figure 4 reveals there is more source-to-source variation below 1 kHz and the resulting impact the enclosure will have on the radiated sound power depending on the source location. Recognizing that axial modes carry more energy than tangential and oblique modes, the frequencies of the enclosure’s first couple of axial modes may significantly affect the output of the source, depending on its location.<sup>9</sup> This was investigated to find better and poorer locations for each enclosed source that would lead to more consistent ISO 3741 measurements.

Considering the modal behavior of the enclosure below 1 kHz, only the first two modal indices in each Cartesian direction are present. Figure 5 shows the locations of the nodal planes for these modes, along with source locations tested in two rounds of testing. In Fig. 6a, the blender was placed in random locations within the enclosure on the floor, corresponding to “Random Locations” in Fig. 5, and the resulting ISO 3741 sound power measurements were averaged. Figure 6b shows specific locations within the enclosure on the floor, corresponding to “Specific Locations” in Fig. 5, from which eight of these were chosen for testing. Much of the variation in the sound power obtained from the blender within the enclosure is minimized by avoiding having the source located on a nodal plane for the low-order modes of the enclosure. Furthermore, this also shows that the accuracy of the calibration developed in Fig. 4 can be improved below 1 kHz by avoiding these nodal planes. Further work will be done to finalize a calibration curve for multiple sources with an improved enclosure.



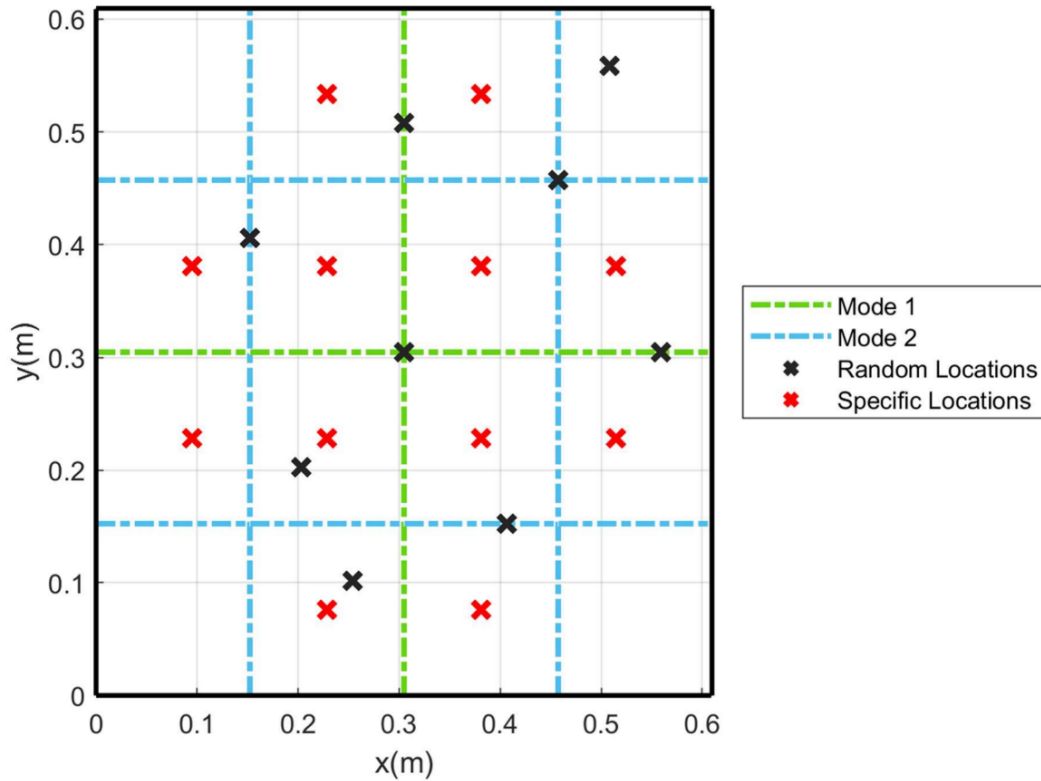
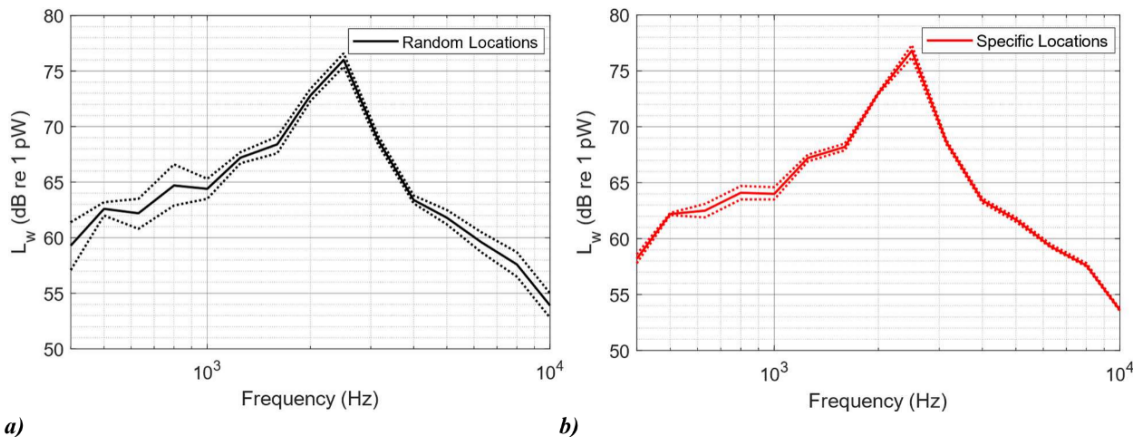


Figure 5. Top view schematic of the enclosure. The pressure node lines for the first two modes are shown as the dashed lines. Measurements were made with the blender placed on random locations (black 'x') and specific locations (green 'x') to assess the impact of the nodal planes.



a) b)  
Figure 6. The blender's sound power response,  $L_w$ , within the MDF enclosure. a) Average of nine enclosed ISO 3741 measurements of a blender at random locations (solid black) with standard deviation (dotted). b) Average of eight enclosed ISO 3741 measurements of a blender at specific locations (solid red) with standard deviation (dotted). By strategically placing the sources in the specific locations, the deviation between measurements tightened up. Note: The abscissa for these figures starts at 400 Hz – the usable bandwidth for the ISO 3741 standard measurements made.

#### 4. COMPUTATIONAL MODEL

The sound power for this method depends on the normal surface velocities and the radiation resistance matrix, which depends on the vibrating surface geometry. The baffled flat plate form of the  $\mathbf{R}$  matrix is well established in the literature.<sup>2-7,13</sup> However, the mylar face is a 0.61 m (2 ft) square raised off the ground by another 0.61 m, so it is possible that a modified  $\mathbf{R}$  matrix could be needed when the mylar is no longer approximated well using a baffle.

A vibroacoustic model, shown in Fig. 7, was developed using the ESI software package VA One 2021 to identify the range of frequencies where the baffled flat plate form of the  $\mathbf{R}$  matrix will approximate the radiation well for the mylar enclosure. This software inherently uses the correct form of the  $\mathbf{R}$  matrix needed for the 0.61 m cube enclosure. The top face in the model is a very thin flexible panel to approximate the fixed mylar membrane, and the remaining sides are rigid.

The radiated power emitted from an enclosed acoustic source, with a pressure magnitude of 1 Pa for each OTO band, was quantified using the boundary element method (BEM). Then, the normal surface velocities from the top face were exported from VA One and processed through the VBSP method using the baffled flat plate form of the  $\mathbf{R}$  matrix. Finally, the results were quantified in Table 1. These results show both methods agree within about 1 dB above 630 Hz, indicating that the baffled flat plate  $\mathbf{R}$  matrix is a good approximation for obtaining the sound power of this enclosure above that frequency. If more error can be tolerated in the 400 and 500 Hz bands, this baffled flat plate  $\mathbf{R}$  matrix can be used down to about 200 Hz.

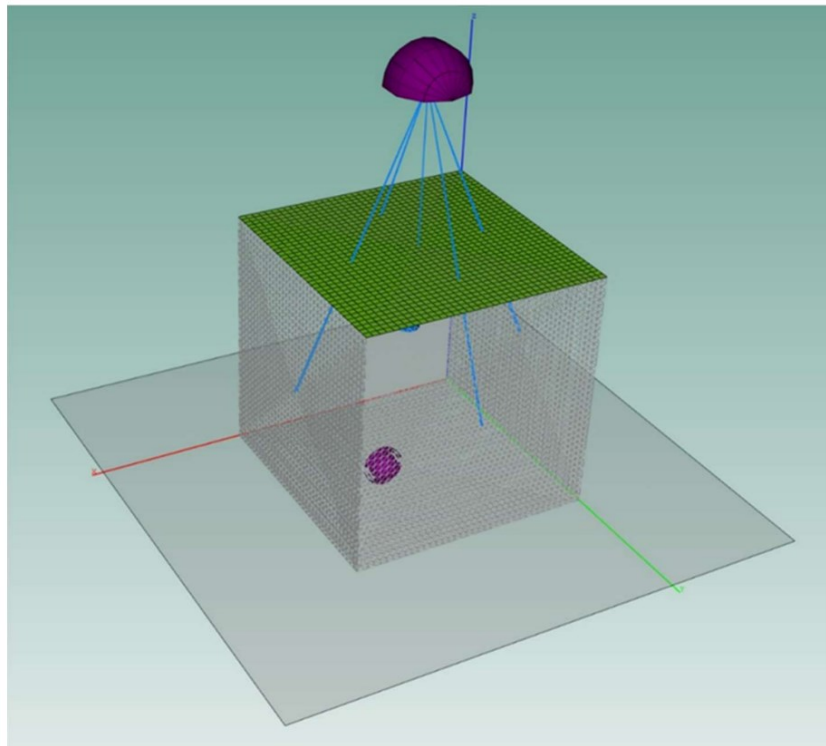


*Figure 7. The VA One model of the enclosure with an ideal acoustic source. A BEM fluid (magenta hemisphere) is connected (blue lines) to the enclosure so that the BEM results can be obtained for this structural-acoustic system.*

*Table 1: The OTO band sound power of an ideal acoustic source computed with the VA One BEM model, the baffled flat plate form of the VBSP method, and the difference between the two methods (units are in dB re 1 pW).*

OTO Freq (Hz)	BEM	VBSP	Difference (VBSP - BEM)
100	73.1	76.0	2.8
125	64.7	68.1	3.3
160	61.2	64.1	2.8
200	64.0	66.3	2.3
250	67.0	67.5	0.6
315	67.3	68.1	0.8
400	89.8	92.1	2.2
500	67.0	69.2	2.2
630	55.9	56.6	0.7
800	47.7	47.7	0.0
1000	44.1	44.5	0.4
1250	62.1	63.3	1.2
1600	57.1	57.4	0.3
2000	57.5	57.7	0.2
2500	64.6	65.1	0.5

## 5. RESULTS

Now that a calibration curve has been developed, and the current VBSP method for a flat plate is accurate from the 630 Hz OTO band upward, the next step was to scan the mylar face with the SLDV. Figure 8 compares the VBSP measurement of a blender inside the enclosure with the enclosed ISO 3741 sound power measurement. From 2-10 kHz, both methods agree to within about 1 dB. From 630 Hz to the 1,630 Hz OTO band, the measured sound power using the VBSP method is anywhere from 2-5 dB lower than the ISO 3741 measurement. This indicates that the mylar is not capturing all the radiated energy in its vibrations and that some of the energy from the noise source being measured is radiating through the MDF sides or leaking out of the enclosure via flanking path(s). After sealing off the mylar side to prevent radiation leak, the results indicated that there was still non-negligible radiation through the MDF walls. The MDF walls were not rigid enough to sufficiently inhibit energy from transmitting through them since the ports and floor were sealed with putty and Gaff tape.

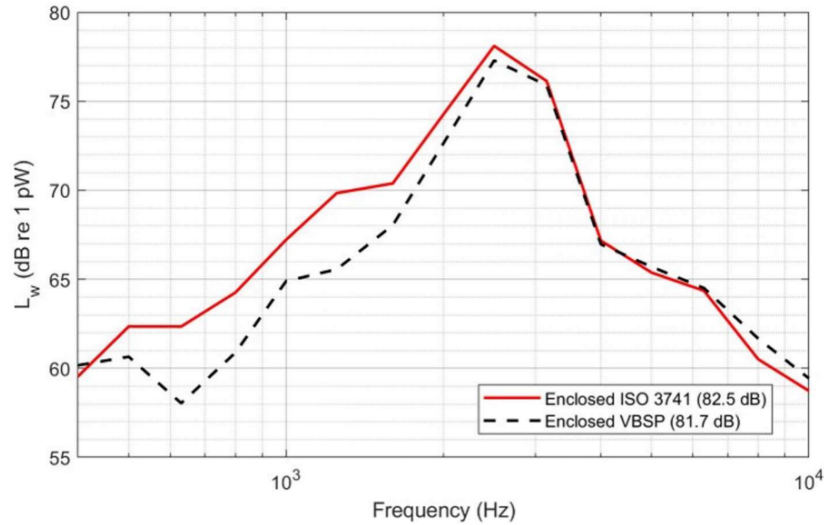


**Figure 8.** The ISO 3741 (red) and VBSP (black) sound power measurements of a blender inside the enclosure. Note: The abscissa for this figure starts at 400 Hz – the usable bandwidth for the ISO 3741 standard measurements made.

The calibration curve obtained previously was applied to the enclosed VBSP measurement and was compared to the free-field ISO 3741 measurement, as shown in Fig. 9. The I-VBSP method is within +/- 1 to 2 dB of the ISO 3741 method from 1.63-10 kHz. This result is encouraging, but the accuracy could still be improved. While investigating potential causes for this lack of desired accuracy, an updated reverberation time ( $T_{60}$ ) is required for the ISO 3741 method to account for extra absorption within the reverberation chamber with the enclosure and measurement equipment present. This might explain why the vibrational energy is higher than the total energy present in the chamber at high frequencies and will be tested in future work.

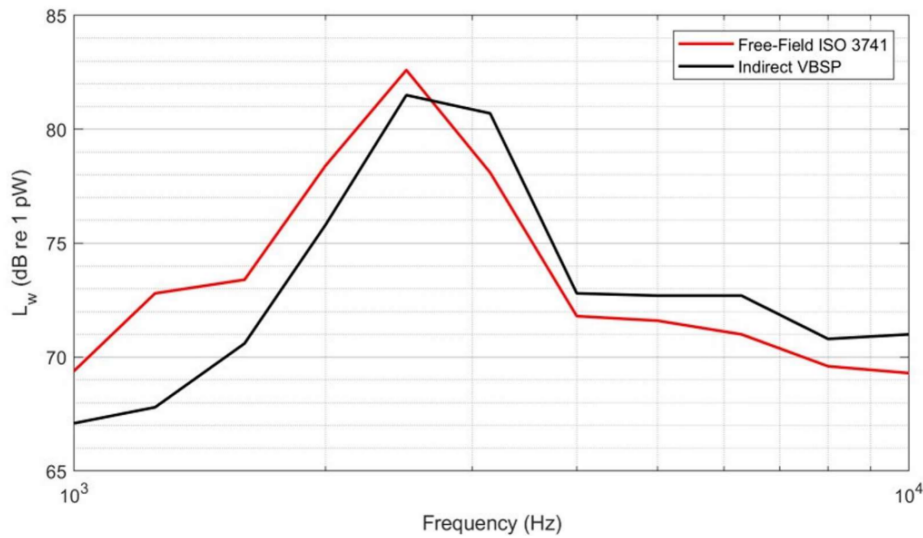


**Figure 9.** The I-VBSP blender measurement (black) compared to the free-field blender ISO 3741 measurement (red). Note: The abscissa for this figure is scaled to 1,000-10,000 Hz to visualize the sound power level increments between curves better.



---

## 6. CONCLUSION

It has been shown that there are source locations chosen that minimize the variance associated with the calibration curve used for the I-VBSP method. A BEM model predicted that the baffled flat plate radiation resistance matrix can be used to approximate the sound power radiated from the 0.61 m cube enclosure used in this work above the 630 Hz OTO band, enabling the indirect method to work above that frequency for this enclosure. Experimental analysis showed that the I-VBSP method is accurate to within +/- 1 to 2 dB of the free-field acoustic power above 1.63 kHz. This supports the hypothesis that the MDF sides are radiating significantly more than the sides of the enclosure in the VA One model below 1.63 kHz. Therefore, the transmission loss through the MDF sides of the enclosure need to be improved for future testing.

These results indicate that the I-VBSP method shows promise for obtaining the sound power of a noise source, although there is room for accuracy improvement. To improve the results, a new enclosure will need to be fabricated to improve the rigidity of the sides so that more of the source energy will radiate into the room through the membrane. This will ensure that the SLDV picks up the low frequency energy the ISO 3741 standard measures.

Future work will include improving the transmission loss of a new enclosure so that the scanned face captures a higher percentage of the acoustic energy radiating from the enclosed sources. Different material panels such as thin aluminum will be investigated to see if there may be a better choice than mylar for the I-VBSP method that will be more consistent between measurements. The new enclosure will also have unique dimensions to reduce the modal degeneracy of the acoustic field inside the enclosure simply to improve the diffuseness within the enclosure so that the sources can be moved around more freely without affecting the radiated power output. A new calibration curve for this enclosure will be obtained using the "Specific Locations" to improve accuracy. For the enclosed ISO 3741 measurements, an updated reverberation time will be obtained to account for the added absorption of the extensive measurement equipment within the reverberation chamber.

## 7. ACKNOWLEDGEMENTS

John C. Ebeling and Gibson H. Campbell contributed to the ISO 3741 measurements for many of the sources within the enclosure. Trent P. Bates simplified the figures for the average ISO 3741 measurements. Praveen Jayasheela provided VA One support to better understand the software. Additional support was provided by the BYU Department of Physics & Astronomy Wood Shop. This project was funded by the National Science Foundation, grant number 527136.

---

## 8. REFERENCES

- <sup>1</sup> ISO 3740:2019. “Acoustics – Determination of sound power levels of noise sources – Guidelines for the use of basic standards” (International Organization for Standardization, Geneva, 2019).
- <sup>2</sup> T. P. Bates, I. C. Bacon, J. D. Blotter, and S. D. Sommerfeldt, “Vibration-based sound power measurements of arbitrarily curved panels,” *J. Acoust. Soc. Am.* **151**, 1171-1179 (2022), doi: 10.1121/10.0009581.
- <sup>3</sup> T. P. Bates, *Experimental validation of a vibration-based sound power method*, Master’s Thesis, Brigham Young University, Provo, UT (2022).
- <sup>4</sup> P. Aslani, S. D. Sommerfeldt, and J. D. Blotter, “Analysis of external radiation from circular cylindrical shells,” *J. Sound Vib.* **408**, 154-167 (2017), doi: 10.1016/j.jsv.2017.07.021.
- <sup>5</sup> C. B. Goates, C. B. Jones, S. D. Sommerfeldt, and J. D. Blotter, “Sound power of vibrating cylinders using the radiation resistance matrix and a laser vibrometer,” *J. Acoust. Soc. Am.* **148**, 3553–3561 (2020), doi: 10.1121/10.0002870.
- <sup>6</sup> C. B. Jones, C. B. Goates, J. D. Blotter, and S. D. Sommerfeldt, “Experimental validation of determining sound power using acoustic radiation modes and a laser vibrometer,” *Applied Acoustics*, **164**, Jul. 2020, doi: 10.1016/j.apacoust.2020.107254.
- <sup>7</sup> F. Fahy and P. Gardonio, *Sound and Structural Vibration: Radiation, Transmission and Response*, 2nd ed. (Academic Press, Oxford, UK, 2007), pp. 165-175.

- 
- <sup>8</sup> I. Bacon, S. D. Sommerfeldt, and J. D. Blotter, “Determination of radiated sound power from acoustic sources using the VBSP method and a mylar boundary,” *Proc. Mtgs. Acoust.* **46**, 065003 (2022), doi: 10.1121/2.0001663.
- <sup>9</sup> M. Kleiner and J. Tichy, *Acoustics of Small Rooms*, (CRC, New York, 2017), pp. 28-32, 37-48, 64-71.
- <sup>10</sup> L. E. Kinsler, A. R. Frey, A. B. Coppens, & J. V. Sanders, *Fundamentals of acoustics*, 4th ed., (John Wiley & Sons, New York, 2000), pp. 286-291.
- <sup>11</sup> ISO 3741:2010. “Acoustics – Determination of sound power levels and sound energy levels of noise sources using sound pressure – Precision methods for reverberation test rooms” (International Organization for Standardization, Geneva, 2010).
- <sup>12</sup> H. Kuttruff, *Room acoustics*, 5th ed. (CRC Press LLC, 2009), pp. 83-91.
- <sup>13</sup> J. C. Ebeling, I. C. Bacon, T. P. Bates, S. D. Sommerfeldt, and J. D. Blotter, “Improved efficiency of vibration-based sound power computation through multi-layered radiation resistance matrix symmetry,” *JASA Express Lett.* **2**, 125601 (2022), doi: 10.1121/10.0015355.

## Chapter 12 Development for Rectangular Enclosures

This chapter presents the development and application of the indirect vibration-based sound power (I-VBSP) method using a rectangular “box-in-box” enclosure, designed to minimize sound power radiation from the four perimeter sides. To improve measurement repeatability, a thin aluminum plate replaced the original mylar face.

The chapter outlines the design of this new enclosure, emphasizing its role in confining acoustic energy to the top face, which improves measurement accuracy. Calibration procedures for the new enclosure appear in detail in Ch. 13. This chapter includes reverberation ( $T_{60}$ ) time measurements to account for additional absorption in a reverberation chamber, which were required to improve the accuracy of the ISO 3741 standard due to absorption changes caused by additional materials within the chamber.

*\*\* I contributed to this work by designing the new enclosure and replacing the mylar face with the aluminum plate, which directly improved the measurement repeatability. I also did experimental work and validated the I-VBSP method with a Bluetooth speaker. Finally, I found challenges posed by non-stationary sources, where the scanning laser Doppler vibrometer (SLDV) exhibited low coherence. \*\**



## 12.1 Introduction

Many consumer products contain internal components that radiate sound that cannot be scanned directly due to casing. An enclosure facilitates use of the scanning laser Doppler vibrometer (SLDV) in the indirect vibration-based sound power (I-VBSP) method as an “acoustic tent” around the sound sources. The enclosure, however, introduces absorption and can affect the radiation impedance of the internal sources (see Ch. 11). To provide proof-of-concept, constant volume velocity sources are desirable, since they experience minor changes to volume velocity within the enclosure due to their high internal impedances. Furthermore, these minor changes in sound power due to the enclosure are attributed to absorption and/or radiation impedance change, which can be corrected with a suitable calibration [1], [2].

The rectangular enclosure design has the bottom face open. The four walls are made of medium dense fiberboard (MDF) and a treated foam layer. The top face is a 0.02” thick aluminum sheet clamped down by a steel frame (see Figs. 12.1a and 12.1b); the aluminum sheet acts as a flexible panel. The enclosure’s size is 1/9 the size of BYU’s reverberation chamber to reduce the modal degeneracy of the acoustic field within the enclosure. This size improves the diffuseness internally so that sources can be moved around more freely within the enclosure without affecting the radiated sound power output [3]. The ability to move the source enables more consistent ISO 3741 measurements throughout the enclosure, which tightens the calibration for this method in the mid-to-high frequency range. To account for the absorption caused by the enclosure materials, updated reverberation times are computed for more accurate ISO 3741 results [4].

The introduction of the enclosure into the I-VBSP method led to several questions about the appropriate  $\mathbf{R}$  matrix and the suitable frequency range. Computational work (Ch. 11) showed that for most of the one-third octave (OTO) frequency bands (800 Hz to 10 kHz) the baffled flat plate

form of the  $\mathbf{R}$  matrix can be used for computing sound power of the flexible panel. However, the flexible panel is a 0.56 m x 0.66 m rectangular aluminum plate raised off the ground by 0.78 m, so it is possible that a modified  $\mathbf{R}$  matrix is necessary when the plate is no longer well approximated using a baffle.

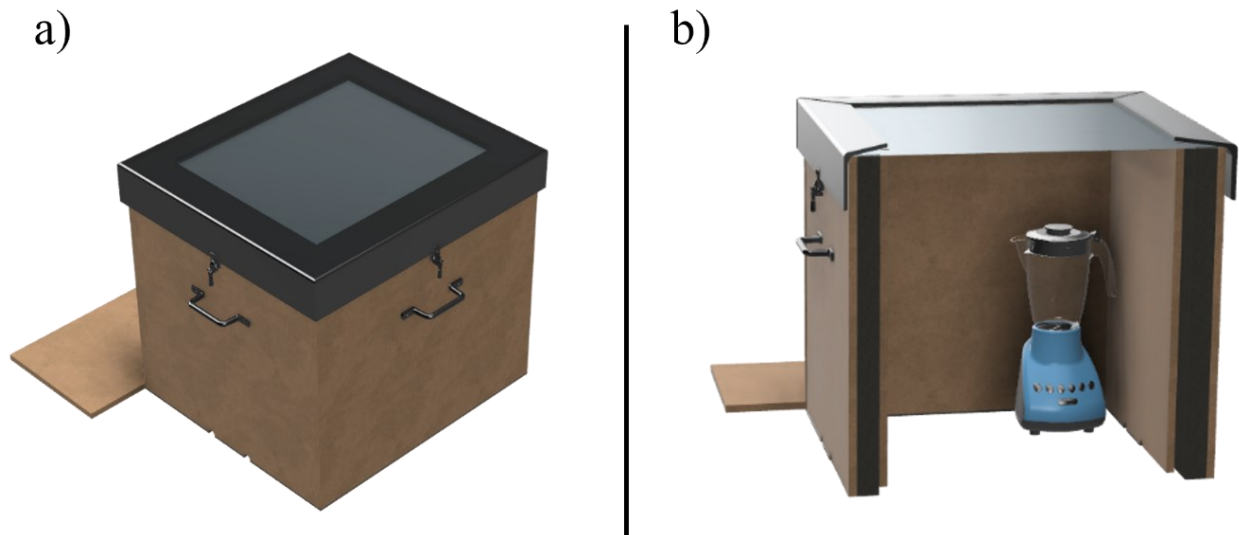


**Figure 12.1:** a) A model of the rectangular enclosure used for the I-VBSP method. The steel frame (black) clamps down the thin flexible aluminum panel (light gray). The ports in the bottom are necessary for cabling and are sealed off, using weather stripping during measurements. The hinge on the left tilts the enclosure back so the source can easily be moved internally for testing. b) A blender inside the enclosure. This view shows treated foam with constrained layer damping between the boxes.

The proposed I-VBSP method:

1. Place the source into a rectangular enclosure that has four high transmission loss sides, a reflective floor surface, and a single elastic face that can be scanned using an SLDV.

Figures 12.1a and 12.1b illustrate this.

2. Develop a calibration curve to remove the influence of the enclosure on the source (see Fig. 12.2), using ISO 3741 measurements to obtain the sound power for multiple sources to account for sound from the enclosed noise source that radiates through the enclosure into the larger space (see Ch. 13).
3. Compute the sound power from the elastic face using the VBSP method.
4. Apply the calibration to the VBSP results to determine the free-field sound power of the source of interest.
5. Compare the free-field ISO 3741 result with the corrected VBSP result to verify precision.

Using the enclosure, the I-VBSP method can estimate sound power for numerous acoustic sources that cannot be scanned effectively using existing technology.

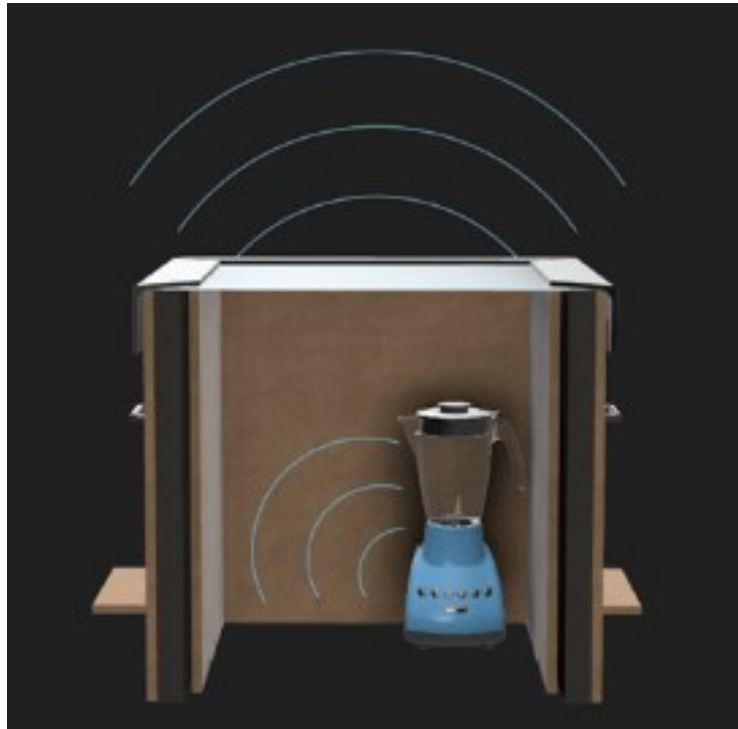


**Figure 12.2:** Illustration of an acoustic source radiating within the enclosure and the acoustically induced vibration of the aluminum panel which radiates the transmitted sound power.

## 12.2 VA One Model

This section focuses on using a computational model to determine which **R** matrix to use for this enclosure. A VA One model identified the range of frequencies where the baffled flat plate form of the **R** matrix well approximates the acoustic radiation for this new enclosure. This computational model uses the boundary element method (BEM) to estimate sound power from the enclosed source (see Fig. 12.3a). The blue BEM measurement surfaces from Fig. 12.3a were removed in Fig. 12.3b to show the flexible panel, location of the internal noise source, and the air cavity used in the BEM.

Results from the BEM model can be compared with the VBSP method to evaluate the applicability of the chosen **R** matrix. To obtain these VBSP estimates, the normal surface velocities computed for the aluminum face can be exported from VA One and processed through the VBSP method using the baffled flat plate form of the **R** matrix. Finally, comparing the sound power from the BEM model with the VBSP method identifies the usable bandwidth for which the baffled flat plate form of the **R** matrix provides a good approximation. The usable bandwidth for this enclosure is the same as the bandwidth found in Ch. 11, Table 1. In the future, the VA One model might also be able to identify how the **R** matrix could be modified for lower frequencies to extend the bandwidth.

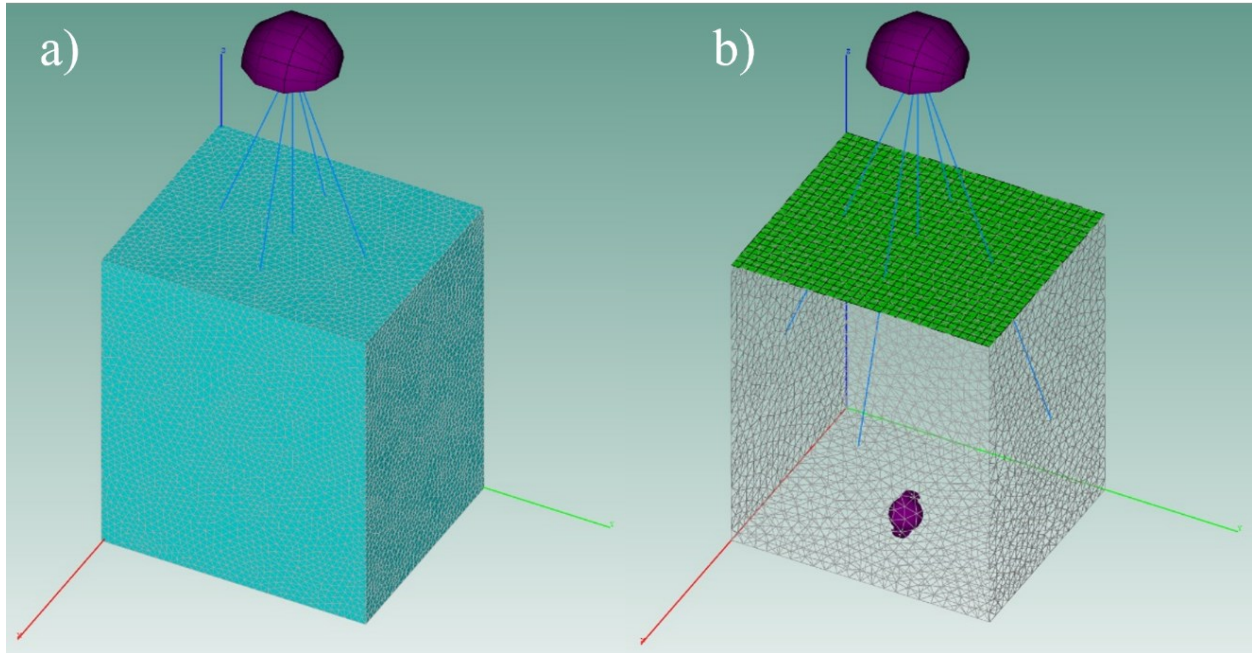


**Figure 12.3:** a) The VA One model showing the blue BEM measurement surfaces, and the purple hemisphere represents the fluid. b) The BEM model of the enclosure shows the flexible panel (green), location of the internal noise source (purple), and air cavity (gray).

The VA One model also performed a modal analysis of the enclosure. Figures 12.4a and 12.4b show the vibroacoustic modes of the rectangular enclosure from the VA One model. The fundamental enclosure mode appears to be adding an additional force on the plate. This model indicated the ideal locations to place the acoustic source and provided insights into what to expect during the experimental work.

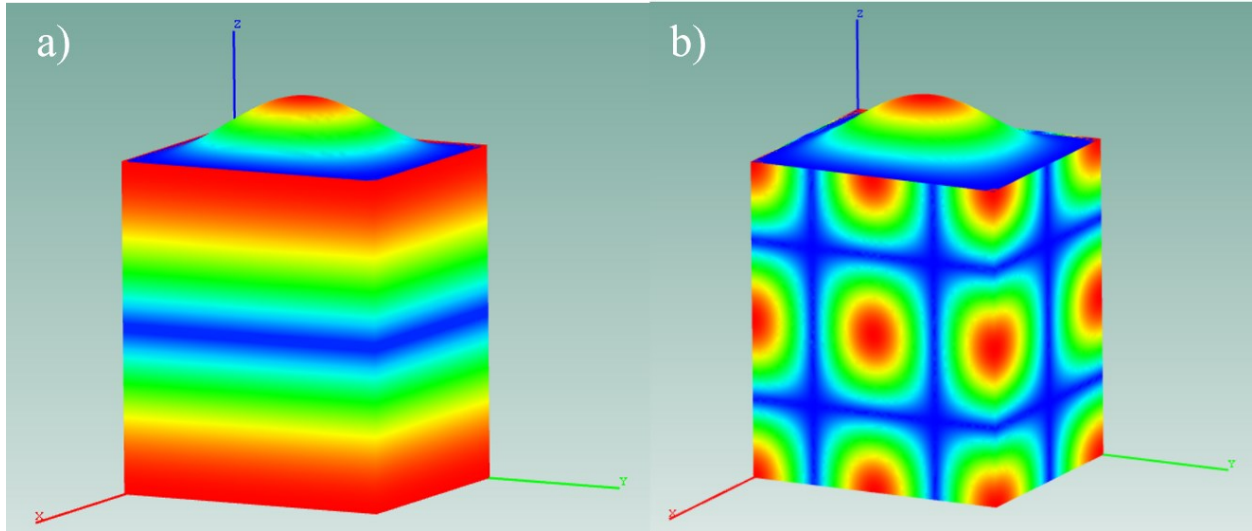


**Figure 12.4:** a) The vibroacoustic response of the enclosure showing the first mode of the enclosure and mode of the clamped plate. b) A higher order mode of the enclosure.

## 12.3 Experimental Work

Experiments conducted in BYU's reverberation chamber validated the I-VBSP method for sound power estimation. Figure 12.5 shows the experimental set up of the microphones and SLDV in the chamber. A loudspeaker emitted a broadband linear chirp signal (89 Hz to 11.2 kHz) in the chamber, while eight microphones recorded the signal's decay with all the equipment present to measure the acoustic absorption. Reverse Schroeder integration was used to estimate the OTO band  $T_{60}$  [4]. The  $T_{60}$  is the time it takes a sound to decay by 60 dB and is a common metric for talking about absorption in a room due to an impulse or sound. A good estimate of  $T_{60}$  enables the ISO 3741 standard to be applied correctly.

Figure 12.6a shows the SLDV set up. The raised SLDV can make a 2D scan of the aluminum plate on top of the enclosure. The blue tape on the inside perimeter of the steel frame reduces the glare of the ambient light from reflecting off the frame and hindering the SLDV scan near the plate

edges. A point-and-shoot laser from Polytec provided a reference for uncontrolled acoustic sources. This approach allows the SLDV to keep track of waves within the plate and improves the coherence of the measurement. The SLDV scans the surface of the aluminum plate (Fig. 12.6b) to obtain the surface velocities. From surface velocity data, normal velocities are computed, which are used to obtain the sound power levels of the source within the enclosure using the VBSP method.



**Figure 12.5:** The microphones set up to take the ISO 3741 measurement and the absorption measurements with the experimental set up in the reverberation chamber.



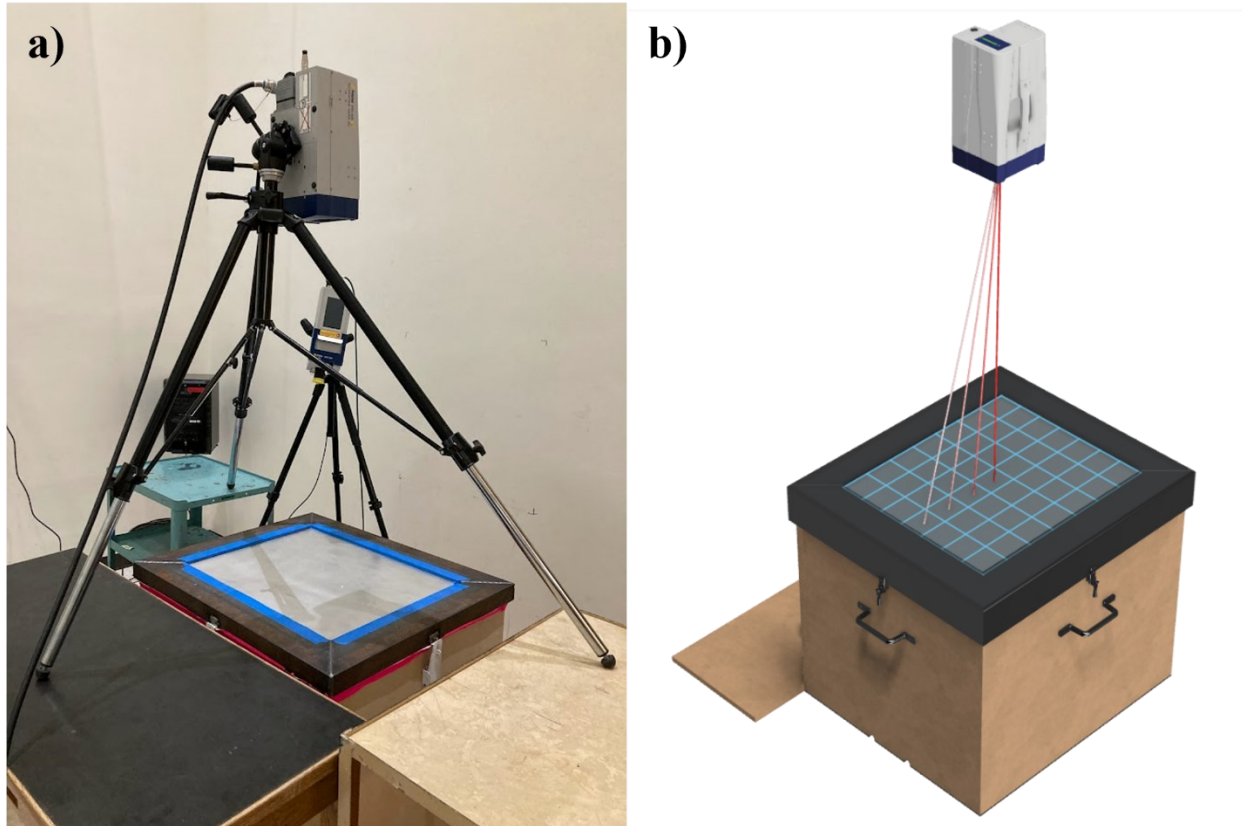


**Figure 12.6:** a) The SLDV set up to scan the aluminum plate while using a point-and-shoot laser as a reference for the source. b) Illustration of the Polytec SLDV scanning the vibrating surface of the flat plate to obtain sound power using the VBSP method. The pale laser color shows where the laser had been during the scanning process.

## 12.4 Results

As proof of concept for this method, a Bluetooth speaker was placed in this enclosure. Estimates of the sound power were obtained using ISO 3741 standard and VBSP. The Bluetooth speaker produced a broadband pseudorandom signal. Figure 12.7 shows the OTO band sound power levels for both the VBSP method and ISO 3741 standard. The difference in sound power level estimates between the methods is within 1 dB from the 200 Hz OTO band to the 10 kHz



band. This comparison indicates that the VBSP method accurately estimated the sound power from the Bluetooth speaker within the enclosure.

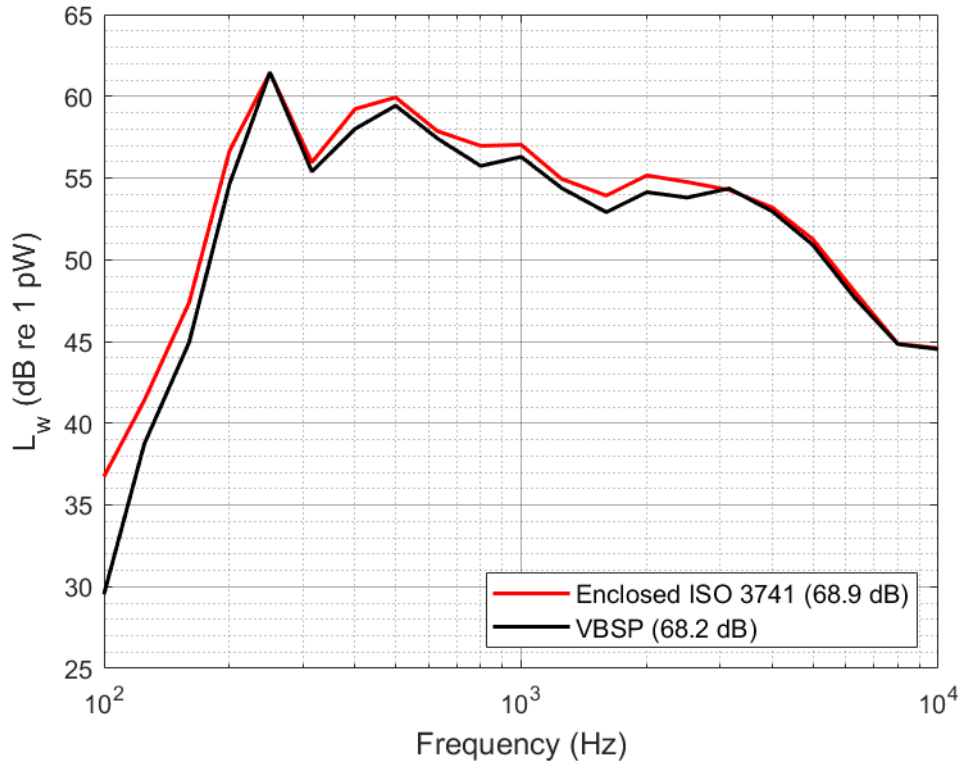


**Figure 12.7:** The sound power levels for a Bluetooth speaker in the rectangular enclosure obtained via the VBSP method and ISO 3741 are compared.

While the VBSP method accurately estimates the sound power levels of the Bluetooth speaker inside the enclosure, the I-VBSP results yield the sound power estimates of the Bluetooth speaker outside of the enclosure. The VBSP result is then calibrated (see Ch. 13) to remove the influence of the enclosure to estimate the free-field sound power levels of the speaker. Figure 12.8 illustrates the resulting I-VBSP estimates along with the estimates from the ISO 3741 standard applied to the speaker outside of the enclosure.

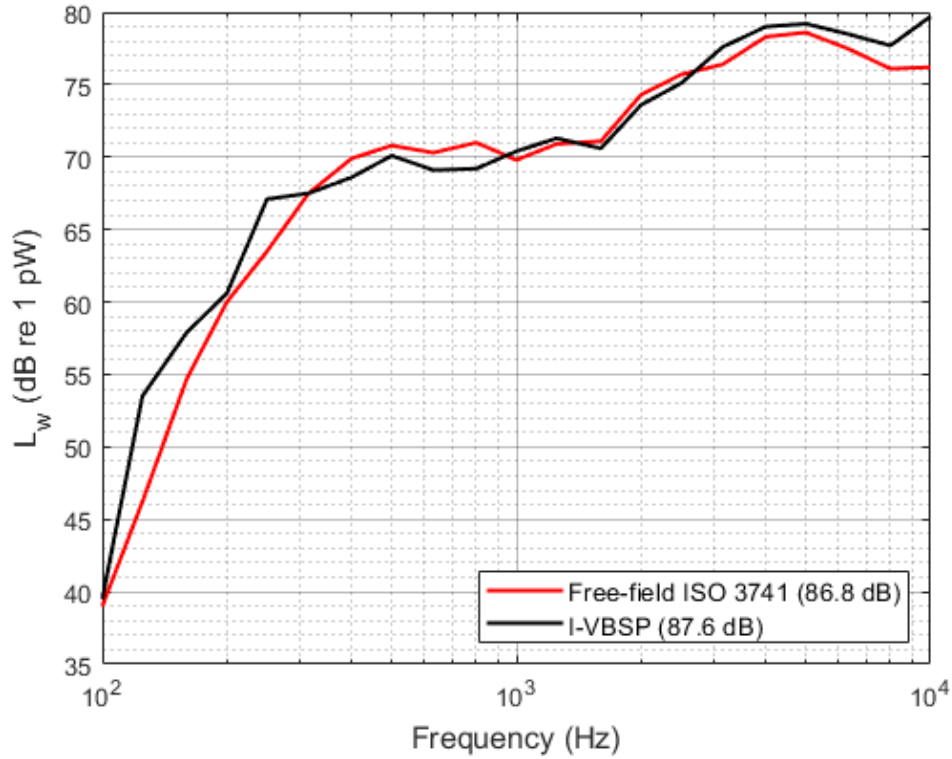


**Figure 12.8:** Comparison of I-VBSP and free-field ISO 3741 for sound power levels of the Bluetooth speaker outside of the enclosure.

To further quantify the agreement between these two sound power methods, Table 12.1 summarizes the sound power levels obtained using the I-VBSP method and the ISO 3741 standard and the difference between the methods. The difference in overall sound power level is 0.8 dB, and the difference in OTO band sound power levels is within 1 to 2 dB from 315 Hz to 8 kHz. The slight reduction in accuracy of the I-VBSP method compared to the accuracy of the VBSP step likely emanates from the calibration curve that was applied. More discussion of this topic and improved calibration curve appears in Ch. 13.

**Table 12.1:** OTO band sound power levels from ISO 3741 and I-VBSP method. The difference in the overall sound power level is 0.8 dB, and the difference in OTO band sound power levels is within 1 to 2 dB from 315 Hz to 8 kHz.

OTO Frequency (Hz)	ISO 3741	I-VBSP	Difference (I-VBSP - ISO 3741)
100	39.0	39.5	0.5
125	46.2	53.5	7.3
160	54.7	57.9	3.1
200	60.0	60.6	0.6
250	63.5	67.1	3.6
315	67.5	67.5	-0.1
400	69.9	68.6	-1.3
500	70.8	70.1	-0.7
630	70.3	69.1	-1.2
800	71.0	69.2	-1.8
1000	69.8	70.4	0.6
1250	70.9	71.3	0.4
1600	71.1	70.6	-0.5
2000	74.3	73.6	-0.8
2500	75.7	75.1	-0.6
3150	76.4	77.6	1.2
4000	78.3	79.0	0.7
5000	78.6	79.2	0.6
6300	77.5	78.5	0.9
8000	76.1	77.7	1.6
10000	76.2	79.7	3.5
<b>Overall Sound Power Level</b>	86.8	87.6	0.8

## 12.5 Conclusions

The I-VBSP method provided accurate sound power estimates of a Bluetooth speaker within 1 to 2 dB of the ISO 3741 standard from 315 Hz to 8 kHz. This method will enable a user to scan a single face and obtain overall sound power levels of a source. It also works for the mylar enclosure discussed in Chs. 10 and 11. Later experiments during this study of the rectangular

enclosure revealed that the absorption in the room needed to be accounted for, which would have improved the I-VBSP result for the mylar enclosure.

Applying the I-VBSP method to some other noise sources such as a blender, hand mixer, drills, and razors encountered a greater challenge. These sources were recorded one at a time in an anechoic chamber for five minutes to verify whether they were stationary. The recorded sources used were found to be non-stationary across OTO bands. This led to changing sound power levels during the ISO 3741 measurements which likely affected the accuracy of the calibration curve. The non-stationary acoustic excitation of the plate yielded greater incoherence between the SLDV scan and the reference laser since the vibration was changing during the scan. Chapter 15 details future work for the I-VBSP method.

## 12.6 References

- [1] M. Kleiner and J. Tichy, *Acoustics of Small Rooms*, (CRC, New York, 2017), pp. 28-32, 37-48, 64-71.
- [2] L. E. Kinsler, A. R. Frey, A. B. Coppens, & J. V. Sanders, *Fundamentals of Acoustics*, 4th ed. (John Wiley & Sons, New York, 2000), pp. 286-291.
- [3] H. Kuttruff, *Room Acoustics*, 5th ed. (CRC Press LLC, 2009), pp. 83-91.
- [4] M. R. Schroeder, "New Method of Measuring Reverberation Time," *J. Acoust. Soc. Am.* **37**, 409-412 (1965).

## Chapter 13 Rectangular Enclosure Calibration

### 13.1 Introduction

To gather all of the research pertaining to the I-VBSP method in this dissertation, this chapter contains work published in the Acoustical Society of America's *Proceedings of Meetings on Acoustics*. I co-authored this paper with undergraduate research assistant, Naomi Jensen. This paper serves as an example of the process laid out in Chs. 10 and 11. The focus of this paper was to calibrate the new enclosure design discussed in Ch. 12.

*\*\* I contributed to this paper by serving as a mentor to the first author, an undergraduate student, in all aspects of the I-VBSP testing and analysis. I taught her how to perform  $T_{60}$  measurements, wrote a MATLAB© script to process the impulse data to calculate the OTO band  $T_{60}$  times, and showed her how to make ISO 3741 measurements. I also co-authored the paper and provided revisions. \*\**

## 13.2 Required Copyright Notice

The following article appeared in the Acoustical Society of America's *Proceedings of Meetings on Acoustics* and may be found at <https://doi.org/10.1121/2.0001788> under the title "The dependence of sound radiation on position of acoustic source in an enclosure." It is reproduced in its original published format here by rights granted in the JASA Transfer of Copyright document, item 3.

<https://pubs.aip.org/DocumentLibrary/files/publications/jasa/jascpyrt.pdf>

Citation:

N. Jensen, I. Bacon, and S. Sommerfeldt, "The dependence of sound radiation on position of acoustic source in an enclosure," *Proc. Mtgs. Acoust.* **51**(1), 065001 (2023).

I hereby confirm that the use of this article is compliant with all publishing agreements.

OCTOBER 10 2023

## The dependence of sound radiation on position of acoustic source in an enclosure **FREE**

Naomi Jensen; Ian Bacon; Scott Sommerfeldt 

 Check for updates

*Proc. Mtgs. Acoust.* 51, 065001 (2023)  
<https://doi.org/10.1121/2.0001788>



20 June 2024 04:44:22



 **ASA**

Advance your science and career as a member of the  
**Acoustical Society of America**

[LEARN MORE](#)





# POMA

Proceedings of  
Meetings on Acoustics

Volume 51

<http://acousticalsociety.org/>

## 184th Meeting of the Acoustical Society of America

Chicago, Illinois

8-12 May 2023

### Structural Acoustics and Vibration: Paper 4aSA3

## The dependence of sound radiation on position of acoustic source in an enclosure

**Naomi Jensen, Ian Bacon and Scott Sommerfeldt**

*Department of Physics, Brigham Young University, Provo, UT, 84602; [jensnao1@byu.edu](mailto:jensnao1@byu.edu);  
[icbacon@student.byu.edu](mailto:icbacon@student.byu.edu); [scott\\_sommerfeldt@byu.edu](mailto:scott_sommerfeldt@byu.edu)*

In some applications, acoustic sources may be confined to a small enclosure but still radiating sound outwards through the enclosure. However, the sound power that is radiated from the enclosure may potentially be impacted by the location of the source within the enclosure and the properties of the enclosure. The dependence of source position on sound power radiated from the enclosure was investigated using a small rigid rectangular enclosure with a flexible aluminum panel as one of the sides of the enclosure. An acoustic source was moved to numerous locations in the enclosure and sound power measurements were made using the ISO 3741 standard. Results will be shown to numerically quantify the effect of acoustic source position on radiated sound power. These results are used to develop a calibration curve between the sound radiated by the enclosed source vs. the sound radiated by the source in a free field environment. This curve can be used in the development of an alternative method of determining sound power for a source.

Published by the Acoustical Society of America



© 2023 Acoustical Society of America. <https://doi.org/10.1121/2.0001788>  
Proceedings of Meetings on Acoustics, Vol. 51, 065001 (2023)

Page 1

---

## 1. INTRODUCTION

Noise control is a major issue for many product developers and manufacturers, especially those who specialize in loud products such as appliances and tools. Thus, there is a need for reliable noise measurement methods. Sound power is a universally accepted metric for determining noise radiation from an acoustic source. It is considered a global metric because it quantifies the total sound emitted and does not depend on observer distance. The International Organization for Standardization (ISO) has established ten sound power measurement standards.<sup>1-10</sup> Seven of these standards require specialized acoustic environments like anechoic or reverberation chambers, making them inconvenient and expensive for many. Alongside the standards, ISO has published two technical specifications that utilize structural vibration methods to compute sound power.<sup>11,12</sup> However, these specifications do not afford high accuracy.

Addressing these limitations, a new sound power measurement method is being developed. This method, called indirect vibration-based sound power measurement (I-VBSP) method, involves placing an object that makes noise inside a small enclosure, thereby creating an “acoustic tent” around the object. A 3D scanning laser Doppler vibrometer (SLDV) is then used to scan one vibrating surface of the enclosure, and the total sound power is estimated. This method requires a calibration between free field and enclosed sound power of acoustic sources. In the creation of this calibration, it becomes important to understand how the sound power radiated from the enclosure changes with respect to the acoustic source position inside the enclosure. If the sound power of an enclosed object has a large dependence on position, then any potential calibration would be inaccurate for certain source locations. Thus, there is a need to quantify the effect of source location on enclosed sound power.

Preliminary work has been conducted at Brigham Young University to determine the effect of source position on enclosed sound power. One such study used a rectangular enclosure with four high impedance medium density fiberboard (MDF) walls, one rigid wall (the ground) and a thin mylar face as the acoustic tent enclosure.<sup>13</sup> The placement of a powered blender relative to the first and second axial pressure nodes was investigated. It was found that the sound power results indicated location-dependent variations when a combination of node and non-node locations were used for measurements. Above the 1 kHz one-third octave (OTO) band, the results varied over a range of +/- 1.5 dB from the average. However, when the sound power results with the source located at the node locations for the first and second axial modes were removed, there was less variation in sound power measurements. For these non-node location measurements, all but two OTO bands above 1 kHz had a variation of less than +/- 0.5 dB from the average. These results suggest that the position of the acoustic source relative to the first and second harmonic axial node planes does indeed influence the sound power produced from the enclosure. The position of source with respect to the first and second harmonic axial nodes is of particular interest. This is because these low modal planes have low density, and can guarantee an isolated response for the size of any acoustic source. However, as the modal value increases, the modal planes increase in density and become trivial relative to the size of acoustic source.

The focus of this research is to develop a calibration between the sound power of acoustic sources within an I-VBSP enclosure and the corresponding sound power in free field. The enclosure utilized for this research differs from the enclosure used in previous work, and it incorporates a greater number of acoustic sources to establish a more robust calibration. The calibration process involves assessing the flexibility users have in object placement within the enclosure while maintaining acceptable sound power results. This builds upon the foundational work of previous research, which explored the impact of source placement on enclosed sound power. The goal is to quantify this influence for a significant variety of acoustic sources, ultimately providing error estimates for the final calibration.

## 2. METHODS

### A. FREE FIELD MEASUREMENTS

The calibration process for the enclosure involved seven carefully selected acoustic sources: a Bluetooth speaker, edge grinder, circular saw, sander, rotary saw, blender, and hand mixer. These particular sources were chosen because of their ability to maintain a nominally constant volume velocity within the desired frequency range (100 Hz to 10 kHz) and to produce levels well above the noise floor of the reverberation chamber when placed within the enclosure. Free field sound power measurements of these seven sources were taken in the

reverberation chamber at Brigham Young University.<sup>14</sup> The measurements were conducted using the ISO 3741 standard, utilizing six  $\frac{1}{4}$ " PCB 130F20 microphones. These microphones were positioned at a minimum distance of 1.5 m from the source and at least 1 m away from all other microphones and reflective surfaces, as specified by the standard.

### B. ENCLOSED MEASUREMENTS

The I-VBSP measurement method requires an enclosure that surrounds the acoustic source of interest. The dimensions of the rectangular enclosure used for this calibration project are 0.78 m x 0.66 m x 0.56 m. Each side of the box consists of two layers of medium density fiberboard (MDF) with a damping foam material between them. The top is made of a thin aluminum sheet that is clamped down on the edges by a steel frame as shown in Fig. 1. The bottom is left open, allowing the enclosure to create a seal with the floor, effectively enclosing the acoustic source. In Fig. 2, the enclosure is shown tilted back so that the acoustic source may be repositioned.



*Figure 1: Top-down view of the I-VBSP enclosure.*



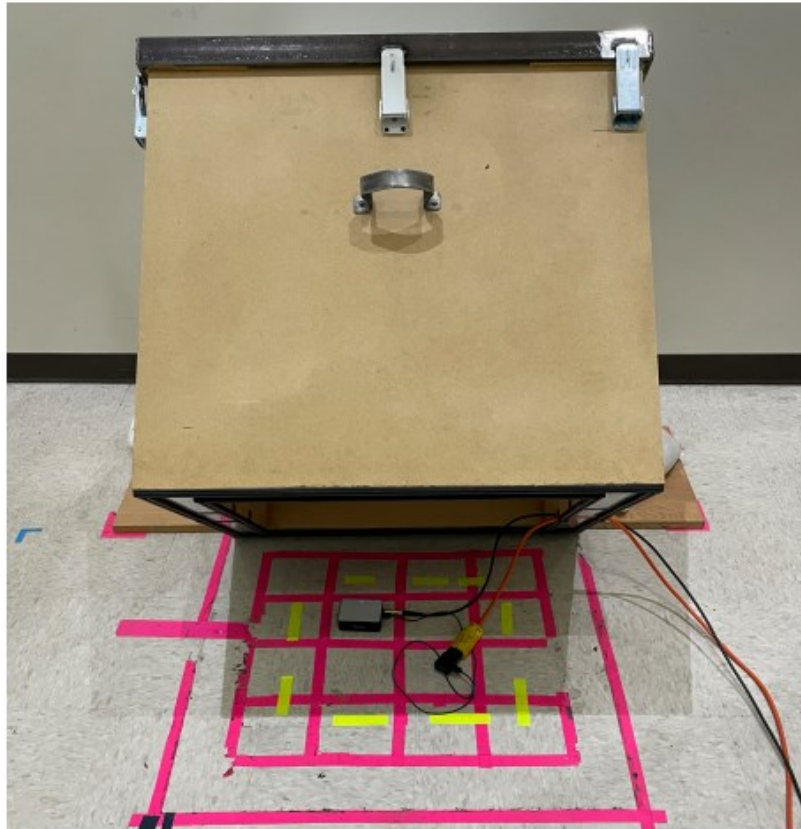


*Figure 2: Picture of the enclosed sound power measurement set up for a Bluetooth speaker.*

Each acoustic source was placed inside the enclosure and sound power measurements were taken. Like the free field measurements, all enclosed measurements were taken in accordance with ISO 3741 in the reverberation chamber. For each acoustic source, the source was moved to 11 different locations shown in Fig. 3. These source locations were grouped into three categories: edge location, node location, and non-edge non-node location. These locations were chosen to investigate how the position of acoustic source relative to these nodes and edges affect the sound power produced from the enclosure.

### **C. CALIBRATION PROCEDURE**

For each acoustic source, the average enclosed sound power was calculated across the OTO bands. The average enclosed measurement was then subtracted from the free field sound power measurement to obtain the calibration for that source. All seven calibrations were then averaged together to produce the final calibration of the enclosure.

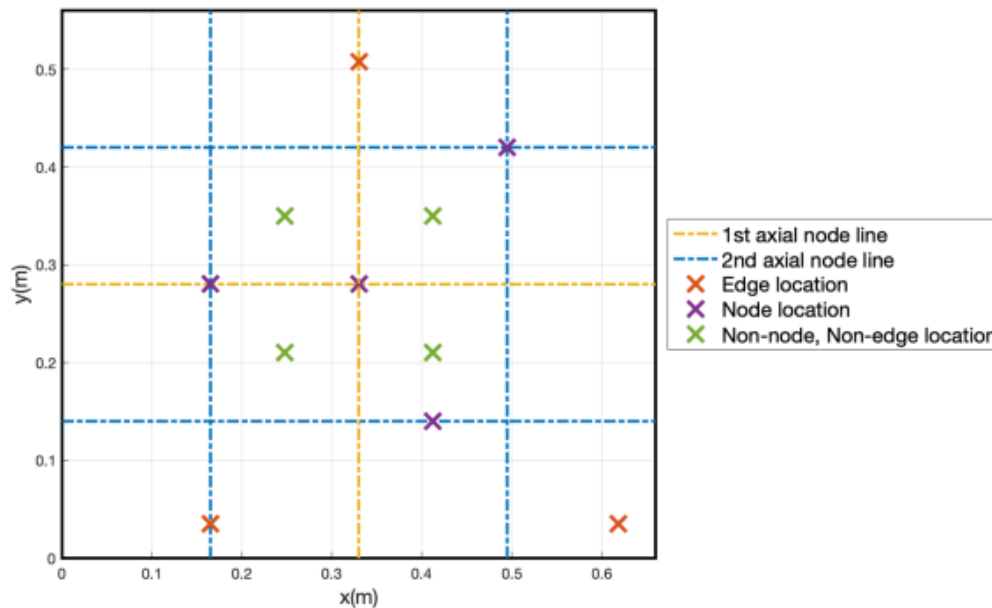
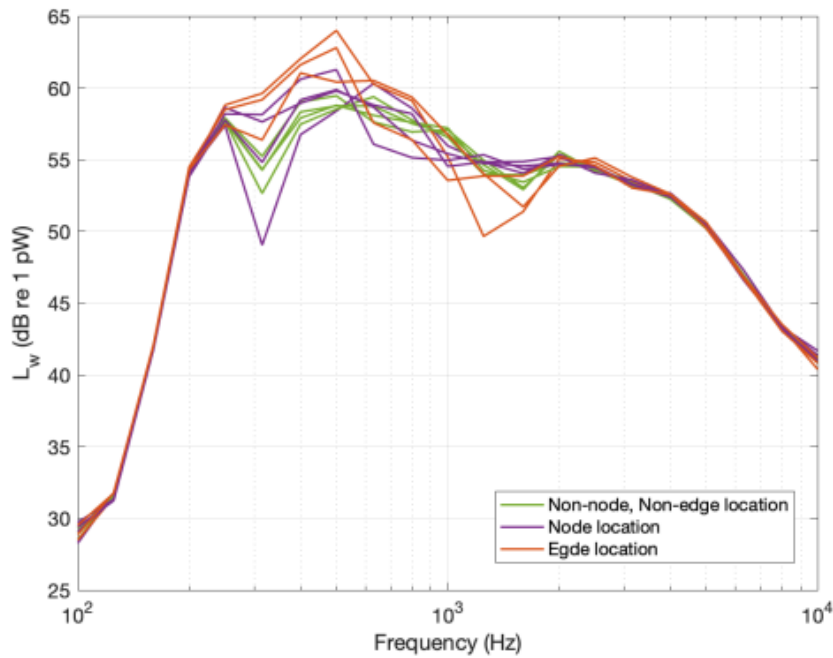


Figure 3: Top-down view of the 11 locations that each acoustic source was placed. All sources were placed on the ground in these locations.

### 3. RESULTS

#### A. ENCLOSED SOUND POWER MEASUREMENTS

Enclosed sound power measurements were taken in each of the 11 locations for the seven acoustic sources. Figure 4 shows the enclosed sound power measurement results of white noise from the Bluetooth speaker across the OTO bands. These results are grouped into the three categories that are once again delineated by color. As shown in the red curves, the ‘edge location’ sound power measurements show an increase in sound power around 500 Hz compared to the other location measurements. The ‘node location’ measurements also exhibit more variation in sound power in the 250-1000 Hz region, as well as a distinct grouping between 1-2 kHz. However, the ‘non-edge non-node’ location measurements, shown in green, are much more consistent from location to location. These results indicate that the enclosed speaker measurements exhibit a considerable degree of location dependence. This is likely due to the relative size of the Bluetooth speaker to the node plane positionings. The Bluetooth speaker measures 0.09 m by 0.06 m while the smallest distance between first and second harmonic nodal planes is 0.14 m. This means that the Bluetooth speaker can fit all of its noise radiating components entirely between the first and second harmonic nodal planes created by the enclosure. However, for larger sources, the location dependence becomes harder to distinguish through sound power measurements.



**Figure 4: Sound power measurements from the Bluetooth speaker while enclosed.**

One such example of a larger acoustic source is the circular saw that measures 0.18 m by 0.21 m. This means it cannot fit its entire structure between the first and second harmonic nodal planes. Figure 5 shows the enclosed sound power measurement results of the circular saw across the OTO bands. Like the enclosed speaker measurements, the enclosed saw measurements show a spread in sound power, particularly below 1 kHz. In contrast however, the circular saw results do not exhibit any predictable response based on location type. There are no general trends or distinct groupings that all sound power results of a certain location type follow. Thus, for larger acoustic sources, the enclosed power from that source is less location dependent than for smaller sources.

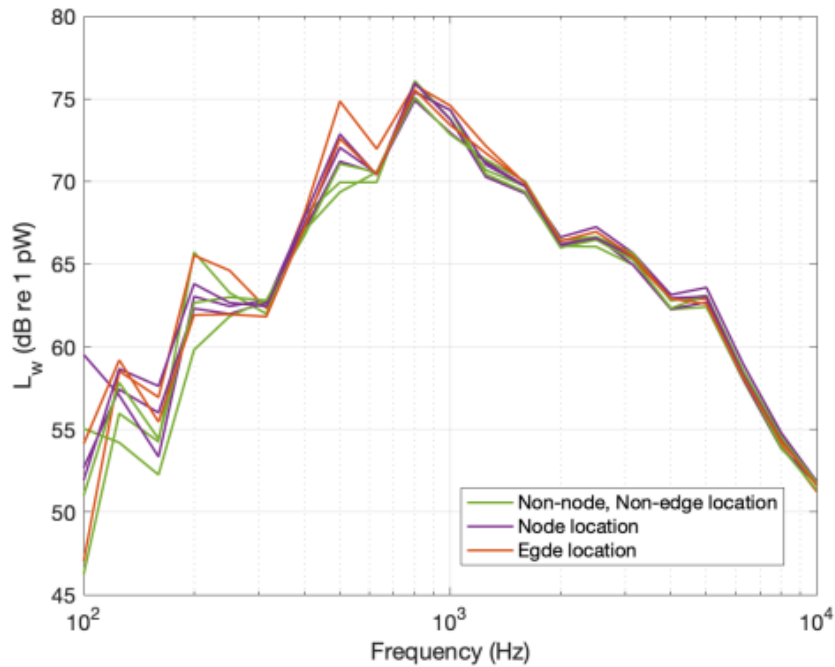


Figure 5: Sound power measurements of the enclosed circular saw.

## B. CALIBRATION

Figure 6 shows two calibrations created for the enclosure. One calibration, shown in green, was derived solely from measurements taken at ‘non-node non-edge’ locations for each average. The other calibration was calculated using all location types. Overall, the two calibrations exhibit remarkable similarity, differing by only 1 dB at 500 Hz. The strong correlation between these two calibrations suggests that any location-dependent variations in the overall calibration become insignificant when multiple source types are averaged together. This is likely attributed to the fact that larger sources tend to exhibit reduced location dependence in enclosed sound power results. This result highlights the considerable flexibility users have in placing the acoustic source within the enclosure while maintaining an accurate calibration above 1 kHz. However, the large error bars below 1 kHz indicate a large degree of variability in measurements across these lower frequencies. This is likely due to the modal density phenomenon described previously. The low modal planes have low modal density (large distances between node planes relative to all acoustic sources used). Thus, when compared to higher order axial nodes, the low order axial nodes are more sensitive to changes in position of acoustic source. The frequencies of these lower order modes lie below 1 kHz. This could explain the variation seen below 1 kHz.

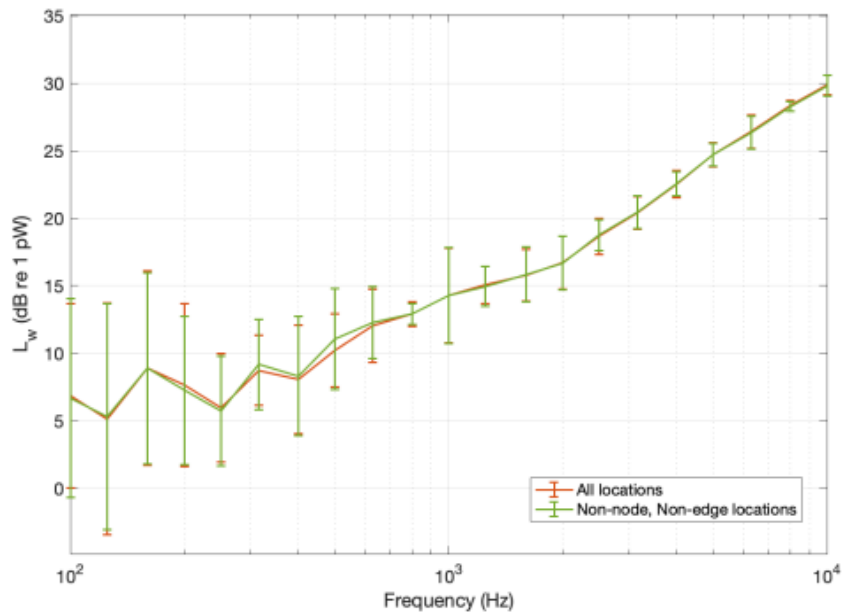


Figure 6: The two calibration curves created for the enclosure. The error bars represent 95% confidence interval.

#### 4. CONCLUSION

A total of seven acoustic sources were used to calibrate an I-VBSP enclosure. Through the process of relocating each acoustic source to 11 different positions and comparing the enclosed sound power across position types, it became evident that smaller acoustic sources demonstrate a higher degree of location compared to larger ones. To address this, an overall calibration was developed by averaging calibrations from each source type. When each of the source calibrations were averaged together, the final calibration showed minimal dependence on source location relative to nodal planes or edges. As a result, users of this enclosure can confidently place a source in various locations without compromising the calibration's accuracy.

#### ACKNOWLEDGEMENTS

The first author acknowledges the mentoring program of the College of Physical and Mathematical Sciences at Brigham Young University. The second and third author acknowledge the National Science Foundation for supporting this research. The authors also acknowledge Micah Shepherd for editorial assistance.

#### REFERENCES

<sup>1</sup> ISO 3741:2010. "Acoustics – Determination of sound power levels and sound energy levels of noise sources using sound pressure – Precision methods for reverberation test rooms" (International Organization for Standardization, Geneva, 2010).

<sup>2</sup> ISO 3743-1:2010. "Acoustics – Determination of sound power levels and sound energy levels of noise sources using sound pressure – Engineering methods for small movable sources in reverberant fields – Part 1:



---

Comparison method for a hard-walled test room” (International Organization for Standardization, Geneva, 2010).

<sup>3</sup> ISO 3743-2:2018. “Acoustics – Determination of sound power levels of noise sources using sound pressure – Engineering methods for small, movable sources in reverberant fields – Part 2: Methods for special reverberation test rooms” (International Organization for Standardization, Geneva, 2018).

<sup>4</sup> ISO 3744:2010. “Acoustics – Determination of sound power levels and sound energy levels of noise sources using sound pressure – Engineering methods for an essentially free field over a reflecting plane” (International Organization for Standardization, Geneva, 2010).

<sup>5</sup> ISO 3745:2012. “Acoustics – Determination of sound power levels and sound energy levels of noise sources using sound pressure – Precision methods for anechoic rooms and hemi-anechoic rooms” (International Organization for Standardization, Geneva, 2012).

<sup>6</sup> ISO 3746:2010. “Acoustics – Determination of sound power levels and sound energy levels of noise sources using sound pressure – Survey method using an enveloping measurement surface over a reflecting plane” (International Organization for Standardization, Geneva, 2010).

<sup>7</sup> ISO 3747:2010. “Acoustics – Determination of sound power levels and sound energy levels of noise sources using sound pressure – Engineering/survey methods for use in situ in a reverberant environment” (International Organization for Standardization, Geneva, 2010).

<sup>8</sup> ISO 9614-1:1993. “Acoustics – Determination of sound power levels of noise sources using sound intensity – Part 1: Measurement at discrete points” (International Organization for Standardization, Geneva, 1993).

<sup>9</sup> ISO 9614-1:1996. “Acoustics – Determination of sound power levels of noise sources using sound intensity – Part 2: Measurement by scanning” (International Organization for Standardization, Geneva, 1996).

<sup>10</sup> ISO 9614-1:2002. “Acoustics – Determination of sound power levels of noise sources using sound intensity – Part 3: Precision method for measurement by scanning” (International Organization for Standardization, Geneva, 2002).

<sup>11</sup> ISO/TS 7849-1:2009. “Acoustics – Determination of airborne sound power levels emitted by machinery using vibration measurement – Part 1: Survey method using a fixed radiation factor” (International Organization for Standardization, Geneva, 2009).

<sup>12</sup> ISO/TS 7849-2:2009. “Acoustics – Determination of airborne sound power levels emitted by machinery using vibration measurement – Part 2: Engineering method including determination of the adequate radiation factor” (International Organization for Standardization, Geneva, 2009).

<sup>13</sup> I.C. Bacon, S.D. Sommerfeldt, & J.D. Blotter, “Determination of radiated sound power from acoustic sources using the VBSP method and a mylar boundary”, *Proceedings of Meeting on Acoustics*, 46(1), 065003 (2022). <https://doi.org/10.1121/2.0001663>

<sup>14</sup> D.B. Nutter, “Sound Absorption and Sound Power Measurements in Reverberation Chambers Using Energy Density Methods”, Publication No. 28108904, [Master’s thesis, Brigham Young University], (2006).

# Unit 5

## Conclusions and Future Work

This unit consolidates the key findings from the research presented in the dissertation, emphasizing the advancements made in the development and application of the VBSP method. The conclusions summarize the contributions of each unit, demonstrating how these innovations have improved sound power measurement techniques. The unit then transitions into recommendations for future research, outlining the next steps needed to address unresolved challenges and explore new areas of application for the VBSP and I-VBSP methods.

## Chapter 14 Summary of Findings and Contributions

This dissertation presents several key contributions to the development and application of the Vibration-Based Sound Power (VBSP) method, advancing it as a robust tool for measuring sound power. The work in Unit 2 was pivotal in refining the VBSP method through experimental testing and the implementation of stitching techniques, now allowing for accurate 3D measurements. A specialized wall was designed and constructed within an anechoic chamber to measure the directivity of baffled sources, compliant with the ISO 3745 standard, thus enabling precise validation of the VBSP method's accuracy below 400 Hz. This infrastructure will be an asset for future research and coursework at BYU.

The research confirmed that the VBSP method can effectively compute sound power from *in situ* measurements. In Ch. 3, the VBSP method successfully computed sound power from baffled curved plates in varied acoustic environments, including anechoic, reverberant, and uncontrolled settings. Through experimental testing, it was demonstrated in Ch. 4 that the method is applicable to arbitrarily curved plates with stitching further enhancing its utility for these complex structures. Chapter 5 introduced a distance matrix and radiation resistance (**R**) matrix for thin unbaffled flat plates, which enabled the VBSP method to estimate sound power with great accuracy—within 1 to 2 dB above 1 kHz and within 3 dB below that threshold. This work lays a solid foundation for future studies involving unbaffled plates.

In Ch. 6, the vibroacoustic response of pickleball paddles was investigated. Testing identified the primary structural and acoustic modes excited during paddle-to-ball impact, with the membrane mode in the 950-1,450 Hz range as a major contributor to impact noise across ten paddle brands. Sound power levels were predicted using velocity data and the **R** matrix for a thin unbaffled flat plate. Although a direct comparison with the ISO 3741 standard was intended, limitations in

reverberation chamber precision during campus construction prevented this, leaving this task for future research.

A significant observation, discussed in Ch. 7, was that  $\mathbf{R}$  matrices for simpler geometries, such as baffled flat plates, cylinders, and simply curved plates, can approximate more complex geometries like baffled arbitrarily curved plates. This insight arises from the contraction or dilation of acoustic radiation modes across these geometries. These connections hold promise for simplifying future computational efforts.

In Unit 3, translational symmetry inherent in baffled structures was shown to produce Toeplitz symmetry in the  $\mathbf{R}$  matrix due to acoustic reciprocity, provided that the number of elements remains consistent across rows and columns (see Ch. 8). This symmetry significantly reduces computational demand by a factor of  $1/n$ , where  $n$  is the number of mesh elements. For unbaffled structures (see Ch. 9), a double-layer rotational symmetry was identified, yielding approximately a 75% reduction in computational effort. Together, these symmetries offer a promising approach to expedite calculations in applications involving the Kirchhoff-Helmholtz integral equation.

In Unit 4, three custom enclosures were designed and fabricated to allow the VBSP method to estimate sound power from sources with encased components that are otherwise challenging for scanning. This indirect VBSP (I-VBSP) approach was successfully demonstrated with a Bluetooth speaker over a 400 Hz to 10 kHz one-third octave (OTO) bandwidth, achieving accuracy within about 1 dB. Future research may include developing empirical calibration formulas for these enclosures and assessing their applicability to other noise sources.

Overall, this research establishes the VBSP method as a significant alternative for sound power measurement, especially in scenarios where traditional methods are limited, such as *in situ* testing in uncontrolled acoustic environments with variable conditions. While the VBSP method's

extended scan times remain a challenge, substantial progress has been made in reducing computational demands through physical and acoustical symmetries. Furthermore, enhanced 3D scanning and stitching techniques facilitate measurements of complex structures, and the potential to scale up the indirect method using an acoustic tent was demonstrated. This work lays the groundwork for future advancements, with the prospect of streamlining sound power estimation through fewer, more efficient scans around a structure.

# Chapter 15 Recommendations for Future Research

## 15.1 VBSP Method

For the VBSP method, there are several theoretical and computational steps. The theoretical development for thin and thick unbaffled plates needs to be finished. The study of joining two or more vibrating structures to compute the radiated sound power should be completed. The experimental validation of the VBSP method for composite structures to obtain sound power needs to be done. Finally, the generalized radiation resistance ( $\mathbf{R}$ ) matrix development will round off this project nicely. The development of a code to compute the shortest distances between all element combinations along the surface of a vibrating structure will help quantify the uncertainty using the general  $\mathbf{R}$  matrix.

## 15.2 Symmetry

The script to compute the geodesic between any two elements on a surface or given geometry will also need to incorporate high-performance computing (HPC) techniques will wrap this portion up for BEM and VBSP problems.

## 15.3 I-VBSP Method

While the Indirect Vibration-Based Sound Power (I-VBSP) method has proven effective for speakers, its application to other sound sources requires further investigation. Key areas of exploration include the impact of enclosure size relative to the internal source, the identification of additional acoustic sources that maintain a steady response, and the development of an empirical calibration formula potentially incorporating mass law principles so any enclosure can be constructed and effectively applied.

One approach is to use a sand-filled enclosure to enhance wall rigidity. The performance of various materials in this context is currently being evaluated. After successful verification of the I-VBSP method's precision for additional sources, a new rectangular enclosure (similar to that described in Ch. 12) can be constructed, which may involve filling the air gap with sand or concrete to increase rigidity. Previous enclosures in Unit 4 reduced acoustic transmission through the perimeter's four sides, but the goal is to make these sides rigid to direct as much acoustic energy as possible toward the flexible face. A calibration curve will need to be developed and with steady acoustic sources, a mylar face can also be used to significantly reduce the enclosure's weight.

The next phase may include implementing a cylindrical enclosure with a mounted circular plate to measure sound power from noise-induced vibrations in circular panels. This investigation will assess the advantages of cylindrical geometry over rectangular configurations.

Radiation from vibrating circular panels is particularly significant due to their prevalence in various engineering and acoustics applications, including electro-acoustic transducers, electrostatic speakers, earphones, microphones, diaphragms, covers, musical instruments, and structures. Preliminary investigations have focused on determining the radiated sound power from clamped and simply supported circular plates, utilizing the **R** matrix for low-frequency analysis

[1]-[5]. Researchers such as Rayleigh [6], Morse and Ingard [7], and Rao [8] have extensively studied the vibrations of circular panels. Initial identification of the first few radiation modes for circular plates has been conducted for potential use in Active Structural Acoustic Control (ASAC) [4]. However, partitioning these circular plates into equally sized elements presents challenges. Beckers [9] proposed a solution to partitioning the plate by dividing the plate into concentric rings, facilitating the creation of equal-area elements (though not necessarily of equal shape), as illustrated in Fig. 15.1. If an analytical expression for the  $\mathbf{R}$  matrix of a circular plate is desired, then employing the I-VBSP method using a circular plate on a cylindrical enclosure could facilitate experimental validation.

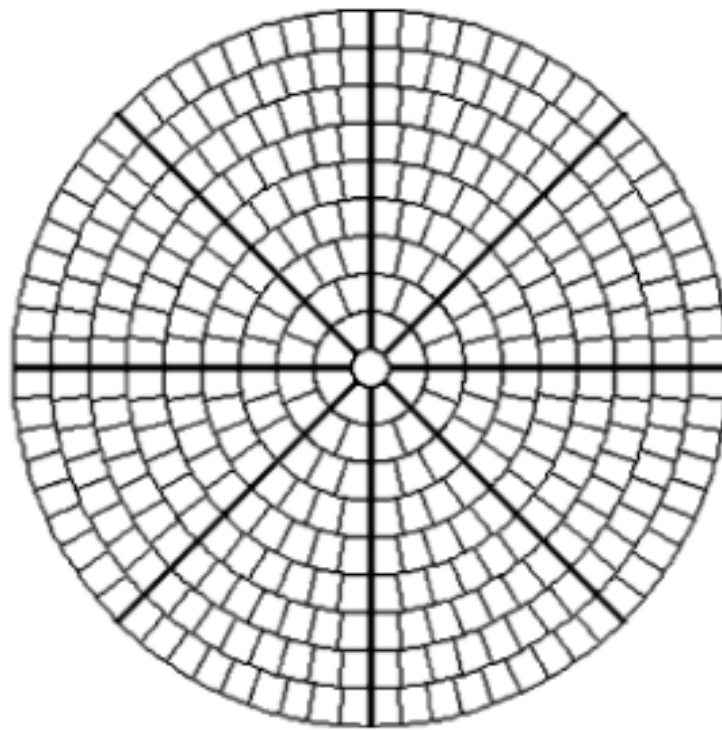


**Figure 15.1:** An example of the discretized circular plate using the methods described in [9].



## 15.4 References

- [1] W. P. Rdzanek, "Sound radiation of a vibrating elastically supported circular plate embedded into a flat screen revisited using the Zernike circle polynomials," *J. Sound Vib.* **434**, 92-125 (2018). doi: 10.1016/j.jsv.2018.07.035
- [2] W. P. Rdzanek Jr., W. J. Rdzanek, and Z. Engel, "Theoretical analysis of sound radiation of an elastically supported circular plate," *J. Sound Vib.* **265**(1), 155-174 (2003). doi: 10.1016/S0022-460X(02)01445-1
- [3] J. P. Arenas, "Matrix method for estimating the sound power radiated from a vibrating plate for noise control engineering applications," *Lat. Am. Appl. Res.* **39**(4), 345-352 (2009).
- [4] W. R. Johnson, P. Aslani, S. D. Sommerfeldt, J. D. Blotter, and K. L. Gee, "Acoustic radiation mode shapes for control of plates and shells," *Proc. Mtgs. Acoust.* **19**, 065036 (2013). doi: 10.1121/1.4799718
- [5] J. P. Arenas, "On the Sound Radiation from a Circular Hatchway," *Int. J. Occup. Saf. Ergon.* **15**(4), 401-407 (2009). doi: 10.1080/10803548.2009.11076819
- [6] J. Rayleigh, *The Theory of Sound: Vol. I*, 2nd ed. (Macmillan, New York, 1894), pp. 480.
- [7] P. M. Morse and K. U. Ingard, *Theoretical Acoustics*, (McGraw-Hill Inc., New York, 1968), pp. 642-649.
- [8] S. Rao, *Vibrations of Continuous Systems*, (Wiley, New Jersey, 2007), pp. 720.
- [9] B. Beckers and P. Beckers, "A general rule for disk and hemisphere partition into equal-area cells," *J. Comput. Geom.* **45**(7), 275-283 (2012). doi: 10.1016/j.comgeo.2012.01.011